Discipline of Engineering and Energy

Synthesis of electrolytic manganese dioxide (EMD) and biomass waste-derived carbon for hybrid capacitors

Wickrama Arachchi Muhandiramlage Kethaki Pabasara Wickramaarachchi

This thesis is submitted in fulfillment of the requirements

for the degree of

Doctor of Philosophy (Ph.D.)

at

Murdoch University

Perth, Australia

June 2022

Declaration

I declare that this thesis is my own research and does not incorporate any material previously submitted for a degree or diploma in any other University or institute of higher learning, and to the best of my knowledge and belief, it does not contain any material previously published or written by another person except where the acknowledgment is made in the text. I also acknowledge that the copyright of published manuscripts included in this thesis resides with the copyright holder of those works. I hereby grant Murdoch University the non-exclusive right for a copy of this thesis to be deposited in the University Library and on the web, through the University's digital research repository, subject to provisions of the Copyright Act 1968.

W A M K P Wickramaarachchi
June 2022

Dedication

To the people who have supported me throughout my education.

Thanks for making me see this adventure through to the end.

Acknowledgments

This Ph.D. project would not have been possible without the opportunity given by Murdoch University to offer me a doctoral scholarship. I'm grateful for all the personnel who have provided their valuable support.

I would like to express my sincere gratitude to my primary supervisor, Associate Professor Manickam Minakshi, for the continuous support and guidance and being patient to ensure my graduate experience and scholarly work are enriched. I owe my deepest gratitude to my co-supervisor, Dr. Xiangpeng Gao, for his assistance and critical review of the work in completing this thesis. My sincere thank goes to Associate Professors Gamini Senanayake and David Henry for their encouragement and insightful comments.

I would like to thank the Microscopy and Microanalysis Facility (MMF) - John de Laeter Centre at Curtin University. I would also like to acknowledge the ANSTO at Lucas Heights, Australia for providing beam time for neutron powder diffractometer ECHIDNA (Proposal 8656) and the Australian Synchrotron for providing beamtime for THz/Far-infrared (Proposal 16929). I'm incredibly thankful to the staff members in the discipline of Engineering and Energy, Chemistry and Physics at Murdoch University.

Special thanks to my friends Jinping, Vida, and Voon for the stimulating conversations and for giving me a hand whenever needed. I would like to thank my colleagues Prati, Rukshima, Dessy, Saleha, Seema, Dag, Ferdous, Dean, and Mohammet, for all the support and company.

Finally, I must express my profound gratitude to my parents for their unconditional love, care, and sacrifices in educating and preparing me for my future. I am very much thankful to my husband Solitha for his love, admiration, understanding, and unwavering support.

Abstract

Renewable energy (RE) is expected to be the primary energy supplier in the future energy mix. This has created the necessity for low-cost, safe, and reliable energy storage to guarantee a continuous energy supply by the intermittent RE sources. Due to the inbuilt rich chemistry of manganese dioxide (MnO_2) and the advantageous characteristics; of low cost, environmentally friendliness, and nontoxic, it can be adapted for a wide range of applications such as biosensors, humidity sensors, catalysts, and so on. Among the different forms of MnO_2, electrolytic manganese dioxide (EMD) is well-demanded energy storage material. However, the limitations such as lower capacitance, irreversibility, and cyclability of EMD in comparison with other metal oxides such as cobalt and nickel oxides, have hindered its application in capacitor energy storage, which was one of the focuses of this thesis.

Therefore, this Ph.D. research project aimed at synthesizing modified EMD materials as the positive electrode for hybrid capacitor applications. The modified EMD was coupled with the biomass-derived activated carbon (AC) which is synthesized as the negative electrode to fabricate hybrid capacitors. This Ph.D. research work has contributed to the existing knowledge through the following: 1) synthesizing pristine EMD using galvanostatic electrodeposition and studying its suitability for capacitor applications via experimental and theoretical analysis, 2) biopolymer alginate assisted EMD synthesis and optimization via experimental and computational modeling, 3) studying the effect of varying surfactants to improve the electrochemical characteristics of EMD, 4) synthesis of biomass waste-derived activated carbon and modeling their parameters for capacitance prediction.

The results indicated the challenge and importance of the delicate tailoring of the EMD characteristics for capacitor application. Pristine EMD was synthesized under different electrodeposition experiment conditions by varying applied current density (100, 200, 300 A m^{-2}) and deposition duration (4, 5, 6 h). The electrodeposition was carried out in a low acidic medium electrolytic bath where a lead (Pb) anode and stainless steel (SS) cathode were used. The EMD was deposited on the Pb anode via Mn^{2+} oxidation to form Mn^{4+} and its oxide MnO_2. The physicochemical and electrochemical characterization of the obtained EMD powder concluded that the material deposited at

200 A m^{-2} for 5 hours, showing the spindle-like morphology was suitable over others for supercapacitor (SC) application. The pristine EMD at these experimental conditions delivered 98 F g^{-1} capacitance at 1 mA cm^{-2} applied current density tested in 2 M NaOH aqueous electrolyte and proved its potential development by modifying its characteristics. Therefore, the pristine EMD was modified by introducing the biopolymer alginic acid crosslinking to improve its electrochemical performance. The alginic acid was added to the electrolytic bath at varying concentrations; 0, 0.1, 0.25, 0.5, and 1 g l^{-1}, to optimize the added bio-polymer amount to maximize the capacitance. At 0.5 g l^{-1}, the pristine EMD morphology was rearranged to a cactus-shaped with flutes. The calculated specific capacitance of the modified EMD was ~5 times higher (487 F g^{-1}) than the pristine EMD. The molecular dynamics simulation results determined the polymer-ion interactions in the electrolytic bath and provided evidence, showing that the alginic acid could act as a template for binding the Mn^{2+} ions in a relatively ordered manner for the growth of the EMD deposit. 0.42 of pyrolusite and 0.58 of ramsdellite fractions present in the modified material were quantitatively determined using the neutron powder diffraction (NPD) data. The slight increments of the lattice spacing observed in high-resolution transmission electron microscopy (HRTEM) images were well aligned with the NPD results of unit cell volume expansions of the EMD-polymer composite showing the polymer intercalation within the EMD structure influencing its characteristics. At 2 mA cm^{-2}, the fabricated hybrid capacitor delivered 52 F g^{-1} specific capacitance, 14 Wh g^{-1} specific energy, 500 W g^{-1} specific power, and 94 % capacitance retention over 5000 cycles. The results highlighted the importance of the functional molecular structure of the biopolymer alginic acid to produce a binary composite of EMD-polymer as a capacitor material.

Further, the pristine EMD was modified by electrodepositing the MnO_2 using surfactant mediated electrolyte solutions. The electrochemical performance of the synthesized EMD in the presence of three novel cationic surfactants was compared with the pristine EMD and the EMD co-deposited with commonly used cetyltrimethylammonium ammonium bromide (C-AB) surfactant. The three surfactants with different molecular structures are Tetradecyltrimethylammonium bromide (T-AB), Didodecyldimethylammonium bromide (D-AB), Benzyldodecyldimethylammonium bromide (B-AB) used at varying concentrations (15, 30, 60 g l^{-1}) in the electrolytic bath. Among the B-AB surfactant at 30 mg l^{-1}, the

EMD (EMD/B-AB_{30}) showed the highest capacitance of 602 F g^{-1} tested at 1 mA cm^{-2} current density. The molecular dynamics simulation indicated that when the B-AB surfactant was attached to the Pb electrode via electrostatic, Van der Walls interactions, then the nucleation of MnO_2 particles occurred surrounding the surfactant molecule. The unique molecular structure influenced the nucleation formation well-ordered, whereas, for pristine EMD, the nucleation was random. The hybrid capacitor comprises the best performed modified EMD (EMD/B-AB_{30}), and biomass waste-derived AC exhibited 91 F g^{-1} specific capacitance, an outstanding energy density of 32.4 Wh kg^{-1} for a corresponding power density of 971 W kg^{-1}.

Valorization of the biomass waste, Mango seed husk (MS), and the Grape marc (GM) was carried out by converting the waste into AC for capacitor electrodes. The MS was carbonized, followed by chemical activation using KOH as the activating agent. Activation temperature was varied at 800, 900, 1000, and 1100 °C temperatures, among at 1100 °C highest surface area of 1943 m^2 g^{-1}, and the specific capacitance of 135 F g^{-1} was obtained for the MS-AC. The MS-AC experimental data were incorporated in four machine learning (ML) algorithms; linear regression (LR), decision tree (DT), support vector regression (SVR), and multi-layer perceptron (MLP) for capacitance prediction. Among, the MLP model showed the best correlation (R^2 = 0.9868) between the experimental and predicted capacitance values and proved its potential application for computing the complex non-linear relationships between the input and output datasets. Further, the porous carbon materials were derived from GM using four synthesis routes by varying the parameters of activating agent (KOH and $ZnCl_2$), dopant (Nitrogen), and carbonization (450, 600 °C) and activation (450, 800 °C) temperatures. Among the different GM-AC products, the GM carbon, doped with urea and activated by KOH (KAC_{urea}), exhibited better morphology, hierarchical pore structure, larger surface area (1356 m^2 g^{-1}), and the highest specific capacitance of 139 F g^{-1} in 2 M NaOH aqueous electrolyte. The miscellaneous collection of datasets based on AC experiments was used for specific capacitance and power prediction using the MLP ML model.

Overall, this thesis showed that the EMD could be produced in bulk to be used for hybrid capacitor applications. Particularly, it provided insights about the specie interactions in the electrolyte solution that improved the material performance. This built the platform for further studies on altering the additive concentrations and

combinations for developing high-performing EMD materials. This Ph.D. work also highlighted the opportunities to valorize the biomass waste to produce AC with desired characteristics of hierarchical pore structure, larger surface area, etc., to replace the conventional AC electrodes. Finally, the electrochemical performance of the hybrid capacitor fabricated using best performed EMD material (EMD/B-AB_{30}) and biomass-waste derived AC (MS-AC 1100) surpassed the energy density values of the existing supercapacitors, proving its potential development in commercial applications.

Publications and achievements from this thesis

Peer-reviewed journal papers

Kethaki Wickramaarachchi, Manickam Minakshi, "Consequences of electrodeposition parameters on the microstructure and electrochemical behavior of electrolytic manganese dioxide (EMD) for supercapacitor", Ceramics International 2022 48 (14), 19913-19924, https://doi.org/10.1016/j.ceramint.2022.03.266

Kethaki Wickramaarachchi, Manickam Minakshi, David J. Henry, and Xiangpeng Gao, "Alginate Biopolymer Effect on the Electrodeposition of Manganese Dioxide on Electrodes for Supercapacitors" ACS Applied Energy Materials 2021 4 (7), 7040-7051, https://doi.org/10.1021/acsaem.1c01111

Kethaki Wickramaarachchi, Manickam Minakshi, David J. Henry, "Surfactant-mediated electrodeposition of a pseudocapacitive manganese dioxide a twofer" Journal of Energy Storage 2022 55 (A), 105403
DOI: https://doi.org/10.1016/j.est.2022.105403

Kethaki Wickramaarachchi, Manickam Minakshi, Xiangpeng Gao, Rukshima Dabare, Kok Wai Wong, "Hierarchical porous carbon from mango seed husk for electro-chemical energy storage", Chemical Engineering Journal Advances 2021 (8), 100158, https://doi.org/10.1016/j.ceja.2021.100158

Kethaki Wickramaarachchi, Manickam Minakshi, S.Assa Aravindh, Rukshima Dabare, Xiangpeng Gao, Zhong-Tao Jiang, and Kok Wai Wong, "Repurposing N-Doped Grape Marc for the Fabrication of Supercapacitors with Theoretical and Machine Learning Models", Nanomaterials 2022, 12, 1847, https://doi.org/10.3390/nano12111847

Conference and symposia

Kethaki Wickramaaracchchi, Manickam Minakshi, "Electrolytic Manganese Dioxide/Activated Carbon Hybrid Capacitor for Energy Storage", Postgraduate research competition - 2021, WA Universities, IChemE, Engineers Australia.
Runner up in the competition

Kethaki Wickramaaracchchi, Manickam Minakshi, Xiangpeng Gao, "Repurposing Winery Waste in Western Australia for Future Energy Storage" Poster competition for postgraduate students, Royal Society of Western Australia, 2021.

Table of contents

List of Figures

List of Tables

Nature of thesis

This thesis is prepared and formatted as a thesis by publication. The individual chapters of Chapters 3, 4, 5, 6, and 7 have been published in peer-reviewed journals. In relevant chapters, the references are formatted in accordance with the requirements of the journal of publication. Necessary modifications have been made for the headings, figures, tables, equations numbering, and style to keep the clear and consistent presentation flow throughout the thesis. The content of the supplementary information from the published version has been incorporated into the chapter to improve the clarity of the thesis. Inevitably, some content, particularly in the chapter introductions, can be repetitive up to a certain degree due to the nature of the publications. Additional paragraphs are added at the end of each chapter to link to the next chapter.

Author contributions to the thesis

Contributor	Contribution (%)	Nature of contribution
Kethaki Wickramaarachchi	70	Conceptualization, experimentation and data collection, data analysis and interpretation, drafting, reviewing, and editing thesis chapters.
Manickam Minakshi	30	Conceptualization, interpretation of data, critical revision of the thesis in respective areas.
Xiangpeng Gao		Critical revision of the thesis in respective areas.
David Henry		Molecular dynamics modeling and data interpretation.
Rukshima Dabare		Machine learning modeling.
Kok Wai Wong		Machine learning data interpretation.
Assa Aravindh		Density functional theory insights and data interpretation.
Zhong-Tao Jiang		Procured funding for the research project.

By signing this document, the Candidate and Principal Supervisor acknowledge that the above information is accurate and has been agreed to by all other authors.

Candidate

Principal Supervisor

Chapter 1 Introduction

The historical figure of fossil fuel consumption is as old as human civilization. The fossil fuel types; coal, crude oil, and natural gas, played a constructive role in prehistoric times, supporting the evolution of humankind and still continue. Ever since, for more than two centuries, the energy requirement has increased due to growing population, technological development, economic development, and so forth. Fossil fuel occupies more than 80 % of the world's primary energy generation for transportation, domestic usage, thermal power stations, etc. On the one hand, the large energy consumption depletes the fossil fuel reserves, while on the other hand, it increases the global climate change risk. Since the late 1970s, a significant increment in average global temperature has been experienced, which has resulted in this tragic incident of global warming due to the emission of greenhouse gases, primarily carbon dioxide (CO_2). The other compounds such as CH_4, CFCs, halons, NO_x, SO_x, ozone, and peroxyacetyl nitrate also contribute to this phenomenon as heat-trapping gases. In fact, it has already alarmed about the energy crisis in the near future, which requires proactive solutions to fulfill growing energy demand [1–6].

Renewable energy is the best alternative to fossil fuel due to its desired qualities of being replenished, nearly zero carbon impact on the environment, and less operational cost. It will help achieve dual objectives of shifting to alternative energies while making the adverse effects of climate change minimal [7,8]. These natural energy resources, hydropower, biomass, solar, wind, geothermal, wave, and tidal, are converted into usable forms of energy such as electricity, heat, and fuel. Among those applications, solar home systems and water heaters are already on the market [5,9]. Currently, renewable energy supplies ~18 % of the total energy consumption, and it is expected to have a 30-80 % share in 2100. Thus in the future, it will be a prominent contributor to the energy mix to fulfill the growing energy demand [9,10]. It has been reported that renewable energy can provide 3000 times more magnified amounts than the current energy needs [8]. Solar and wind are the most effective, while the biomass, geothermal, marine, and hydro will fulfill the rest. According to the estimations, by 2035, a higher portion of the energy generation, nearly 31 %, will be used for electricity generation [8]. Even if it is sufficiently good compared to fossil fuel,

renewable energy sources depend on the time of the day and weather conditions. Thus, the rapid advancement of energy storage technologies is required for the efficient use of renewables to avoid the issues of energy shortages [7,11]. Batteries, fuel cells, and capacitors currently exist; however, none of them can be used as a standalone solution for energy storage. Therefore, the present energy storage systems should be improved while searching for new breakthroughs. Supercapacitors (SC) have several advantages, such as fast charging, longer cycling over conventional capacitors. However, the low energy density, cost of synthesis, availability of material resources are still challenging, therefore these aspects are presently being explored worldwide.

The capacitors, a form of electrical energy storage invented in 1745, have been developed into SCs with relatively higher energy densities. The conventional capacitor (dielectric capacitor) was composed of a pair of conducting plates (ceramic, glass, paper, plastic, aluminium oxide) separated by a dielectric medium. The plates get oppositely charged to form an electric double layer (EDL) by applying voltage from an external power supply. Accumulation of the opposite charges at the plates is shown in Figure 1.1. When connected to an external load, the current flows, and the entire amount of charge is delivered as energy. Due to the charge which is physically stored, the charge-discharge is highly reversible; hence the capacitor has an unlimited cycle life.

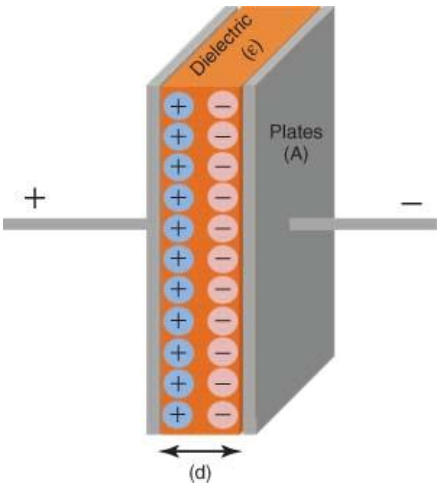

Figure 1.1 Charge arrangement in a dielectric material at the charged state of a conventional capacitor. Reproduced from ref. [12] with permission, copyright 2015, Wiley Online Library.

The charge stored (Q) is proportional to the capacitor voltage (V), and the capacitance (C) is the proportionality constant as given in the equation (1.1).

$$Q = CV \tag{1.1}$$

The capacitance (C in Farad/F) is directly proportional to the geometric area of the plate (A in m^2) and inversely proportional to the separation distance between the two plates (d in m), also depends on the permittivity (ε in F m^{-1}) of the medium. Accordingly, the capacitance is given by the equation (1.2).

$$C = \varepsilon A/d \tag{1.2}$$

The major drawback of the conventional capacitor is its low energy density. As evidenced by equation (1.2), increasing the surface area leads to higher capacitance. As a result, supercapacitors (SCs) were invented in 1957, unlike the conventional capacitors, the SCs are composed of high surface area materials and store more charge to deliver high capacitance values (Figure 1.2). Henceforth, the SCs are still being developed to bridge the gap between the capacitors and batteries. The SCs can be either symmetric or asymmetric configurations. In symmetric capacitors, both electrodes have the same capacitance, whereas in asymmetric, the two electrodes are different in terms of charge storage mechanism. In order to achieve the higher energy densities, increasing the specific capacitance of carbon-based electrodes by synthesizing novel carbon structures, developing pseudocapacitors using transition metal oxides, and conducting polymers (CPs), new electrolytes to enlarge the cell voltage are possible approaches.

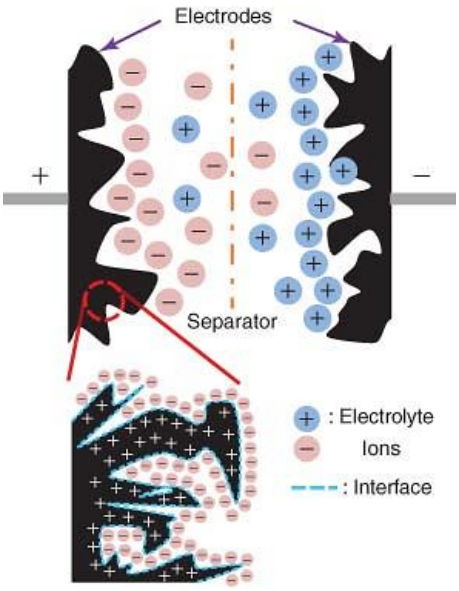

Figure 1.2 Schematic representation of the charged state of high surface area SC electrodes. Reproduced from ref. [12] with permission, copyright 2015, Wiley Online Library.

Generally, an SC can provide a high-power density (>10 kW kg^{-1}) and long cycle life (>10000 cycles) but lower energy density (~5 Wh kg^{-1}). SCs have a wide range of uses, such as portable electronic devices, memory backup systems, industrial power, and energy management [13]. Batteries tend to degrade during their continuous usage, which has also been overcome by the SCs [14]. The energy density (E) is proportional to the specific capacitance (C_{sp}) and the square of the cell voltage (V). The power density at a constant current relies on the energy value and the discharge time (t_d). For energy and power densities, the relationships are given by equations (1.3) and (1.4), respectively [15].

$$E = \frac{1}{2} C_{sp} V^2 \qquad (1.3)$$

$$P = \frac{E}{t_d} \qquad (1.4)$$

Increasing either or both of C_{sp} and V can scale up the energy density. The hybrid capacitors are composed of both battery type (e.g., metal oxide) and capacitor type (e.g., carbon) electrodes which can widen the application scope of the energy storage devices by increasing the energy densities without compromising the high-power

densities of capacitors. When coupling the two electrodes, it is essential to analyze their individual performance in an electrochemical cell to establish the potential window and calculate the capacitance. For this purpose, the electrochemical cell can be constructed using three electrodes: the working electrode (WE - with the material being analyzed), the counter electrode (CE - which completes the circuit allowing charge to flow through the cell), and the reference electrode (RE - which keeps constant potential independent of the solution properties), and an electrolyte solution as the ion-conducting medium. The electrode's surface acts as a junction between the ionic conductor and the electronic conductor. Figure 1.3 shows a schematic diagram of the three-electrode system.

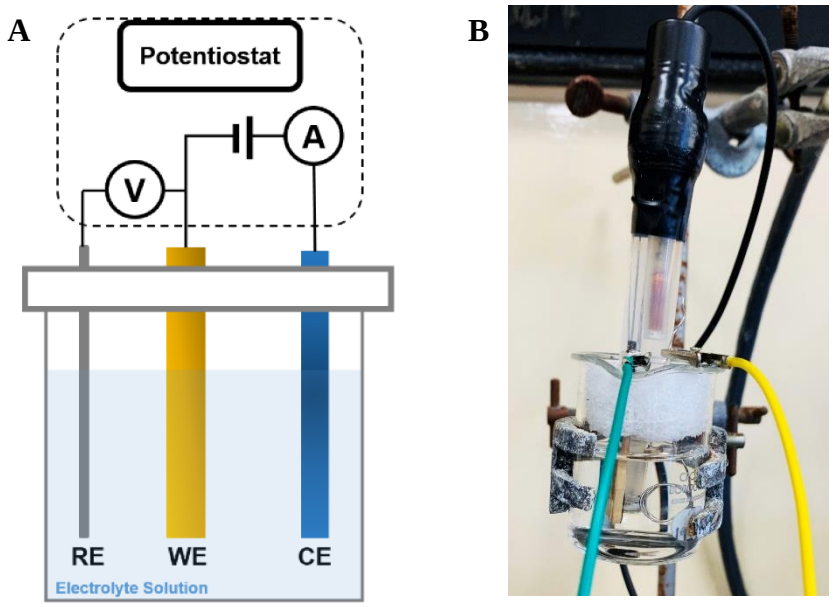

Figure 1.3 (A) Schematic representation of an electrochemical cell with three electrodes: working electrode (WE), counter electrode (CE), and reference electrode (RE). Reproduced from [16], open-access Creative Commons CC BY 4.0 license, MDPI., (B) The three-electrode cell composed of EMD (WE), Pt wire (CE), and Hg/HgO (RE) we have used for electrochemical performance tests of EMD in the laboratory at Murdoch University.

Once each electrode's potential window and the capacitance are determined, they can be used to construct the hybrid cell to maximize its performance. Cyclic voltammetry (CV), galvanostatic charge-discharge (GCD), and electrochemical impedance

spectroscopy (EIS) are the three widely used techniques in electrochemical performance analysis.

CV is the first analysis to carry out in electrochemical studies. CV studies give the details of the redox potentials of electroactive species, the potential window, faradaic-non faradaic contribution, and the effect of scan rate. The scan rate is the crucial parameter that can be changed over the experiment. The value of the scan rate indicates how fast the applied potential is varied. If the scan rate is at a constant value, the potential is linearly varied throughout the experiment. At low scan rates, the measured capacitance can be maximum, whereas the faster scan rates cause reducing the size of the diffusion layer, as a result, higher CV currents and lower capacitances can be observed. The obtained CV results can be reported using two conventions as given in Figure 1.4. The cathodic and anodic peaks (characteristic peaks shown in Figure 1.4) in the CV profiles occur due to a diffusion layer formation near the electrode surface. The diffusion layer thickness expanded with the surface concentration. The peaks reflect the continuous changes in the concentration. An increase in the peak current corresponds to diffusion control. When the starting potential is lower, then it gains a higher potential, referred to as anodic oxidation. The opposite is known as cathodic reduction [17]. The total charge passed is calculated from the CV by integrating the current with respect to voltage, then converted to specific capacitance as in the equation (1.5).

$$C_{sp,CV} = \int_{v^-}^{v^+} \frac{i\,dv}{V_s m \Delta v} = \frac{Q}{m\Delta v} \qquad (1.5)$$

where, $C_{sp,CV}$ - specific capacitance given by CV measurements (F g^{-1}), i - current (A), V_s - scan rate (V s^{-1}), m - active mass of working electrode (g), $\Delta v = (v^+ - v^-)$ - potential window (V). For a three-electrode cell, the voltage is applied with respect to the reference electrode.

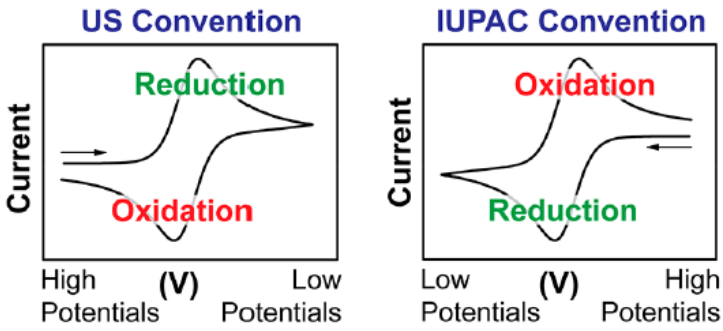

Figure 1.4 Commonly used conventions to report CV data. Reproduced from ref. [18] with permission, copyright 2018, ACS Publications.

The equilibrium of two concentrations of the specie at its oxidation state and the specie at its reduction state can be described by the Nernst equation. The Nernst equation relates the electrochemical cell potential (E) to the standard potential of species (E°) and the relative activities of the oxidized (Ox) and reduced (Red) analyte in the system at the equilibrium;

$$E = E° + \frac{RT}{nF} ln \frac{(Ox)}{(Red)} = E° + 2.3026 \frac{RT}{nF} log_{10} \frac{(Ox)}{(Red)} \qquad (1.6)$$

where, F – Faraday's constant, R – Universal gas constant, n – number of electrons, and T – temperature. The duck shape of the voltammogram (Figure 1.4) is due to several factors such as the concentration of oxidized vs. reduced forms relative to the distance from the electrode surface, the potential applied, and the movement of species between the electrode surface and the bulk solution. As a result, anodic and cathodic peaks can be observed in that the peak separation happens due to diffusion of the analyte to and from the electrode. If the reactions are reversible by means of chemically and electrochemically, the difference given by the anodic and cathodic peak potentials is called peak to peak separation (ΔE_P), is 57 mV at 25 °C (2.22 RT/F), and the width at half max on the forward scan of the peak is 59 mV [17].

Chemical and electrochemical reversibility is essential for a better performing material. In order to be chemically reversible, the analyte must be stable upon reduction reaction and be reoxidized. Typically, the process is not chemically reversible when the reduction reaction is homogeneous. Electron transfer kinetics

between the electrode and the analyte affects the electrochemical stability. The unstable electrochemical processes cause larger values of ΔE_p as it requires more negative (positive) potentials for reduction (oxidation). The electrochemically reversible process is known as "Nernstian" since that follows the Nernst equation (1.6).

In addition to the CV, galvanostatic charge-discharge (GCD) measurements can be used to determine the specific capacitance using the equation (1.7). The GCD tests are conducted at a constant charge/discharge current density. It can be used to determine the performance over time, the effect of different current densities, capacitance retention, etc. Figure 1.5 demonstrate the typical charge-discharge curves obtained for EDLC and pseudocapacitive materials.

$$C_{sp,CD} = \frac{i\,\Delta t}{m\,\Delta v} \qquad (1.7)$$

where, $C_{sp,CD}$ - specific capacitance given by charge-discharge measurements (F g^{-1}), i - specific current (A), Δt - discharge time (s).

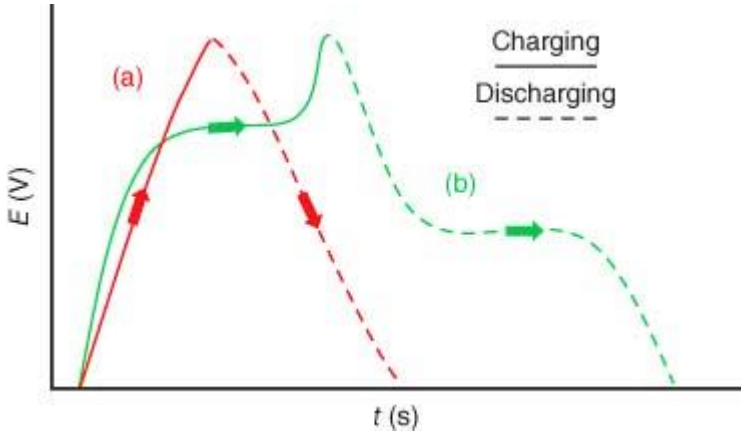

Figure 1.5 Galvanostatic charge-discharge plots of (a) EDLC and (b) pseudocapacitive materials. Reproduced from ref. [19] with permission, copyright 2015, John Wiley & Sons, Ltd.

Electrochemical impedance spectroscopy (EIS) is also an effective technique for understanding electrochemical reaction rates. Impedance is the complex resistance encountered when current flows through a circuit of combinations of resistors, capacitors, or inductors. Electrochemical transformation occurring at the electrode-solution interface can be modeled using components of the electronic equivalent

circuitry that correspond to the experimental impedance spectra. Particularly useful to model interfacial phenomena is the Randles and Eshler electronic equivalent-circuit model (Figure 1.6). It includes the double-layer capacitance ($C2$), the ohmic resistance of the electrolyte solution ($R1$), the electron transfer resistance ($R2$), and the Warburg impedance ($W2$) resulting from the diffusion of ions from the bulk solution to the electrode surface. The impedance of the interface derived by the application of Ohm's law consists of two parts, a real number Z' and an imaginary number Z'' [20]. Nyquist plots commonly include a semicircular region lying on the axis followed by a straight line. The semicircular portion (observed at high frequencies) corresponds to the electron-transfer limited process, while the straight line (characteristic of the low-frequency range) represents the diffusion-limited process. Such spectra can be used for extracting the electron transfer kinetics and diffusional characteristics. An impedance spectrum includes only a linear impedance representing a very fast electron transfer process, while a large semicircular region characterizes a very slow electron transfer process.

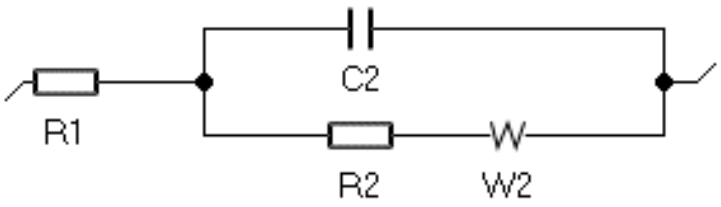

Figure 1.6 Randles circuit model fits the EIS data (drawn using the Z-fit tool in EC-Lab software.

When constructing the asymmetric/hybrid capacitor cell, the overall capacitance of two electrodes in series can be expressed as in equation (1.8) [21].

$$\frac{1}{C_T} = \frac{1}{C^-} + \frac{1}{C^+} \qquad (1.8)$$

where, C^- - capacitance given by the negative electrode, C^+ - capacitance given by the positive electrode, C_T - cell capacitance. When the two electrodes are identical (symmetric capacitor), the total capacitance becomes half of the electrode's capacitance. If the two electrodes have different capacitance values, C_T is dominated

by the electrode with a smaller capacitance. As discussed before, to increase the energy density of the capacitor, one electrode can be substituted using an alternative electrode with very high capacitance to fabricate an asymmetric/hybrid cell, which can be explained as follows.

Assume that, C^+ is the highest capacitance, then, $C^+ \gg C^-$, thus $\frac{1}{C_T} \approx \frac{1}{C^-}$, therefore, $C_T \approx C^-$. In this case, the capacitance obtained from the asymmetric cell nearly becomes twice the value for the symmetric cell.

In addition, the mass ratio of the two electrode materials should be optimized when used in the asymmetric/hybrid device to achieve its optimum performance in terms of specific energy. The following relationships are given in equations (1.9) [21] and (1.10) [22] are commonly used to maximize the capacitance and the cell voltage, respectively.

$$\left(\frac{m^+}{m^-}\right)_{C_{T\,max}} = \sqrt{\frac{C^-}{C^+}} \qquad (1.9)$$

$$\left(\frac{m^+}{m^-}\right)_{C_{T\,max}} = \frac{C^- \, \Delta {E_m}^-}{C^+ \, \Delta {E_m}^+} \qquad (1.10)$$

where, m^+ - mass of the positive electrode, m^- - mass of the negative electrode, $\Delta {E_m}^-$ - the potential window of the positive electrode, $\Delta {E_m}^+$ - the potential window of the negative electrode.

Accordingly, new asymmetric/hybrid capacitor energy storage devices can be developed using the two electrode types; a suitable battery-type material (nickel oxides, cobalt oxides, iron oxide, manganese oxides, etc.) and a porous carbon material. As previously mentioned (in paragraph 2), increasing use of non-steady renewable energies requires such systems with high specific energy and power, longer cycle life, low cost, and safety. It should be noted that it also concerns the material resource abundance, cost of synthesis, and recycling processes of the used materials. In fact, for all energy storage technologies, using the materials causing minimum footprint on the environment, eco-efficient synthesis, and recycling should be

considered in new research towards energy storage development. Mn is one of the most abundant metals and sustainable and has a high demand in the battery field. The potential use of Mn to produce the capacitor electrodes using facile, efficient synthesis can be examined and integrated into the energy storage field. In this thesis, we have focused on utilizing the electrolytic manganese dioxide (EMD) and biomass waste-derived porous activated carbon (AC) materials as positive and negative electrodes, respectively, to construct hybrid capacitors and optimize their performances. Figure 1.7 represents the two-electrode cell composed of EMD (+) and AC (-) electrodes used for electrochemical performance tests.

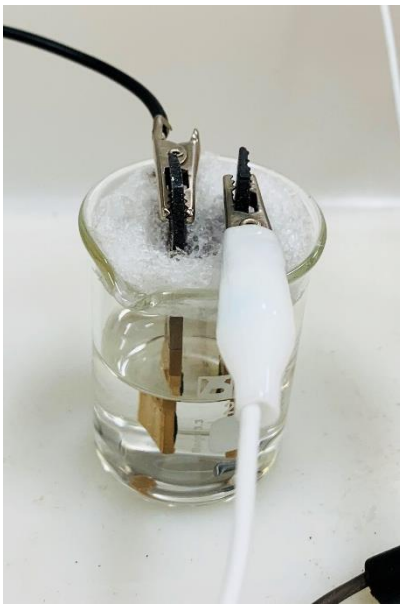

Figure 1.7 Electrochemical cell with two electrodes (EMD *vs.* AC).

Manganese dioxide (MnO_2) has a relatively long history as a battery material, commonly used in primary 1.5 V Zn/MnO_2 cells. Additionally, it can be found in rechargeable lithium-ion (Li-ion) batteries in the form of $Li_{1-x}Mn_2O_4$ incorporated as a cathode material [23]. In addition, the MnO_2 can be employed in supercapacitors (SCs) due to its high theoretical capacitance of ~1370 F g^{-1}, the fast redox chemical reactions at the electrode surface leading to high power densities in electrochemical performance. The other advantageous factors are low cost, low toxicity, and abundance on the earth [24–26]. MnO_2 materials are generally synthesized using thermal decomposition, co-precipitation, simple reduction, hydrothermal, sol-gel, micro-emulsion process, etc. Depending on the method, the MnO_2 material can have diverse

crystallographic forms (amorphous and crystalline), morphology, surface, and pore properties that affect its electrochemical performances [27].

An electrochemical synthesis method was used in this thesis to produce the manganese dioxide electrode material of γ-MnO_2 in bulk by depositing it onto an anode electrode. The anodic oxidation technique was used to convert Mn^{2+} to its higher oxidation state, Mn^{4+}, by electrolysis. The archetypal explanation of electrochemical synthesis is passing an electric current between two or more electrodes. The synthesis occurs at the electrode-electrolyte interface, where the electrolyte separates the electrodes from contact with each other. In this method, a potential gradient is applied at the electrodes directing to electrodeposit the material, which cannot be expected from chemical synthesis. The product obtained by the electrochemical synthesis in this thesis is γ-MnO_2, which will be discussed in the following chapters as a primary focus of this thesis. Generally, this is carried out at lower temperatures as it cannot exceed the boiling point of the electrolyte. The current and voltage applied to the cell control the kinetics and thermodynamics of the system. Besides, the choice of parameters, namely, electrode type, electrolyte, temperature, pH, solution composition, type of cell, and electrolysis mode, determines the deposited product quality. Generally, the electrolysis method can be either way of potentiostatic (PS) [28] or galvanostatic (GS) [29,30], depending on the applied voltage or current. A three-electrode cell is needed to carry out the PS synthesis where the desired potential is applied to the electrode with respect to the reference electrode. Thus, it tends to give a pure single-phase product in this case. The galvanostatic synthesis is used in this Ph.D. thesis as it can produce the electrochemically active γ-MnO_2 phase of electrolytic manganese dioxide (EMD) from an Mn^{2+} electrolyte solution. A step-by-step process of bulk synthesis of EMD followed in this thesis is given in Figure 1.8(A-K). Initially, the pristine EMD material was synthesized and characterized. Then EMD was modified using the additives such as bio-polymer and surfactants to obtain high-quality EMD materials, which is one of the objectives of this thesis. The EMD (γ-MnO_2) is composed of pyrolusite and ramsdellite intergrowth structure. Additionally, GS controls the reaction rate leading to a perfect adherence of the deposit to the electrode with controlled morphology [31,32]. Therefore, the manganese dioxide materials were synthesized using the electrochemical method and were tested as positive supercapacitor electrodes.

Material modifications were conducted and studied via computational modeling to improve the electrochemical performance of the EMD electrodes.

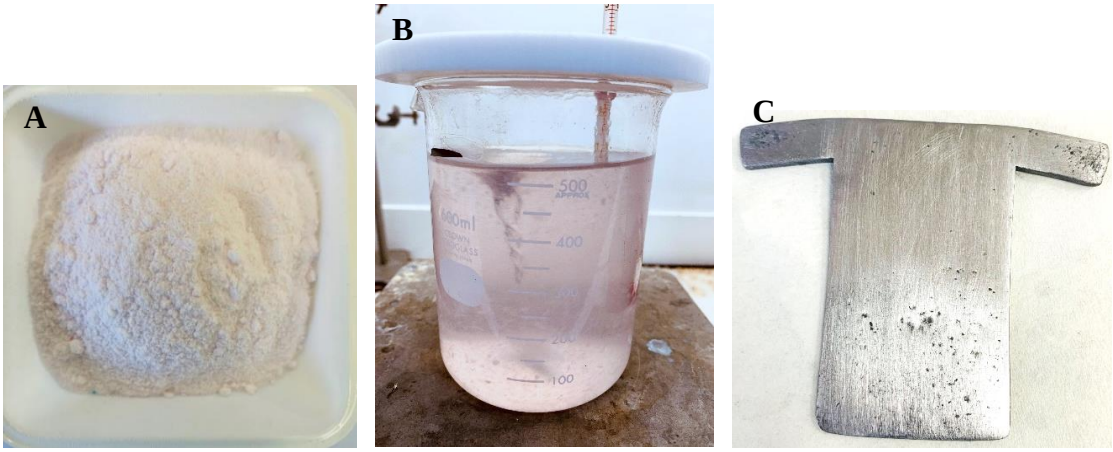

Figure 1.8 (A) Manganese sulfate precursor, (B) Preparing the electrolyte solution using Manganese sulfate, Sulfuric acid, and Deionized water, (C) Polished Lead (Pb) anode used in the galvanostatic anodic electrodeposition.

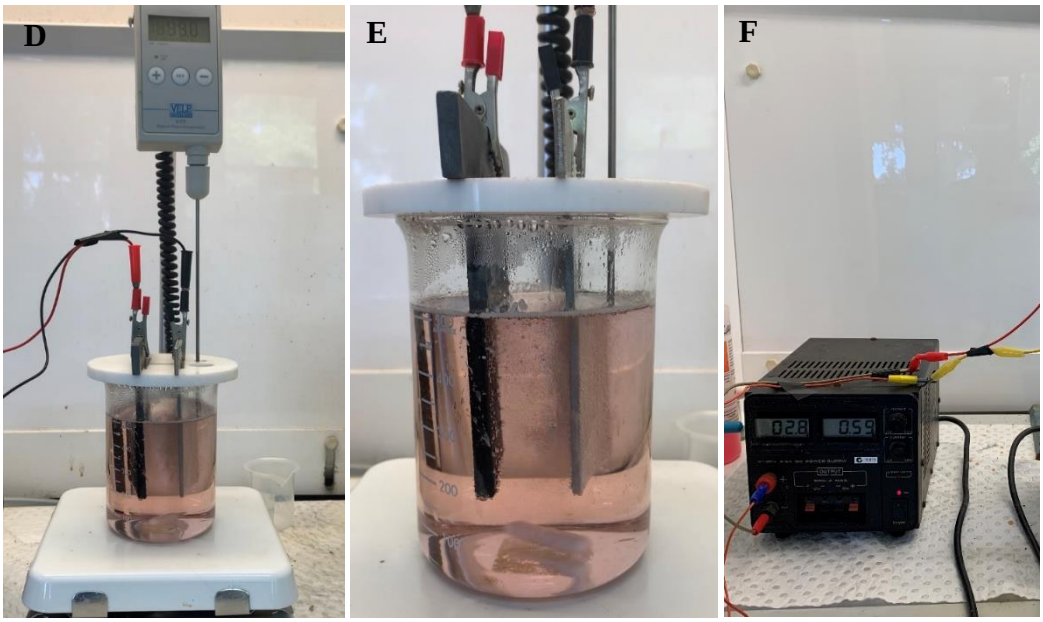

Figure 1.8 (D, E) Electrodeposition is taking place at the anode (electrode-left side), (F) Power supply to the process showing constant current of 0.59 A.

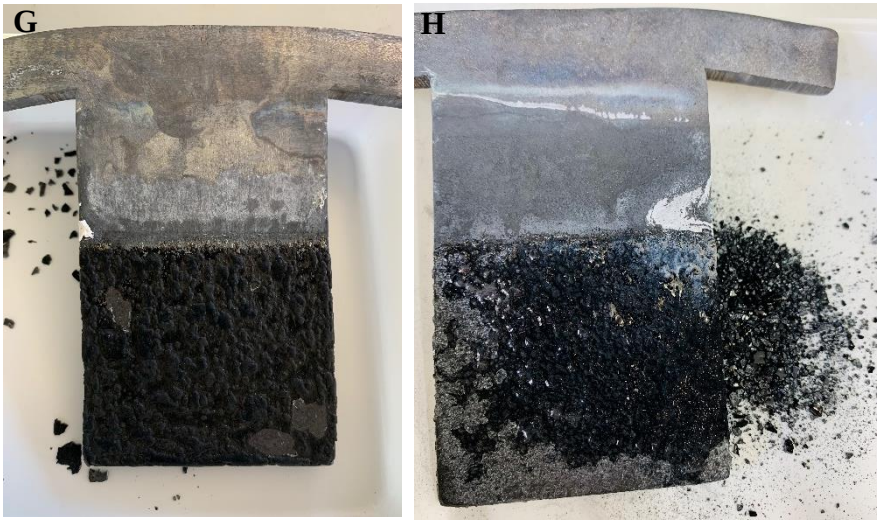

Figure 1.8 (G) The electrode after the electrodeposition experiment - MnO_2 deposited on the Pb anode, termed as 'EMD', (H) Scrapped EMD material from the Pb anode without damaging the Pb surface to avoid Pb contamination.

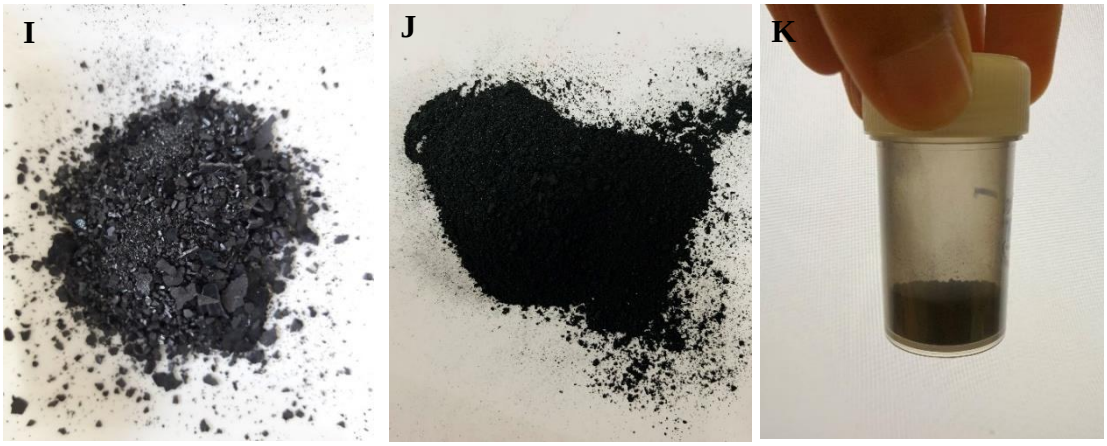

Figure 1.8 (I) EMD flakes after scraping the material from the Pb anode, (J, K) Ground EMD powder is used for further physicochemical and electrochemical characterization.

The battery-type materials (EMD in this thesis) are used as the positive electrode in hybrid capacitors, and the carbon-based electrodes are used as the negative electrodes. Types of carbon can be such as carbon nanotubes, activated carbons, and carbon aerogels that possess attractive features of affordable cost, high conductivity, and high thermal and chemical stability. When employed in the capacitor devices, they also show near electrochemical double-layer capacitance (EDLC) behavior [33]. In this

Ph.D. work, the porous AC has been synthesized using biomass waste carbon precursors using thermo-chemical treatment methods. The step-by-step synthesis AC used in this thesis is shown in Figure 1.9(A-H). The experimental conditions have been optimized, and machine learning (ML) models have been integrated with the collected input data (synthesis temperature, dopant amount, morphology, etc.) to predict the capacitance performance in SCs. Finally, a hybrid capacitor composed of modified EMD and biomass waste-derived AC was tested in an aqueous electrolyte, which showed potential use in the capacitor field.

Figure 1.9 (A) Mango seed waste, (B) Mango seed husk obtained from the mango seed, (C) Ground Mango seed husk (MS) powder, (D) Grape marc (GM) from winery waste, (E) Ground Grape marc powder.

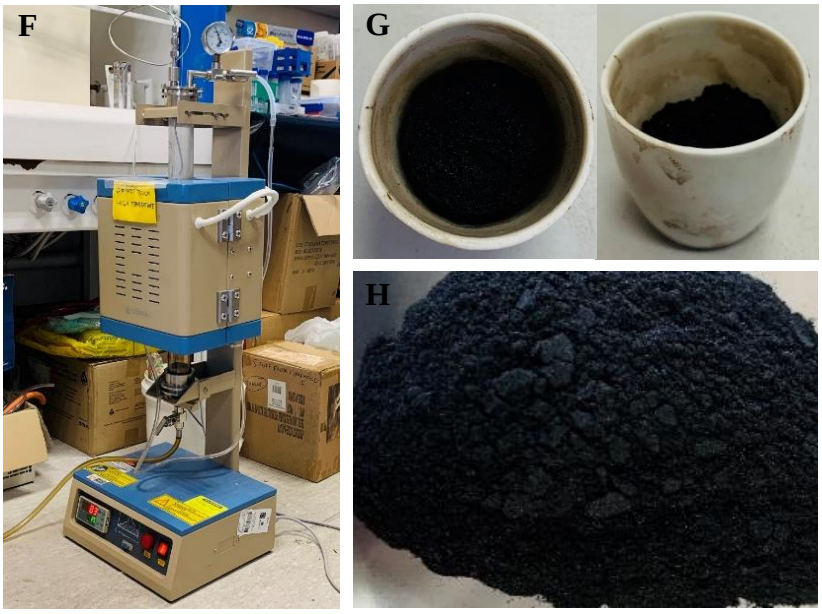

Figure 1.9 (F) Carbonization and activation carried out using the vertical furnace, (G, H) Carbonized and activated biomass waste.

References

[1] P. Poizot, F. Dolhem, Clean energy new deal for a sustainable world: from non-CO_2 generating energy sources to greener electrochemical storage devices, Energy Environ. Sci. 4 (2011) 2003–2019.

[2] International Energy Agency, Key world energy statistics, Paris Cedex 15 France, 2017.

[3] H.D. Pritchard, R.J. Arthern, D.G. Vaughan, L.A. Edwards, Extensive dynamic thinning on the margins of the Greenland and Antarctic ice sheets, Nature. 461 (2009) 971–975.

[4] C.M. Domingues, J.A. Church, N.J. White, P.J. Gleckler, S.E. Wijffels, P.M. Barker, J.R. Dunn, Improved estimates of upper-ocean warming and multi-decadal sea-level rise, Nature. 453 (2008) 1090–1093.

[5] N.L. Panwar, S.C. Kaushik, S. Kothari, Role of renewable energy sources in environmental protection: A review, Renew. Sustain. Energy Rev. 15 (2011) 1513–1524.

[6] J. Goldenberg, T.B. Johansson, World Energy Assesment Overview 2004 Update, New York, 2004.

[7] I.. Dresselhaus, M.S.; Thomas, Alternative energy technologies, Nature. 414 (2001) 332–337.

[8] O. Ellabban, H. Abu-Rub, F. Blaabjerg, Renewable energy resources: Current status, future prospects and their enabling technology, Renew. Sustain. Energy Rev. 39 (2014) 748–764.

[9] A. Demirbaş, Global renewable energy resources, Energy Sources, Part A Recover. Util. Environ. Eff. 28 (2006) 779–792.

[10] I.B. Fridleifsson, Geothermal energy for the benefit of the people, Renew. Sustain. Energy Rev. 5 (2001) 299–312.

[11] G.L. Soloveichik, Battery Technologies for Large-Scale Stationary Energy Storage, Annu. Rev. Chem. Biomol. Eng. 2 (2011) 503–527.

[12] B.K. Kim, S. Sy, A. Yu, J. Zhang, Electrochemical Supercapacitors for Energy Storage and Conversion, in: J. Yan (Ed.), Handb. Clean Energy Syst., John Wiley & Sons, Ltd, 2015: pp. 1–25.

[13] M. Huang, F. Li, F. Dong, Y.X. Zhang, L.L. Zhang, MnO_2-based nanostructures for high-performance supercapacitors, J. Mater. Chem. A. 3 (2015) 21380–21423.

[14] Sravankumarpadala, Super Capacitors - Different Than Others (part 1), Electr. Eng. Portal. (2013).

[15] C. Zhong, Y. Deng, W. Hu, J. Qiao, L. Zhang, J. Zhang, A review of electrolyte materials and compositions for electrochemical supercapacitors, Chem. Soc. Rev. 44 (2015) 7484–7539.

[16] S. Damiati, B. Schuster, Electrochemical biosensors based on S-layer Proteins, Sensors. 20 (2020) 1721.

[17] M. Yassine, D. Fabris, Performance of commercially available supercapacitors, Energies. 10 (2017) 1340.

[18] N. Elgrishi, K.J. Rountree, B.D. McCarthy, E.S. Rountree, T.T. Eisenhart, J.L.

Dempsey, A Practical Beginner's Guide to Cyclic Voltammetry, J. Chem. Educ. 95 (2018) 197–206.

[19] J. Wang, Study of Electrode Reactions and Interfacial Properties, in: Anal. Electrochem., 3rd ed., John Wiley & Sons, 2006: pp. 29–66.

[20] G.A. Snook, G.J. Wilson, A.G. Pandolfo, Mathematical functions for optimisation of conducting polymer/activated carbon asymmetric supercapacitors, J. Power Sources. 186 (2009) 216–223.

[21] R. Ruiz-Rosas, Design of hybrid asymmetric capacitors in aqueous electrolyte using ZTC and ultraporous activated carbons Diseño de condensadores asimétricos híbridos en electrolito acuso mediante ZTC y carbones activados utraporosos, 2015.

[22] D. Bélanger, T. Brousse, J.W. Long, Manganese oxides: Battery materials make the leap to electrochemical capacitors, Electrochem. Soc. Interface. 17 (2008) 49–52.

[23] P. Simon, Y. Gogotsi, B. Dunn, Where do batteries end and Supercapacitors Begin?, Science. 343 (2014) 1210–1211.

[24] S. Chou, F. Cheng, J. Chen, Electrodeposition synthesis and electrochemical properties of nanostructured γ-MnO_2 films, J. Power Sources. 162 (2006) 727–734.

[25] C.C. Hu, T.W. Tsou, Capacitive and textural characteristics of hydrous manganese oxide prepared by anodic deposition, Electrochim. Acta. 47 (2002) 3523–3532.

[26] S.H. Li, Q.H. Liu, L. Qi, L.H. Lu, H.Y. Wang, Progress in research on manganese dioxide electrode aterials for electrochemical capacitors, Chinese J. Anal. Chem. 40 (2012) 339–346.

[27] P.P. Sahay, A.K. Kushwaha, Electrochemical supercapacitive performance of potentiostatically cathodic electrodeposited nanostructured MnO_2 films, J. Solid State Electrochem. 21 (2017) 2393–2405.

[28] S. Devaraj, N. Munichandraiah, High capacitance of electrodeposited MnO_2 by the effect of a surface-active agent, Electrochem. Solid-State Lett. 8 (2005)

A373–A377.

[29] J.N. Broughton, M.J. Brett, Variations in MnO_2 electrodeposition for electrochemical capacitors, Electrochim. Acta. 50 (2005) 4814–4819.

[30] M. Paunovic, M. Schlesinger, Fundamentals of Electrochemical Deposition, 2nd ed., John Wiley & Sons, Canada, 1998.

[31] G.H.A. Therese, P.V. Kamath, Electrochemical Synthesis of Metal Oxides and Hydroxides, Chem. Mater. 12 (2000) 1195–1204.

[32] G. Wang, L. Zhang, J. Zhang, A review of electrode materials for electrochemical supercapacitors, Chem. Soc. Rev. 41 (2012) 797–828.

Chapter 2 Review of the progress of electrochemical capacitor materials for energy storage application

2.1. Introduction

The electrochemical capacitors (ECs) can store relatively higher energy content than conventional ones. With their advantages, such as fast charge-discharge, long cycle life, and broad operating temperature ranges, the ECs are useful in different applications (e.g., hybrid or electric vehicles). However, some challenges still exist, mainly the lower energy density than batteries, requiring the development of novel and high-performing materials. One approach is combining both battery and capacitor electrodes in a cell as a hybrid capacitor that can yield higher energy density. The oxides of ruthenium, nickel, cobalt, iron, and manganese are a few battery material types that can be employed in capacitors. Manganese-based oxides are used as a cathode material in primary (manganese dioxide-zinc, primary lithium battery) and secondary batteries (manganese dioxide-zinc, lithium-ion battery) in aqueous and non-aqueous battery systems. Besides, manganese-based oxides are widely used in capacitor applications due to their pseudocapacitive behavior. Among the available forms of manganese dioxides, the γ-MnO_2 form is the most electrochemically active form of manganese dioxide due to the random growth of ramsdellite and pyrolusite. Electrodeposition is one of the processes to synthesize γ-MnO_2, which is widely called as "*electrolytic manganese dioxide (EMD)*". The synthesized EMD can be coupled with the carbon to fabricate the hybrid capacitors to obtain higher electrochemical performances resulting in larger storage. Therefore, the review in this chapter summarizes the perspective of EMD positive electrode materials that can be deployed in hybrid capacitors versus carbon negative electrode materials for energy storage applications.

The overall content in this review chapter is organized as follows. First, a general introduction is given to the electrochemical energy storage systems (section 2.2). Then, we have classified the types of ECs and their mechanisms (section 2.3). Subsequently, the development of capacitor electrode materials from the past to the present limited to transition metal oxides has been reviewed (section 2.4). In the following sections (sections 2.5 - 2.7), we discuss about the EMD in energy storage applications, a focal point of this thesis. Further, the physical and electrochemical properties of EMD are also analyzed. In addition to transition metal oxides, the widely used conducting polymers in the electrochemical energy storage field are discussed in the next section (section 2.8). In section 2.9, we discuss another focal point of this thesis, the carbon materials used for electrochemical energy storage, and the biomass waste-derived carbon materials are analyzed in the subsection. A brief review of the prediction by Machine Learning (ML) models and their development in the energy storage field is given in section 2.10. After concluding this review (section 2.11), we have presented the Ph.D. project aims, objectives, and an illustration of the subsequent thesis chapters (section 2.12).

2.2. Electrochemical energy storage systems

Electrochemical energy storage technology is one of the cleanest, most feasible, environmentally friendly, and sustainable energy storage systems among the various energy technologies, namely mechanical storage, thermal storage, electrochemical storage, and chemical storage [1]. Electrochemical energy storage/conversion systems include batteries, fuel cells, and ECs. Despite the difference in energy storage and conversion mechanisms of the three systems, the common electrochemical feature is that the reactions occur at the phase boundary of the electrode/electrolyte interface near the two electrodes [2]. Their similarities and differences related to their mechanisms are given in subsections 2.2.1 – 2.2.3.

2.2.1. Batteries

Batteries store energy via chemical interventions (faradaic reactions/redox reactions) at the anode and cathode. The anode is the negatively charged electrode, whereas the cathode is the positively charged electrode. The faradaic reactions can occur reversible or irreversible, but the battery materials often involve irreversible chemical reactions [3]. The irreversibility has caused limitations of battery cycle life to one thousand to several thousand charge-discharge cycles, which vary based on the battery type and the electrodes employed. Batteries are closed systems where the anode and cathode active materials play a prominent role in the redox reactions to store and convert energy. Table 2.1 displays a summary of battery types and their mode of energy storage [4].

Table 2.1 Battery types and modes of storing the energy [3,4].

Type		**Mode of energy storage**
Primary	Leclanché, Zinc-MnO_2	Faradaic
	Alkaline, Zinc-MnO_2	
	Mg-AgCl	
	Mg-$PbCl_2$	
	Li-$SOCl_2$ and other cathodes	
	Li-CF_x	
	Al-air (catalyzed)	
	Zn-air (catalyzed)	
Secondary (rechargeable)	Lead-acid, Pb-PbO_2	Faradaic
	Nickel-cadmium, Ni-O-OH-Cd	
	Nickel-hydrogen, Ni-O-OH-metal hydride	
	Nickel-zinc, Ni-O-OH-Zn	
	Mercuric oxide-zinc, HgO-Zn	
	Silver oxide(s)-zinc, AgO-Zn	
	Zinc-air (catalyzed)	

	Li-TiS_2	Faradaic (exhibiting intercalative pseudocapacitance)
	Li-MoS_2	
	Li-MnO_2	
	Li-CoO_2	
	Li-C-CoO_2 and other cathodes	
	Li-iron sulfides	
	Na-S	

2.2.2. Fuel cells

Using the chemical/redox reactions involved during the electrochemical process, both the battery and fuel cell function similarly. However, the fuel cells are open systems where the anode and cathode provide the charge-transfer media for the active materials supplied from outside to perform the redox reactions. The active materials/fuels can be hydrogen, natural gas, oxygen, air, hydrogen peroxide gases, etc. [2].

2.2.3. Capacitors

The conventional (dielectric) capacitors can only store a small charge at the electrode plates, providing a low energy density for electrical energy storage. However, the electrical double-layer capacitors (EDLCs) can store charge depending on the accessible area of the electrodes. Unlike the redox reactions in batteries and fuel cells, the energy-delivering process deviates in ECs. No electron transfer occurs across the electrode interface in an ideal capacitor but only accommodates electrostatic charge storage. A capacitor generally has unlimited cyclability with no chemical reactions (non-faradaic) taking place during the electrochemical process. The capacitors are highly reversible compared to the batteries but exhibit lower energy density and higher power densities which are the primary characteristic differences between batteries and capacitors [5]. Table 2.2 summarizes the types of capacitors and their energy stores in one of the modes, such as electrostatic or faradaic.

Table 2.2 Capacitor types and modes of storing the energy [4,6].

Type	Mode of energy storage	Examples
Vacuum	Electrostatic	-
Dielectric	Electrostatic	Ceramic, mica, polymer
Oxide electrolytic (thin film)	Electrostatic	Ta_2O_5, Al_2O_3
Double layer	Electrostatic (charge separation at double layer at electrode interface)	Carbon materials
Colloidal electrolyte	Electrostatic (special double layer system)	Undeveloped
Redox oxide film	Faradaic charge transfer (pseudocapacitance)	RuO_x, IrO_x, Co_3O_4
Redox polymer film	Faradaic charge transfer (pseudocapacitance)	Polyaniline, Polythiophenes
Soluble redox system	Faradaic charge transfer (pseudocapacitance)	$Fe(CN)_6^{4-}$- $Fe(CN)_6^{3-}$, $V^{2+}/V^{3+}/VO^{2+}$

The existing energy and power trade from the electrochemical/electrical devices is expressed from the Ragone plot (power density *vs.* energy density) shown in Figure 2.1. The devices with high power densities have lower energy densities and vice versa. Therefore, multiple devices must be utilized together to accomplish both high power and energy for a required system. For instance, a battery-capacitor hybrid system for pulsed power loads is frequently encountered in communication systems such as mobile phones, cellular devices, and military applications [7]. As illustrated in Figure 2.1, batteries and capacitors are the two leading electrochemical energy-storage devices. The electrochemical capacitors (ECs), also termed supercapacitors (SC), display intermediate properties of batteries and capacitors. Therefore, it can either complement or even replace batteries in some applications [8–10]. Consequently, this has led to a proliferation of studies about the materials for complementary utilization

of battery and capacitor properties that can result in fast charging, excellent cycling stability, and high energy-power requirements. The goal is to achieve high energy storage without sacrificing the high-power density and cycling stability of the capacitors [11,12]. Therefore, more experimental and computational investigations should be conducted to develop efficient and sustainable materials for future energy storage applications.

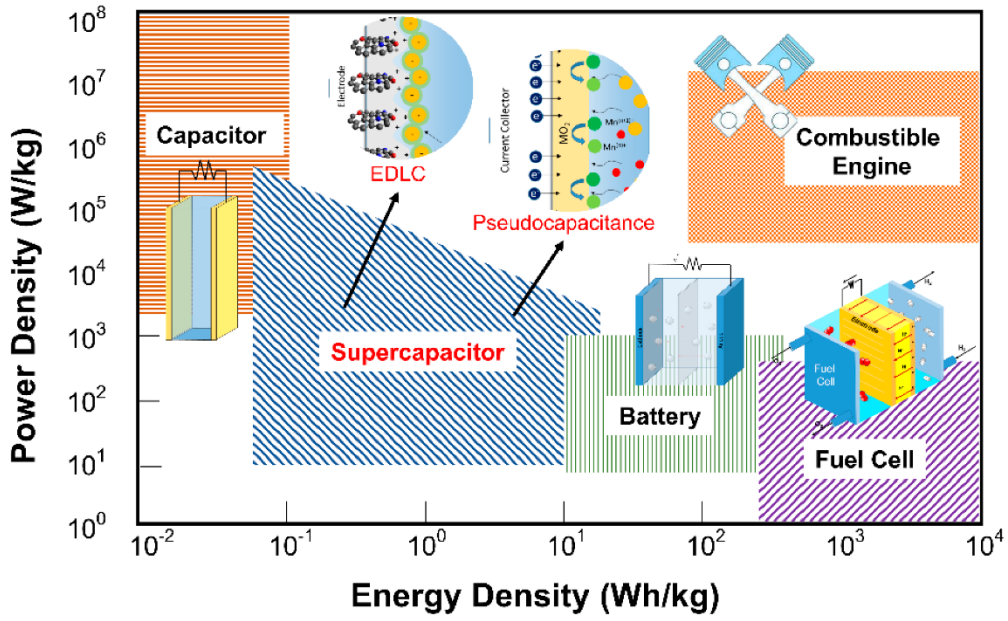

Figure 2.1 Power density (specific power) against energy density (specific energy) - Ragone plot for current electrochemical energy storage technologies. Reproduced from [13], open-access Creative Commons CC BY 4.0 license, MDPI.

2.3. Electrochemical Capacitors (ECs)

2.3.1. Classification of ECs

The development of EDLCs dates back to the mid-1900s. Since then, with the rapid growth of using electronic devices, hybrid vehicles, etc., a variety of ECs have become available in the market. Figure 2.2 shows the general classification of ECs, which includes three types, namely EDLCs, pseudocapacitors, and asymmetric capacitors [14]. The asymmetric capacitors can be categorized into two types, i.e., two capacitive

electrodes of different materials having the same reaction type [15] or a hybrid capacitor comprising electrodes having different (faradaic/capacitive) mechanisms [16]. A hybrid capacitor consists of one battery-type electrode, which uses a faradaic charge storage mechanism, coupled to another electrode stores charge using a capacitive (EDLC) mechanism. An asymmetric capacitor is advantageous in extending the potential window using the different operational voltages of the two electrodes from dissimilar materials. Generally, the symmetric capacitor voltage ~1V can be increased beyond 2 V by an asymmetric capacitor [17,18]. Further details on the charge storage mechanism are detailed in section 2.3.2.

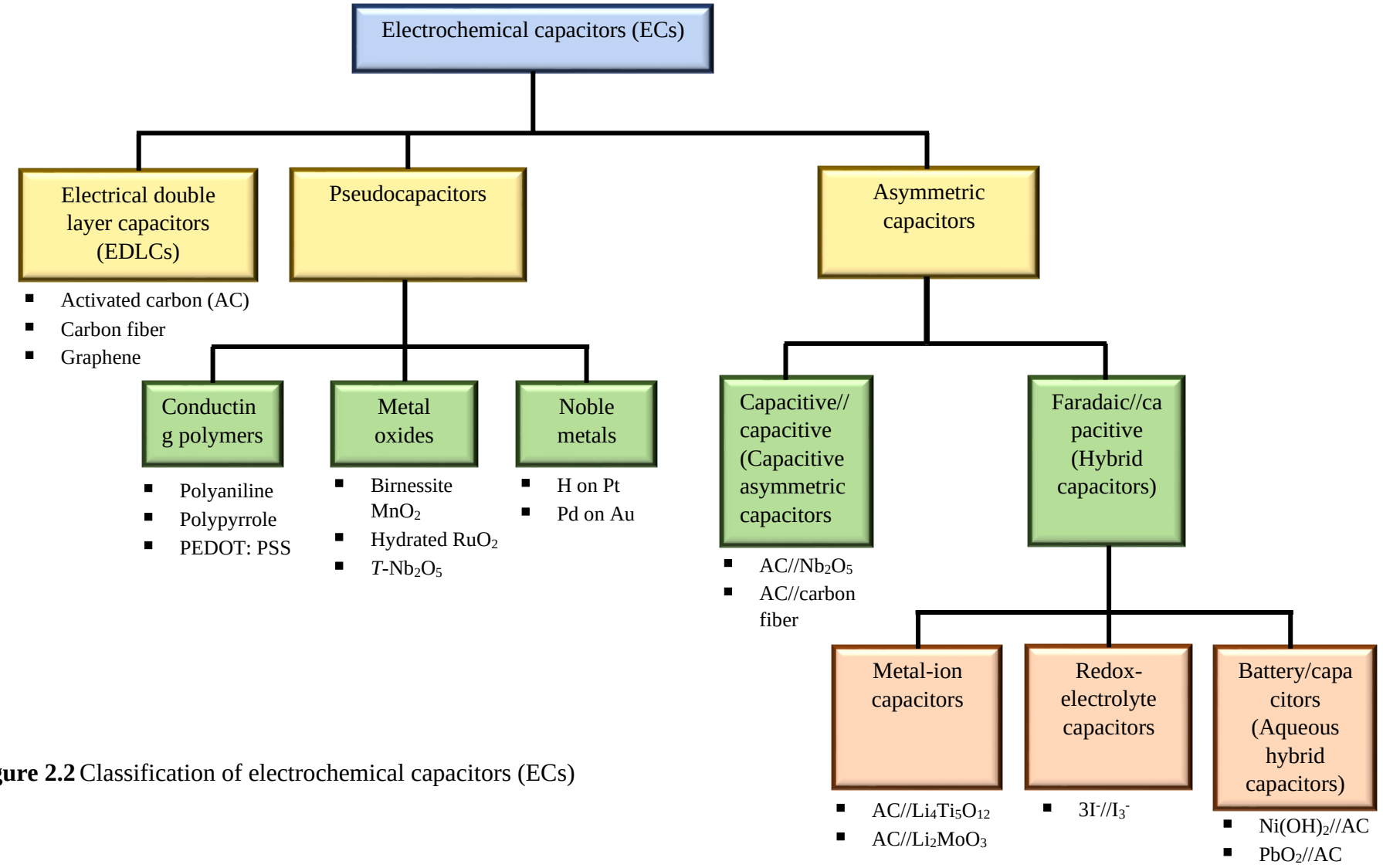

Figure 2.2 Classification of electrochemical capacitors (ECs)

2.3.2. Energy storage mechanisms

2.3.2.1. Electric double-layer capacitors (EDLCs)

The heart of the EDLCs is the charge arrangement at the electrode-electrolyte interface when the electrode is immersed in an ion-conductive electrolyte solution. When voltage is applied, it creates opposite polarities at the two electrodes, attracting the electrolyte ions towards the charged surfaces. The charge is only physically stored by ion adsorption at the electrodes, and no charge transfer reactions (faradaic reactions) occur between the interfaces of the electrode and electrolyte (Figure 2.3A) [9,19]. Therefore, the specific capacitance of an EDLC is mainly determined by the accessible surface area and the surface properties of the electrodes. In addition, if the electrolyte has excellent conductivity, it can reduce the internal resistance and increase the electrode's wettability and ion mobility into the pores, further enhancing the capacitance [20]. The EDLC capacitor can be considered the simplest and most commercially available type of capacitor. In practical applications, the capacitance is about 100 - 250 F g^{-1} with a lower deliverable energy density of 3 - 10 Wh kg^{-1} [21].

2.3.2.1. Pseudocapacitors

The term 'pseudocapacitance' designates the behavior of an electrode material, which shows an electrochemical signature of a capacitor but in which the charge storage is dominated by electron transfer mechanisms across the double layer [22]. Therefore, unlike the EDLC capacitors, faradaic reactions (electrosorption or redox processes) occur in pseudocapacitive electrode materials. The reactions can take place at the electrode surface or near-surface at a distance, $l << (2Dt)^{1/2}$, where D is the diffusion coefficient (cm^2 s^{-1}), and t is the time (s) for charge-compensating ions [23]. The Faradaic mechanisms can be different, as shown in Figure 2.3(B-D). The underpotential deposition (UPD) shown in Figure 2.3B refers to metal monolayer(s) electrodeposition on a foreign metal substrate at potentials more positive than Nernst potential [24]. H or Pd in monolayers on noble metals (such as Pt or Au) and

oxidation/reduction in microporous transition metal hydrous oxides (RuO_2, IrO_2, and various metal oxides) are a few common examples of this type [24,25].

When the pseudocapacitance is based on redox reactions with fast and reversible electrons transfer at the electrode-electrolyte interface, which is also known as electrochemical adsorption of cations as given by the reaction R(2.1) [26].

$$M + z(C^+ + e^-) \leftrightarrow M/C_z \qquad \text{R(2.1)}$$

where, M is the pseudocapacitive material, C is the surface absorbed electrolyte cation C^+ (H^+, K^+, Na^+, …), z is the number of transferred electrons. Ruthenium dioxide (RuO_2) was the first and thoroughly investigated material in a faradaic redox system (Figure 2.3C) due to having multiple redox phases (i.e., Ru(IV)/(III), Ru(III)/(II)) in proton-rich environments; e.g., Sulfuric acid (H_2SO_4), therefore more electron transfers occur enhancing greater capacitance [27,28]. Despite the outstanding performance of RuO_2, its toxicity, high cost, and scarcity limited its practical applications, which shifted the direction to research on less toxic and inexpensive alternatives such as manganese oxides [29] and some conducting polymers [30], which also offer the redox pseudocapacitance. The pseudocapacitance also occurs due to ion intercalation (Figure 2.3D), where ion intercalation to redox-active materials takes place with no crystallographic phase change (e.g., Nb_2O_5) [31], which is illustrated in the reaction R(2.2). This retains the crystal structure even after several cycling of charge-discharge processes.

$$MO_y + z(C^+ + e^-) \leftrightarrow C_zMO_y \qquad \text{R(2.2)}$$

where, MO_y is the electrode material.

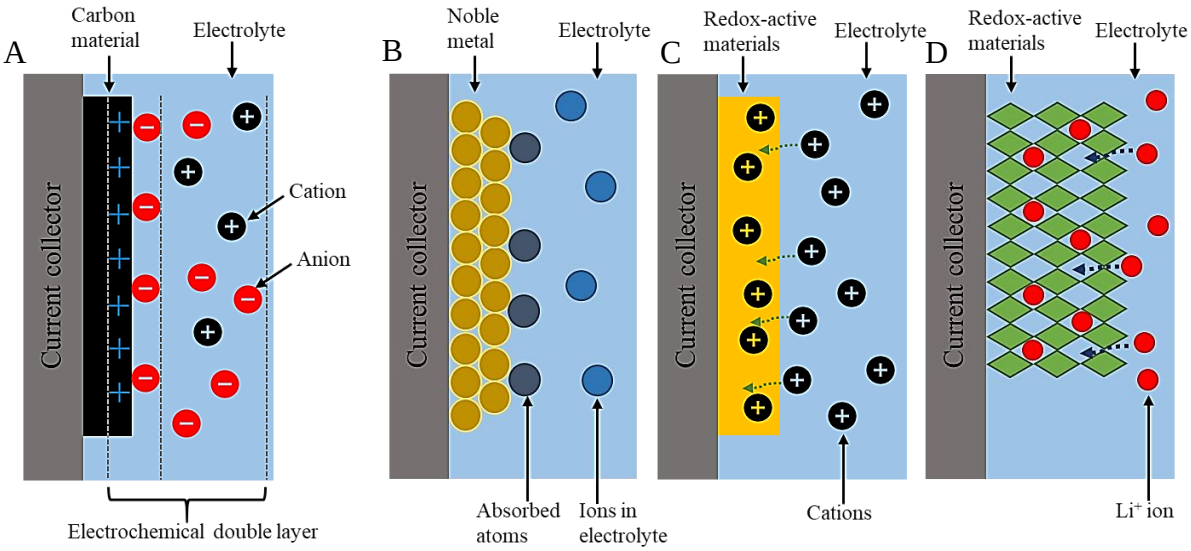

Figure 2.3 Schematics of charge-storage mechanisms for (A) an EDLC and (B-D) types of pseudocapacitive materials: (B) underpotential deposition, (C) redox pseudo capacitor, (D) ion intercalation pseudocapacitor. The diagrams are modified according to ref. [21].

It is noted that the pseudocapacitor can result in a capacitance 10 -100 times larger than that of an EDLC. Driven by the exemplary results, the pseudocapacitive materials, either fast redox pseudocapacitance or intercalation pseudocapacitance, have gained much attraction in asymmetric supercapacitor devices. The cyclic voltammetric (CV) behavior of the different electrode types is shown in Figure 2.4.

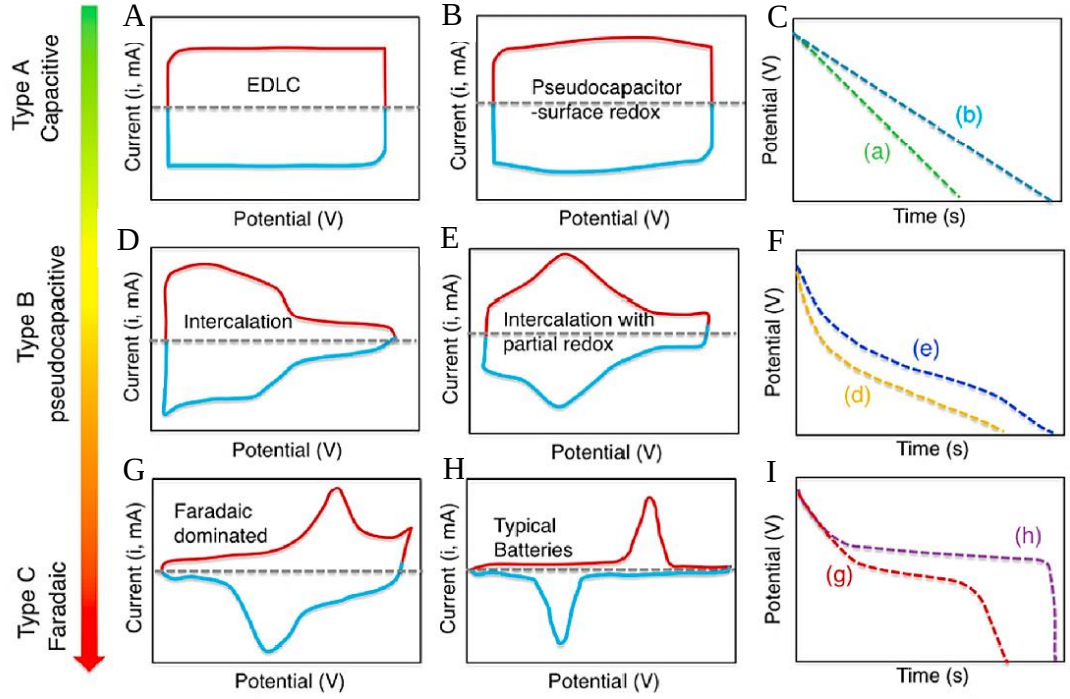

Figure 2.4 (A, B, D, E, G, H) schematic illustrations of various cyclic voltammograms and (C, F, I) their corresponding galvanostatic discharge curve for different energy storage materials. A pseudocapacitive material will generally have one or a combination of electrochemical characteristics from the following categories: (B) surface redox materials, (D) intercalation-type materials, or (E) intercalation-type materials showing broad but electrochemically reversible redox peaks. Electrochemical responses in (G-I) correspond to battery-like materials. Reproduced from ref. [23] with permission, copyright 2018, ACS Publications.

2.3.2.2. Capacitive asymmetric capacitors *vs.* hybrid capacitors

It should be noted that the definition for the 'asymmetric' and 'hybrid' only refers to devices, not the single electrodes as explained for EDLCs and pseudocapacitors. Based on the generally accepted terminology, the hybrid capacitor consists of two electrodes with two different charge-storage mechanisms; capacitive and battery-type [11,32,33]. It can be a combination of a battery component (conducting polymers, metal oxides, etc.) and a capacitor component (primarily carbons). A faradaic electrode such as $Ni(OH)_2$ [34] and Co_3O_4 [35] coupled with a carbon electrode is an example of a typical

hybrid device. On the other hand, the asymmetric capacitors apply to a wide range of electrode combinations (e.g., Figure 2.5). This device has two different electrode materials or can even contain the same EDLC material with different masses and surface functional groups, implying that hybrid capacitors are also a category of asymmetric capacitors. With this as the fundamental background required for understanding the charge storage mechanisms in hybrid capacitors, suitable electrode materials have been reviewed in section 2.4.

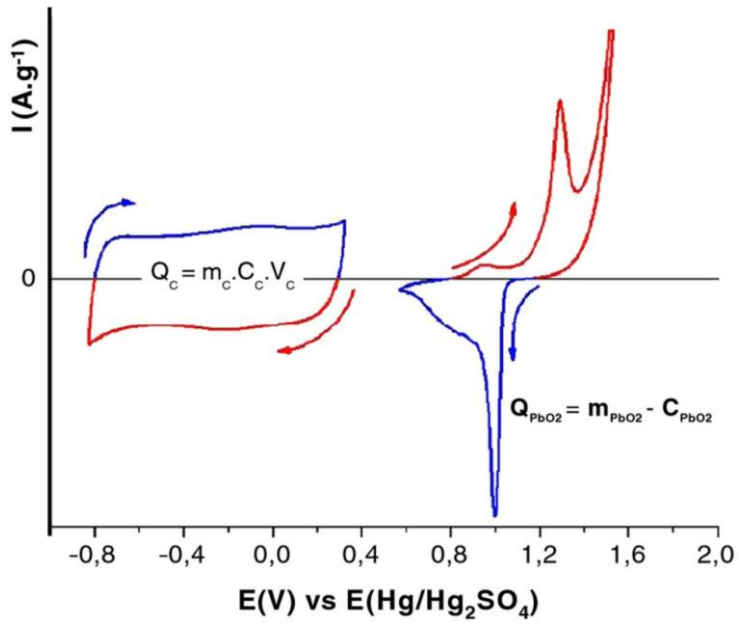

Figure 2.5 Activated carbon/PbO_2 hybrid (asymmetric) device in 1M H_2SO_4. m_c is the mass of carbon and m_{PbO_2} is the mass of PbO_2, C_c is the gravimetric capacitance (F g^{-1}) of the carbon electrode, C_{PbO_2} is the gravimetric capacity (C g^{-1} or mAh g^{-1}) of the lead oxide electrode, V_c is the potential window in which the carbon electrode is cycled. Reproduced from ref. [22], open access Creative Commons CC BY-NC-ND, Journal of the Electrochemical Society.

2.4. Mapping transition metal oxide electrodes for hybrid capacitors

As mentioned earlier, RuO_2 was the first material found to exhibit the pseudocapacitive behavior in transition metal oxides, which was discovered in 1970 by Trasatti and Buzzanca [36]. Following this, several studies were carried out based

on the RuO_2 material. Many other materials also became of interest in the field of pseudocapacitors, mostly by repurposing the battery-type materials (titanium dioxide, niobium pentoxide, metal sulfides, etc.) to perform as capacitors [37]. Figure 2.6 shows a few examples of the different synthetic routes. Different transition metal oxide materials are detailed in sections 2.4.1 - 2.4.6.

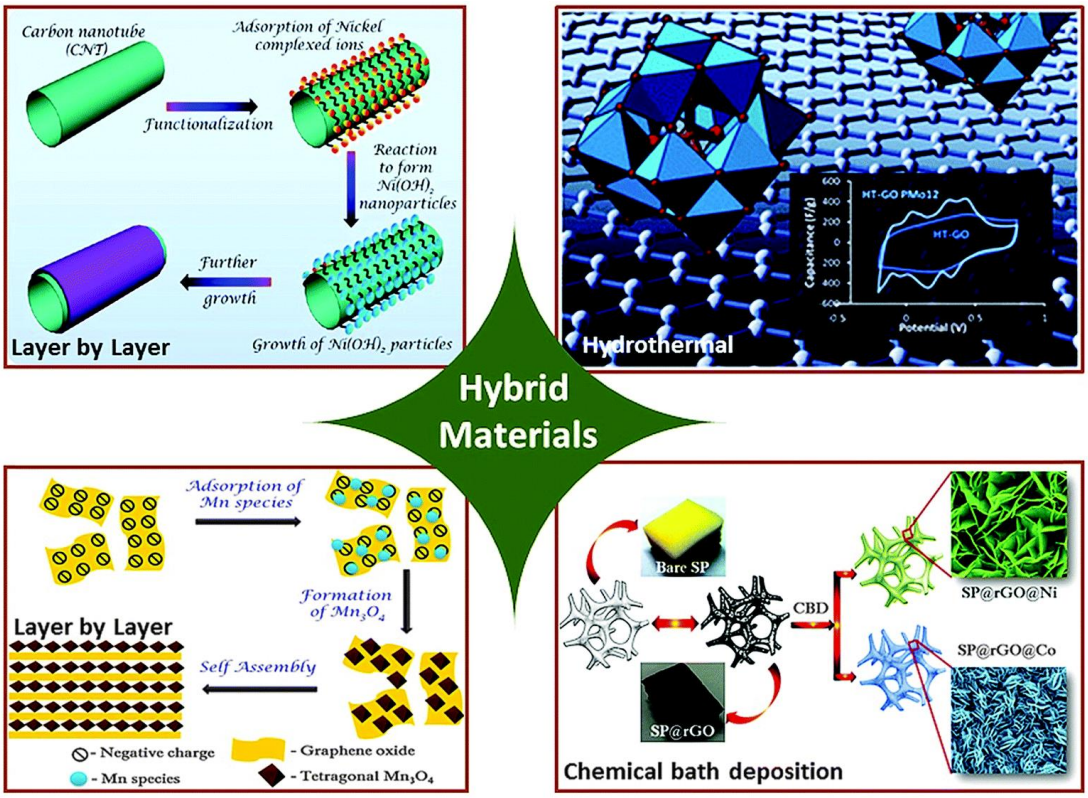

Figure 2.6 Schematic representation of various chemical synthetic routes used to synthesize hybrid electrode materials. Reproduced from ref. [38] with permission, copyright 2015, Royal Society of chemistry.

2.4.1. Ruthenium dioxide (RuO_2)

The first discovered pseudocapacitive material, RuO_2, was a ground-breaking step to understanding pseudocapacitance. Conway and co-authors [25,39] carried out further fundamental work to bring out the difference between batteries and SCs, the charge storage via Helmholtz double-layer, and the faradaic charge transfer between electrode and electrolyte ions. A consequent study by Ardizzone *et al.* [40] found that

capacitance arises from the RuO_2 extremely dependent on the hydrated and nanostructural formation of the material. Zheng *et al.* [41] found that the annealing temperature above 150 °C, the crystalline phase formation of RuO_2, led to a significant drop in the capacitance. The measured capacitance was ~720 F g^{-1} (the equivalent of 200 mAh g^{-1}) at a 1 V potential window at a scan rate of 2 mV s^{-1}. In terms of the energy density, the RuO_2 delivered 26.7 Wh kg^{-1}, greater than the carbon-based EDLCs, which have around 12 Wh kg^{-1} [42]. Despite the electrochemical performance of RuO_2, the commercial application in energy storage devices is limited due to the high cost of USD 8000 kg^{-1} (price quoted in 2020). Therefore, the academic interest in research shifted toward finding other cost-effective potential metal oxide materials such as NiO [43], V_2O_5 [44], Fe_3O_4 [45], TiO_2 [46], and MnO_2 [47]. Several synthesis methods have been used to produce these metal oxides, discussed in the following sections. Before moving onto the case EMD, other similar metal oxides with their merits and demerits are reviewed to showcase the capability of yielding high-quality electrolytic deposition of manganese dioxide.

2.4.2. Nickel oxides

The fact that the NiO has a high theoretical capacitance of about 2584 F g^{-1} (at 0.5 V potential window), impressive redox reactions Ni^{2+}/Ni^{3+}, and lower cost attracted the interest among researchers in assessing this material for capacitors. However, the poor electrical conductivity of the material inhibited its performance. Therefore, researchers have explored various methods to increase its conductivity while keeping the high capacitance of NiO. By co-deposition of NiO with conductive materials such as other metal oxides, carbon nanotubes (CNTs), conducting polymers were employed, which improved the capacitance up to ~1000 F g^{-1} [48–50]. Further, doping with a guest element (transition metal elements and rare earth elements such as Co, Mn, Cu, and La) was also conducted. The ions of Co^{2+} and La^{3+} induced changes in morphology [51]. The Co/Mn co-doped NiO reached up to 673.73 F g^{-1} due to the co-doping and crystal defect [52]. Cu^{2+} doping increased the proton transportation within the NiO structure. The well-accepted surface redox reactions of NiO electrodes in an alkaline

solution can be expressed as in reaction R(2.3) [53]. When the OH^- ions dispersed into $Ni(OH)_2$, they converted to NiOOH as given in the reaction R(2.4) [54].

$$NiO + OH^- \leftrightarrow NiOOH + e^- \quad \text{R(2.3)}$$

$$Ni(OH)_2 + OH^- \leftrightarrow NiOOH + H_2O + e^- \quad \text{R(2.4)}$$

2.4.3. Cobalt oxides

Cobalt oxide (Co_3O_4 and CoO) are promising materials for capacitors as they show intercalative pseudocapacitance properties with a theoretical capacitance of >2000 F g^{-1} [55]. Numerous nanostructured morphologies are reported for cobalt oxides, such as nanowires, nanoflakes, nanocages, nanorods, nanoparticles, nano bowls, and nanospheres, which have been produced using different solution-based synthesis methods [56]. In addition, cobalt oxides display good efficiency, long-term cycling, and good corrosion resistance [57,58]. The following reactions R(2.5 and 2.6) can occur for Co_3O_4 in an alkaline electrolyte solution [59,60].

$$Co_3O_4 + OH^- + H_2O \leftrightarrow 3CoOOH + e^- \quad \text{R(2.5)}$$

$$CoOOH + OH^- \leftrightarrow CoO_2 + H_2O + e^- \quad \text{R(2.6)}$$

2.4.4. Vanadium oxides

Vanadium combined with oxygen forms several compounds such as vanadium monoxide (VO), vanadium trioxide (V_2O_3), vanadium dioxide (VO_2), etc. [61]. Among all the vanadium oxides, V_2O_5 and VO_2 exhibit higher capacitances and wide operating voltage, thus potentially being used in energy storage devices. Wittingham, in 1976 [62], first described that the V_2O_5 could undergo fast reversible reactions as a result of the layered structure of the material. After several years, in 1999, Lee and Goodenough [63] explained the pseudocapacitive behavior of V_2O_5 powder heated at 1183 K, which was tested in a 2 M KCl electrolyte that exhibited capacitance of 350 F g^{-1}. Vanadium is relatively cheap and non-toxic; however, similar to other metal oxides like NiO, V_2O_5 is also a poorly conductive material [44]. Moreover, the V_2O_5

morphology tends to change significantly on cycling, reducing the surface area and inter-particle contact. This was observed by Zhang *et al.* [64] in their work by synthesizing three different morphologies (Figure 2.7) of V_2O_5 and evaluating them for capacitor applications.

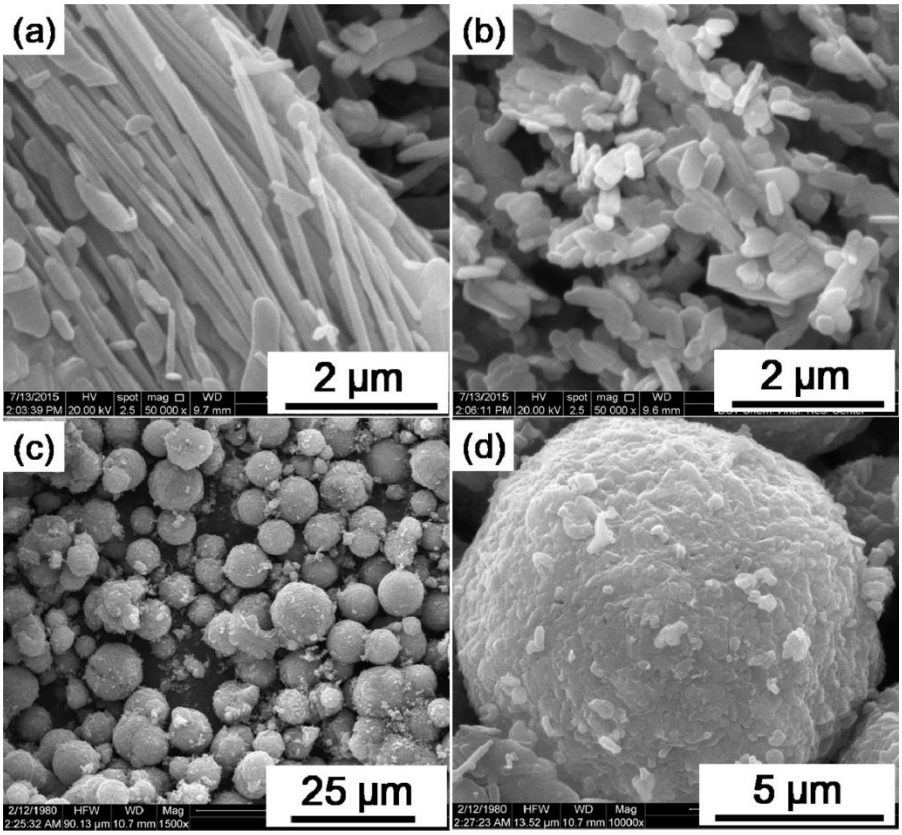

Figure 2.7 SEM images of the as-obtained V_2O_5 with various morphologies: (a) nanobelts, (b) nanoparticles, and (c, d) microspheres. Reproduced from ref. [64] with permission, copyright 2016, Elsevier.

2.4.5. Iron oxides

Iron is the fourth most abundant element in the Earth's crust, ~3.6 % by weight, and creates three oxides of Fe_2O_3, Fe_3O_4, and FeO. Among the iron oxides, magnetite (Fe_3O_4) is inexpensive and has been attracted as an excellent capacitor electrode material. Compared to the other metal oxides, iron oxides are highly conductive; however, the charge-discharge process during cycling causes irreversible volume

change degrading the capacitance, hence not meeting the practical requirements [65]. Wu *et al.* [66] synthesized magnetite deposited on carbon black to form a magnetite/carbon composite electrode. Wang *et al.* [67] reported the capacitances of magnetite are 170, 25, 3 F g^{-1} in 1 M Na_2SO_3, Na_2SO_4, and KOH aqueous electrolytes, respectively, tested in a three-electrode system (-0.8 to -0.1 V). From the above studies, it was evident that for Fe_3O_4, the capacitance arises solely by the anion adsorption, with no cation involvement.

2.4.6. Manganese oxides

In a series of transition metal oxides reviewed, next is manganese, which holds the twelfth position of being one of the most abundant elements on the Earth, nearly 0.096 % [68]. Other attractive features of manganese oxide are its natural abundance, low cost, low toxicity, and high theoretical capacitance of 1370 F g^{-1} [69,70]. The pseudocapacitance of the manganese oxide materials arises from the redox transitions between Mn^{3+}/Mn^{2+}, Mn^{4+}/Mn^{3+}, and Mn^{6+}/Mn^{4+} [71] attracted this as an excellent material for energy storage applications. The manganese can exhibit the oxidation states from +2 to +7. Among the various forms of available manganese oxides, MnO (Mn^{2+}), Mn_2O_3 (Mn^{3+}), Mn_3O_4 ($Mn^{2.66+}$), and MnO_2 (Mn^{4+}), the MnO_2 is widely used, having the most reversible redox couple of Mn^{4+}/Mn^{3+}. MnO_2 exists in several polymorphs, as shown in Figure 2.8. Generally, the polymorphs are reported to influence the specific capacitance, which increases in the following trend of the crystal structure: $\beta < \lambda < \gamma < \delta \approx \alpha$ [72]. However, Ghodbane *et al.* [73] have explained that this trend between the crystal structure and the capacitance is not necessarily the same. Accordingly, in their work, the 3D spinel λ-MnO_2 exhibited the highest capacitance of 241 F g^{-1}, while the 2D δ-MnO_2 rated with 225 F g^{-1} capacitance. This could be explained due to the microtwinning and related morphologies rather than solely relying on the polymorphs. Interesting morphologies, such as nanoflowers [74], nanowires [75], nanospheres [76], nanosheets [77], and nanorods [78], for manganese oxide materials, and their influence on energy storage have also been reported in the literature [79].

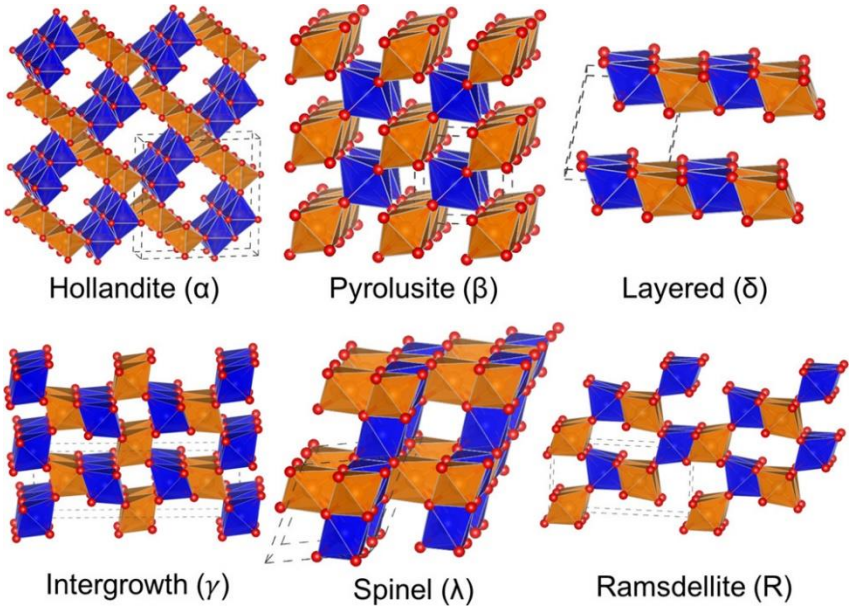

Figure 2.8 Common polymorphs of MnO_2. The orange and blue octahedra surround spin-up and sown Mn atoms, respectively; the red atoms represent 'O'. Reproduced from ref. [80] with permission, copyright 2018, American Chemical Society.

Lee and Goodenough [81] conducted the pioneering work on MnO_2 in 1999 by producing amorphous $MnO_2.nH_2O$ using a hydrothermal technique and demonstrating its pseudocapacitive behavior. They obtained 203 F g^{-1} specific capacitance (C_{sp}) at a current density of 2 mA cm^{-2} in 2 M KCl aqueous electrolyte tested in a potential window of -0.2 to 1.0 V *vs.* standard calomel electrode (SCE). In 2000, Pang *et al.* [82] reported 698 F g^{-1} for sol-gel-derived MnO_2 thin film electrodes with 1.05 µg cm^{-2} active electrode mass loading. The thin film mass loading was increased to ~75 µg cm^{-2} by Broughton and Brett [83] in 2004 to synthesize MnO_2 electrodes by sputter deposition, in which the capacitor delivered 700 F g^{-1}. In several other research studies, the authors explored the electrochemical performance based on mass loading, and the major of the reports concluded that increasing mass decreased the electrochemical performance. For instance, Kang *et al.* [84] reported in their work that the mass increment from 0.33 to 3.41 mg cm^{-2} caused a capacitance reduction from 539 to 188 F g^{-1}. Researchers have also put efforts into incorporating other elements such as Al, Cu, Co, Fe, Mo, Ni, Sn, and Zn into the MnO_2 structure to increase the conductivity and performance [85–87]. Even though theoretically obtained capacitance is much

higher, practically, the capacitance reported is mostly less than 350 F g^{-1} for MnO_2 material. The ternary composites of the MnO_2/PP_y@carbon electrode reached a higher specific capacitance of 705 F g^{-1} at 2 mV s^{-1}, and PANI/mesoporous carbon/MnO_2 delivered 695 F g^{-1} [88,89]. As reported in the literature, different synthesis routes have been used to prepare the manganese oxide materials and their composites. In the following section 2.5, we have comprehensively reviewed the electrodeposition method, which is used in this thesis.

2.5. Electrochemical synthesis of manganese oxides (EMD)

Several chemical synthesis methods have been employed to produce manganese dioxide materials suitable for energy storage applications. The material properties can be varied by controlling the synthesis parameters. Hydrothermal/solvothermal, sol-gel coating, electrodeposition, electrochemical oxidation of Mn films, and electrophoretic deposition are a few examples of different synthesis methods reported in which electrodeposition is one of the several approaches. In this section, we exclusively focus on reviewing the state-of-art of electrodeposition to produce manganese oxides for energy storage applications. we have primarily used this synthesis method to yield high-quality EMD in bulk and enhance their physical electrochemical properties.

Electrodeposition is a unique technique for fabricating metal oxide, polymer, and composite electrodes as it can easily tune the material properties (composition, morphology, crystal structure) by adjusting experimental conditions. Compared to chemical synthesis, electrochemically synthesized materials show better energy storage performances [90]. Further, electrodeposition is preferred over chemical synthesis in commercial energy storage systems as it endows high purity, high content of MnO_2, easy processing, and inherent flexibility at scale. Previous researchers [91,92] have presented five techniques to carry out the electrosynthesis process: electromigration of reactant species, electrolysis of fused salts, electro-generation of the base by cathodic reduction, anodic oxidation, and alternate current synthesis. In sections 2.5.1. and 2.5.2, we intend to compare the cathodic reduction and anodic oxidation processes and bring out their differences in terms of their reaction mechanisms.

2.5.1. Cathodic electrodeposition

Generally, the manganese oxide films are obtained by the electrochemical reduction of Mn^{7+} to Mn^{4+} in $KMnO_4$ or $NaMnO_4$ solutions. The reduction reaction occurs in a neutral aqueous solution as in reaction R(2.7) [93].

$$MnO_4^- + 2H_2O + 3e^- \rightarrow MnO_2 + 4OH^- \qquad \text{R(2.7)}$$

The MnO_4^- species in the solution determine the deposition kinetics, composition, and structural properties of the material [94,95]. An increase of MnO_4^- concentration provides a counterintuitive result by decreasing the deposition rate at a constant current due to the diffusion against an adverse potential gradient and inter-ion interaction, causing an enhanced friction effect [96]. The reaction of Mn^{2+} with MnO_4^- to produce MnO_2 has also been reported as represented by the reaction R(2.8) [97].

$$Mn^{2+} + 2MnO_4^- + 2H_2O \rightarrow 5MnO_2 + 4H^+ \qquad \text{R(2.8)}$$

In a method based on the electro generation of the base, the H^+ ions are consumed by the reactions, or the water electrolysis occurs. The reduction reactions at the cathode surface increase the electrolyte pH either by H^+ consumption or OH^- generation. These compete with the metal ion reduction reactions and become the overriding reactions to ensure no metal deposition takes place; the metal ion deposits in the form of hydroxide as follows in the reaction R(2.9). The manganese hydroxide can then be converted to the oxide by thermal treatment [71].

$$Mn^{2+} + 2(OH)^- \rightarrow Mn(OH)_{2\,(s)} \qquad \text{R(2.9)}$$

The researchers have investigated the cathodic electrodeposition as a possible method for co-deposition of the materials, producing the manganese oxide composites with varying properties for modification of the film electrodes [93,94,96]. The following sections describe free-standing (thin film) and powder (bulk) manganese oxide cathodic deposition.

2.5.1.1. Free-standing (thin film) electrodes

Manganese oxide thin film electrodeposited on carbon substrates as a binder-free standing electrode for supercapacitors is widely used. Nagarajan *et al.* [98] fabricated MnO_x films on Ni foil using a galvanostatic method using $MnCl_2$ solution with polyethyleneimine (PEI) as an additive. The films were smooth, crack-free, and relatively dense and showed 425 F g^{-1} capacitance in a potential window of 0-0.9 V. however, after cycling, the MnO_x electrode surfaces were transformed into cracked films. A similar process was followed by Xiao *et al.* [99] using manganese acetate solution to produce ε-MnO_2 films containing porous/nanoflaky hierarchical architecture.

In 2011, Wang and Zhitomirsky [100] published a work in which cathodic deposition was developed for fabricating Ag-doped MnO_2 films from $KMnO_4$ aqueous solutions containing $AgNO_3$. Compared to pure MnO_2, the Ag-doped material showed improved capacitance of 770 F g^{-1} at 2 mV s^{-1} tested in 0.5 M Na_2SO_4 aqueous electrolyte. Gibson *et al.* [101] suggested two primary mechanisms when MnO_2 was deposited from neutral $KMnO_4$ and Na_2SO_4 solution. A specific capacitance of 363 F g^{-1} was obtained at a scan rate of 25 mV s^{-1}. In another study carried out by Mishra *et al.* [102], MnO_2 films were obtained by three different electrodeposition modes, termed potentiostatic (PS), potentiodynamic (PD), and galvanostatic (GS), using MnO_4^- precursor. All the deposited material showed an ε-MnO_2 crystallographic phase. The MnO_2 deposited via PS mode has the maximum specific capacitance of 259.4 F g^{-1} due to the porous morphology indicating effective electrolyte ion transfer led to enhanced storage properties. Followed by PS, the films deposited via PD and GS obtained 187.1 and 180.3 F g^{-1}, respectively. Thus, a considerable amount of literature has been published on preparing free-standing (thin film) manganese oxide electrodes using cathodic electrodeposition.

2.5.1.2. Powder (bulk) material deposition

To date, little evidence has been found associating with fabricating the powdered manganese oxides by the cathodic electrodeposition method. Tizfahm *et al.* [103]

synthesized MnO_2 nano-worms through pulse current (PC) electrodeposition followed by heat treatment using $Mn(NO_3)_2$ aqueous solution. A stainless-steel cathode was used with two parallel graphite anodes. The deposition was carried out for 40 minutes at 80 °C bath temperature. The prepared MnO_2 was mixed with the acetylene black and polytetrafluorethylene (PTFE) binder and pressed onto a nickel foam current collector. The tested electrode exhibited 202 F g^{-1} specific capacitance with 91.1 % retention after 1000 cycling. However, MnO_2 produced cathodic in a bulk powdered form has not been widely researched.

2.5.2. Anodic electrodeposition

The background of the anodic electrodeposition has been comprehensively discussed from the perspective of reaction pathways, as this is the key point to determining the quality of EMD, which will be illustrated here. The anodic deposition is highly suitable for synthesizing the electrochemically active gamma-manganese dioxide (γ-MnO_2), while the previously discussed cathodic deposition (in section 2.5.1) is not suitable for γ-MnO_2 synthesis.

In the anodic deposition, γ-MnO_2 is electrolytically deposited on the anode by the electrolysis of aqueous electrolyte containing manganese ions (Mn^{2+}). The obtained product is popularly known as EMD. The Mn^{2+} containing electrolyte can be on one of the Mn salts such as manganese sulfate ($MnSO_4$), manganese chloride ($MnCl_2$), or manganese acetate ($Mn(CH_3COO)_2$) [104–106]. At the selected pH, Mn^{2+} should be stable in the electrolyte, and its higher oxidation states can go through hydrolysis to produce hydroxides or oxides [91,107]. In the presence of sulphuric acid, its concentration is kept at a value that does not increase the pH above 5.3, as it can cause $Mn(OH)_2$ precipitation during hydrolysis. Generally, the current density lies within 50-300 A m^{-2}, while large current densities of 500-1000 A m^{-2} are also reported. The bath temperature is controlled at 80-98 °C [108,109]. Thus, at a specific sulphuric concentration (< pH 5.3), the Mn^{2+} in the aqueous medium presents in the form of a complex hexaaquo ion and participates in hydrolysis reaction as follows in R(2.10) [110,111].

$$[Mn(H_2O)_6]^{2+} \leftrightarrow [Mn(H_2O)_5(OH)]^{+} + H^{+} \qquad \text{R(2.10)}$$

Mn^{3+} is known as an active ion participating in redox reactions in aqueous solutions. It also can exist as a hexaaquo ion, though it shows rapid hydrolysis at lower pH according to the reaction R(2.11).

$$[Mn(H_2O)_6]^{3+} \leftrightarrow [Mn(H_2O)_5(OH)]^{2+} + H^{+} \qquad \text{R(2.11)}$$

Albeit the Mn^{2+} and Mn^{3+} ions are stable in aqueous solutions depending on the environment as described previously, and as such, there is no evidence for Mn^{4+} of its stability in a complex form ($[Mn(H_2O)_6]^{4+}$). Therefore, the plausible option is rapid hydrolysis reaction led to producing solid manganese dioxide [111,112]. The main reactions that take place at the anode and cathode are given by the reaction R(2.12) and R(2.13), respectively; the overall reaction is given by R(2.14).

Anode	$Mn^{2+} + 2H_2O \rightarrow MnO_2 + 4H^{+} + 2e$	R(2.12)
Cathode	$2H^{+} + 2e \rightarrow H_2$	R(2.13)
Overall	$Mn^{2+} + 2H_2O \rightarrow MnO_2 + 2H^{+} + H_2$	R(2.14)

The above illustration is quite simple when considering the actual deposition mechanism of EMD. Thus far, several systematic descriptions have been suggested to understand this phenomenon. Fleischmann *et al.* [113] conducted an electrodeposition experiment at a constant potential using platinum electrodes and proposed the following mechanism, R(2.15 - 2.22). It was based on the adsorption of components to the electrode during oxidation conversions. The first two reactions, R(2.15) and R(2.16) are kinetically fast, while the formation of MnO_2 to create the crystal growth by dehydration represented by R(2.18 - 2.22) has become the rate-determining steps (r.d.s).

$$[Mn(H_2O)_n]^{2+}_{sol} \leftrightarrow [Mn(H_2O)_n]^{3+}_{ads} + e \quad \text{R(2.15)}$$

$$[Mn(H_2O)_n]^{2+}_{sol} \leftrightarrow [Mn(H_2O)_n]^{4+}_{ads} + 2e \quad \text{R(2.16)}$$

$$[Mn(H_2O)_n]^{3+}_{ads} + [Mn(H_2O)_n]^{3+}_{ads} \leftrightarrow [Mn(H_2O)_n]^{2+}_{sol} + [Mn(H_2O)_n]^{4+}_{ads} \quad \text{R(2.17)}$$

$$[Mn(H_2O)_n]^{4+}_{ads} \leftrightarrow [Mn(H_2O)_{n-1}(OH)]^{3+}_{ads} + H^+ \quad \text{R(2.18)}$$

$$[Mn(H_2O)_{n-1}(OH)]^{3+}_{ads} \leftrightarrow [Mn(H_2O)_{n-2}(OH)_2]^{2+}_{ads} + H^+ \quad \text{R(2.19)}$$

$$[Mn(H_2O)_{n-2}(OH)_2]^{2+}_{ads} \leftrightarrow [Mn(H_2O)_{n-3}(OH)_3]^{+}_{ads} + H^+ \quad \text{R(2.20)}$$

$$[Mn(H_2O)_{n-3}(OH)_3]^{+}_{ads} \leftrightarrow [Mn(H_2O)_{n-4}(OH)_4]_{ads} + H^+ \quad \text{R(2.21)}$$

$$[Mn(H_2O)_{n-4}(OH)_4]_{ads} \rightarrow MnO_2 + (n-2)H_2O \quad \text{R(2.22)}$$

According to the model suggested by Cartwright and Paul [114], the conversion process might be chemical or electrochemical. Based on this fact, two mechanisms have been considered as represented by A and B (illustrated below). The diffusion step R(2.23, 2.27) is also the r.d.s. Then the diffused Mn^{2+} ions produce MnO_2 via reactions R(2.24 - 2.26, 2.28-2.30).

Mechanism A:

$$Mn^{2+}_{bulk} \xrightarrow{diffusion} Mn^{2+}_{MnO_2} \quad \text{rds} \quad \text{R(2.23)}$$

$$Mn^{2+}_{MnO_2} \rightarrow Mn^{3+} + e \quad \text{fast} \quad \text{R(2.24)}$$

$$Mn^{3+} + 2H_2O \rightarrow MnOOH + 3H^+ \quad \text{R(2.25)}$$

$$MnOOH \rightarrow MnO_2 + H^+ + e \quad \text{slow} \quad \text{R(2.26)}$$

Mechanism B:

$$Mn_{bulk}^{2+} \xrightarrow{diffusion} Mn_{MnO_2}^{2+} \quad \text{rds} \quad \text{R(2.27)}$$

$$Mn_{MnO_2}^{2+} \rightarrow Mn^{4+} + 2e \quad \text{fast} \quad \text{R(2.28)}$$

$$Mn^{4+} + 4H_2O \rightarrow Mn(OH)_4 + 4H^+ \quad \text{R(2.29)}$$

$$Mn(OH)_4 \rightarrow MnO_2 + 2H_2O \quad \text{slow} \quad \text{R(2.30)}$$

Kao and Weibel [115] claimed that initially, there was no occurrence of adsorption of Mn^{2+} onto Pt electrode surfaces for the reactions. Mn^{3+} is formed as the initial oxidation product as it can stay stable by an equilibrium process to control the concentration. There is less possibility of forming Mn^{4+} as the intermediate product as it shows very low stability by reacting with water to produce $Mn(OH)_4$, which is easily dehydrated to give MnO_2. Further, the Mn^{3+} can undergo hydration to yield MnOOH solid intermediate. The following reactions, R(2.31) and R(2.32), instigate the nucleation of MnO_2 on the Pt surfaces. A subsequent reaction of MnOOH oxidation also forms MnO_2.

$$2Mn^{3+} + 2H_2O \leftrightarrow Mn^{2+} + MnO_2 + 4H^+ \quad \text{R(2.31)}$$

$$Mn^{3+} + 2H_2O \leftrightarrow MnOOH + 3H^+ \quad \text{R(2.32)}$$

However, the deposited MnO_2 is then reduced by reacting with Mn^{2+} to yield MnOOH/Mn^{3+} as in reactions R(2.33) and R(2.34). The yielded Mn^{3+} should also agree with the equilibrium as in the reaction R(2.31). The MnOOH oxidizes into MnO_2, which is given in the reaction R(2.35). Diffusion of the generated protons through the solid phase determines the rate of EMD surface growth.

$$Mn^{2+} + MnO_2 + H^+ \rightarrow MnOOH + Mn^{3+} \quad \text{R(2.33)}$$

$$Mn^{2+} + MnO_2 + 2H_2O \rightarrow 2MnOOH + 2H^+ \quad \text{R(2.34)}$$

$$MnOOH \rightarrow MnO_2 + H^+ + e \quad \text{R(2.35)}$$

Further, in the study carried out by Clarke *et al.* [111], they developed two mechanisms for lower and higher acid concentrations in the electrolyte. The oxidation mechanism under low acid concentration can be applied to yield quality products, which is presented in this Ph.D. work. The acid concentration is kept lower than 1.0 M.

Low concentration (<1.0 M)

$$[Mn(H_2O)_6]^{2+} \leftrightarrow [Mn(H_2O)_6]^{2+}_{ads} \quad \text{R(2.36)}$$

$$[Mn(H_2O)_6]^{2+}_{ads} \rightarrow [Mn(H_2O)_6]^{3+}_{ads} + e \quad \text{R(2.37)}$$

$$[Mn(H_2O)_6]^{3+}_{ads} \rightarrow [Mn(H_2O)_5(OH)]^{2+}_{ads} + H^+ \quad \text{R(2.38)}$$

$$\downarrow \quad \text{fast}$$

$$\downarrow$$

$$MnOOH$$

$$MnOOH \rightarrow MnO_2 + H^+ + e \quad \text{slow} \quad \text{R(2.39)}$$

High concentration (>1.0 M)

$$[Mn(H_2O)_6]^{2+} \leftrightarrow [Mn(H_2O)_6]^{2+}_{ads} \quad \text{R(2.40)}$$

$$[Mn(H_2O)_6]^{2+}_{ads} \rightarrow [Mn(H_2O)_6]^{3+}_{ads} + e \quad \text{R(2.41)}$$

$$[Mn(H_2O)_6]^{3+}_{ads} \rightarrow [Mn(H_2O)_6]^{3+} \quad \text{slow} \quad \text{R(2.42)}$$

$$2[Mn(H_2O)_6]^{3+} \rightarrow [Mn(H_2O)_6]^{2+} + [Mn(H_2O)_6]^{4+} \quad \text{R(2.43)}$$

$$[Mn(H_2O)_6]^{4+} \rightarrow\rightarrow MnO_2 \quad \text{R(2.44)}$$

2.5.2.1. Free-standing (thin film) electrodes

Mn-based mixed oxides in free-standing (thin-film) form have become the interest of many researchers due to their potential applications as micro-scale energy storage systems such as integrated devices. In the thin film formation, the manganese oxide layers are directly assembled on the working electrode to get desired properties. The

first-ever reported thin film MnO_2 electrode was by Pang. *et al*. [82] in 2000 employed anodic deposition by potentiostatic method for electrochemical capacitors. Following their work, numerous articles have been published to date, focusing on the anodic thin film deposition of manganese oxides [116–118]. Hu and co-workers [119] fabricated a porous hybrid EMD on an electroformed Ni substrate using a 0.1 M $Mn(CH_3COO)_2$ and 0.1 M Na_2SO_4 bath. The deposition current was increased from 1 to 14 mA cm^{-2}, and the nature of the electrode changed from porous and fibrous to a denser film. Further, most of the published research has focused on changing the experimental parameters to obtain desired morphologies, surface areas, high capacitances, cycling stability, etc. Having a three-dimensional mesoporous architecture was found to be desirable for electrolyte penetration to store more charge in the material [120–122]. Most of the existing literature on manganese oxide as supercapacitor materials has been prepared as thin-film electrodes. However, the electrodeposited thin-film materials encounter issues such as lower mass loading and difficulty in scalability that can be overcome in the bulk synthesis of powder material, as illustrated in the following section 2.5.2.2.

2.5.2.2. Powder (bulk) material deposition

Preisler [123] studied different anode materials, pure lead (Pb), antimonial lead, graphite, and titanium (Ti), then elaborated that Ti can be a good selection as the anode. In their work, Rethinaraj and Visvanathan also discussed using different substrates for EMD (γ-MnO_2) production [124]. γ-MnO_2 was synthesized via electrodeposition under a supergravity field (*i.e.,* gravity >9.8 m s^{-2}) by Du *et al.* [125]. The authors observed that the effective surface area of the deposited material was reduced with the supergravity field, which affected the capacitance values. The researchers used an $Mn(CH_3COO)_2$ solution and deposited the material on a Ti ring coated with Pt. The prepared electrode exhibited a maximum specific capacitance of 277.9 F g^{-1} at 0.5 A g^{-1} current density. Dupont *et al.*[126] examined the effect of cation species on the charge storage behavior of EMD prepared using an electrolyte bath containing acidic $MnSO_4$ (1 M) solution, deposited onto a Ti electrode. Copper (Cu) sheets were used as cathode electrodes. An anodic current of 65 A m^{-2} was applied, and a 98 °C

temperature was maintained during the experiment. The changes in the capacitance values were observed by changing the electrolyte (cation). The highest capacitance of 45 F g^{-1} was obtained for the Li_2SO_4 aqueous electrolyte.

Apart from the few studies discussed above, the research on powder EMD has not been very well explored for supercapacitor applications. Therefore, synthesizing (bulk) EMD to tweak its quality with appropriate additives to the electrolytic bath and assessing its potential for SC application have been discussed in the following sections.

2.6. Electrochemical synthesis of manganese dioxide composites

Extensive investigations on improving MnO_2 by incorporating transition metal oxides are found in the literature. As discussed in the earlier sections, the transition metal oxides are semiconducting. Incorporating the foreign elements into the MnO_2 structure is a possible path to create more defects and charge carriers within the material to increase the charge storage capability. It can also tailor the electrode (EMD) material architecture to improve porosity and surface area and shorten the electron transport distance to obtain an electronically conducting structure. In addition, the capacitance fading over cycling (5 to 30 % in 1000 cycles [127]) can be overcome by providing high mechanical stability to the material. Further to this, strategies to yield high-quality EMD composites are discussed in sections 2.6.1 - 2.6.3.

2.6.1. Metal composites

Transition metal oxides such as Fe, Co, Ni, Mo, and Ru have been commonly used as dopants to prepare MnO_2 mixed composites prepared via electrochemical co-deposition [128–130]. Chen and Hu [128] obtained binary manganese-nickel oxides prepared by anodic deposition. A relatively positive potential region (1.0-1.2 V) and a high Ni^{2+}/Mn^{2+} ratio (10/1) in the deposition solution increased the influence of Ni on the capacitive characteristics. The specific capacitance of the sample was 160 F g^{-1} measured at 50 mV s^{-1}. Prasad and Miura [131] employed a PD method to deposit microporous nickel-manganese oxide (NMO) and cobalt-manganese oxide (CMO)

onto a stainless-steel substrate. The highest specific capacitances obtained for NMO and CMO were 621 and 498 F g^{-1} measured by cyclic voltammetric (CV) data (scan rate of 20 mV s^{-1}) in 1 M Na_2SO_4 electrolyte. Chuang and Hu [132] performed an anodic deposition of hydrous manganese-cobalt oxides onto a graphite substrate from $MnCl_2$ and $CoCl_2$ solutions with varying pH values. The pH change did not significantly influence the CV performance; however, morphology and composition were affected, showing cracks on the deposit with higher Co content. Nakayama *et al.* [133] prepared mixed Mn/Mo oxide, and the experiment was carried out in a standard three-electrode glass cell housing a Pt working electrode, a Pt gauze counter electrode, and an Ag/AgCl reference electrode. The electrolyte solution consists of 2 mM $MnSO_4$ with a range of concentrations; 0-20 mM of Na_2MoO_4 which gives the maximum molar ratio of 1:10 ($MnSO_4$:Na_2MoO_4). According to their results, the increasing MoO_4^{2-} concentrations shifted the CV profiles in a cathodic direction. This was recognized as there is a chemical reaction of MoO_4^{2-} taking place with protons released during the oxidation of Mn^{2+}. This concluded that polymolybdate co-precipitated with manganese oxide, although Mo_xO_y was not identified in the material. Rusi [134] studied the electrochemical performance of MnO_2-NiO composite prepared using chronoamperometry (CA), chronopotentiometry (CP), and CV methods. The electrode prepared using the CV method by depositing the composite for 7 cycles exhibited high homogeneity, a highly amorphous nature, and good capacitive behaviors compared to CA and CP methods. Figure 2.9 shows the morphologies of electrodes synthesized using a different number of deposition cycles by the CV method. Further, several other researchers have reported on producing MnO_2-metal composites for SCs via various electrochemical syntheses such as Ag-doped manganese dioxide by cathodic electrodeposition [100], Fe-MnO_2 electrodes by GS deposition [129], Co_3O_4 nanoparticles/MnO_2 composites [130]. Different morphologies obtained for MnO_2-metal composites synthesized by the electrochemical method are published in the literature, such as nanowires [128], interconnected web-like network [129], sphere-like morphology [130], and nanoscale fibres [135].

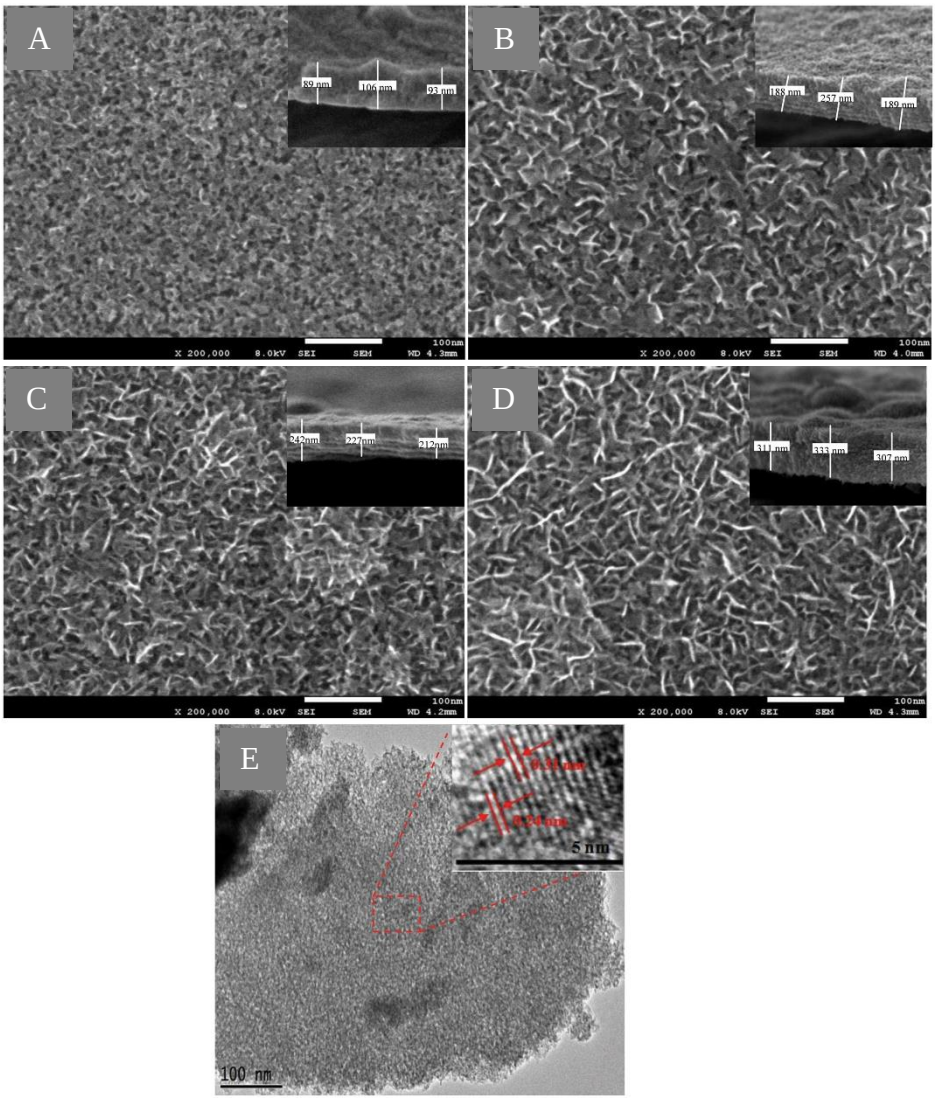

Figure 2.9 FESEM images of the samples electrodeposited using CV mode with (A) 4 deposition cycles, (B) 7 deposition cycles, (C) 10 deposition cycles, (D) 13 deposition cycles, (E) TEM of the sample deposited with 4 deposition cycles (inset: lattice spacing). Reproduced from [134], open-access Creative Commons CC BY 4.0 license, PLoS One.

2.6.2. Polymer composites

Manganese oxide electrodes are subjected to dissolving in the electrolyte during electrochemical cycling, which generates soluble Mn^{2+} species. It can be massive in acidic environments compared to the other electrolyte types of mild acidic (~pH 4.4),

neutral (~pH 7), and alkaline (pH >7) [136,137]. Therefore, many electrodes have been tested in neutral or alkaline electrolytes; however, the insertion of the cations Li^+, Na^+, and K^+ are not captivating as the fast H^+ insertion in an acidic medium for SCs. To overcome these limitations, the manganese dioxide materials have been modified using polymers to produce desirable hybrid manganese oxide-polymer configurations which are stable and efficient in varying electrolytes.

When a polymer is distributed in a solution ready for deposition, three major characteristics affect deposited material properties. Polydispersity (dispersity) describes the non-uniformity of the polymer distribution; therefore, a range of molecular weights in the solution is expected. A polymer has several configurations in the same structure. It also has several points that are active to make bonds and get attached. Many of the polymers used as additives are generally polydisperse. Therefore, it is recommended to use limited molecular weight fractions of the component for good reproducibility. Then the other two factors, the number of configurations and the number of points, determine the adsorption rates of the species. A flexible molecule distorts its shape from the typical shape in the solution in the vicinity of the surface [92]. PANI is a conducting polymer that has the potential to be used for SCs due to its high stability and conductivity. Prasad and Miura [138] carried out the first research to prepare a MnO_2-PANI composite by depositing manganese oxide on the PANI matrix, which delivered a high capacitance of 715 F g^{-1}. The resulted capacitance was ascribed to the increased surface area by incorporating the 3D PANI architecture. An electrochemical co-deposition was conducted by Sun and Liu [139] using a solution of aniline and $MnSO_4$ through potential cycling between -0.2 and 1.45 V *vs.* SCE. It produced a fibrous MnO_2-PANI structure with a larger surface area. The characteristic redox peaks of PANI were observed in CV measurements taken in an acidic aqueous electrolyte, and the hybrid electrode displayed 532 F g^{-1} capacitance. The images and the electrochemical measurements for these samples are shown in Figure 2.10.

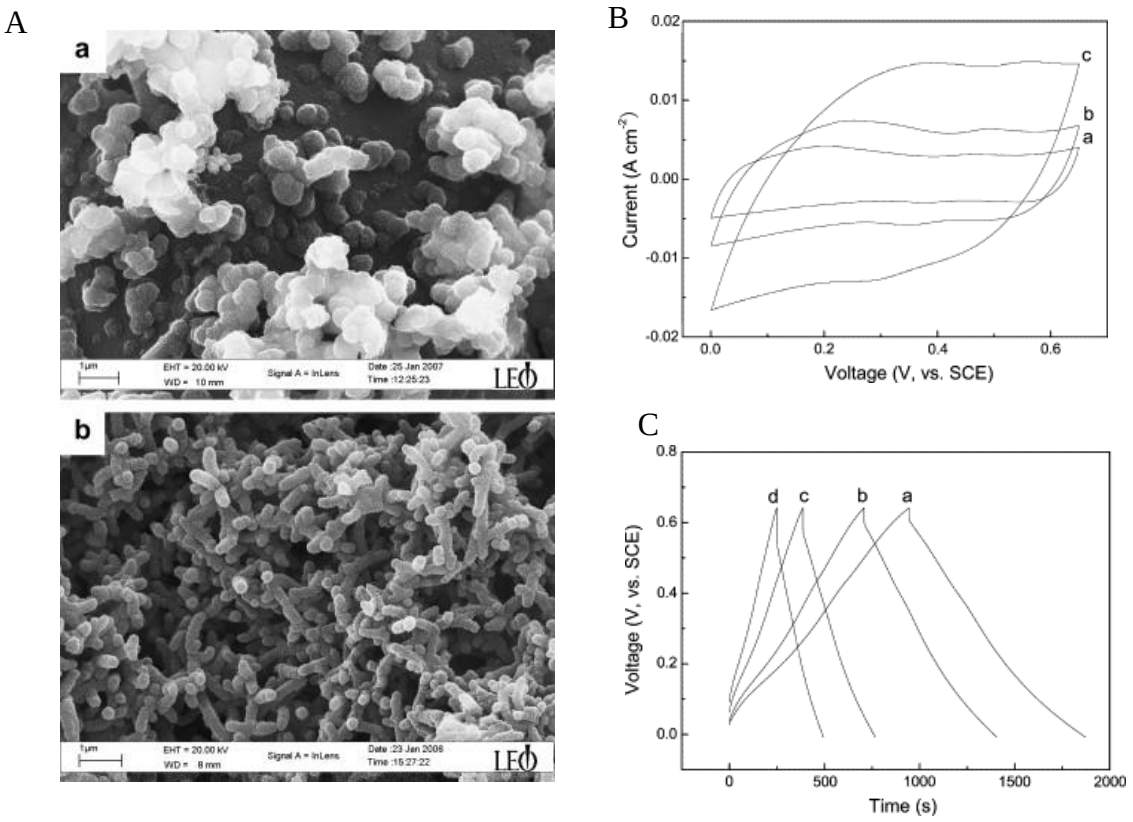

Figure 2.10 (A) SEM images of (a) PANI film, (b) hybrid MnO_2-PANI film, (B) CV measured in 1 M $NaNO_3$ at pH 1 between 0 and 0.65 V at (a) 1, (b) 2, (c) 5 mV s^{-1}, (C) GCD curves in 1 M $NaNO_3$ at pH 1 between 0 and 0.65 V at (a) 2.4, (b) 3.0, (c) 5.0, (d) 7.0 mA cm^{-2}. Reproduced with permission from ref. [139], copyright 2008, Elsevier.

The MnO_2 embedded in PP_y nanocomposite was prepared as thin-film electrodes by Sharma *et al*. [117]. Compared to the pristine MnO_2 (~225 F g^{-1}) and PP_y (~250 F g^{-1}), the composite MnO_2/PP_y significantly improved the redox reactions with a specific capacitance of ~620 F g^{-1}. A flexible capacitor electrode was synthesized by depositing the PP_y, graphene oxide, and manganese oxide onto a highly porous nickel foam [140]. For a flexible capacitor, all the components should work within their elastic limit to get an undegraded electrochemical response [141]. In the produced composite, the Mn_3O_4 and MnO_2 manganese components were detected by FTIR and Raman analyses. A layer-by-layer assembly of PP_y, graphene oxide, and manganese oxide has been prepared by electrodeposition by Kulandaivelu *et al*. [142]. FTIR, Raman, and

X-ray diffraction analysis confirmed the presence of the layer of each component. From the above examples and other published work [139,143], researchers have made more efforts to incorporate PANI, PP_y, PTh, and CP to produce MnO_2-polymer composites. These polymers have also been used in ternary composite materials of metal/polymer/carbon [144,145]. A typical example is given in Figure 2.11 for assembling manganese oxide/PPy/graphene oxide on an indium tin oxide electrode [142]. However, using bio-polymers is scarcely reported in the development of EMD materials. we have reported that the Alginate biopolymer incorporated into the EMD structure modified the material, enhancing the electrochemical properties. Environmental friendliness and cost-effectiveness are the added advantages of sustainable biopolymer additives in the bath.

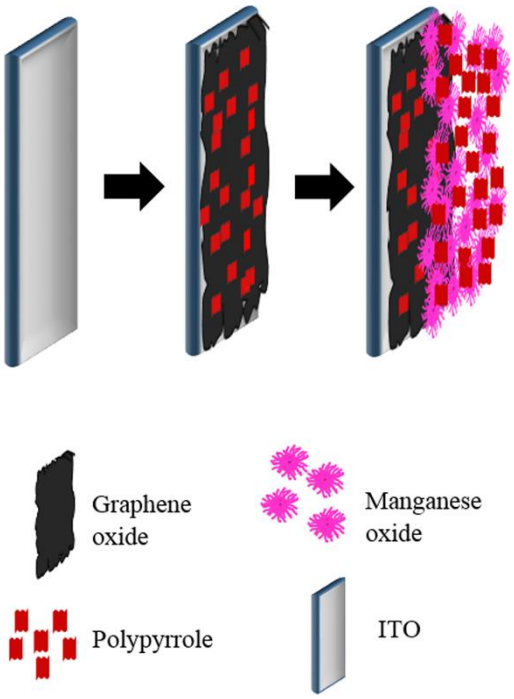

Figure 2.11 Schematic illustration of the preparation procedure of PP_y/GO|PP_y/MnO_2 (ITO: Indium tin oxide). Reproduced with permission from ref. [142], copyright 2019, nature.

2.6.3. Surfactant composites

Surfactants can act as structure-directing agents or soft templates in manganese dioxide preparation. The self-assembly function of the surfactants is an advantage in regulating and controlling materials morphology and structure [146]. Devaraj and Munichandraiah [147] synthesized MnO_2, which was electrodeposited on a Ni substrate from a neutral electrolyte in the presence of sodium lauryl sulfate (SLS). The specific capacitance was improved to 310 F g^{-1}, compared to the 240 F g^{-1} given by the MnO_2 deposited in the absence of the SLS. Li *et al.* [148] conducted a study dealing with two surfactants, cetyltrimethylammonium bromide (CTAB) or cetyltrimethylammonium chloride (CTAC), to produce manganese dioxide nanocomposites which are shown in the SEM in Figure 2.12(A-C). The morphology of MnO_2: CTAC was like nanosheets, while MnO_2:CTAB changed its morphology from a mixture of nanosheets and nanoparticles to big blocks with increasing CTAB concentration. Thus the MnO_2:CTAC showed the best electrochemical performance than pristine and MnO_2:CTAB (Figure 2.12D). Faridi *et al.* [149] reported about electrodepositing MnO_2 in the presence of both CTAB surfactant and Ag^+ ions in the electrolyte. They observed that adding Ag and CTAB provided more active sites for pseudocapacitive reaction during charge-discharge. Recently, Aghazadeh *et al.* [150] synthesized CTAB-assisted MnO_2 ultra-fine nanoparticles (~10 nm) via cathodic electrodeposition, which delivered 232 F g^{-1} maximum specific capacitance at 0.5 A g^{-1} current density. Therefore, based on the published work [148–151], it is noted that CTAB is the mostly used surfactant to produce the capacitor materials.

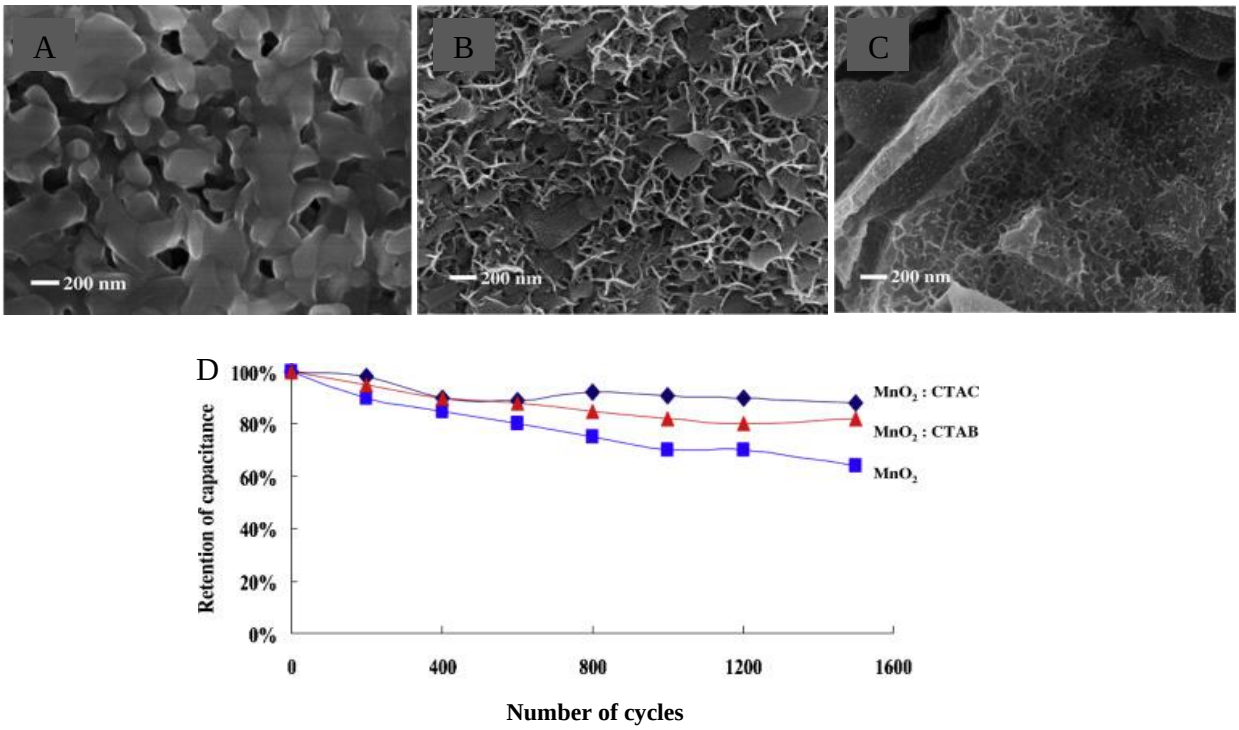

Figure 2.12 SEM images of (A) MnO_2, (B) CTAC: 50 Mm, (C) CTAB: 50 mM, and (D) capacitance retention comparison of MnO_2, MnO_2: CTAC, and MnO_2: CTAB after 1500 cycles. Reproduced with permission from ref. [148], copyright 2014, Elsevier.

2.7. EMD for energy storage applications

2.7.1. EMD as a battery material

The concept of using the EMD as a pseudocapacitive electrode in SCs was derived based on its wide application in the battery field. Currently, EMD is commercially used as electrodes to produce primary alkaline cells (Zn-MnO_2) in aqueous electrolytes [152] and rechargeable lithium batteries in non-aqueous electrolytes [153]. Thus, to add a favour, the EMD application as a battery material is briefly discussed in this section. EMD has a theoretical discharge capacity of 308 mAh g^{-1} depending on its one-electron discharge step. The battery systems mainly consist of two different electrolyte media, either aqueous or non-aqueous solvents. In primary cells using aqueous media, the protons (H^+) insert into the MnO_2 structure, and irreversible chemical reactions occur that limit the battery to a single-use. While under specific

conditions, the insertion can also become reversible [154,155]. The protons are incorporated, keeping the charge balance in the manganese dioxide lattice [156]. Besides, in Li-ion non-aqueous media, Li ions (Li^+) intercalate instead of protons. Generally, in Li/MnO_2 systems, initially, the EMD is heat-treated to remove water and enhance the structure to become more suitable for battery applications [157,158]. Even in the aqueous media, better electrochemical performances were observed for heat-treated EMD [159]. Jouanneau *et al.* [160], Minakshi *et al.* [161], and Rus *et al.* [162] have conducted studies for comparative analysis of the role of EMD in both types of solutions.

The researchers have given different explanations for the reaction mechanisms that occurred during the charging and discharging of EMD in the KOH electrolyte. In the study carried out by Kozawa *et al.*, they mentioned a two-step mechanism for cathodic reduction. The first and second steps occur in homogeneous and heterogeneous phases, respectively. In this case, MnO_2 reduces its oxidation state from 4^+ to 2^+ [156,163,164]. A comprehensive explanation is given by McBreen [165] on both the reduction and oxidation mechanisms of EMD in battery use. Later, many authors published their work on investigating the redox behavior of EMD using CV and GCD techniques in Zn/MnO_2 batteries in the presence of aqueous KOH [166–169]. The KOH is mostly limited to primary batteries though the studies so far could prove the rechargeability of EMD/modified EMD in KOH [170–173]. Besides the KOH electrolyte, investigations have been carried out for LiOH and NaOH. For instance, several researchers reported that cells made of EMD/LiOH are better functioning with higher energy density, cycle life, and higher reliability against overcharge/discharge compared to the cells of CMD/LiOH [174,175]. In summary, EMD materials have been widely used for battery applications.

2.7.2. EMD as a capacitor material

Several studies have been conducted to understand the charge storage mechanisms of manganese dioxide electrode materials in different electrolytes. Up to now, various types of electrolytes such as organic, aqueous, ionic liquids, and solid-state polymer

electrolytes have been studied by researchers. The mainly used electrolytes to research the supercapacitors are given in Table 2.3.

Table 2.3 The electrolytes commonly reported for SCs

Electrolyte	Voltage window (V)	Reference
1 M H_2SO_4	1.3	Jurcokava *et al.* [176]
6 M KOH	1.0	Wang *et al.* [177]
1 M Na_2SO_4	1.8	Wang *et al.* [177]
1 M Li_2SO_4	2.2	Fic *et al.* [178]
1 M $TEABF_4$/PC*	3.0	Jung *et al.* [179]
2 M $EMIPF_6$**	3.6	McEwen *et al.* [180]
*$TEABF_4$ - Tetraethylammonium tetrafluoroborate/propylene carbonate **$EMIPF_6$ -1-ethyl-3-methylimidazolium hexafluorophosphate		

Organic solvents provide a wider voltage window for both batteries and SCs, however, the higher cost, lower specific capacitance, inferior conductivity, and safety concerns (flammability, volatility, and toxicity) are the major drawbacks. Additionally, the issues with the organic electrolytes are matching the electrolyte ion size with the pore diameters of the metal oxide electrodes and keeping the water content lower by about 3-5 ppm, failing to achieve these can cause a reduction of specific capacitance, and the voltage window [181]. In contrast to organic electrolytes, aqueous electrolytes have higher ionic concentration, lower resistance, and a much higher ionic conductivity. For example, the conductivity of 1 M H_2SO_4 is 0.8 S cm^{-1} and for 6 M KOH 0.6 S cm^{-1} at 25 °C [182]. Aqueous electrolytes can be classified as acidic, neutral, and alkaline; H_2SO_4, Na_2SO_4, and KOH are the most popular [181].

The unique pseudocapacitance charge storage mechanism of MnO_2 can be either surface adsorption/desorption or bulk intercalation/deintercalation of the cations in the electrolyte medium given by the reaction R(2.45) and R(2.46), respectively. Both mechanisms involve the reversible transition of Mn^{4+} to Mn^{3+} [82,183].

$$(MnO_2)_{surface} + A^+ + e^- \leftrightarrow (MnO_2 - A^+)_{surface} \quad \text{R(2.45)}$$

$$MnO_2 + A^+ + e^- \leftrightarrow MnOOA \quad \text{R(2.46)}$$

$$A^+ refers\ H^+, Li^+, Na^+, K^+$$

Chou *et al.* [184] obtained the thin films of carambola-like γ-MnO_2 nanoflakes on nickel sheets prepared by PS and CV combined electrodeposition techniques. The γ-MnO_2 electrode showed a specific capacitance of 240 F g^{-1} at 1 mA cm^{-2} tested in 0.1 M Na_2SO_4 electrolyte. MnO_2 nanowires electrodeposited onto CNT paper were also examined in 0.1 M Na_2SO_4, which exhibited 167.5 F g^{-1} at a current density of 77 mA g^{-1} [185]. Jeyasubramanian *et al.* [122] applied the electrodeposition process to coat MnO_2 nanocrystals over Cu nano leaves. Before the electrodeposition, the Cu nano leaves were grown on fluorine-doped tin oxide material (FTO-Cu). The highest capacitance of 486 F g^{-1} (at 5 mV s^{-1}) in 0.1 M Na_2SO_4 electrolyte was observed for the electrode deposited for 350 s on FTO-Cu. These works show that Na_2SO_4 has widely been used for EMD due to its advantages, such as a larger working potential window, less corrosion, and safety [182]. Additionally, Xiao *et al.* [186] studied MnO_2 electrode performance in a 3 M KCl electrolyte. The deposited electrode using the GS method exhibited 160 F g^{-1}, while it was 252 F g^{-1} for the PC deposited electrode at 10 mV s^{-1}. A nanostructured α-MnO_2 was derived using commercial EMD and prepared as an α-MnO_2/graphene oxide (GO) nanocomposite. The composite material was studied in 1 M Li_2SO_4 aqueous electrolyte delivered 280 F g^{-1} (35 Wh kg^{-1} energy density and 7.5 kW kg^{-1} power density) at 0.5 A g^{-1}. The step potential electrochemical spectroscopy (SPECS) technique has been used by Dupont *et al.* [126] to examine the effect of different cations on the charge storage behavior of EMD. They observed that the different cations are likely to have different mechanisms of interacting with the surface and bulk electrode and affect the specific capacitance. Further, the effect of the cation also varied depending on the scan rate. Figure 2.13 displays the resulted overall capacitances over the experimented scan rates, where Li_2SO_4 delivered the largest values at all scan rates except for the scan rates higher than ~20 mV s^{-1}.

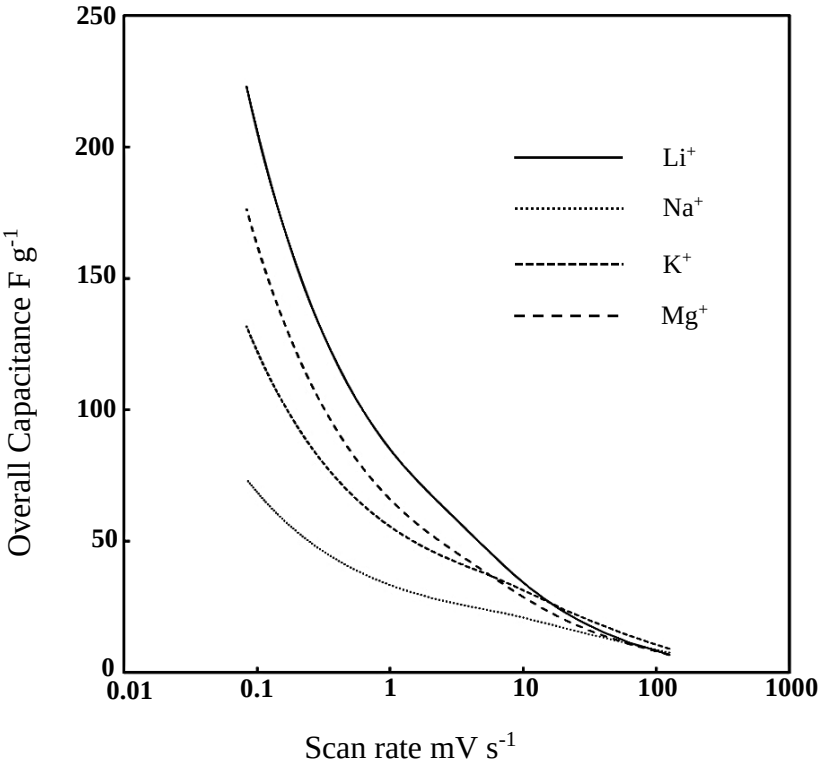

Figure 2.13 Overall capacitance as a function of scan rate for different electrolyte cations (0.5 M Li_2SO_4, Na_2SO_4, K_2SO_4, $MgSO_4$). Reproduced with permission from ref. [126], copyright 2018, Elsevier.

Consequently, EMD electrodes used potential Na-ion electrolytes to test the electrodes for SC applications. The EMD as the positive (cathode) electrode is coupled with carbon material (commercial and in-house synthesized) as the negative electrode (anode) to fabricate hybrid capacitors. The progress of developing the carbon electrodes is discussed in a later section in 2.9. The varying configurations of cathode and anode materials in the electrode cell when using the Na^+ ion electrolytes (sodium ion capacitors-SIC) are shown in Figure 2.14.

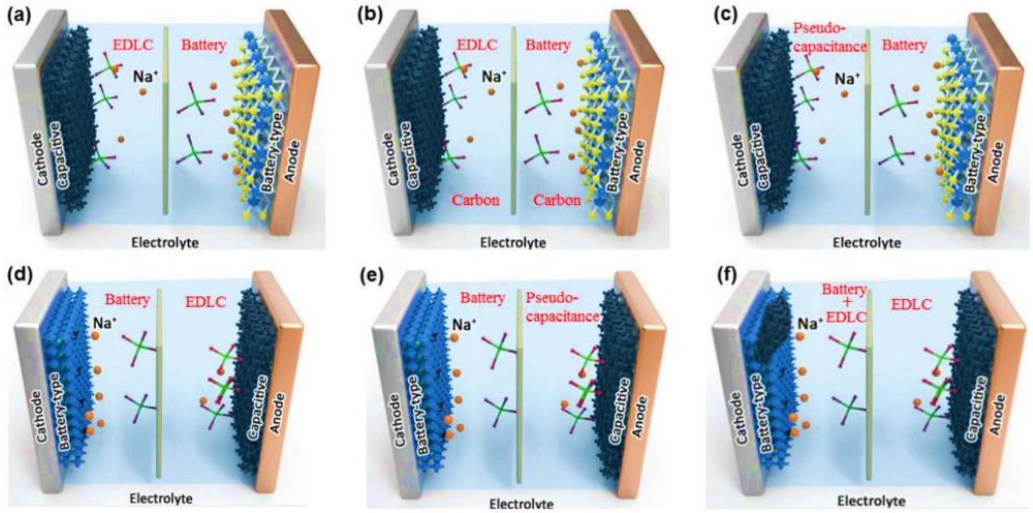

Figure 2.14 Cell structures and charge storage mechanisms of the nine electrochemical energy storage devices based on Na^+ ion electrolyte: a) Battery-type anode and EDLC cathode SICs cell configurations, b) dual carbon configurations, c) battery-type anode and pseudocapacitive cathode SICs cell configurations, d) EDLC anode and battery-type cathode SIC cell configurations, e) pseudocapacitive anode and battery-type cathode SICs cell configurations, f) capacitive anode and hybrid cathode SICs cell configurations, respectively. Reproduced with permission from ref. [187], Copyright 2021, WILEY-VCH.

2.8. Conducting polymers

The ability of the conducting polymers to transfer the electrons via the polymer backbone has taken the attraction to be employed in SC electrodes. In 1963, Weiss *et al.* [188–190] first published about the conductivity of conducting polymers. After three decades, in 1994, the first conducting polymer-based SC application was demonstrated by Rudge *et al.* [191,192]. Generally, conducting polymers are better conductors than metal oxides. However, it tends to swell during cycling causing poor cycle life performance [193]. The commonly studied conducting polymers are polypyrrole (PPy) [194], polyaniline (PANI) [195], polythiophene (PTh), and derivatives of polythiophene [196], etc. The charge storage mechanism of the conducting polymers is p-doped during oxidation (dedoped during reduction) with

counter anions and n-doped during reduction (dedoped during oxidation) with counter cations. The reaction can take place as follows [197]:

$$CP \leftrightarrow CP^{n+}(A^-)_n + ne^- \ \ (p-doping\ and\ dedoping)[A^-: anion] \qquad \text{R(2.47)}$$

$$CP + ne^- \leftrightarrow (C^+)_n CP^{n-} \ \ (n-doping\ and\ dedoping)[C^+: cation] \qquad \text{R(2.48)}$$

where, CP is a conducting polymer, A^- - anion, and C^+ - cation. A schematic depiction of the PPy charge storage mechanism is illustrated in Figure 2.15. PPy and PANI are in the p-doped category, while PTh and its derivatives are n-doped. Compared to conventional carbon-based EDLCs, CP-based SCs display higher energy density (~10 Wh kg^{-1} *vs.* 5 Wh kg^{-1}) due to pseudo-faradaic charge storage. Despite that, the power density is lower (2 kW kg^{-1} *vs.* 4 kW kg^{-1}) due to ion diffusion limitations in the bulk electrode [198]. The energy density can be further increased by varying the doping amount; increasing amounts accelerate the structural degradation over cycling due to volume change. This problem is addressed by the recent research by producing robust polymeric moieties by designing composites of carbonaceous materials (activated carbon, carbon black, graphite, graphene, etc.), metallic compounds (oxides, hydroxides, carbides, nitrides, etc.) with conducting polymers [199–201].

To evaluate the practical performance of a hybrid capacitor, a full cell is fabricated by coupling two electrodes. In this thesis, we have shown EMD metal oxide versus activated carbon (AC) materials for supercapacitor applications. The following section briefly discusses the activated carbon and other carbon allotropes used as the carbon-based negative electrodes.

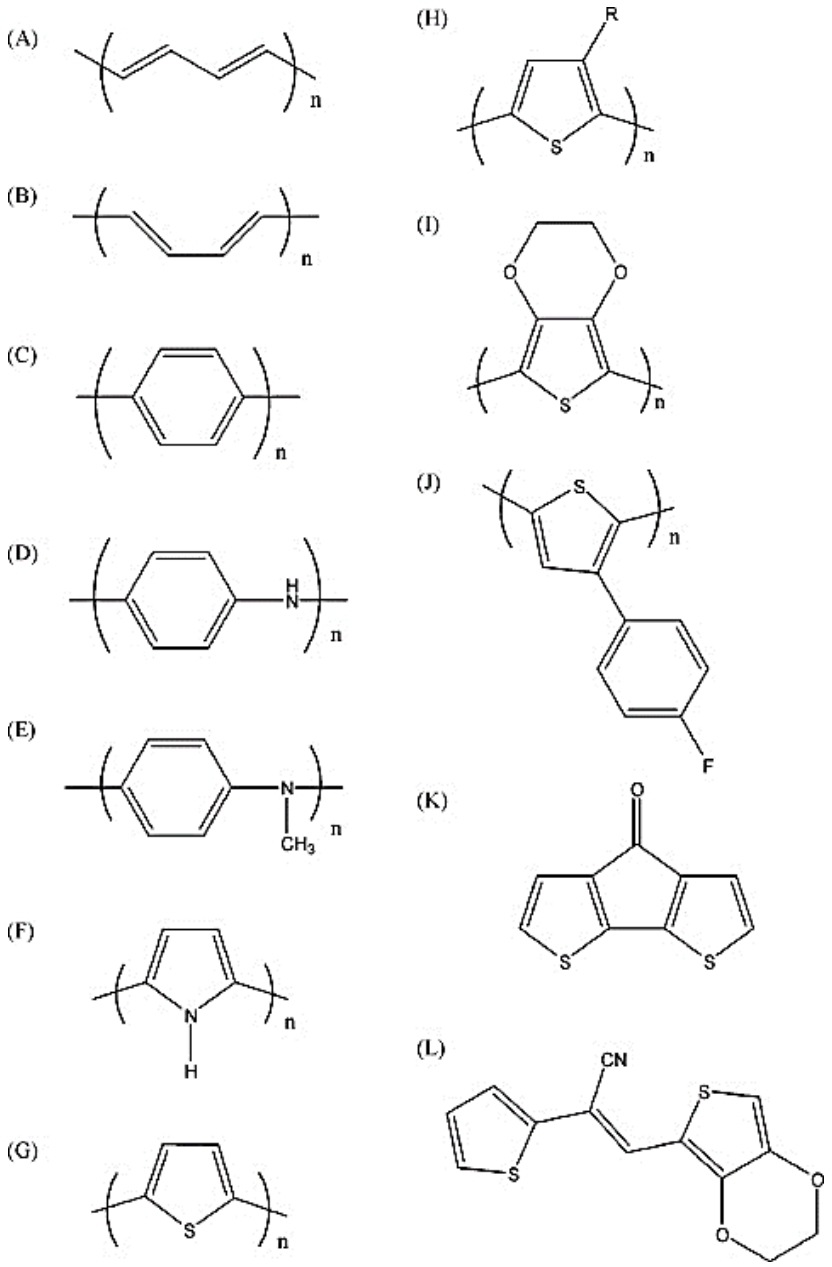

Figure 2.15 Various conducting polymer structures. (A) Trans-poly(acetylene), (B) cis-poly(acetylene), (C) poly(p-phenylene), (D) polyaniline (PANI), (E) poly(n-methylaniline), (F) polypyrrole (PPy), (G) polythiophene (PTh), (H) 3-substitued polythiophene, (I) poly(3,4-ethlenedioxythiophene), (J) poly(3-4-fluorophenyl)thiophene), (K) poly(cyclopenta[2,1-b;3,4-b-dithiophen-4-one]), (L) 1-cyano-2-(2-[3,4-ethylenedioxylthienyl])-1-(2-thienyl)vinylene (PThCNVEDT). Reproduced from ref. [193] with permission, copyright 2015, Elsevier.

2.9. Mapping the carbon-based materials as negative electrodes

Carbon materials are highly used to produce ideal EDLCs because of their electrostatic ion adsorption and higher electrical conductivity, large surface area, and low-density properties. Electrochemical double-layer capacitors are uniquely made from carbon electrode materials. Carbon exists in several allotropic forms among; diamond and graphite are well-known as the two natural allotropes. Many other synthetics include activated carbon (AC), fullerenes, graphene, carbon nanotubes, nanobuds, and nanoribbons [202]. Generally, the carbon electrode materials possibly approach 1.0 V in aqueous solutions and 3.5 V in non-aqueous electrolytes [4]. Carbon-carbon, symmetric SCs, offer better cycle stability, rate capability, and higher power than metal oxides. However, their self-discharge is higher, and the energy density is lower (< 12 Wh kg^{-1}) [42]. Therefore, exploring porous carbon materials and rational designing of these materials has become the interest of the researchers to develop advanced electrode materials to obtain higher energy densities. Therefore, the developed carbon at a premium price fails to sustain in the market [203].

Compared to the other carbon materials, ACs have a large surface area (~1000 m^2 g^{-1} [204]), good electrical properties, and can be produced at a moderate cost [205,206]. The SC carbon market is more sensitive to the price than its performance. Currently, the initial AC prices have dropped from USD150-200 kg^{-1} to USD15 kg^{-1}. Half of the material cost of an SC is due to the carbon materials; therefore, the lower price of AC is the key strong fact that omits the entrance of the other carbon [203]. There are two common pathways to produce AC, either with physical activation or chemical activation of the char produced from the precursor. Physical activation is considered a green approach as it is a chemical-free synthesis. However, the main drawbacks are the long activation time, the low adsorption capacity of synthesized AC, and high energy consumption [207,208]. The chemical activation method is advantageous over the physical activation process of being more economical due to lower activation temperatures, shorter processing time, and higher carbon efficiency [209,210]. There are two common pathways to produce AC, either with physical activation or chemical activation of the char produced from the precursor. Physical activation is considered a green approach as it is a chemical-free synthesis. However, the main drawbacks are

the long activation time, the low adsorption capacity of synthesized AC, and high energy consumption [207,208]. The chemical activation method is advantageous over the physical activation process of being more economical due to lower activation temperatures, shorter processing time, and higher carbon efficiency [209,210].

2.9.1. Biomass waste-derived carbon-based electrodes

The electrodes for the EDLC are mainly carbon-based materials (activated carbon, carbon nanotube, graphene, etc.). Activated carbon is derived from petroleum coke, is non-renewable, and obtained under harsh conditions [211]. Graphene synthesis by vapor deposition method using fossil fuel causes severe environmental issues hence unsustainable [212]. The biomass waste resource includes renewable crops and animal residue, is less environmentally polluting, and is a sustainable material. Therefore, it has become a realistic alternative for the formerly explained carbon material synthesis. On the other hand, it is an effective option for waste disposal problems resulting from more than 100 billion tons of waste produced every year from biomass crops and animal husbandry [212,213].

Some of the biomass waste precursors that have been utilized to prepare carbon electrodes are algae [214], orange peel [215], sugar cane bagasse [216], rice stem [217], sunflower stalk [218], tamarind seed coat [219], etc. Upon the heat treatment, the biomass precursor produces a carbon-rich material. Other elements such as H, O, N, and S can be removed to some extent by thermochemical conversion [220]. In addition to these elements, some trace elements of Ca, K Mg, Na, and Si can also be present and contribute to the energy storage performance [221]. The synthesis of biomass waste-derived activated carbon has two processes: carbonization and activation. Carbonization can occur in a temperature range of 400-900 °C in an inert atmosphere. In the activation process, the biomass is transferred into a functional material at a relatively high temperature, either physical or chemical activation. Generally, the physical activation is performed immediately after the carbonization (temperature up to 1200 °C) using steam or CO_2 atmosphere [222]. Physical activation is a faster method; however, serval drawbacks have been reported, such as lack of pore formation, low surface area, and extensive energy consumption compared to chemical

activation. Chemical activation can be conducted in a temperature range of 450-900 °C. Since the pyrolyzed carbon is mixed with an activating agent (NaOH, KOH, H_3PO_4, $ZnCl_2$), it forms many channels and pores in the carbon skeleton and results in efficient electrolyte ions transportation into the capacitor material [222].

Figure 2.16 gives another example of the chemical synthesis of AC reported by Zhu *et al.* [223]. The authors used pine needles as the precursor, and the derived AC contained a 0.5 - 2 nm pore size range and 2433 m^2 g^{-1} surface area. Up to date, a variety of biomass precursor types have been examined as carbon electrode materials. As well as, studies have been conducted to improve microscopic properties, surface area, and porosity properties mainly by altering the experimental parameters. The conventional understanding is that a higher surface area of carbon material is proportional to its capacitance. However, the evidence is found in the literature to prove that is not always the case [224,225]. A solution could be finding the quantitative correlations between structural properties, energy, and power densities. Conventionally, the equivalent circuit models are used to identify the charge-discharge kinetics of the electrodes [226]. However, this model lacks the capability to best evaluate ion transportation, particularly for microporous electrodes. The molecular models can well describe this ionic behavior, but the limitations occur in its applicability to the capacitor electrodes caused by the system and near-equilibrium conditions. Therefore, a gap exists in best describing the correlation between microscopic structures and the macroscopic performances on energy and power delivery. Machine learning (ML) technologies have recently become a trend in the energy storage field to assist in designing, developing, and discovering novel materials. A brief overview of the ML modeling and applications in energy storage is given in the next section, 2.10.

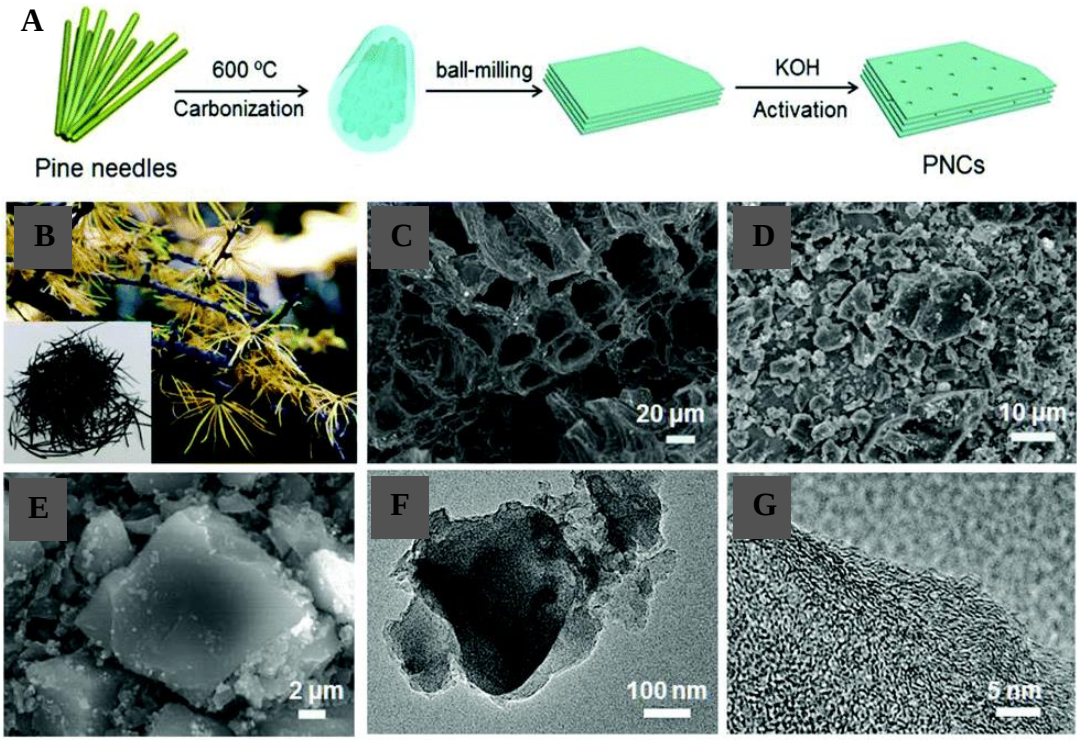

Figure 2.16 (A) Synthesis process of pine needle carbons (PNC), (B) pine needles precursor (inset: photo of pine needles after pre carbonization at 600 °C, (C) SEM of carbonized pine needles, (D, E) SEM images, (F) TEM image, (G) HRTEM image of PNC activated at 900 °C. Reproduced with permission from ref. [223], Copyright 2017, Royal Society of Chemistry.

2.10. Machine Learning (ML) modeling

The commonly used ML algorithms can be unsupervised, supervised, or deep learning. Unsupervised ML algorithms are applied to analyze and cluster unlabelled data sets. In this way, the unlabelled data will be categorized considering their similarities or differences. K-mean clustering algorithm, Gaussian mixture model, and mean-shift algorithm are examples of unsupervised learning. Supervised learning is widely used to solve problems in classification and regression using labeled data sets. It can build a direct relationship between the independent and dependent variables. Linear regression (LR), polynomial regression, and exponential regression are a few regression algorithms of supervised learning [227]. Deep learning is based on an

artificial neural network (ANN), which can be either unsupervised or supervised. ANN contains an input layer, hidden layer(s), and output layer, where additional hidden layers can optimize the result and improve the model accuracy [228].

In the topic of supercapacitors, correlating the microscopic details of materials to obtain macroscopic performances of capacitance predictions is a significant challenge. As explained in section 2.9.1, recently, biomass waste materials have received much attention for recycling the waste into carbon electrodes. Given that various types of biomasses are available, ML can be employed to build the relationships between the material's properties and energy storage performance to make decisions on performance improvements. Generally, only a few samples can be analyzed and compared through physicochemical experiments, instead, ML can be used to analyze a range of data sets to understand the relationships between the precursors, carbon properties, and energy performances. For instance, Zhu *et al.* [229] established a correlation between EDLC capacitance and physical, chemical features (specific surface area, pore volume, pore size, etc.) using an ANN model. Su *et al.* [230] used regression trees (RT) and multi-layer perceptron (MLP) models. Additional inputs such as the effect of electrolyte properties and the electrochemical parameters can also be included in the ML model analysis.

2.11. Conclusion

In this review, hybrid capacitors have shown to be an efficient way to improve electrochemical performances in terms of both energy and power densities. The metal oxides and conductive polymers have been widely employed, which exhibit the pseudocapacitive behavior and used as the positive electrode in hybrid capacitors. Typical transition metal oxides reported for hybrid capacitors are RuO_2, NiO, CoO, Co_3O_4, VO, V_2O_3, FeO, Fe_2O_3, and MnO, while the conducting polymers are PANI, PPy, PTh, etc. Among different transition metal oxides reported for both batteries and supercapacitors, the MnO_2 has several advantages of being one of the most abundant elements on the Earth, inexpensive, environmentally friendly, and having a high theoretical capacitance 1370 F g^{-1}. Several synthesis methods such as hydrothermal, sol-gel coating, electrodeposition, and electrochemical oxidation of Mn films can be used to produce manganese dioxide materials. We conclude that the anodic

electrodeposition method can derive electrolytic manganese dioxide (EMD), the most electrochemically active γ-MnO_2 form, which is suitable for fabricating the capacitor electrode materials. However, the issues such as capacitance fading during charge-discharge limiting the application of MnO_2 in the capacitors have been resolved by producing high-quality EMD deposits.

Carbon materials show the EDLC behavior and are used as the negative electrode in the hybrid capacitors. Recently, there has been a significant interest in using abundant renewable resources to produce carbon electrodes via green, facile fabrication methods as alternatives for fossil fuel and petroleum coke-derived carbon. Thermochemical treatments to lignocellulosic biomass precursors can modulate the interconnected hierarchical pore structure and higher surface areas to enhance the capacitance of the derived carbon. However, the existing literature lacks information on mapping the relationship of structure, the functionality of the precursor, and the derived carbon to the resulted capacitance. The modeling may assist in screening the precursors and correlating to maximize the physicochemical and electrochemical performances.

2.12. Aims, objectives, and outline of this thesis

This thesis aimed to fabricate hybrid capacitors by incorporating electrolytic manganese dioxide (EMD) powder and biomass waste-derived activated carbon (AC) materials, respectively, as positive and negative electrodes in the device. The next five chapters (chapters 3 to 7) in this thesis discuss the synthesis and characterization of the pristine EMD, modified EMD and biomass waste-derived AC. The EMD powder material is well demanded in the primary battery industry. However, the current literature has not much explored the synthesis of EMD powder (bulk) electrodes for capacitor energy storage. This is mainly due to the material limitations in this application caused by the irreversibility of the redox reactions that arise with localized buckling of the EMD structure upon charging-discharging. The EMD structure becomes unstable, and the capacitance starts fading over cycling. Most work reported in the literature on manganese dioxide electrodeposition focused on setting the experimental conditions and then investigating the capacitance. we have synthesized the EMD materials with modifications by optimizing the electrodeposition parameters,

using additives: polymer, and surfactants, and tested them as capacitor electrodes. An attempt was also made using computational modeling to draw the link between molecule interactions in the electrolyte bath and the nucleation and growth of the EMD deposit, which influenced the resulted capacitances. The biomass-waste materials are an excellent alternative to be utilized in the capacitors; however, using a diversity of precursors needs mapping their properties to obtain desired electrochemical performance. Therefore, insights into using ML modeling were given to develop a sophisticated criterion for selecting and utilizing a biomass precursor for optimized carbon electrode performance. In this thesis, we have addressed the limitations of the EMD and AC capacitor electrode materials while considering their competitive advantages of being the most abundant, environmentally friendly, and low-cost over the other electrode materials such as Ru, Co, Ni, petroleum coke, etc., used in the field. The intended research explored the EMD and AC materials and their development to improve the electrochemical performance (specific capacitance, deliverable energy, power, cycle life), which ultimately leads to a value-added commercial product for hybrid capacitor energy storage. Therefore, the following objectives were defined and achieved, which underline the gist of this thesis.

- Optimize the electrodeposition parameters of electrolytic manganese dioxide (EMD) bulk synthesis.
- Modify the EMD using additives, characterize and analyze the materials using physicochemical and electrochemical techniques to find the best performance.
- Elucidate the interactions between species present in the electrolyte bath in the electrodeposition.
- Recycle the biomass waste materials as carbon capacitor electrodes.
- Fabricate and analyze the EMD/AC hybrid capacitor for energy storage application.

Following the literature review chapter (chapter 2), the subsequent chapters 3, 4, 5, 6, 7, and 8 will be as follows, which were conducted to achieve the above objectives.

In chapter 3, the EMD was synthesized using the anodic deposition method by oxidizing $MnSO_4$ at different experimental conditions. The experimental parameters

were evaluated, and the optimum was chosen to conduct further experiments. The pseudocapacitive potential of the synthesized EMD was quantitatively analyzed to describe its potential application in capacitors. The EMD electrode was compared with the literature considering several parameters to differentiate it from the reported works.

In chapter 4, the EMD material was synthesized by modifying it using a low-cost natural biopolymer, alginic acid. The polymer concentrations were varied to obtain desired morphologies by crosslinking with the manganese dioxide structure. A detailed analysis was conducted to understand each material's physiochemical characteristics and electrochemical performance. Further investigations explored the effect of the interactions between the alginic acid polymer and the ions present in the electrolyte solution for the electrodeposition.

In chapter 5, the EMD was fabricated using novel surfactants in the capacitor field as additives in the electrolyte medium. The surfactants were chosen considering their varying configurations of the chain length and head group. Surfactant's concentrations were changed, and its influence on changing the EMD properties was studied. The manganese dioxide particle nucleation on the substrate was examined with and without the surfactants in the electrolytic bath.

In chapter 6, the Mango seed husk waste was utilized as the biomass precursor to synthesize the activated carbon via chemical activation using KOH activating agent. The activation temperature was varied to find the optimum temperature to produce the material. Experimental data were used as inputs in four different machine learning models to select a model that provides the highest accuracy in correlating the inputs and output parameters to predict the electrode capacitance.

In chapter 7, Grape marc from winery waste residues, a by-product of Australian wineries, was used as the raw precursor to produce activated carbon materials. The synthesis process included four synthesis routes depending on activating agents, dopants, carbonization, and activation temperatures. Accordingly, the effect of these synthesis parameters on electrochemical performance was studied. The varying synthesis conditions used in this chapter were incorporated into the multi-layer perceptron (MLP) machine learning model to predict the capacitance and power density values.

In chapter 8, the thesis outcomes were summarized, and the conclusions were presented. Moreover, we have suggested future recommendations which can be commenced to contribute to the capacitor field through further research.

2.13. References

[1] P. Bhojane, Recent advances and fundamentals of Pseudocapacitors: Materials, mechanism, and its understanding, J. Energy Storage. 45 (2022) 103654.

[2] M. Winter, R.J. Brodd, What are batteries, fuel cells, and supercapacitors?, Chem. Rev. 104 (2004) 4245–4269.

[3] M.R. Palacín, Recent advances in rechargeable battery materials: A chemist's perspective, Chem. Soc. Rev. 38 (2009) 2565–2575.

[4] B.E. Conway, Electrochemical Supercapacitors: Scientific fundamentals and Technological applications, Kluwer-Plenum, New York, 1999.

[5] W. Zuo, R. Li, C. Zhou, Y. Li, J. Xia, J. Liu, Battery-Supercapacitor Hybrid Devices: Recent Progress and Future Prospects, Adv. Sci. 4 (2017) 1–21.

[6] B. Fan, F. Liu, G. Yang, H. Li, G. Zhang, S. Jiang, Q. Wang, Dielectric materials for high-temperature capacitors, IET Nanodielectrics. 1 (2018) 32–40.

[7] G. Sikha, B.N. Popov, Performance optimization of a battery-capacitor hybrid system, J. Power Sources. 134 (2004) 130–138.

[8] R. Kotz, M. Carlen, Principles and applications of electrochemical capacitors, Electrochim. Acta. 45 (2000) 2483–2498.

[9] L. Zhang, X.S. Zhao, Carbon-based materials as supercapacitor electrodes, Chem. Soc. Rev. 38 (2009) 2520–2531.

[10] T. Brousse, D. Bélanger, K. Chiba, M. Egashira, F. Favier, J. Long, J.R. Miller, M. Morita, K. Naoi, P. Simon, W. Sugimoto, Materials for

electrochemical capacitors, Springer Handbooks. (2017) 495–561.

[11] K. Naoi, W. Naoi, S. Aoyagi, J.I. Miyamoto, T. Kamino, New generation "nanohybrid supercapacitor," Acc. Chem. Res. 46 (2013) 1075–1083.

[12] J. Yan, Q. Wang, T. Wei, Z. Fan, Recent advances in design and fabrication of electrochemical supercapacitors with high energy densities, Adv. Energy Mater. 4 (2014) 1300816.

[13] F.A. Permatasari, M.A. Irham, S.Z. Bisri, F. Iskandar, Carbon-based quantum dots for supercapacitors: Recent advances and future challenges, Nanomaterials. 11 (2021) 1–34.

[14] T. Pandolfo, V. Ruiz, S. Sivakkumar, J. Nerkar, Supercapacitor: Materials, System, Applications, Wiley-VCH Verlag GmbH & Co. KGaA, 2013.

[15] F. Wang, S. Xiao, Y. Hou, C. Hu, L. Liu, Y. Wu, Electrode materials for aqueous asymmetric supercapacitors, RSC Adv. 3 (2013) 13059–13084.

[16] V. Aravindan, J. Gnanaraj, Y.S. Lee, S. Madhavi, Insertion-type electrodes for nonaqueous Li-ion capacitors, Chem. Rev. 114 (2014) 11619–11635.

[17] V. Khomenko, E. Raymundo-Piñero, E. Frackowiak, F. Béguin, High-voltage asymmetric supercapacitors operating in aqueous electrolyte, Appl. Phys. A Mater. Sci. Process. 82 (2006) 567–573.

[18] K. Łępicka, P. Pieta, R. Gupta, M. Dabrowski, W. Kutner, A redox conducting polymer of a meso-Ni(II)-SaldMe monomer and its application for a multi-composite supercapacitor, Electrochim. Acta. 268 (2018) 111–120.

[19] E. Frackowiak, F. Beguin, Carbon materials for the electrochemical storage of energy in capacitors, Carbon N. Y. 39 (2001) 937–950.

[20] W. Chen, R.B. Rakhi, L. Hu, X. Xie, Y. Cui, H.N. Alshareef, High-performance nanostructured supercapacitors on a sponge, Nano Lett. 11 (2011) 5165–5172.

[21] Y. Shao, M.F. El-Kady, J. Sun, Y. Li, Q. Zhang, M. Zhu, H. Wang, B. Dunn, R.B. Kaner, Design and Mechanisms of Asymmetric Supercapacitors, Chem.

Rev. 118 (2018) 9233–9280.

[22] T. Brousse, D. Bélanger, J.W. Long, To Be or Not To Be Pseudocapacitive?, J. Electrochem. Soc. 162 (2015) A5185–A5189.

[23] Y. Gogotsi, R.M. Penner, Energy Storage in Nanomaterials - Capacitive, Pseudocapacitive, or Battery-like?, ACS Nano. 12 (2018) 2081–2083.

[24] E. Herrero, L.J. Buller, H.D. Abruña, Underpotential deposition at single crystal surfaces of Au, Pt, Ag and other materials, Chem. Rev. 101 (2001) 1897–1930.

[25] B.E. Conway, Transition from “supercapacitor” to “battery” behavior in electrochemical energy storage, J. Electrochem. Soc. 138 (1991) 1539.

[26] N. Choudhary, C. Li, J. Moore, N. Nagaiah, L. Zhai, Y. Jung, J. Thomas, Asymmetric Supercapacitor Electrodes and Devices, Adv. Mater. 29 (2017) 1605336.

[27] J.P. Zheng, T.R. Jow, A New Charge Storage Mechanism for Electrochemical Capacitors, J. Electrochem. Soc. 142 (1995) L6–L8.

[28] C.C. Hu, K.H. Chang, M.C. Lin, Y.T. Wu, Design and Tailoring of the Nanotubular Arrayed Architecture of Hydrous RuO_2 for Next Generation Supercapacitors, Nano Lett. 6 (2006) 2690–2695.

[29] M. Toupin, T. Brousse, D. Bélanger, Charge storage mechanism of MnO_2 electrode used in aqueous electrochemical capacitor, Chem. Mater. 16 (2004) 3184–3190.

[30] J. Zhang, L. Bin Kong, H. Li, Y.C. Luo, L. Kang, Synthesis of polypyrrole film by pulse galvanostatic method and its application as supercapacitor electrode materials, J. Mater. Sci. 45 (2010) 1947–1954.

[31] L. Kong, C. Zhang, J. Wang, W. Qiao, L. Ling, D. Long, Free-Standing T-Nb_2O_5/Graphene Composite Papers with Ultrahigh Gravimetric/Volumetric Capacitance for Li-Ion Intercalation Pseudocapacitor, ACS Nano. 9 (2015) 11200–11208.

[32] P. Simon, Y. Gogotsi, B. Dunn, Where do batteries end and Supercapacitors Begin?, Science. 343 (2014) 1210–1211.

[33] D. Cericola, R. Kötz, Hybridization of rechargeable batteries and electrochemical capacitors: Principles and limits, Electrochim. Acta. 72 (2012) 1–17.

[34] S. Nohara, T. Asahina, H. Wada, N. Furukawa, H. Inoue, N. Sugoh, H. Iwasaki, C. Iwakura, Hybrid capacitor with activated carbon electrode, $Ni(OH)_2$ electrode and polymer hydrogel electrolyte, J. Power Sources. 157 (2006) 605–609.

[35] I. Rabani, J. Yoo, H.S. Kim, D. Van Lam, S. Hussain, K. Karuppasamy, Y.S. Seo, Highly dispersive Co_3O_4 nanoparticles incorporated into a cellulose nanofiber for a high-performance flexible supercapacitor, Nanoscale. 13 (2021) 355–370.

[36] S. Trasatti, G. Buzzanca, Ruthenium dioxide: A new interesting electrode material. Solid state structure and electrochemical behaviour, J. Electroanal. Chem. 29 (1971) A1–A5.

[37] X. Zhao, Y. Zhang, Y. Wang, H. Wei, Battery-Type Electrode Materials for Sodium-Ion Capacitors, Batter. Supercaps. 2 (2019) 899–917.

[38] D.P. Dubal, O. Ayyad, V. Ruiz, P. Gómez-Romero, Hybrid energy storage: The merging of battery and supercapacitor chemistries, Chem. Soc. Rev. 44 (2015) 1777–1790.

[39] B.E. Conway, V. Briss, J. Wojtowicz, The role and utilization of pseudocapacitance for energy storage by supercapacitors, J. Power Sources. 66 (1997) 1–14.

[40] S. Ardizzone, G. Fregonara, S. Trasatti, “Inner” and “Outer” active surface of RuO_2 electrodes, Electrochim. Acta. 35 (1990) 263–267.

[41] J.P. Zheng, P.J. Cygan, T.R. Jow, Hydrous Ruthenium Oxide as and electrode materials for electrochemical capacitors, J. Electrochem. Soc. 142 (1995) 2699.

[42] H. Ji, X. Zhao, Z. Qiao, J. Jung, Y. Zhu, Y. Lu, L.L. Zhang, A.H. MacDonald, R.S. Ruoff, Capacitance of carbon-based electrical double-layer capacitors, Nat. Commun. 5 (2014).

[43] J.W. Lang, L. Bin Kong, W.J. Wu, Y.C. Luo, L. Kang, Facile approach to prepare loose-packed NiO nano-flakes materials for supercapacitors, Chem. Commun. (2008) 4213–4215.

[44] B. Saravanakumar, K.K. Purushothaman, G. Muralidharan, Interconnected V_2O_5 nanoporous network for high-performance supercapacitors, ACS Appl. Mater. Interfaces. 4 (2012) 4484–4490.

[45] J. Chen, K. Huang, S. Liu, Hydrothermal preparation of octadecahedron Fe_3O_4 thin film for use in an electrochemical supercapacitor, Electrochim. Acta. 55 (2009) 1–5.

[46] X. Lu, G. Wang, T. Zhai, M. Yu, J. Gan, Y. Tong, Y. Li, Hydrogenated TiO_2 nanotube arrays for supercapacitors, Nano Lett. 12 (2012) 1690–1696.

[47] T. Brousse, M. Toupin, R. Dugas, L. Athouël, O. Crosnier, D. Bélanger, Crystalline MnO_2 as Possible Alternatives to Amorphous Compounds in Electrochemical Supercapacitors, J. Electrochem. Soc. 153 (2006) A2171.

[48] K.-W. Nam, E.-S. Lee, J.-H. Kim, Y.-H. Lee, K.-B. Kim, Synthesis and Electrochemical Investigations of $Ni_{1-x}O$ Thin Films and $Ni_{1-x}O$ on Three-Dimensional Carbon Substrates for Electrochemical Capacitors, J. Electrochem. Soc. 152 (2005) A2123.

[49] W. Xu, B. Mu, A. Wang, Facile fabrication of well-defined microtubular carbonized kapok fiber/NiO composites as electrode material for supercapacitor, Electrochim. Acta. 194 (2016) 84–94.

[50] Z. Zeng, B. Xiao, X. Zhu, J. Zhu, D. Xiao, J. Zhu, Flower-like binary cobalt-nickel oxide with high performance for supercapacitor electrode via cathodic electrodeposition, Ceram. Int. 43 (2017) S633–S638.

[51] J. Jia, F. Luo, C. Gao, C. Suo, X. Wang, H. Song, X. Hu, Synthesis of La-doped NiO nanofibers and their electrochemical properties as electrode for

supercapacitors, Ceram. Int. 40 (2014) 6973–6977.

[52] G. Srikesh, A.S. Nesaraj, Chemical synthesis of Co and Mn co-doped NiO nanocrystalline materials as high-performance electrode materials for potential application in supercapacitors, Ceram. Int. 42 (2016) 5001–5010.

[53] Y.Q. Zhang, X.H. Xia, J.P. Tu, Y.J. Mai, S.J. Shi, X.L. Wang, C.D. Gu., Self-assembled synthesis of hierarchically porous NiO film and its application for electrochemical capacitors, J. Power Sources. 199 (2012) 413–417.

[54] Š. Trafela, J. Zavašnik, S. Šturm, K.Ž. Rožman, Formation of a $Ni(OH)_2$/NiOOH active redox couple on nickel nanowires for formaldehyde detection in alkaline media, Electrochim. Acta. 309 (2019) 346–353.

[55] T.C. Liu, W.G. Pell, B.E. Conway, Stages in the development of thick cobalt oxide films exhibiting reversible redox behavior and pseudocapacitance, Electrochim. Acta. 44 (1999) 2829–2842.

[56] X. Xia, Y. Zhang, D. Chao, C. Guan, Y. Zhang, L. Li, X. Ge, I.M. Bacho, J. Tu, H.J. Fan, Solution synthesis of metal oxides for electrochemical energy storage applications, Nanoscale. 6 (2014) 5008–5048.

[57] Y.Q. Zhang, L. Li, S.J. Shi, Q.Q. Xiong, X.Y. Zhao, X.L. Wang, C.D. Gu, J.P. Tu, Synthesis of porous Co_3O_4 nanoflake array and its temperature behavior as pseudo-capacitor electrode, J. Power Sources. 256 (2014) 200–205.

[58] Y. Shan, L. Gao, Formation and characterization of multi-walled carbon nanotubes/Co_3O_4 nanocomposites for supercapacitors, Mater. Chem. Phys. 103 (2007) 206–210.

[59] Y. Gao, S. Chen, D. Cao, G. Wang, J. Yin, Electrochemical capacitance of Co_3O_4 nanowire arrays supported on nickel foam, J. Power Sources. 195 (2010) 1757–1760.

[60] X.H. Xia, J.P. Tu, Y.Q. Zhang, Y.J. Mai, X.L. Wang, C.D. Gu, X.B. Zhao, Freestanding Co_3O_4 nanowire array for high performance supercapacitors, RSC Adv. 2 (2012) 1835–1841.

[61] S. Beke, A review of the growth of V_2O_5 films from 1885 to 2010, Thin Solid Films. 519 (2011) 1761–1771.

[62] M.S. Whittingham, The Role of Ternary Phases in Cathode Reactions, J. Electrochem. Soc. 123 (1976) 315–320.

[63] H.Y. Lee, J.B. Goodenough, Ideal supercapacitor behavior of amorphous $V_2O_5.nH_2O$ potassium chloride (KCl) aqueous solution, J. Solid State Chem. 148 (1999) 81–84.

[64] Y. Zhang, J. Zheng, Y. Zhao, T. Hu, Z. Gao, C. Meng, Fabrication of V_2O_5 with various morphologies for high-performance electrochemical capacitor, Appl. Surf. Sci. 377 (2016) 385–393.

[65] S.K. Park, J. Sure, D. Sri Maha Vishnu, S.J. Jo, W.C. Lee, I.A. Ahmad, H.K. Kim, Nano-Fe_3O_4/carbon nanotubes composites by one-pot microwave solvothermal method for supercapacitor applications, Energies. 14 (2021) 2908.

[66] N.L. Wu, S.Y. Wang, C.Y. Han, D.S. Wu, L.R. Shiue, Electrochemical capacitor of magnetitie in aqueous electrolytes, J. Power Sources. 113 (2003) 173–178.

[67] S.-Y. Wang, K.-C. Ho, S.-L. Kuo, N.-L. Wu, Investigation on Capacitance Mechanisms of Fe_3O_4 Electrochemical Capacitors, J. Electrochem. Soc. 153 (2006) A75.

[68] W. Zhang, C.Y. Cheng, Manganese metallurgy review. Part I: Leaching of ores/secondary materials and recovery of electrolytic/chemical manganese dioxide, Hydrometallurgy. 89 (2007) 137–159.

[69] M. Toupin, T. Brousse, D. Bélanger, Influence of microstucture on the charge storage properties of chemically synthesized manganese dioxide, Chem. Mater. 14 (2002) 3946–3952.

[70] J.K. Chang, M.T. Lee, W.T. Tsai, In situ Mn K-edge X-ray absorption spectroscopic studies of anodically deposited manganese oxide with relevance to supercapacitor applications, J. Power Sources. 166 (2007) 590–594.

[71] W. Wei, X. Cui, W. Chen, D.G. Ivey, Manganese oxide-based materials as electrochemical supercapacitor electrodes, Chem. Soc. Rev. 40 (2011) 1697–1721.

[72] S. Devaraj, N. Munichandraiah, Effect of crystallographic structure of MnO_2 on its electrochemical capacitance properties, J. Phys. Chem. C. 112 (2008) 4406–4417.

[73] O. Ghodbane, J.L. Pascal, F. Favier, Microstructural effects on charge-storage properties in MnO_2-based electrochemical supercapacitors, ACS Appl. Mater. Interfaces. 1 (2009) 1130–1139.

[74] W. Li, K. Xu, B. Li, J. Sun, F. Jiang, Z. Yu, R. Zou, Z. Chen, J. Hu, MnO_2 Nanoflower Arrays with High Rate Capability for Flexible Supercapacitors, ChemElectroChem. 1 (2014) 1003–1008.

[75] P. Yang, Y. Ding, Z. Lin, Z. Chen, Y. Li, P. Qiang, M. Ebrahimi, W. Mai, C.P. Wong, Z.L. Wang, Low-Cost High-Performance Solid-State Asymmetric Supercapacitors Based on MnO_2 Nanowires and Fe_2O_3 Nanotubes, Nano Lett. 14 (2014) 731–736.

[76] X. Tang, Z. huai Liu, C. Zhang, Z. Yang, Z. Wang, Synthesis and capacitive property of hierarchical hollow manganese oxide nanospheres with large specific surface area, J. Power Sources. 193 (2009) 939–943.

[77] M. Huang, Y. Zhang, F. Li, L. Zhang, R.S. Ruoff, Z. Wen, Q. Liu, Self-assembly of mesoporous nanotubes assembled from interwoven ultrathin birnessite-type MnO_2 nanosheets for asymmetric supercapacitors, Sci. Rep. 4 (2014) 1–8.

[78] X. Lu, D. Zheng, T. Zhai, Z. Liu, Y. Huang, S. Xie, Y. Tong, Facile synthesis of large-area manganese oxide nanorod arrays as a high-performance electrochemical supercapacitor, Energy Environ. Sci. 4 (2011) 2915–2921.

[79] Y. Tang, S. Zheng, Y. Xu, X. Xiao, H. Xue, H. Pang, Advanced batteries based on manganese dioxide and its composites, Energy Storage Mater. 12 (2018) 284–309.

[80] T.R. Juran, J. Young, M. Smeu, Density Functional Theory Modeling of MnO_2 Polymorphs as Cathodes for Multivalent Ion Batteries, J. Phys. Chem. C. 122 (2018) 8788–8795.

[81] H.Y. Lee, J.B. Goodenough, Supercapacitor Behavior with KCl Electrolyte, J. Solid State Chem. 144 (1999) 220–223.

[82] S.-C. Pang, M.A. Anderson, T.W. Chapman, Novel Electrode Materials for Thin-Film Ultracapacitors: Comparison of Electrochemical Properties of Sol-Gel-Derived and Electrodeposited Manganese Dioxide, J. Electrochem. Soc. 147 (2000) 444–450.

[83] J.N. Broughton, M.J. Brett, Investigation of thin sputtered Mn films for electrochemical capacitors, Electrochim. Acta. 49 (2004) 4439–4446.

[84] J.G. Wang, Y. Yang, Z.H. Huang, F. Kang, Coaxial carbon nanofibers/MnO_2 nanocomposites as freestanding electrodes for high-performance electrochemical capacitors, Electrochim. Acta. 56 (2011) 9240–9247.

[85] A.M. Hashem, H.M. Abuzeid, N. Narayanan, H. Ehrenberg, C.M. Julien, Synthesis, structure, magnetic, electrical and electrochemical properties of Al, Cu and Mg doped MnO_2, Mater. Chem. Phys. 130 (2011) 33–38.

[86] G. Wang, L. Liu, L. Zhang, J. Zhang, Nickel, cobalt, and manganese oxide composite as an electrode material for electrochemical supercapacitors, Ionics (Kiel). 19 (2013) 689–695.

[87] C.L. Tang, X. Wei, Y.M. Jiang, X.Y. Wu, L.N. Han, K.X. Wang, J.S. Chen, Cobalt-doped MnO_2 hierarchical yolk-shell spheres with improved supercapacitive performance, J. Phys. Chem. C. 119 (2015) 8465–8471.

[88] J.G. Wang, Y. Yang, Z.H. Huang, F. Kang, Rational synthesis of MnO_2/conducting polypyrrole@carbon nanofiber triaxial nano-cables for high-performance supercapacitors, J. Mater. Chem. 22 (2012) 16943–16949.

[89] Y. Yan, Q. Cheng, V. Pavlinek, P. Saha, C. Li, Fabrication of polyaniline/mesoporous carbon/MnO_2 ternary nanocomposites and their enhanced electrochemical performance for supercapacitors, Electrochim. Acta.

71 (2012) 27–32.

[90] Y. Chabre, J. Pannetier, Structural and electrochemical properties of the proton / γ-MnO_2 system, Prog. Solid State Chem. 23 (1995) 1–130.

[91] G.H.A. Therese, P.V. Kamath, Electrochemical Synthesis of Metal Oxides and Hydroxides, Chem. Mater. 12 (2000) 1195–1204.

[92] M. Paunovic, M. Schlesinger, Fundamentals of Electrochemical Deposition, John Wiley & Sons, Canada, 1998.

[93] J. Wei, I. Zhitomirsky, Electrosynthesis of manganese oxide films, Surf. Eng. 24 (2008) 40–46.

[94] J. Wei, N. Nagarajan, I. Zhitomirsky, Manganese oxide films for electrochemical supercapacitors, J. Mater. Process. Technol. 186 (2007) 356–361.

[95] G.M. Jacob, I. Zhitomirsky, Diffusion-controlled electrosynthesis of nanoporous electrodes for electrochemical supercapacitors, J. Nano Res. 7 (2009) 87–92.

[96] G.M. Jacob, I. Zhitomirsky, Microstructure and properties of manganese dioxide films prepared by electrodeposition, Appl. Surf. Sci. 254 (2008) 6671–6676.

[97] S.W. Donne, G.A. Lawrance, D.A.J. Swinkels, The chemostat: a novel approach to the synthesis of manganese dioxide, Mater. Res. Bull. 30 (1995) 859–869.

[98] N. Nagarajan, H. Humadi, I. Zhitomirsky, Cathodic electrodeposition of MnO_x films for electrochemical supercapacitors, Electrochim. Acta. 51 (2006) 3039–3045.

[99] W. Xiao, H. Xia, J.-Y.-H. Fuh, L. Lu, Electrochemical Synthesis and Supercapacitive Properties of ε-MnO_2 with Porous/Nanoflaky Hierarchical Architectures, J. Electrochem. Soc. 156 (2009) A627.

[100] Y. Wang, I. Zhitomirsky, Cathodic electrodeposition of Ag-doped manganese

dioxide films for electrodes of electrochemical supercapacitors, Mater. Lett. 65 (2011) 1759–1761.

[101] A.J. Gibson, K.G. Latham, R.C. Burns, S.W. Donne, Electrodeposition Mechanism of Cathodically-Prepared Manganese dioxide Thin Films from Permanganate for use in Electrochemical Capacitors, Electrochim. Acta. 236 (2017) 198–211.

[102] R.K. Mishra, C.S. Prajapati, R.R. Shahi, A.K. Kushwaha, P.P. Sahay, Influence of electrodeposition modes on the electrochemical performance of MnO_2 films prepared using anionic MnO^{4-} (Mn^{7+}) precursor, Ceram. Int. 44 (2018) 5710–5718.

[103] J. Tizfahm, M. Aghazadeh, M.G. Maragheh, M.R. Ganjali, P. Norouzi, F. Faridbod, Electrochemical preparation and evaluation of the supercapacitive performance of MnO_2 nanoworms, Mater. Lett. 167 (2016) 153–156.

[104] A.B. Yuan, M. Zhou, X.L. Wang, Z.H. Sun, Y.Q. Wang, Synthesis and characterization of nanostructured manganese dioxide used as positive electrode material for electrochemical capacitor with lithium hydroxide electrolyte, Chinese J. Chem. 26 (2008) 65–69.

[105] P.G. Perret, P.R.L. Malenfant, C. Bock, B. MacDougall, Electro-Deposition and Dissolution of MnO_2 on a Graphene Composite Electrode for Its Utilization in an Aqueous Based Hybrid Supercapacitor, J. Electrochem. Soc. 159 (2012) A1554–A1561.

[106] M. Zhang, X. Dai, C. Zhang, Y. Fuan, D. Yang, J. Li, High specific capacitance of the electrodeposited MnO_2 on porous foam nickel soaked in alcohol and its dependence on precursor concentration, Materials (Basel). 13 (2020).

[107] M. Murthy, G.S. Nagarajan, J.W. Weidner, J.W. Van Ze, A Model for the Galvanostatic Deposition of Nickel Hydroxide, 143 (1996) 2319–2327.

[108] M. Devenney, S.W. Donne, S. Gorer, Application of combinatorial methodologies to the synthesis and characterization of electrolytic manganese

dioxide, J. Appl. Electrochem. 34 (2004) 643–651.

[109] P.N. Naguman, Obtaining manganese dioxide under conditions of diaphragm-free electrolysis, Russ. J. Non-Ferrous Met. 50 (2009) 13–16.

[110] A. G.H., F. T.J.V., SI Chemical data, 5th ed., 2002.

[111] C.J. Clarke, G.J. Browning, S.W. Donne, An RDE and RRDE study into the electrodeposition of manganese dioxide, Electrochim. Acta. 51 (2006) 5773–5784.

[112] Cotton, F. Albert, Advanced Inorganic Chemistry, 6th ed., Wiley, 1999.

[113] B.Y.M. Fleischmann, H.R. Thirsk, I.M. Tordesillas, Kinetics of Electrodeposition of Gamma-Manganese Dioxide, (1962).

[114] A. Cartwright, A.L. Paul, The Mechanism of Manganese Dioxide Mechanism, in: Proc. MnO2 Symp. Vol 2, Tokyo, 1980: pp. 290–304.

[115] W.H. Kao, V.J. Weibel, Electrochemical oxidation of manganese (II) at a platinum electrode, J. Appl. Electrochem. 22 (1992) 21–27.

[116] C.C. Hu, T.W. Tsou, Capacitive and textural characteristics of hydrous manganese oxide prepared by anodic deposition, Electrochim. Acta. 47 (2002) 3523–3532.

[117] R.K. Sharma, A.C. Rastogi, S.B. Desu, Manganese oxide embedded polypyrrole nanocomposites for electrochemical supercapacitor, Electrochim. Acta. 53 (2008) 7690–7695.

[118] X. Dai, M. Zhang, J. Li, D. Yang, Effects of electrodeposition time on a manganese dioxide supercapacitor, RSC Adv. 10 (2020) 15860–15869.

[119] X. Hu, X. Lin, Z. Ling, Y. Li, X. Fu, Fabrication and characteristics of galvanostatic electrodeposited MnO_2 on porous nickel from etched aluminium, Electrochim. Acta. 138 (2014) 132–138.

[120] J.N. Broughton, M.J. Brett, Variations in MnO_2 electrodeposition for electrochemical capacitors, Electrochim. Acta. 50 (2005) 4814–4819.

[121] S.C. Pang, M.A. Anderson, Novel electrode materials for electrochemical capacitors: Part II. Material characterization of sol-gel-derived and electrodeposited manganese dioxide thin films, J. Mater. Res. 15 (2000) 2096–2106.

[122] K. Jeyasubramanian, T.S. Gokul Raja, S. Purushothaman, M.V. Kumar, I. Sushmitha, Supercapacitive performances of MnO_2 nanostructures grown on hierarchical Cu nano leaves via electrodeposition, Electrochim. Acta. 227 (2017) 401–409.

[123] E. Preisler, Material problems encountered in anodic MnO_2 deposition, J. Appl. Electrochem. 19 (1989) 559–565.

[124] J.P. Rethinaraj, S. Visvanathan, Anodes for the preparation of EMD and application of manganese dioxide coated anodes for electrochemicals, Mater. Chem. Phys. 27 (1991) 337–349.

[125] J. Du, G. Shao, X. Qin, G. Wang, Y. Zhang, Z. Ma, High specific surface area MnO_2 electrodeposited under supergravity field for supercapacitors and its electrochemical properties, Mater. Lett. 84 (2012) 13–15.

[126] M.F. Dupont, M. Forghani, A.P. Cameron, S.W. Donne, Effect of electrolyte cation on the charge storage mechanism of manganese dioxide for electrochemical capacitors, Electrochim. Acta. 271 (2018) 337–350.

[127] Y.C. Hsieh, K.T. Lee, Y.P. Lin, N.L. Wu, S.W. Donne, Investigation on capacity fading of aqueous $MnO_2 \cdot nH_2O$ electrochemical capacitor, J. Power Sources. 177 (2008) 660–664.

[128] Y.S. Chen, C.C. Hu, Capacitive characteristics of binary manganese-nickel oxides prepared by anodic deposition, Electrochem. Solid-State Lett. 6 (2003) 210–213.

[129] D.P. Dubal, W.B. Kim, C.D. Lokhande, Galvanostatically deposited Fe: MnO_2 electrodes for supercapacitor application, J. Phys. Chem. Solids. 73 (2012) 18–24.

[130] C. Yuan, H. Lin, H. Lu, E. Xing, Y. Zhang, B. Xie, Anodic preparation and

supercapacitive performance of nano-Co_3O_4/MnO_2 composites, RSC Adv. 4 (2014) 64675–64682.

[131] K. Rajendra Prasad, N. Miura, Electrochemically synthesized MnO_2-based mixed oxides for high performance redox supercapacitors, Electrochem. Commun. 6 (2004) 1004–1008.

[132] P.Y. Chuang, C.C. Hu, The electrochemical characteristics of binary manganese-cobalt oxides prepared by anodic deposition, Mater. Chem. Phys. 92 (2005) 138–145.

[133] M. Nakayama, A. Tanaka, Y. Sato, T. Tonosaki, K. Ogura, Electrodeposition of manganese and molybdenum mixed oxide thin films and their charge storage properties, Langmuir. 21 (2005) 5907–5913.

[134] R.S.R. Majid, Effects of electrodeposition mode and deposition cycle on the electrochemical performance of MnO_2 -NiO composite electrodes for high-energy-density supercapacitors, PLoS One. 11 (2016) 1–16.

[135] J.K. Chang, M.T. Lee, C.H. Huang, W.T. Tsai, Physicochemical properties and electrochemical behavior of binary manganese-cobalt oxide electrodes for supercapacitor applications, Mater. Chem. Phys. 108 (2008) 124–131.

[136] S. Bakardjieva, P. Bezdička, T. Grygar, P. Vorm, Reductive dissolution of microparticulate manganese oxides, J. Solid State Electrochem. 4 (2000) 306–313.

[137] S. Nijjer, J. Thonstad, G.M. Haarberg, Oxidation of manganese(II) and reduction of manganese dioxide in sulphuric acid, Electrochim. Acta. 46 (2000) 395–399.

[138] K.R. Prasad, N. Miura, Polyaniline-MnO_2 composite electrode for high energy density electrochemical capacitor, Electrochem. Solid-State Lett. 7 (2004) 7–11.

[139] L.J. Sun, X.X. Liu, Electrodepositions and capacitive properties of hybrid films of polyaniline and manganese dioxide with fibrous morphologies, Eur. Polym. J. 44 (2008) 219–224.

[140] C.H. Ng, H.N. Lim, Y.S. Lim, W.K. Chee, N.M. Huang, Fabrication of flexible polypyrrole/graphene oxide/manganese oxide supercapacitor, Int. J. Energy Res. 39 (2015) 344–355.

[141] L. Wen, F. Li, H.M. Cheng, Carbon Nanotubes and Graphene for Flexible Electrochemical Energy Storage: from Materials to Devices, Adv. Mater. 28 (2016) 4306–4337.

[142] S. Kulandaivalu, N. Suhaimi, Y. Sulaiman, Unveiling high specific energy supercapacitor from layer-by-layer assembled polypyrrole/graphene oxide|polypyrrole/manganese oxide electrode material, Sci. Rep. 9 (2019) 1–10.

[143] R. Liu, B.L. Sang, MnO_2/poly(3,4-ethylenedioxythiophene) coaxial nanowires by one-step coelectrodeposition for electrochemical energy storage, J. Am. Chem. Soc. 130 (2008) 2942–2943.

[144] A. Tounsi, F. Habelhames, A. Sayah, A. Bahloul, L. Lamiri, B. Nessark, Electrosynthesis of a ternary composite film polyaniline-MnO_2-graphene in a one-step, Ionics (Kiel). 28 (2022) 317–328.

[145] Y. Shi, M. Zhang, L. Zhang, X. Cui, X. Zhu, J. Zhao, D. Jin, D. Yang, J. Li, Reduced graphene oxide coated manganese dioxide electrode prepared by polyvinylpyrrolidone assisted electrodeposition, Vacuum. 199 (2022) 110925.

[146] H. Zhang, J. Gu, Y. Jiang, Y. Wang, J. Zhao, X. Zhang, C. Wang, Calcination removing soft template cetyl trimethyl ammonium bromide and its effects on capacitance performance of supercapacitor electrode MnO_2, Energy Convers. Manag. 86 (2014) 605–613.

[147] S. Devaraj, N. Munichandraiah, High capacitance of electrodeposited MnO_2 by the effect of a surface-active agent, Electrochem. Solid-State Lett. 8 (2005) 0–5.

[148] Y. Li, X. Cai, W. Shen, Preparation and performance comparison of supercapacitors based on nanocomposites of MnO_2 with cationic surfactant of CTAC or CTAB by direct electrodeposition, Electrochim. Acta. 149 (2014)

306–315.

[149] M. Faridi, A. Nari, H. Kalhor, M.H. Dadjoo, A comparative study on Ag-doped and surfactant assisted MnO2 prepared by direct and pulse current electrodeposition on surgical grade stainless steel as high-performance supercapacitor, J. Braz. Chem. Soc. 28 (2017) 168–178.

[150] M. Aghazadeh, M.R. Ganjali, M.G. Maragheh, CTAB-assisted cathodic electrosynthesis of MnO_2 ultra-fine nanoparticles and investigation of their charge storage performance, Int. J. Electrochem. Sci. 13 (2018) 1161–1172.

[151] M. Sawangphruk, S. Pinitsoontorn, J. Limtrakul, Surfactant-assisted electrodeposition and improved electrochemical capacitance of silver-doped manganese oxide pseudocapacitor electrodes, J. Solid State Electrochem. 16 (2012) 2623–2629.

[152] Zn-MnO_2 technology, Sunergy Batter. (n.d.).

[153] Manganese rechargeable lithium batteries (ML series), Panasonic Ind. Eur. GmbH. (n.d.).

[154] C. Mondoloni, M. Laborde, J. Rioux, E. Andoni, C. Lévy-Clément, Rechargeable Alkaline Manganese Dioxide Batteries, J. Electrochem. Soc. 139 (1992) 954–959.

[155] D. Balachandran, D. Morgan, G. Ceder, First Principles study of H-insertion in MnO2, J. Solid State Chem. 166 (2002) 91–103.

[156] A. Kozawa, R.A. Powers, The Manganese Dioxide Electrode in Alkaline Electrolyte; The Electron-Proton Mechanism for the Discharge Process from MnO2 to MnO1.5, J. Electrochem. Soc. 113 (1966) 870.

[157] W.M. Dose, S.W. Donne, Heat treated electrolytic manganese dioxide for primary Li/MnO2batteries: Effect of manganese dioxide properties on electrochemical performance, Electrochim. Acta. 105 (2013) 305–313.

[158] Y. Shao-Horn, Structural Characterization of Heat-treated Electrolytic Manganese Dioxide and Topotactic Transformation of Discharge Products in

the Li-MnO2 Cells, J. Electrochem. Soc. 144 (1997) 3147.

[159] A.P. Malloy, G.J. Browning, S.W. Donne, Surface characterization of heat-treated electrolytic manganese dioxide., J. Colloid Interface Sci. 285 (2005) 653–64.

[160] S. Jouanneau, S. Sarciaux, A. Le Gal La Salle, D. Guyomard, Influence of structural defects on the insertion behavior of γ-MnO2: Comparison of H+and Li+, Solid State Ionics. 140 (2001) 223–232.

[161] M. Minakshi, P. Singh, M. Carter, K. Prince, The Zn–MnO[sub 2] Battery: The Influence of Aqueous LiOH and KOH Electrolytes on the Intercalation Mechanism, Electrochem. Solid-State Lett. 11 (2008) A145.

[162] E.D. Rus, G.D. Moon, J. Bai, D.A. Steingart, C.K. Erdonmez, Electrochemical Behavior of Electrolytic Manganese Dioxide in Aqueous KOH and LiOH Solutions: A Comparative Study, J. Electrochem. Soc. 163 (2016) A356–A363.

[163] A. Kozawa, J.F. Yeager, The Cathodic Reduction Mechanism of Electrolytic Manganese Dioxide in Alkaline Electrolyte, (1965).

[164] A. Kozawa, J.F. Yeager, Cathodic reduction mechanism of MnOOH to $Mn(OH)_2$ in alkaline electrolyte, J. Electrochem. Soc. 115 (1968) 1003–1007.

[165] J. Mcbreen, The electrochemistry of β-MnO_2 and γ-MnO_2 in alkaline electrolyte*, Electrochim. Acta. 20 (1975) 221–225.

[166] J.M. Amarilla, F. Tedjar, C. Poinsignon, Influence of KOH concentration on the γ-MnO_2 redox mechanism, Electrochim. Acta. 39 (1994) 2321–2331.

[167] K. Kordesch, Alkaline manganese dioxide zinc batteries, Batteries. 1 (1974) 241–384.

[168] A. Biswal, B.C. Tripathy, K. Sanjay, D. Meyrick, T. Subbaiah, M. Minakshi, Influence of the microstructure and its stability on the electrochemical properties of EMD produced from a range of precursors, J. Solid State Electrochem. 17 (2013) 3191–3198.

[169] Y. Shen, K. Kordesch, Mechanism of capacity fade of rechargeable alkaline manganese dioxide zinc cells, J. Power Sources. 87 (2000) 162–166.

[170] A. Biswal, B.C. Tripathy, T. Subbaiah, D. Meyrick, M. Ionescu, M. Minakshi, Effect of non-ionic surfactants and its role in K intercalation in electrolytic manganese dioxide, Metall. Mater. Trans. E. 1 (2014) 226–238.

[171] Q. Wang, J. Pan, Y. Sun, Z. Wang, A high capacity cathode material-MnO_2 doped with nano $Ag_4Bi_2O_5$ for alkaline secondary batteries, J. Power Sources. 199 (2012) 355–359.

[172] Y. Wenjian, L. Juan, Z. Xiaogang, Enhanced electrochemical properties of manganese dioxde doped with Ag3BiOx, Int. J. Electrochem. Sci. 1 (2006) 181–188.

[173] V. Raghuveer, A. Manthiram, Improved rechargeability of manganese oxide cathodes in alkaline cells in the presence of TiB_2 and TiS_2, J. Power Sources. 159 (2006) 1468–1473.

[174] R.L. Deutscher, T.M. Florence, R. Woods, Investigations on an aqueous lithium secondary cell, J. Power Sources. 55 (1995) 41–46.

[175] T. Nohma, S. Yoshimura, K. Nishio, Y. Yamamoto, S. Fukuoka, M. Hara, Development of coin-type lithium secondary batteries containing manganese dioxide/Li-Al, J. Power Sources. 58 (1996) 205–207.

[176] H.J. Denisa, A.M. Puziy, O.I. Poddubnaya, S.G. Fabian, J.M.D. Tascón, G.Q. Lu, Highly stable performance of supercapacitors from phosphorus-enriched carbons, J. Am. Chem. Soc. 131 (2009) 5026–5027.

[177] Q. Wang, J. Yan, Y. Wang, T. Wei, M. Zhang, X. Jing, Z. Fan, Three-dimensional flower-like and hierarchical porous carbon materials as high-rate performance electrodes for supercapacitors, Carbon N. Y. 67 (2014) 119–127.

[178] K. Fic, G. Lota, M. Meller, E. Frackowiak, Novel insight into neutral medium as electrolyte for high-voltage supercapacitors, Energy Environ. Sci. 5 (2012) 5842–5850.

[179] N. Jung, S. Kwon, D. Lee, D.M. Yoon, Y.M. Park, A. Benayad, J.Y. Choi, J.S. Park, Synthesis of chemically bonded graphene/carbon nanotube composites and their application in large volumetric capacitance supercapacitors, Adv. Mater. 25 (2013) 6854–6858.

[180] A.B. McEwen, S.F. McDevitt, V.R. Koch, Nonaqueous Electrolytes for Electrochemical Capacitors: Imidazolium Cations and Inorganic Fluorides with Organic Carbonates, J. Electrochem. Soc. 144 (1997) L84–L86.

[181] Y. Wang, Y. Song, Y. Xia, Electrochemical capacitors: Mechanism, materials, systems, characterization and applications, Chem. Soc. Rev. 45 (2016) 5925–5950.

[182] C. Zhong, Y. Deng, W. Hu, J. Qiao, L. Zhang, J. Zhang, A review of electrolyte materials and compositions for electrochemical supercapacitors, Chem. Soc. Rev. 44 (2015) 7484–7539.

[183] M. Toupin, T. Brousse, D. Bélanger, Charge storage mechanism of MnO2 electrode used in aqueous electrochemical capacitor, Chem. Mater. 16 (2004) 3184–3190.

[184] S. Chou, F. Cheng, J. Chen, Electrodeposition synthesis and electrochemical properties of nanostructured γ-MnO_2 films, J. Power Sources. 162 (2006) 727–734.

[185] S.L. Chou, J.Z. Wang, S.Y. Chew, H.K. Liu, S.X. Dou, Electrodeposition of MnO_2 nanowires on carbon nanotube paper as free-standing, flexible electrode for supercapacitors, Electrochem. Commun. 10 (2008) 1724–1727.

[186] F. Xiao, Y. Xu, Pulse electrodeposition of manganese oxide for high-rate capability supercapacitors, Int. J. Electrochem. Sci. 7 (2012) 7440–7450.

[187] P. Cai, K. Zou, X. Deng, B. Wang, M. Zheng, L. Li, H. Hou, G. Zou, X. Ji, Comprehensive Understanding of Sodium-Ion Capacitors: Definition, Mechanisms, Configurations, Materials, Key Technologies, and Future Developments, Adv. Energy Mater. 2003804 (2021) 1–56.

[188] B.A. Bolto, R. McNeill, D.E. Weiss, Electronic conduction in polymers. III.

Electronic properties of polypyrrole, Aust. J. Chem. 16 (1963) 1090–1103.

[189] B.A. Bolto, D.E. Weiss, Electronic conduction in polymers. II. The electrochemical reduction of polypyrrole at controlled potential, Aust. J. Chem. 16 (1963) 1076–1089.

[190] R. McNeill, R. Siudak, J.H. Wardlaw, D.E. Weiss, Electronic conduction in polymers. I. The chemical structure of polypyrrole, Aust. J. Chem. 16 (1963) 1056–1075.

[191] A. Rudge, I. Raistrick, S. Gottesfeld, J.P. Ferraris, A study of the electrochemical properties of conducting polymers for application in electrochemical capacitors, Electrochim. Acta. 39 (1994) 273–287.

[192] A. Rudge, J. Davey, I. Raistrick, S. Gottesfeld, J.P. Ferraris, Conducting polymers as active materials in electrochemical capacitors, J. Power Sources. 47 (1994) 89–107.

[193] G.A. Snook, P. Kao, A.S. Best, Conducting-polymer-based supercapacitor devices and electrodes, J. Power Sources. 196 (2011) 1–12.

[194] S.S. Shinde, G.S. Gund, V.S. Kumbhar, B.H. Patil, C.D. Lokhande, Novel chemical synthesis of polypyrrole thin film electrodes for supercapacitor application, Eur. Polym. J. 49 (2013) 3734–3739.

[195] A. Eftekhari, L. Li, Y. Yang, Polyaniline supercapacitors, J. Power Sources. 347 (2017) 86–107.

[196] A. Laforgue, P. Simon, C. Sarrazin, J.F. Fauvarque, Polythiophene-based supercapacitors, J. Power Sources. 80 (1999) 142–148.

[197] P. Naskar, A. Maiti, P. Chakraborty, D. Kundu, B. Biswas, A. Banerjee, Chemical supercapacitors: a review focusing on metallic compounds and conducting polymers, J. Mater. Chem. A. 9 (2021) 1970–2017.

[198] H. Talbi, P.E. Just, L.H. Dao, Electropolymerization of aniline on carbonized polyacrylonitrile aerogel electrodes: Applications for supercapacitors, J. Appl. Electrochem. 33 (2003) 465–473.

[199] B. Purty, R.B. Choudhary, Ag_3O_4 embedded fibre reinforced polyaniline nanocomposite as an electrode material for supercapacitors, Polym. Bull. (2022).

[200] X. Li, H. Huang, P. Zhang, X. Zhai, B. Chen, Y. He, Z. Guo, Rational preparation of ternary carbon cloth/MnO_2/polyaniline nanofibers for high-performance electrochemical supercapacitors, J. Mater. Sci. Mater. Electron. (2022).

[201] R.B. Rakhi, W. Chen, H.N. Alshareef, Conducting polymer/carbon nanocoil composite electrodes for efficient supercapacitors, J. Mater. Chem. 22 (2012) 5177–5183.

[202] A. Hirsch, The era of carbon allotropes, Nat. Mater. 9 (2010) 868–871.

[203] L. Weinstein, R. Dash, Supercapacitor carbons: Have exotic carbons failed?, Mater. Today. 16 (2013) 356–357.

[204] Y. Cao, S. Li, C. Xu, X. Ma, G. Huang, C. Lu, Z. Li, Mechanisms of Porous Carbon-based Supercapacitors, ChemNanoMat. 7 (2021) 1273–1290.

[205] M. Olivares-Marín, C. Fernández-González, A. MacÍas-García, V. Gómez-Serrano, Preparation of activated carbon from cherry stones by physical activation in air. Influence of the chemical carbonisation with H_2SO_4, J. Anal. Appl. Pyrolysis. 94 (2012) 131–137.

[206] J. Pallarés, A. González-Cencerrado, I. Arauzo, Production and characterization of activated carbon from barley straw by physical activation with carbon dioxide and steam, Biomass and Bioenergy. 115 (2018) 64–73.

[207] M.A. Yahya, Z. Al-Qodah, C.W.Z. Ngah, Agricultural bio-waste materials as potential sustainable precursors used for activated carbon production: A review, Renew. Sustain. Energy Rev. 46 (2015) 218–235.

[208] Y. Gao, Q. Yue, B. Gao, A. Li, Insight into activated carbon from different kinds of chemical activating agents: A review, Sci. Total Environ. 746 (2020) 141094.

[209] M.K.B. Gratuito, T. Panyathanmaporn, R.A. Chumnanklang, N. Sirinuntawittaya, A. Dutta, Production of activated carbon from coconut shell: Optimization using response surface methodology, Bioresour. Technol. 99 (2008) 4887–4895.

[210] C.A. Toles, W.E. Marshall, M.M. Johns, L.H. Wartelle, A. McAloon, Acid-activated carbons from almond shells: Physical, chemical and adsorptive properties and estimated cost of production, Bioresour. Technol. 71 (2000) 87–92.

[211] K.S. Kim, Y. Zhao, H. Jang, S.Y. Lee, J.M. Kim, K.S. Kim, J.H. Ahn, P. Kim, J.Y. Choi, B.H. Hong, Large-scale pattern growth of graphene films for stretchable transparent electrodes, Nature. 457 (2009) 706–710.

[212] H. Yang, S. Ye, J. Zhou, T. Liang, Biomass-derived porous carbon materials for supercapacitor, Front. Chem. 7 (2019) 1–17.

[213] S. Gillet, M. Aguedo, L. Petitjean, A.R.C. Morais, A.M. Da Costa Lopes, R.M. Łukasik, P.T. Anastas, Lignin transformations for high value applications: Towards targeted modifications using green chemistry, Green Chem. 19 (2017) 4200–4233.

[214] S.E.M. Pourhosseini, O. Norouzi, P. Salimi, H.R. Naderi, Synthesis of a Novel Interconnected 3D Pore Network Algal Biochar Constituting Iron Nanoparticles Derived from a Harmful Marine Biomass as High-Performance Asymmetric Supercapacitor Electrodes, ACS Sustain. Chem. Eng. 6 (2018) 4746–4758.

[215] K. Subramani, N. Sudhan, M. Karnan, M. Sathish, Orange Peel Derived Activated Carbon for Fabrication of High-Energy and High-Rate Supercapacitors, ChemistrySelect. 2 (2017) 11384–11392.

[216] A. Phakkhawan, M. Horprathum, N. Chanlek, H. Nakajima, S. Nijpanich, P. Kumnorkaew, S. Pimanpang, P. Klangtakai, V. Amornkitbamrung, Activated carbons derived from sugarcane bagasse for high-capacitance electrical double layer capacitors, J. Mater. Sci. Mater. Electron. 33 (2022) 663–674.

[217] Q. Tian, X. Wang, X. Xu, M. Zhang, L. Wang, X. Zhao, Z. An, H. Yao, J. Gao, A novel porous carbon material made from wild rice stem and its application in supercapacitors, Mater. Chem. Phys. 213 (2018) 267–276.

[218] X. Wang, S. Yun, W. Fang, C. Zhang, X. Liang, Z. Lei, Z. Liu, Layer-Stacking Activated Carbon Derived from Sunflower Stalk as Electrode Materials for High-Performance Supercapacitors, ACS Sustain. Chem. Eng. 6 (2018) 11397–11407.

[219] T. Ramesh, N. Rajalakshmi, K.S. Dhathathreyan, L.R.G. Reddy, Hierarchical Porous Carbon Microfibers Derived from Tamarind Seed Coat for High-Energy Supercapacitor Application, ACS Omega. 3 (2018) 12832–12840.

[220] Z. Wang, H. Guo, F. Shen, G. Yang, Y. Zhang, Y. Zeng, L. Wang, H. Xiao, S. Deng, Biochar produced from oak sawdust by Lanthanum (La)-involved pyrolysis for adsorption of ammonium (NH_4^+), nitrate (NO_3^-), and phosphate (PO_4^{3-}), Chemosphere. 119 (2015) 646–653.

[221] S. Meng, Z. Mo, Z. Li, R. Guo, N. Liu, Oxygen-rich porous carbons derived from alfalfa flowers for high performance supercapacitors, Mater. Chem. Phys. 246 (2020) 122830.

[222] G. Zhao, C. Chen, D. Yu, L. Sun, C. Yang, H. Zhang, Y. Sun, F. Besenbacher, M. Yu, One-step production of O-N-S co-doped three-dimensional hierarchical porous carbons for high-performance supercapacitors, Nano Energy. 47 (2018) 547–555.

[223] G. Zhu, L. Ma, H. Lv, Y. Hu, T. Chen, R. Chen, J. Liang, X. Wang, Y. Wang, C. Yan, Z. Tie, Z. Jin, J. Liu, Pine needle-derived microporous nitrogen-doped carbon frameworks exhibit high performances in electrocatalytic hydrogen evolution reaction and supercapacitors, Nanoscale. 9 (2017) 1237–1243.

[224] J.J. Vilatela, D. Eder, Nanocarbon composites and hybrids in sustainability: A review, ChemSusChem. 5 (2012) 456–478.

[225] G. Hasegawa, K. Kanamori, K. Nakanishi, T. Abe, New insights into the relationship between micropore properties, ionic sizes, and electric double-

layer capacitance in monolithic carbon electrodes, J. Phys. Chem. C. 116 (2012) 26197–26203.

[226] J. Newman, K. Thomas-Alyea, Electrochemical systems, 3rd ed., John Wiley & Sons, 2012.

[227] T. Gao, W. Lu, Machine learning toward advanced energy storage devices and systems, IScience. 24 (2021) 101936.

[228] What is Deep Learning? | IBM, IBM Cloud Educ. (2020).

[229] S. Zhu, J. Li, L. Ma, C. He, E. Liu, F. He, C. Shi, N. Zhao, Artificial neural network enabled capacitance prediction for carbon-based supercapacitors, Mater. Lett. 233 (2018) 294–297.

[230] H. Su, S. Lin, S. Deng, C. Lian, Y. Shang, H. Liu, Predicting the capacitance of carbon-based electric double layer capacitors by machine learning, Nanoscale Adv. 1 (2019) 2162–2166.

Chapter 3 Consequences of electrodeposition parameters on the microstructure and electrochemical behavior of electrolytic manganese dioxide (EMD)

This chapter is published as:

Consequences of electrodeposition parameters on the microstructure and electrochemical behavior of electrolytic manganese dioxide (EMD) for Supercapacitor

Kethaki Wickramaarachchi, Manickam Minakshi

Ceramics International, 2022, 48 (14), 19913-19924

DOI: https://doi.org/10.1016/j.ceramint.2022.03.266

Impact factor: 5.532

Chapter 3. Consequences of electrodeposition parameters on the microstructure and electrochemical behavior of electrolytic manganese dioxide (EMD)

Ceramics International 48 (2022) 19913–19924

Contents lists available at ScienceDirect

Ceramics International

journal homepage: www.elsevier.com/locate/ceramint

Consequences of electrodeposition parameters on the microstructure and electrochemical behavior of electrolytic manganese dioxide (EMD) for supercapacitor

Kethaki Wickramaarachchi, Manickam Minakshi *

College of Science, Health, Engineering and Education, Murdoch University, WA, 6150, Australia

ARTICLE INFO

Keywords:
Manganese dioxide
Electrodeposition
Electrochemistry
Energy storage
Microstructure

ABSTRACT

In this study, manganese dioxide (MnO_2) was electrochemically synthesized on the surface of a lead anode using different current densities (100–300 A m^{-2}) and deposition time (4–6 h). This work intends to highlight the consequences of various electrodeposition parameters via the electrochemical approach. The MnO_2 electrowinning plant must consider the effect of electrodeposition parameters that can ensue on the overall impact of electrolytically derived MnO_2 (EMD) powder on a larger scale. The micrographs of the obtained EMD powder revealed that spindle-like morphology was observed for the current density between 100 and 200 A m^{-2}, whereas moss-like morphology was observed at a current density above 200 A m^{-2} with increased surface roughness. The deposition time has not shown a profound effect. This study highlights the EMD deposited at 200 A m^{-2} for 5 h when tested in 2 M NaOH electrolyte exhibits a storage performance of 98 F g^{-1}. For broader adoption of this material, the asymmetric device comprising EMD versus activated carbon (EMD/AC) has been fabricated. The asymmetric supercapacitor is a key for storing energy, which delivered 36 F g^{-1} at energy and power densities of 10 Wh kg^{-1} and 2352 W kg^{-1}, respectively. The further increase/decrease of current density and deposition time has a deleterious effect on the storage performance.

1. Introduction

The prominence of the manganese dioxide (MnO_2) cathode for electrochemical energy storage devices is much higher as the MnO_2 is a low cost, low toxic, and abundantly available material compared to other transition metal oxides counterparts such as nickel and cobalt oxides. MnO_2-based materials are used worldwide as a solid cathode for both aqueous and non-aqueous rechargeable battery systems. Recently, the use of MnO_2-based materials has been extended to electrochemical capacitor (EC) applications. MnO_2 can exist in several crystallographic forms such as natural MnO_2 (NMD α and β), electrolytic MnO_2 (EMD; γ), chemically synthesized MnO_2 (CMD; δ), and spinel-type MnO_2 (λ-MnO_2) that are widely applied in energy storage applications [1]. Their physicochemical properties and electrochemical behavior largely depend on the crystal structure and varying degrees of hydration. The structures differ based on the interlinks between MnO_6 octahedra, which determines the voids within the material for the faradaic contribution required for charge storage [2]. Among all the structures, the γ-MnO_2 is formed by the intergrowth of the major ramsdellite domain with the pyrolusite domain as an impurity. The dislocations during the structural intergrowth leave the defect sites, leading to higher discharge capacity and flat voltage characteristics, the prerequisites for both batteries and supercapacitor applications [3].

To date, the EMD is renowned material used mainly in primary alkaline batteries. The alkaline Zn–MnO_2 primary battery using KOH electrolyte is commercialized, leading to a powerful system of today. Later, the primary battery was further developed by Kordesch et al. to a rechargeable type available since 1994 [4]. The charge storage mechanisms for batteries and supercapacitors are different; batteries are based on ion diffusion, whereas supercapacitors are based on surface adsorption of cations from the electrolyte. For supercapacitors, the electrodes can be either in the form of powder or self-standing thin-film electrodes. The reports are constrained to the self-standing electrodes directly deposited onto a substrate requiring no further binding or conducting additives [5–7]. The binder-free nature of the electrode could result in higher capacitance along with unique properties, such as low electrode resistance and better electrolyte accessibility through electronic conductivity of the material. However, the increased thickness of the

* Corresponding author.
E-mail address: minakshi@murdoch.edu.au (M. Minakshi).

https://doi.org/10.1016/j.ceramint.2022.03.266
Received 14 February 2022; Received in revised form 18 March 2022; Accepted 25 March 2022
Available online 28 March 2022
0272-8842/© 2022 Elsevier Ltd and Techna Group S.r.l. All rights reserved.

Author contribution

Contributor	Contribution (%)	Nature of contribution
Kethaki Wickramaarachchi	70	Conceptualization, experimentation, data collection, analysis and interpretation, drafting and critical revision of the manuscript.
Manickam Minakshi	30	Conceptualization, interpretation of data, critical revision of the manuscript.

3.1. Abstract

In this chapter, manganese dioxide (MnO_2) was electrochemically synthesized on the surface of a lead (Pb) anode using different current densities (100 - 300 A m^{-2}) and deposition periods (4 - 6 h). This chapter intends to highlight the consequences of various electrodeposition parameters via the electrochemical approach. The MnO_2 electrowinning plant must consider the effect of electrodeposition parameters that can ensue on the overall impact of electrolytically derived MnO_2 (EMD) powder on a larger scale. The micrographs of the obtained EMD powder revealed that spindle-like morphology was observed for the current density between 100 - 200 A m^{-2}, whereas moss-like morphology was observed at a current density above 200 A m^{-2} with increased surface roughness. However, the deposition time period has not shown a profound effect. This chapter highlights the EMD deposited at 200 A m^{-2} for 5 h when tested in 2 M NaOH electrolyte exhibits a storage performance of 98 F g^{-1}. For broader adoption of this material, the hybrid (asymmetric) device comprising EMD versus activated carbon (EMD/AC) has been fabricated. The asymmetric supercapacitor (SC) is a key for storing energy, which delivered 36 F g^{-1} at energy and power densities of 10 Wh kg^{-1} and 2352 W kg^{-1}, respectively. The further increase/decrease of current density and deposition time has a deleterious effect on the storage performance.

3.2. Introduction

The prominence of the manganese dioxide (MnO_2) cathode for electrochemical energy storage devices is much higher as the MnO_2 is a low cost, low toxic, and abundantly available material compared to other transition metal oxides counterparts such as nickel and cobalt oxides. MnO_2-based materials are used worldwide as a solid cathode for both aqueous and non-aqueous rechargeable battery systems. Recently, the use of MnO_2-based materials has been extended to electrochemical capacitor (EC) applications. MnO_2 can exist in several crystallographic forms, such as natural MnO_2 (NMD α and β), electrolytic MnO_2 (EMD; γ), chemically synthesized MnO_2 (CMD; δ), and spinel-type MnO_2 (λ-MnO_2) that are widely applied in energy storage

applications [1]. Their physicochemical properties and electrochemical behavior largely depend on the crystal structure and varying degrees of hydration. The structures differ based on the interlinks between MnO_6 octahedra, which determines the voids within the material for the faradaic contribution required for charge storage [2]. Among all the structures, the γ-MnO_2 is formed by the intergrowth of the major ramsdellite domain with the pyrolusite domain as an impurity. The dislocations during the structural intergrowth leave the defect sites, leading to higher discharge capacity and flat voltage characteristics, the prerequisites for both batteries and SC applications [3].

To date, the EMD is renowned material used mainly in primary alkaline batteries. The alkaline Zn-MnO_2 primary battery using KOH electrolyte is commercialized, leading to a powerful system of today. Later, the primary battery was further developed by Kordesch *et al.* to a rechargeable type available since 1994 [4]. The charge storage mechanisms for batteries and SCs are different; batteries are based on ion diffusion, whereas SCs are based on surface adsorption of cations from the electrolyte. For SCs, the electrodes can be either in the form of powder or self-standing thin-film electrodes. The reports are constrained to the self-standing electrodes directly deposited onto a substrate requiring no further binding or conducting additives [5–7]. The binder-free nature of the electrode could result in higher capacitance along with unique properties, such as low electrode resistance and better electrolyte accessibility through the electronic conductivity of the material. However, the increased thickness of the material will reduce the performance and requires a large surface of the substrates to improve the capacitance. Therefore, the self-standing method largely retards the scalability of the material utilized to develop commercial applications [8]. In contrast, producing the electrochemically synthesized MnO_2 powdered material is scalable and commonly practiced at electrowinning plants, which can be utilized as bulk for various applications, including ECs. Moreover, electrodeposition has attractive features like synthesis at low temperatures, the ability to obtain the powder on complex morphologies, and other physical properties by simply controlling the synthesis parameters. Prior to moving to the work in this chapter, a snapshot of research on the individual electrodeposition parameters such as time, voltage, current density, and

modifications in the electrolytic bath reported in the literature have been discussed in the following section.

Effect on independent electrodeposition parameter: a brief overview

It has been widely reported [9–13] that the electrodeposition parameters such as the deposition time and current density affect the areal-specific capacitance and mass-specific capacitance of the electrode. Dai *et al.* [9] explored the effects of deposition time varying from 30 s to 500 s, in which, at a lower duration of time, the deposited MnO_2 has a porous structure, but the branches are incomplete. While between 150 s - 300 s, the deposition is observed to be complete and uniformly porous. However, for 500 s, the porosity and the specific surface area are reported to be reduced and may not be feasible for the transfer of electrons and ions from the electrolyte to the MnO_2 electrode phase. The authors have further validated these through the storage performance that the sample electrodeposited at 300 s reported to be the highest specific capacitance of 100 mF cm^{-2}. It is discussed that the optimum duration of time is crucial otherwise, the thickness of the film increases with time (as reported for 500 s), led to the insufficient utilization of the active MnO_2 material during the chemical reaction, resulting in a decrease in specific capacitance to 80 mF cm^{-2}. It has also been shown in this article by Dai *et al.* [9] that the current density employed for deposition is also critical for nucleation on the substrate, which is more sensitive to the applied deposition current. Therefore, both the time and current density determine the structure of the electrodeposited MnO_2 on the chosen substrate. On the other hand, Zhang *et al.* [10] showed the importance of electrodeposition potential. The authors varied the deposition potential of MnO_2 in solution from 0.6 V to 1.2 V to electrodeposit MnO_2 on a nickel foam electrode that was soaked in alcohol prior to starting the experiment. At a lower voltage, a uniform crack-free deposit was obtained. However, at a higher voltage, deposition speed rises, and the film becomes dense with the formation of dendrites that weaken the film adhesion to the substrate. The MnO_2 deposited at a lower voltage is reported to have a more desirable rate performance and is suitable for long-term cyclability. To further enhance the available capacitance and cyclability of the electrodeposited MnO_2, Zhang *et al.* [11] have modified the deposition solution by adding the supernatant (reduced graphene oxide - rGO) and reported a high-quality

MnO_2/rGO exhibiting very low solution resistance and charge transfer resistance resulting in 347 F g^{-1} at a current density of 1 A g^{-1} with retention of 93 % after 2500 cycles. The addition of rGO is shown to form a thin layer on the surface of MnO_2, which appears to improve the conductivity of the material and is attributed to the observed high capacitance. Further to this, several other approaches have been made in tuning the electrodeposition process to obtain high specific capacitance. For instance, Zhang *et al.* [12] reported nanostructured MnO_2 by ultrasonic treatment, and NH_4^+ assisted one-step electrodeposition. In this method, authors have shown MnO_2 with a high specific capacitance of 810 F g^{-1} at a current density of 1 A g^{-1}. Another study by Shi *et al.* [13] modified the deposition solution by adding polyvinylpyrrolidone (PVP) surfactant and obtained MnO_2/rGO nanospheres for battery and SC applications. The presence of rGO enabled the expansion of the surface area of the MnO_2 that buffered the lattice expansion with improved cyclability. In addition, several changes in the synthesis, including electrodeposition parameters [14,15], other modifications such as different plating solutions [16], heat treatment [17], etc., have been reported to examine the EMD electrochemical performance.

Significance of work in this chapter

In this chapter, a series of EMD bulk samples were deposited under different conditions in a low acidic electrolytic bath (<1 M) at 0.25 M H_2SO_4. According to the mechanistic path in low acid concentration, Mn^{2+} forms Mn^{3+} followed by hydrolysis to precipitate into MnOOH, which oxidized into MnO_2 [18,19]. An attempt has been made to clarify the electrodeposition mechanism, optimize the parameters, and test its suitability for SC applications. As a consequence of varying the current applied for electrodeposition, the microstructure varied and hence the electrochemical properties of the material. Therefore, in this study, bulk EMD has been deposited at various current densities (100 - 300 A m^{-2}) and deposition time durations (4 - 6 h), and their effects on the microstructure and capacitive behavior were investigated and reported. To be noted, in the previous studies [9–13], authors have deposited MnO_2 at a duration of 500 s. The galvanostatic (constant current) mode of electrodeposition was carried out to synthesize the MnO_2 for capacitor electrodes by adopting the procedure used by A. Biswal *et al.* [20], which is different from those reported by other researchers. EMD

for SC performance was determined in a single electrode cell, with reference to Pt counter electrode and standard Hg/HgO in a Na-based aqueous electrolyte (NaOH) as a potential substitute for Li-based electrolytes. The faradaic and non-faradaic contributions to the total charge obtained from the EMD were also quantified and compared at varying scan rates to bring insights into the kinetics associated with redox reactions. A hybrid (asymmetric) capacitor was fabricated using EMD as the positive electrode and a commercially available activated carbon (AC) as the negative electrode to study the cycling stability. The results indicated the challenge and importance of the delicate tailoring of the electrodeposited materials for improved performance characteristics. The work in this chapter adds value to the mining industry and clarifies the existing knowledge of synthesizing powdered manganese dioxide using the galvanostatic electrodeposition method and its suitability for capacitor applications.

3.3. Experimental

3.3.1. Materials

All the chemicals used in the experiments were bought from commercial suppliers unless it was specifically mentioned. $MnSO_4.H_2O$ (Chem supply; 99.5 %) is used as the manganese source in the electrolyte solution. $MnSO_4.H_2O$ and concentrated H_2SO_4 (Univar; 98 %) were dissolved and thoroughly mixed in deionized (DI) water to make the solution. The composition of Mn and H_2SO_4 used in the electrolytic bath was 50 g l^{-1} and 25 g l^{-1}, respectively. The electrolytic bath used for deposition was a 500 ml glass beaker covered by a machined PTFE lid, a 99.99 % pure Pb plate was the anode, and the Stainless Steel (SS) plate was the cathode.

3.3.2. Method

Before conducting the electrodeposition, both electrodes were mechanically polished and rinsed thoroughly in DI water to remove extra dust attached to the surface and patted with lint-free tissues. The initial weight of the Pb electrode was measured and

noted. Both electrode plates were placed in the bath, and the connections were established to start the electrodeposition. The solution was continuously stirred during the experiment with a Teflon-coated magnetic stirring bar. A set of experiments were carried out under a matrix of conditions changing the deposition time and the current density using galvanostatic electrodeposition mode. The system was left to react and deposit for 4, 5, 6 hour periods, and the current supplied was altered as 100, 200, and 300 Am^{-2}. For convenience, those samples will be denoted as **$EMD_{(t,I)}$,** where 't' represents the time and 'I' represents the current density. Throughout the experiment, bath temperature was maintained at 95 ± 2 °C. The synthesis process of the EMD materials is given in Figure 3.1 (refer to chapter 1, Figure 1.8 for further information). The generalized reaction R(3.1) for the deposition of manganese dioxide from Mn^{2+} is as follows.

$$Mn^{2+} + H_2O \rightarrow MnO_2 + 4H^+ + 2e^- \qquad \text{R(3.1)}$$

Soon after the deposition was finished, the Pb plate was removed from the bath. It was thoroughly rinsed with running DI water to remove entrained electrolytes. Then it was kept in the oven for drying overnight. The final weight was measured to calculate the amount of the material deposited on the Pb plate. The electrodeposited MnO_2 was scraped from the electrode surface cautiously without damaging the electrode to avoid the contamination of Pb. All the small flakes were collected and rinsed till they completely swept away the electrolyte attached and were dried in the oven at 80 °C for 12 hours. The flakes were directly used to observe the morphology. Finely ground EMD was used for other characterizations.

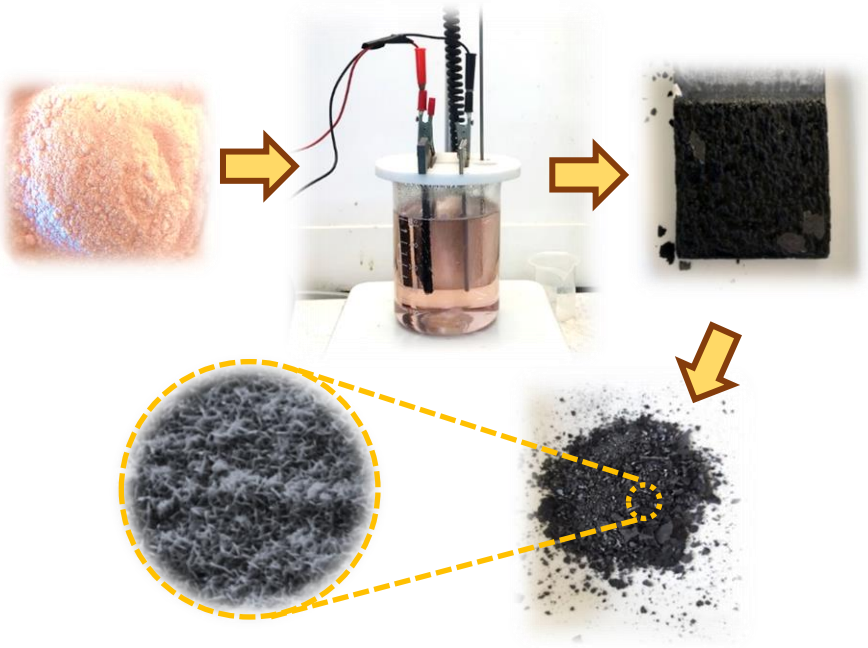

Figure 3.1. Electrolytic manganese dioxide (EMD) synthesis process.

3.4. Method analysis and sample characterization

3.4.1. *Current efficiency and energy consumption of electrodeposition*

The current efficiency (η) of the manganese dioxide electrodeposition was calculated using the equation (3.1) as follows,

$$\eta = \frac{m_{deposited}}{m_{theoritical}} \times 100\% \qquad (3.1)$$

The actual amount of the deposited material is found by the difference in the electrode weights before and after the experiment. The theoretical weight of deposition was calculated using Faraday's law as in equation (3.2) [21,22].

$$m_{theoritical} = ItM/(Fz) \qquad (3.2)$$

where, m - the expected mass of MnO_2 deposit, I - applied current (A), t - time of deposition (h), M - molecular weight of MnO_2 (86.94 g mol^{-1}), and F - Faraday constant (96485 C mol^{-1}) and z - number of electrons transferred from Mn^{2+} to Mn^{4+}.

The energy consumption for the process was determined by the following equation.

$$E_{con} = \frac{VIt}{\eta} \qquad (3.3)$$

where, V - applied voltage, η - current efficiency as calculated by equation (3.1).

3.4.2. Physicochemical characterization

The surface morphology and crystal size of the materials were obtained by field emission scanning electron microscope (FESEM, TESCAN CLARA) and Transmission electron microscope (FEI Talos FEG TEM). X-ray diffraction (XRD) data were collected using Cu Kα radiation as the target source (1.5418 Å, 35 kV, and 28 mA). 2θ was changed from 10 to 70°, scan speed was 1° min^{-1}, and the step size was 0.02. Kratos Ultra DLD instrument was used to perform X-ray photoelectron spectroscopy (XPS) using monochromatic X-ray source Al Kα as the source of excitation. Micromeritics surface area and porosity analyzer were used to obtain adsorption-desorption isotherms in the presence of Nitrogen gas as the adsorbate. A sample mass of 0.2 g was measured and degassed under vacuum at 110 °C, then used for analysis.

3.4.3. Electrochemical characterization

3.4.3.1. Electrode fabrication

The coating of the electrodeposited materials was assembled on a 1cm × 1cm area of graphite substrate, which is 1 cm × 4 cm in size. Graphite was chosen as the substrate due to its good mechanical, chemical stability, conductivity, and the aspects of

reusability and easy preparation of the surface. The substrate surface was smoothed using sandpaper, washed thoroughly with DI water, and dried on a hot plate. After drying, the initial weight was measured. To prepare the electrode, a composition of 75 % EMD (active material), 15 % acetylene black, and 10 % of Polyvinylidene fluoride (PVDF) binder were employed. N-Methyl-2-pyrrolidone (NMP) solution was added to the mixture and thoroughly ground until all materials were distributed uniformly to make a slurry. The slurry was coated in the graphite electrode and dried in the oven at 80 °C for 12 hours. The mass coated (mass loading) on the graphite electrode was determined from the weight difference before and after the coating. All weights were measured by a balance that can weigh at an accuracy of 0.1 mg. EMD was used as the positive electrode for hybrid (asymmetric) capacitor testing, while AC was the negative electrode. A similar procedure was followed for negative electrode coating, considering activated carbon as the active material.

3.4.3.1.1. EMD (positive electrode)

All electrochemical measurements were performed by a Biologic SP-150 potentiostat and EC-Lab software. Cyclic voltammetry (CV) and galvanostatic charge-discharge (GCD) results were analyzed to evaluate the electrochemical performance of the electrodes. EMD materials were tested within the potential of 0-0.6 V for CV and GCD. Various scan (sweep) rates from 2 to 50 mV s^{-1} were used to conduct CV. Current densities from 1 to 5 mA cm^{-2} were used for GCD. The single electrode cell was constructed with the working electrode, Pt counter electrode, and reference electrode (Hg/HgO), using a 2 M NaOH aqueous electrolyte. All the tests were conducted at room temperature. Further calculations were carried out to determine the faradaic and non-faradaic contributions to electrode capacitances.

3.4.3.1.2. Activated carbon (AC) (negative electrode)

The CV and GCD measurements were obtained similar to the EMD described in 3.4.3.1.1. at the varying scan and current rates. The potential window for the negative AC electrode was -1 to 0 V.

3.4.3.1.3. Hybrid (asymmetric) capacitor (EMD *vs.* AC)

The hybrid capacitor was fabricated using the best-performed EMD material and the commercial AC as positive and negative electrodes. The value of the mass ratio of the two electrode materials used in the full cell is determined by equation (3.4). The cell was operated at 1.4 V and tested for the cell capacitance, specific energy (energy density), specific power (power density), and cycling stability.

$$\frac{m^+}{m^-} = \frac{C^- \, \Delta v_{m^-}}{C^+ \, \Delta v_{m^+}} \tag{3.4}$$

where, m^+/m^- is the mass ratio of positive and negative electrodes, C^- and C^+ - specific capacitances of the negative and positive electrodes, Δv_{m^+} and $\Delta v_{m^-}$the potential window of the negative and positive electrodes, respectively.

The equations to calculate the specific capacitance from GCD measurements ($C_{s,GCD}$, F g^{-1}), specific energy (E, Wh kg^{-1}), and specific power (P, W kg^{-1}) are given in the following equations (3.5), (3.6), and (3.7).

$$C_{s,GCD} = \frac{i \, \Delta t}{\Delta v \, m} \tag{3.5}$$

$$E = \frac{1}{2} C_s \frac{\Delta v^2}{3.6} \tag{3.6}$$

$$P = \frac{E}{t} \tag{3.7}$$

where i - current (A), Δt - discharge time (s), m - active electrode mass (g), Δv - potential window (V).

3.5. Results and discussion

3.5.1. Electrodeposition method analysis

Table 3.1 summarizes the energy consumption and current efficiency of the electrodeposited EMD. The lower deposition time and current density yield $EMD_{(5,100)}$ with a current efficiency of 99.9 % and energy consumption of 13.6 Wh m^{-2}. With the higher current density and deposition time, the energy consumption increased to a maximum of 56.3 Wh m^{-2}, with a loss in efficiency typically observed for $EMD_{(5,300)}$. Higher current density with a further increase in deposition time (to 6 h) leads to increased mass deposition. At an elevated value of 200 A m^{-2}, the consumed energy, and the efficiency are quite similar, regardless of the deposition time.

Table 3.1 Energy consumption and efficiency determined for the experiment.

Sample	Current efficiency (%)	Total Energy consumption (Wh m^{-2})	Energy consumed per unit weight (Wh g^{-1} m^{-2})
$EMD_{(5,100)}$	99.9	13.6	4.6
$EMD_{(4,200)}$	99.9	19.4	4.9
$EMD_{(5,200)}$	99.9	25.2	4.7
$EMD_{(6,200)}$	99.4	28.5	4.7
$EMD_{(5,300)}$	92.8	56.3	7.0

The manganese dioxide deposition mechanisms have been reported earlier, which is based on the acidity of the solution, but in this chapter, we found the underlying anodic deposition mechanism of MnO_2 to be more complex. The following competitive reactions are proposed via the ‘disproportionation’ (pathway 1) and ‘hydrolysis’ (pathway 2) mechanisms [8]. The mechanism is found to be dependent on the chosen

electrodeposition parameters. The growth of the nuclei (EMD crystallites) on the lead anode occurs independently from each of the pathways at the initial stage.

Schematic representation of the anodic deposition mechanism of MnO_2

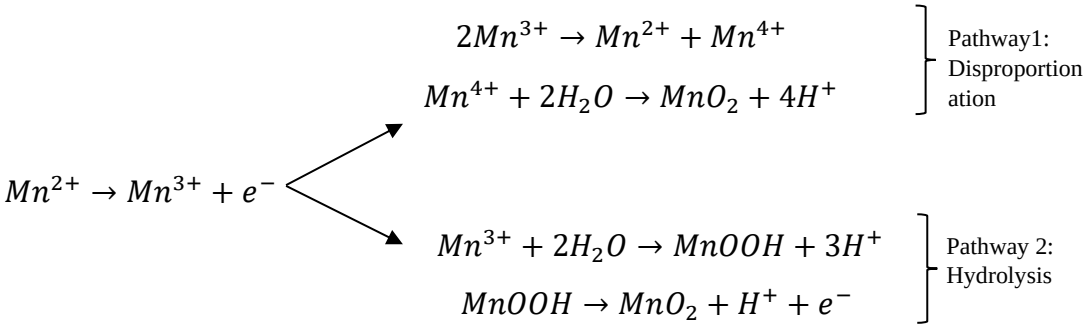

However, under different synthesis conditions, the height of the nuclei and the density of the EMD deposit are dependent that determine the rate of nuclei growth. The independent nuclei that are formed in the initial stages start overlapping diffusion zones around growing nuclei in the succeeding steps. This overlapping results in the development of local concentration and overpotential distribution in the neighborhood of the growing nuclei (clusters). With the increase in the applied current density (100 – 300 A m^{-2}), the fast transport of Mn^{2+} would increase the reaction rate (pathway 1), resulting in larger particle formation and a higher rate of crystallization reactions. The hydrolysis pathway could be the primary mechanism expected at a higher current density, increasing mass transfer of the soluble species Mn^{3+}, which becomes less stable and leads to fast precipitation of MnOOH preferentially. The nucleated regions will not be interlinked to make a uniform deposition layer at higher current rates. On the other hand, at a lower current density of 100 A m^{-2}, the deposition rate becomes relatively low owing to the sluggish transport of the ions, which results in a film-like surface.

3.5.2. Physicochemical characterization

Morphology. The surface morphology of the electrodeposited MnO_2 samples under different conditions; $EMD_{(5,100)}$, $EMD_{(5,200)}$, and $EMD_{(5,300)}$, are given in Figure 3.2. The FESEM micrograph of the $EMD_{(5,100)}$ shown in Figure 3.2A has grown like sea whips with densely packed interlinked particle formation. On the other hand, for the sample $EMD_{(5,200)}$, a spindle-like morphology is observed (Figure 3.2B), covering the entire surface due to the lower current density, which can be attributed to smaller deposited particles. The samples deposited at a current density of 200 A m^{-2} at different deposition time durations did not show significant changes in morphologies. Therefore, FESEM micrographs do not clearly indicate the synergy between the deposition time and the developed nanostructures. The uniformly grown spindle-like particles facilitate the transport of ions from the electrolyte, which suits SC applications. Under favorable electrochemical conditions, the surface nucleation of MnO_2 predominantly occurs on the lead anode, which gradually transits further mass to the nuclei resulting in a growing crystallite upon more prolonged deposition. When the applied current is larger at 300 A m^{-2}, the crystallite nucleation and crystallite growth can occur simultaneously, leading to surface non-uniformity, developing a moss-like morphology observed for $EMD_{(5,300)}$ in Figure 3.2E. The fast reaction rate might create loosened particle to particle deposition, and therefore, unstabilized randomly distributed MnO_2 over the surface is evidenced.

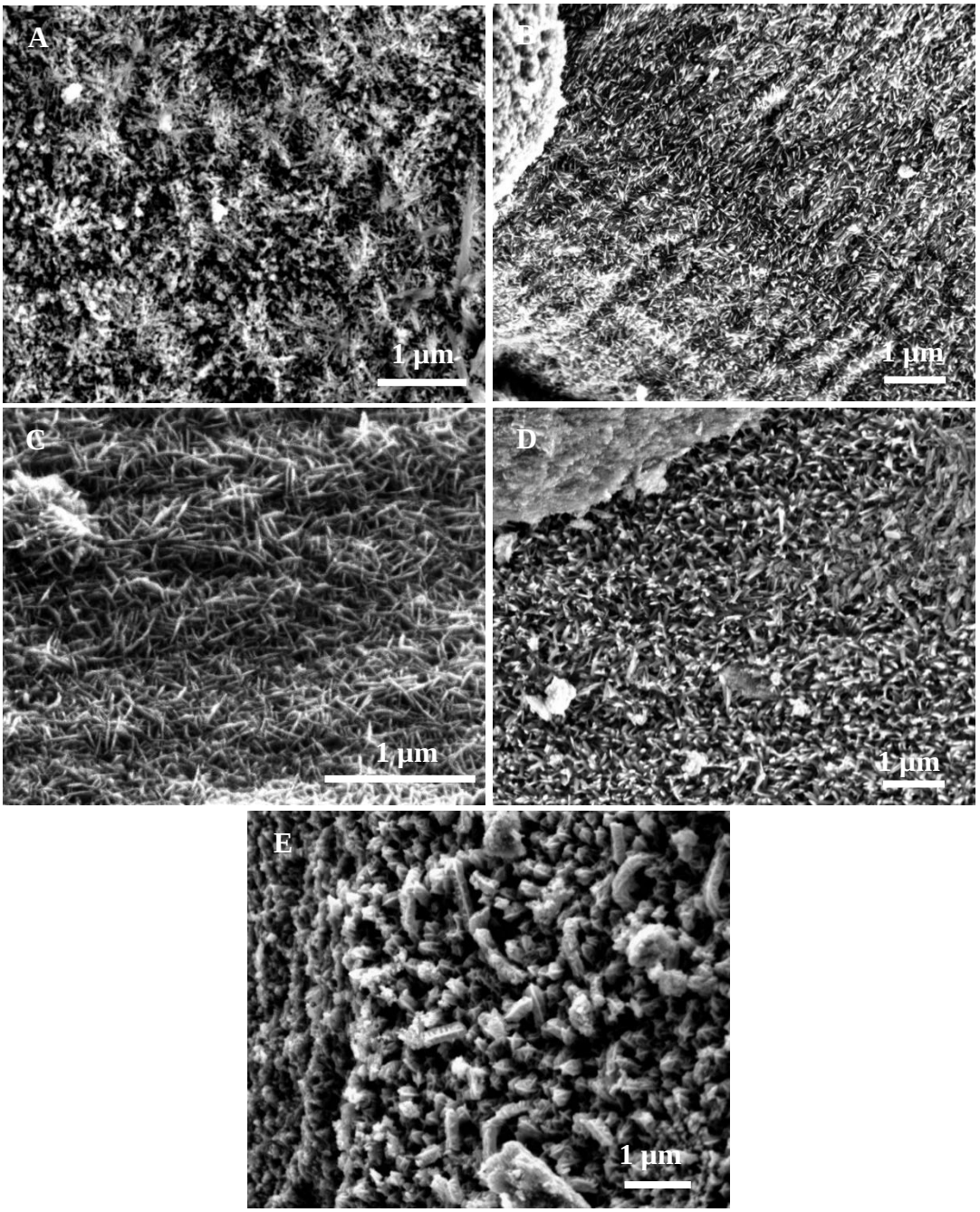

Figure 3.2 FESEM images of (A) $EMD_{(5,100)}$, (B) $EMD_{(4,200)}$, (C) $EMD_{(5,200)}$ (D) $EMD_{(6,200)}$ and (E) $EMD_{(5,300)}$ samples.

XRD patterns of EMD. The XRD patterns of EMD deposited at various electrochemical conditions are shown in Figure 3.3. The XRD pattern of EMD material shows the presence of well-resolved peaks of crystalline nature. However, the broader

peaks in the XRD patterns indicate that the deposited EMD is less crystalline and has more defects in microtwinning corresponding to γ-phase MnO_2 [23]. Five major peaks can be observed in each sample at the 2θ values around 22º, 37º, 42º, 56º, and 67º. The XRD patterns studied under different electrochemical conditions invariably exhibit the characteristics of γ-MnO_2 [3,24,25]. The γ-MnO_2 has an orthorhombic phase (JCPDS file no. 65-1298) with the lattice parameters a = 9.32290 Å, b = 4.45330 Å, and c = 2.84820 Å. Based on the classification postulated by Chabre and Pannetier [3], the EMD samples prepared in this chapter belong to the γ-MnO_2 type III pattern that describes the extensive presence of microtwinning in the samples. Thus, the change in electrochemical parameters had no significant effect on the crystalline structure of EMD bulk samples; however, it influenced the surface morphology. Further, XPS analysis was acquired for $EMD_{(5,200)}$ material to identify the elemental composition and the oxidation states present in the electrodeposited sample.

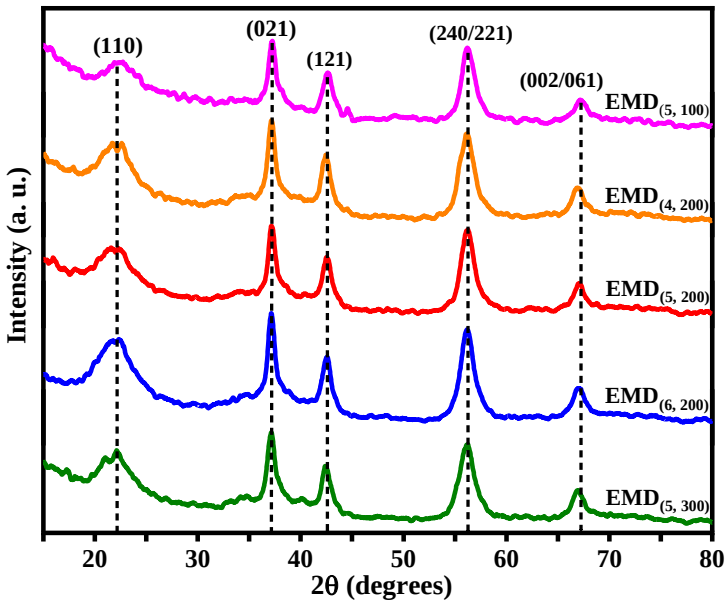

Figure 3.3 X-ray Diffraction (XRD) patterns of EMD electrochemically synthesized at different current densities and deposition time durations.

X-ray photoelectron spectroscopy (XPS). Figure 3.4A shows the survey (broad) XPS spectrum of $EMD_{(5,200)}$ associated with the major elements manganese (Mn), oxygen (O), and carbon (C), which is as expected. The binding energy values have been

corrected using the adventitious carbon (C 1s) peak at 284.8 eV. The spectrum has been fitted using a 70% Gaussian line shape. The higher energy resolution for the Mn 2p region shown in Figure 3.4B represents Mn $2p_{1/2}$, and the Mn $2p_{3/2}$ consists of several peaks. These six multiplets correspond to the Mn^{4+} state, and their peak fitting applied to the spectra of Mn oxides as reported in the literature [26,27]. However, the small peak at low binding energy of 641.25 eV cannot be assigned to Mn^{4+} [28,29] but is attributed to the Mn^{3+} state. Figures 3.4 C and D represent the higher energy resolution for the O 1s and C 1s regions. The O 1s spectrum has a major peak around 530 eV and a distinct, broad shoulder on the higher binding energy, characteristic of MnO_2. Different ranges of binding energies for O 1s bonding with manganese and hydrogen are reported in the literature [28, 30-32]. Mn-O varies from 529.1 to 530.3 eV, Mn-OH varies from 530.5 to 531.5 eV, while the H-O-H is 531.8 to 532.8 eV [28,30–32]. The O 1s spectrum was fitted to these three components (Figure 3.4C), labeled as peaks 1, 2, and 3. The most intense C 1s peak is attributed to carbon atoms in adventitious carbon, while the minor peaks C_2 at 286.15 eV can be attributed to the C-OH or C-O-C functionalities, and C_3 at 288.76 eV to C=O and O-C=O functional groups [33].

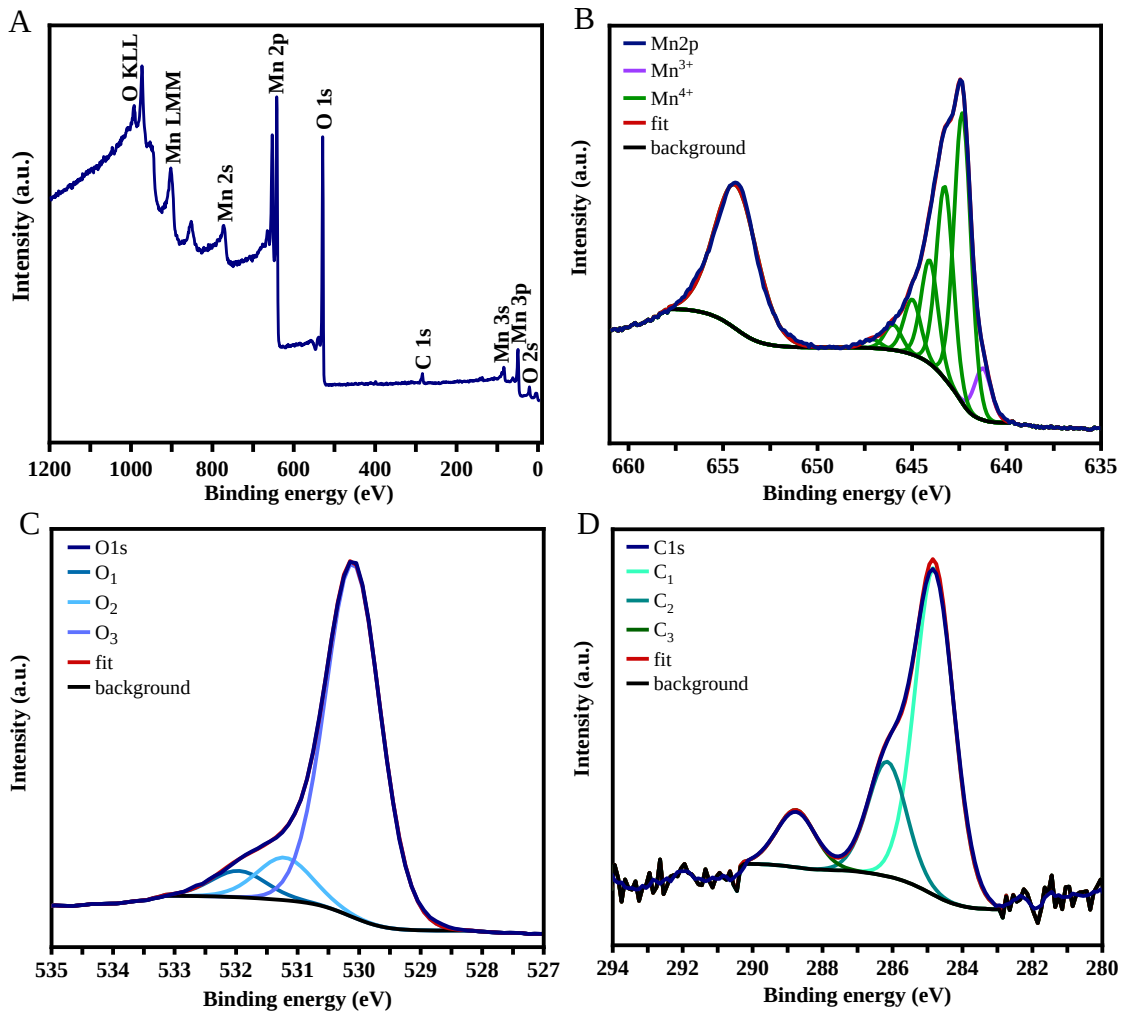

Figure 3.4 (A) XPS survey spectra, (B) Mn 2p spectra, (C), O 1s spectra and (D) C 1s spectra for EMD (5,200).

Surface area. After structural and microscopic analysis, BET surface area analysis and pore size distribution studies were carried out to gain further insight into the structural behavior of bulk-deposited EMD under different conditions. The reported BET surface area values of the EMD deposits were in the range of 10-100 m^2 g^{-1} [34,35]. The BET surface area is usually correlated with the electrochemical reactivity of metal oxides, as a higher surface area results in higher performance. Nevertheless, several studies have also revealed that increasing the surface area further might not proportionally enhance the capacitance [36,37] as several other factors have been involved. Therefore, the BET result can be taken as an approximation for the electrochemically active surface area of the material [36]. The measurements are based on the N_2

adsorption-desorption measurements by the amount of gaseous adsorbate (nitrogen, argon, or carbon dioxide) condensed on the surface of the tested EMD material [38].

The EMD samples were ground, and the powdered form was degassed to remove all the moisture/gas within its volume. During the testing, nitrogen will create a film formation on the surface by penetrating the pores. The analysis gives the specific surface area and the pore size, which influences the capacitive properties. Physisorption isotherms can be grouped into six types. According to the IUPAC classification, the isotherms obtained for EMD samples can be categorized as type IV isotherms with an H2 hysteresis loop in the range 0.4-0.8 P/P_0. Corresponding pore size distribution curves were taken from the Barret-Joyner-Halenda (BJH) data, which indicated the samples are mesoporous. The surface area values, average pore sizes, and volumes for the EMD samples are presented in Table 3.2. The Nitrogen adsorption-desorption isotherms are displayed in Figure 3.5A, and the pore size distribution is given in Figure 3.5B. The lowest surface area of 73.8 $m^2\ g^{-1}$ exhibited by $EMD_{(5,100)}$ could be due to the diffusion of ions into the nucleus on the electrode occurring at a low deposition rate allowing uniformly layered deposition; therefore, small grains are well packed on the surface. The surface area of the EMD deposited at a slightly higher current rate of 200 $A\ m^{-2}$ has not varied much with the deposition duration. $EMD_{(5,300)}$ reported that the largest surface area of 103 $m^2\ g^{-1}$ could be due to the larger current introduced by forced convection. It increased the mass transfer of the Mn species, creating a mossy surface of EMD. The pore size range in Table 3.2 facilitates the transportation of OH^- ions into these pores contributing to the overall capacitance. The BET surface areas of the EMD samples synthesized under different conditions confirm that the current density facilitated the increase in surface area but no significant effect by the deposition duration.

Table 3.2 BET surface area and pore sizes of all the EMD materials.

Sample	BET surface area ($m^2\ g^{-1}$)	BJH average pore diameter (nm)	BJH cumulative volume of pores ($cm^3\ g^{-1}$)
$EMD_{(5,100)}$	73.8	4.15	0.071
$EMD_{(4,200)}$	83.4	4.11	0.080
$EMD_{(5,200)}$	80.5	4.21	0.082
$EMD_{(6,200)}$	81.4	4.16	0.071
$EMD_{(5,300)}$	103.7	4.10	0.087

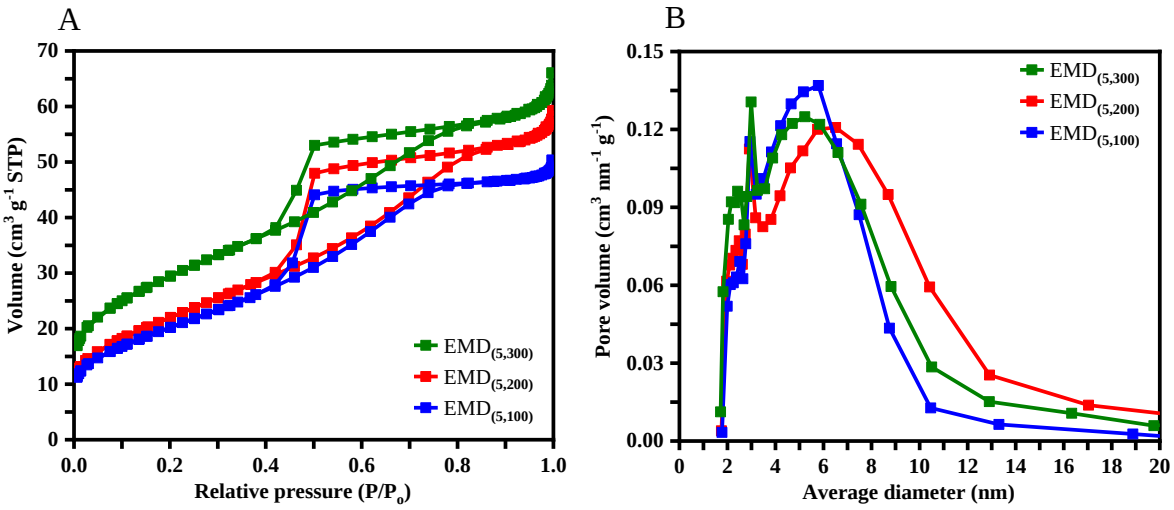

Figure 3.5 Comparison of the (A) Nitrogen adsorption and desorption isotherms and (B) pore size distribution of EMD electrochemically synthesized at different current densities.

Transmission electron microscopy (TEM). The TEM observations of the $EMD_{(5,200)}$ are shown in Figure 3.6. Figure 3.6A demonstrates the nano grain-shaped particles with size ranges from 8 - 39 nm, with ~17 nm mean particle size. The high-resolution transmission electron microscopy (HRTEM) in Figure 3.6B indicates the semi-crystalline nature of the material, which is also evidenced by the XRD pattern. High-angle annular dark-field scanning transmission electron microscopy (HAADF-STEM) image is shown in Figure 3.6C, and the corresponding Energy-dispersive X-ray

spectroscopy (EDS) images (Figure 3.6 D and E) confirmed that the local chemical composition of the deposited material merely consists of manganese and oxygen.

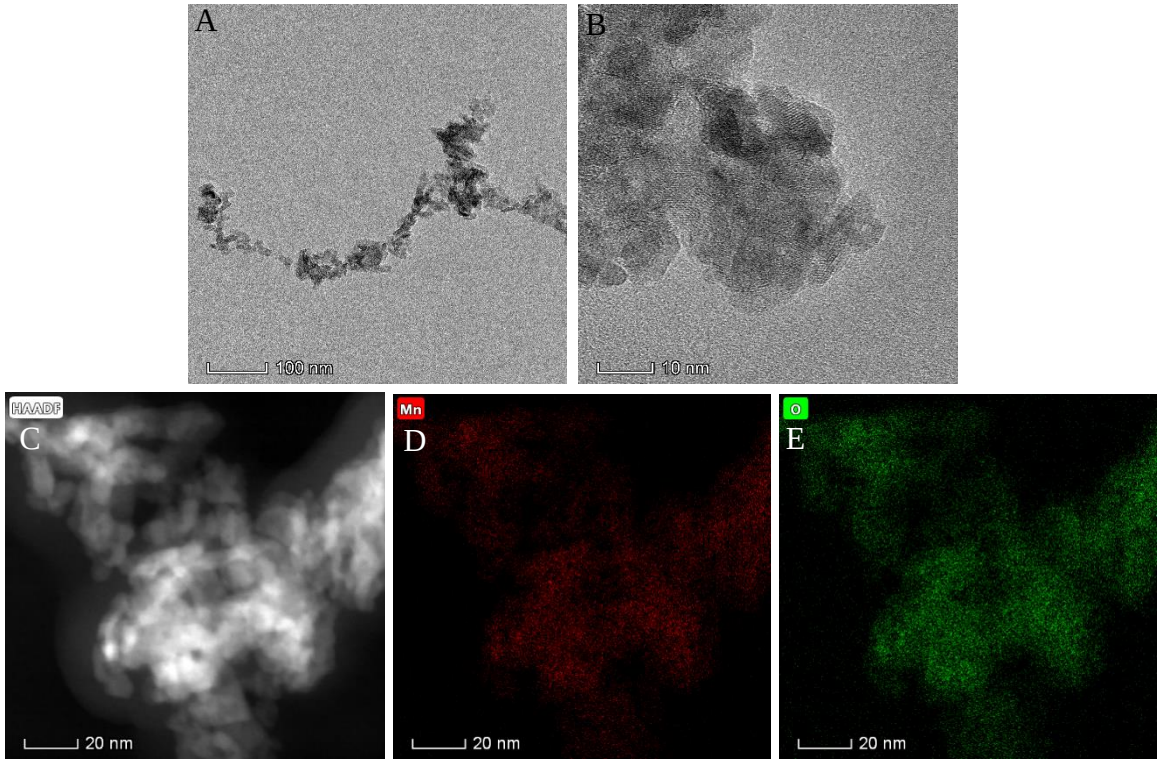

Figure 3.6. (A) Transmission electron microscopy (TEM) image, (B) High-resolution transmission electron microscopy (HRTEM) image, (C) High-angle annular dark-field (HAADF) scanning electron microscopy (STEM), and (D, E) Energy-dispersive x-ray spectroscopy (EDS) elemental mapping showing the presence of 'Mn' and 'O' in the material of $EMD_{(5,200)}$.

3.5.3. Electrochemical characterization

Cyclic voltammetry (CV). Cyclic voltammetry (CV) curves for each EMD are shown in Figure 3.7 (A-I, B-I, C-I, D-I, E-I). The CV curves obtained at a lower scan rate of 2 mV s^{-1} show a more rectangular shape with no observed redox peaks, typical of the capacitive materials. Generally, the samples undergo a few cycles (~ 20 cycles) for equilibration. Overall, the CVs of each EMD sample exhibit the quasi-rectangular shape that is typically shown by pseudo-capacitive materials. At higher scan rates (≥

10 mV s^{-1}), the shape of the CV curve deviates from the quasi-rectangular to the elliptical, indicating the deviation from ideal capacitive behavior [39,40]. This suggests pronounced limitations of the transport phenomena in the single electrode configuration at high scan rates. The charge storage mechanisms for amorphous and crystalline MnO_2 can be elaborated in two ways. The protons (H^+) or alkaline cations (M^+) can be adsorbed/desorbed on the electrode/electrolyte interface involving a non-faradaic process, along with an Mn^{4+}/Mn^{3+} charge-transfer (faradaic) process occurring at the near-surface primarily in amorphous MnO_2. The intercalation/deintercalation of protons and cations involving redox reaction is predominant in crystalline MnO_2 [39]. Since the EMD described in this chapter is less crystalline, it tends to follow the surface adsorption/desorption mechanism through the microporous structure allowing the transportation of electrons and ions. This is further confirmed by the quasi-rectangular CV curves, which do not show the pronounced cathodic/anodic peaks but indicate the electrochemical double-layer capacitor. At slow scan rates, the protons and the cations get sufficient time to transfer to the MnO_2 surface, desolvate then adsorbs, leading to more reactions at the EMD electrode surface. On the other hand, at higher scan rates, the time for adsorption is limited due to the polarization of the desolvation process of the hydrated alkaline ions. Therefore, it does not allow complete adsorption of cations hence the deviation of CV curves from the ideal behavior.

Galvanostatic charge-discharge (GCD). The GCD curves for EMD samples shown in Figure 3.7 (A-II, B-II, C-II, D-II, E-II) depict non-linear behavior, usually expected for pseudocapacitors based on the redox processes and can be complied with CV curves. Increasing the charge-discharge current applied to the electrode lowers the available capacitance. Similar to the CV curves, due to the less time for protons and cations to get adsorbed onto the surface of the material, the rate capability decreases with increasing the current density.

Specific capacitance of EMD - half-cell measurements. The specific capacitances for different EMDs were calculated using GCD measurements. The capacitance contributed by the graphite substrates as a current collector used in this study was insignificant and not comparable with the capacitance provided by the active material.

Hence, the substrate contribution does not influence the calculated specific capacitances from the charge-discharge measurements. At a current density of 1 mA cm^{-2}, the specific capacitances for $EMD_{(5,100)}$, $EMD_{(4,200)}$, $EMD_{(5,200)}$, $EMD_{(6,200)}$, $EMD_{(5,300)}$ are 77, 94, 98, 95, and 90 F g^{-1} respectively. The results indicate that the specific capacitance observed for $EMD_{(5,100)}$ is lower than the other samples. The local resistance of electrolyte ion transport can be higher with a lower surface area possessing a sea-whip morphology and lower porosity [41]. The capacitances observed in the range of 95 F g^{-1} for EMD materials deposited at a current density of 200 A m^{-2} and varying deposition times as 4, 5, and 6 hours show no significant differences. The $EMD_{(5,300)}$ also delivered comparable capacitance similar to $EMD_{(5,200)}$. However, the inefficiency and high energy consumption of the synthesis processes seem less attractive for electrowinning plant operation for EMD production. In conclusion, based on the examined process conditions, 200 A m^{-2} current density was found to be optimal for synthesizing electrolytic manganese dioxide using Pb anode and SS cathode in acidic $MnSO_4$ precursor. As investigated in this chapter, the time duration of deposition did not hugely affect the capacitances and allowed for higher mass yields with increased duration. To evaluate its durability for potential applications, the cycling stability of the $EMD_{(5,200)}$ electrode was evaluated up to 1000 charge-discharge cycles at a 1 mA current rate. Figure 3.7F shows the variation of specific capacitance against the increasing cycle number. The specific capacitance was decreased from 97.1 to 95.6 F g^{-1} after 1000 cycles representing good cyclability with 98.5% of capacitance retention. The Nyquist plots related to $EMD_{(5,200)}$ for before and after cycling are shown in Figure 3.7G. In the high-frequency region, the absence of a semicircle-like shape indicates low interfacial resistance of the EMD electrode. In the low-frequency region, a deviation of the straight line with an inclination of 45º to the Y-axis represents a pseudocapacitor behavior of the material. The corresponding equivalent circuit diagram is shown in the inset of Figure 3.7E. The charge transfer resistance R_2 is found to be decreased from 11.01 to 10.47 Ω during cycling, indicating the insertion process causes a change in the series resistance of the EMD material.

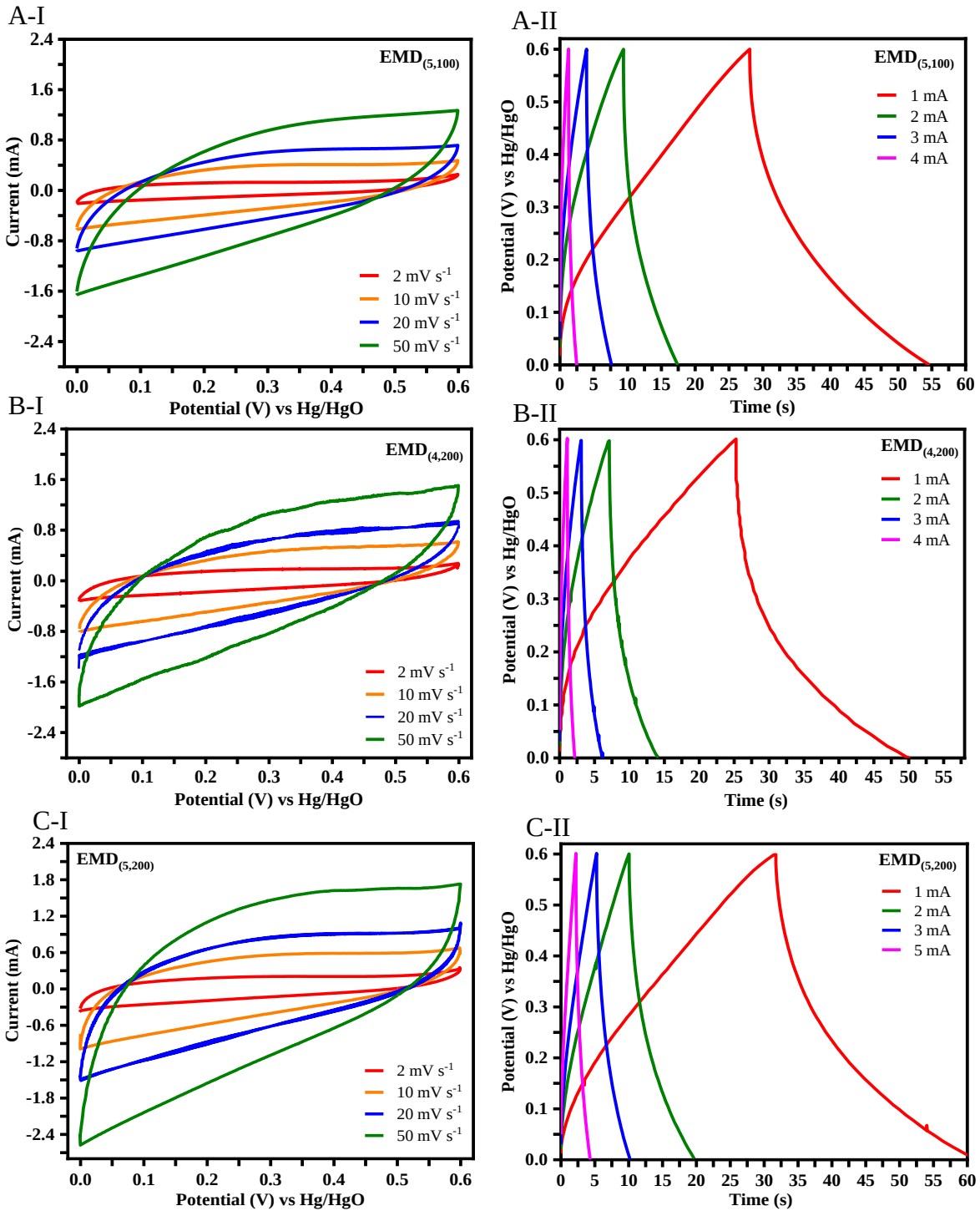
A-I
EMD(5,100)
Current (mA)
Potential (V) vs Hg/HgO
2 mV s-1
10 mV s-1
20 mV s-1
50 mV s-1
A-II
EMD(5,100)
Potential (V) vs Hg/HgO
Time (s)
1 mA
2 mA
3 mA
4 mA
B-I
EMD(4,200)
Current (mA)
Potential (V) vs Hg/HgO
2 mV s-1
10 mV s-1
20 mV s-1
50 mV s-1
B-II
EMD(4,200)
Potential (V) vs Hg/HgO
Time (s)
1 mA
2 mA
3 mA
4 mA
C-I
EMD(5,200)
Current (mA)
Potential (V) vs Hg/HgO
2 mV s-1
10 mV s-1
20 mV s-1
50 mV s-1
C-II
EMD(5,200)
Potential (V) vs Hg/HgO
Time (s)
1 mA
2 mA
3 mA
5 mA

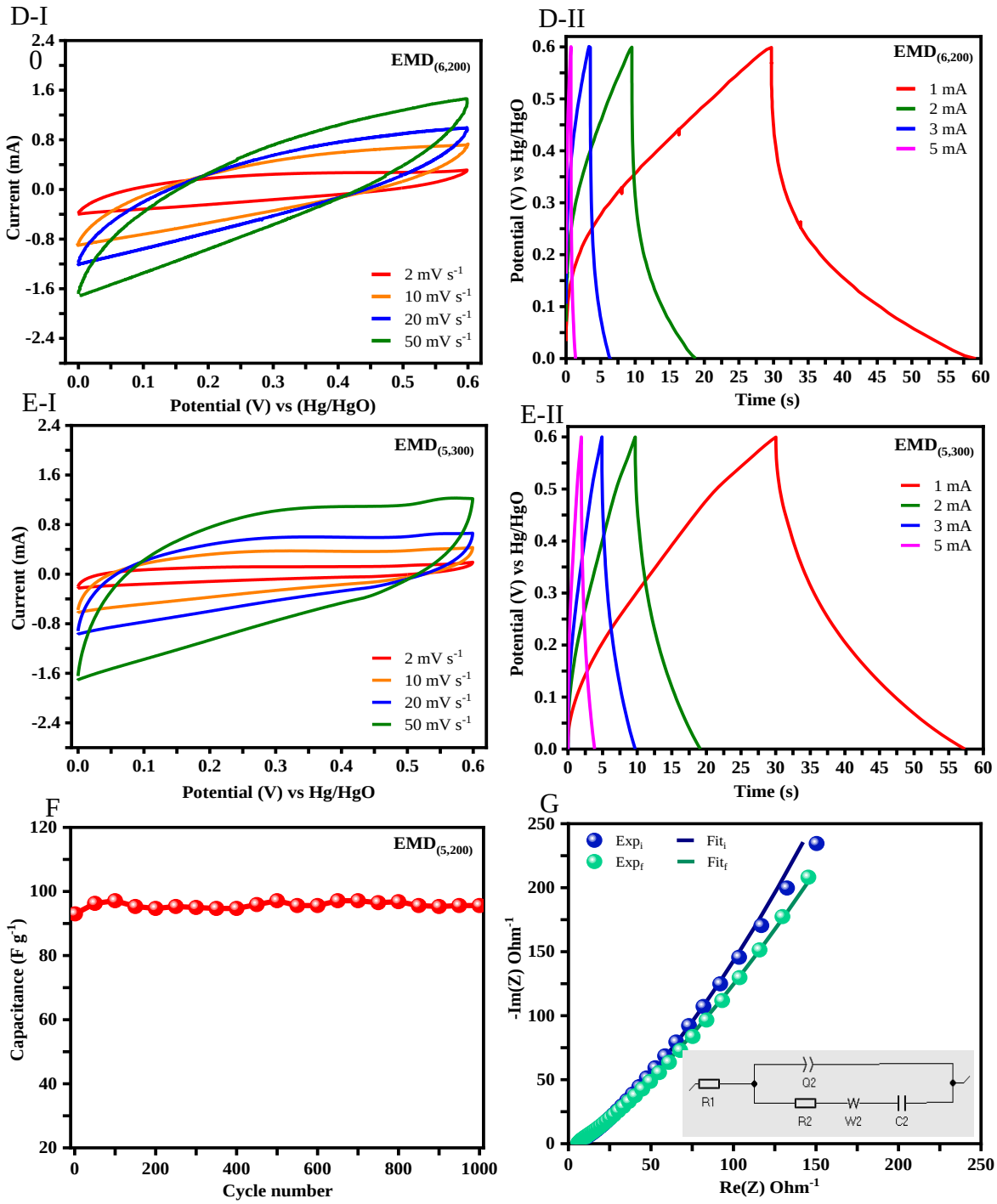

Figure 3.7 Cyclic voltammograms (CV) (A-I, B-I, C-I, D-I, E-I) and galvanostatic charge-discharge (GCD) (A-II, B-II, C-II, D-II, E-II) profiles of EMD samples tested at different scan rates and current rates, (F) Cycling stability for the $EMD_{(5,200)}$ sample in 2M NaOH for 1000 cycles (specific capacitance against cycle number), (G) Nyquist plots for $EMD_{(5,200)}$ electrode for before and after cycling (inset: the equivalent circuit used to fit the EIS data).

Faradaic and non-faradaic contributions to charge storage. The area of the CV curves represents the total charge stored via both faradaic and non-faradaic processes. The faradaic process can be either the H^+/Na^+ ion insertion from the NaOH electrolyte or the charge transfer that takes place at the surface with OH^- surface atoms as pseudocapacitance. The non-faradaic process depends on the electric double layer (EDLC) capacitance. These charge storage phenomena of the $EMD_{(5,200)}$ involve both the faradaic and non-faradaic processes, which were analyzed by using the CV data (Figure 3.7) at different scan rates according to the power-law in equation (3.8).

$$i = av^b \tag{3.8}$$

where i is measured current (mA), v is scan rate (V s^{-1}), and both a and b are adjustable parameters. The b values are determined by the slope of the plot of log i *vs.* log v, which is shown in Figure 3.8. When the b value is closer to 0.5, diffusion-controlled (faradaic) reactions dominate the charge storage, while the values closer to 1 represent the capacitive (non-faradaic) response. The maximum obtained was 0.65 at the potential of 0.45 V. This indicates that the current primarily comes from faradaic reactions. At the potentials higher or lower than 0.45 V, the values lie within 0.5 - 0.6. This explicitly shows that for the EMD discussed in this thesis, the charge storage essentially occurred via the faradic reactions and the potential range (0 - 0.6 V) studied in CV. Further investigation was carried out to identify the quantitative contributions of the faradaic and non-faradaic for the charge storage. Considering the underlying investigations from power law, the current response at a fixed potential can be expressed as a combination of two distinct mechanisms, namely, capacitive effect and diffusion-controlled insertion processes, given by the equation (3.9) [42].

$$i(V) = k_1 v + k_2 v^{1/2} \tag{3.9}$$

where, $k_1 v$ and $k_2 v^{1/2}$ correspond to the current contributions from surface capacitive effects and the diffusion-controlled intercalation process. With the known values of k_1 and k_2, the fraction of current at a specific potential can be determined. The above equation can be rearranged to equation (3.10) for analytical purposes.

$$i(V)/v^{1/2} = k_1 v^{1/2} + k_2 \quad (3.10)$$

Figure 3.8B was plotted using equation (3.10), and the k_1 and k_2 values were found from the slope and y-axis intercept point, respectively. This enabled us to distinguish the current contributions with varying scan rates, as shown in Figure 3.8C. The influence of the capacitive contribution was increased while reducing the diffusion-controlled insertion contribution with increasing scan rates. At 2, 10, 20, 50 mV s^{-1}, the calculated capacitive contributions were 10.8, 21.3, 27.6, and 37.6, respectively. The outcomes agreed with the CV profiles of EMD. The pseudocapacitive nature of the curves gradually deviated to more like elliptical with increasing scan rates due to losing the faradic contributions. Knowing the faradaic and non-faradaic contribution of the material is useful when incorporating it into a hybrid (asymmetric) capacitor, which will be discussed in the following section.

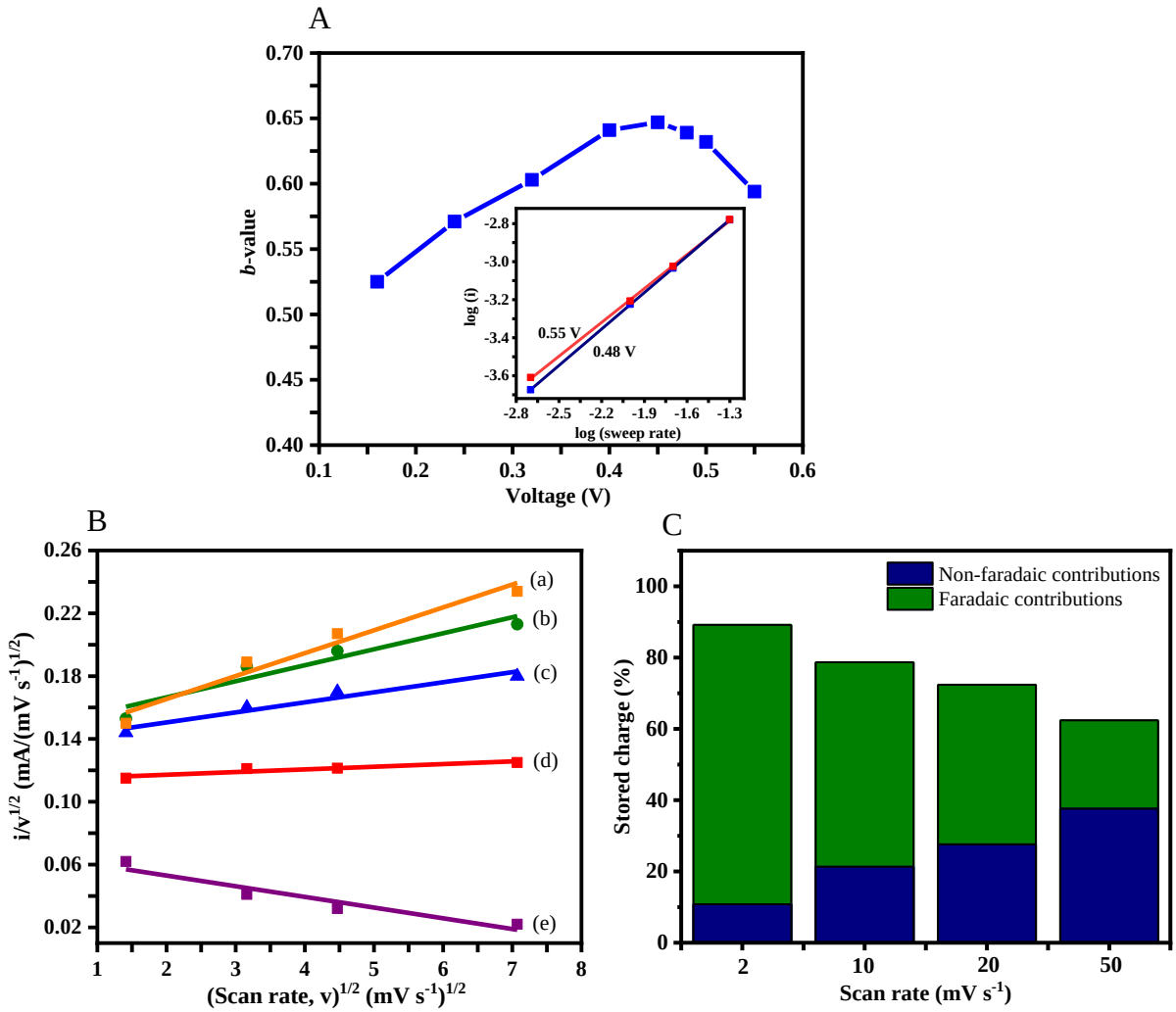

Figure 3.8 (A) b-values obtained for $EMD_{(5,200)}$ plotted against the voltage for anodic sweeps; 2, 10, 20, 50 mV s^{-1} [inset: plot of power law; log (i) as a function of log (sweep rate)], (B) Plot generated using the equation (10) for different voltage regime (a) 0.16 (b) 0.24 (c) 0.32 (d) 0.40 (e) 0.48 V and, (C) comparison of the capacitive and diffusion controlled insertion processes contribution to the total charge storage.

Aqueous hybrid (asymmetric) electrochemical capacitor (EMD/AC). The $EMD_{(5,200)}$ at the optimized synthesis conditions was further examined for the hybrid (two-electrode) configuration. The AC negative electrode capacitance was measured in the three-electrode system to balance the masses of each electrode for the two-electrode cell. AC is generally used as active electrode material in supercapacitors due to its

large surface area of ~3000 m^2 g^{-1} and high electrochemical stability, porosity, conductivity & low cost [43–46]. At a 1 mA applied current rate, activated carbon delivered 81 F g^{-1} capacitance, obtained with a ~3 mg mass loading on a 1 cm^2 area of the graphite substrate. Regardless of the higher theoretical capacitance, practically ~130 F g^{-1} in non-aqueous electrolytes and ~200 F g^{-1} in aqueous electrolytes are achievable for a single electrode system [47,48]. Figure 3.9A and B present respective CV and GCD profiles of AC tested in a 2 M NaOH aqueous electrolyte. As expected, activated carbon exhibited a rectangular-shaped CV curve and a triangular-shaped GCD curve, indicating near electrochemical double-layer capacitor behavior.

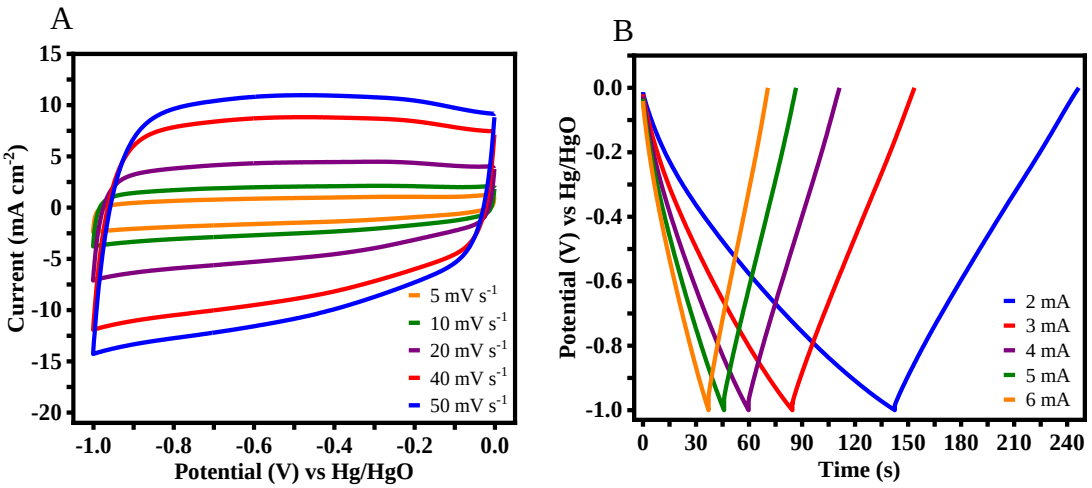

Figure 3.9 (A) Cyclic voltammetry (CV) and (B) galvanostatic charge-discharge (GCD) profiles of the commercial activated carbon (AC) measured at different scan rates and current rates.

The two-electrode consists of $EMD_{(5,200)}$, and AC electrodes are tested for specific capacitance, power, energy performance, and cycling stability. Figures 3.10 A, B, and C show the CV and GCD curves and cycling stability of the device in an aqueous NaOH electrolyte. Compared to the expensive ionic and organic electrolytes, aqueous electrolytes are much cheaper for supercapacitors, reducing the overall cost. While this has been a significant advantage, the cell voltage of symmetric capacitors of AC/AC is limited in aqueous electrolytes. Therefore, hybrid (asymmetric) capacitors are being

developed to enhance the cell voltage and energy density [49]. Initially, from the two-electrode fabricated, the capacitance was 36 F g^{-1}, which decreased to 28 F g^{-1} after 5000 cycles. The calculated energy density and power densities at 2 mA were 10 Wh kg^{-1} and 2352 W $kg^{-1,}$ respectively.

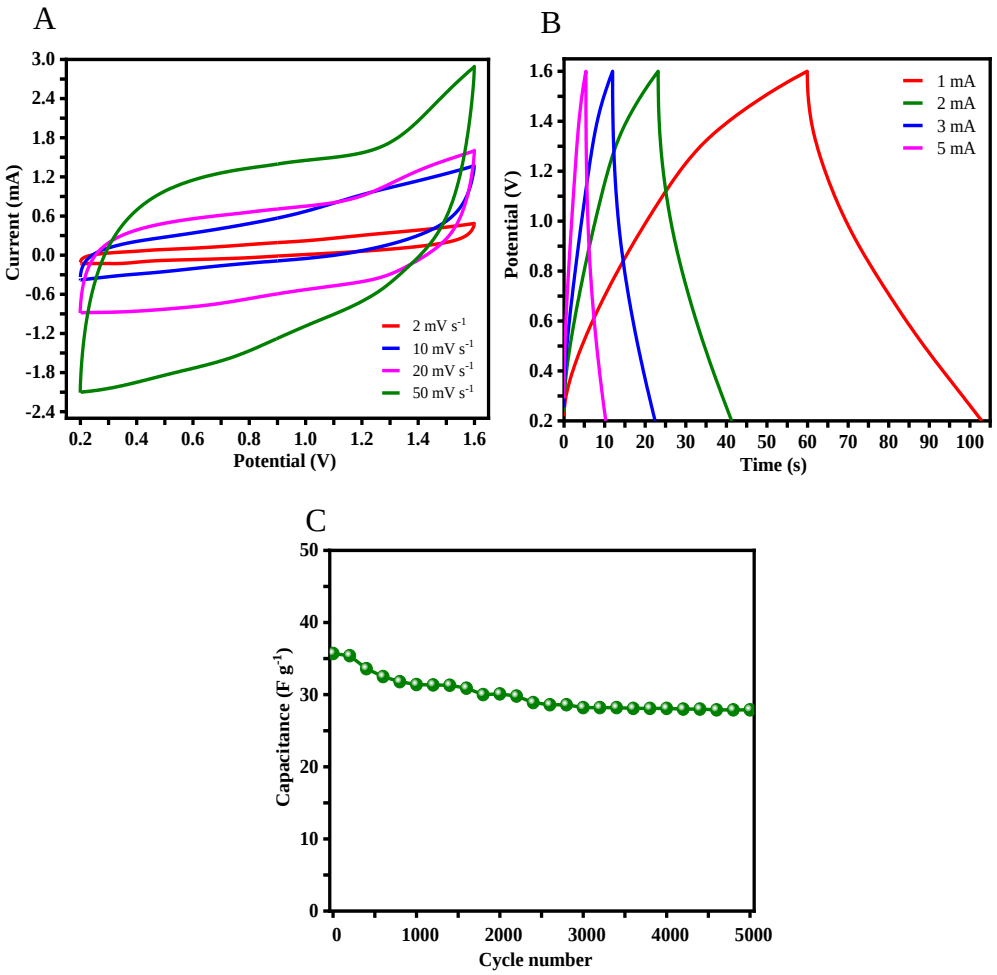

Figure 3.10 (A) Cyclic voltammograms (CV), (B) galvanostatic charge-discharge (GCD) profiles, and (C) cycling stability of the hybrid (asymmetric) capacitor EMD/AC over 5000 cycles.

Summary of electrochemical data from the literature for manganese dioxide powdered electrodes. The current energy storage performance is compared with previously reported work on MnO_2 synthesized by conventional synthesis, and their results are tabulated in Table 3.3. Various synthesis techniques to prepare MnO_2 in different crystallographic forms and their electrode compositions and current collector

used are compared to see their influences on the performance. The summary of the electrochemical data along with their supercapacitor performance values, suggests that the EMD discussed in this chapter is comparable to the MnO_2 with different crystal structures synthesized by varying chemical synthesis methods found in the literature.

Table 3.3 Summary of electrochemical data of composite manganese oxide electrodes.

Ref	Synthesis method	XRD	Electrode composition			Current collector	Surface area ($m^2 g^{-1}$)	Capacitance ($F g^{-1}$)	Electrolyte
			MnO_2 (wt%)	Carbon (wt%)	Binder (wt%)				
Lee and Goodenough [50]	Precipitation	a-MnO_2	70	25	5	Titanium welded on Tantalum foil	303	200 (2 mA cm^{-2})	2 M KCl
Toupin *et al.* [51]	Coprecipitation	a-MnO_2 Cryptomelane	80	15	5	Stainless steel grid	180 ± 30	166 (2 mV s^{-1})	0.1 M Na_2SO_4
Jeong *et al.* [52]	Reduction process	MnO_2	70	25	5	Titanium welded on Tantalum foil	391	250 (2 mA cm^{-2})	2 M NaCl
Toupin *et al.* [53]	Coprecipitation	a-MnO_2	80	15	5	Stainless steel mesh	160 ± 3	150 (5 mV s^{-1})	0.1 M Na_2SO_4
Brousse *et al.* [54]	Sol-gel	γ-MnO_2	68	25	7	Stainless steel	41	30 (5 mV s^{-1})	0.1 M K_2SO_4

						connected to a copper wire			
Zolfaghari *et al.* [55]	Sonochemistry	γ-MnO_2	60	35	5	Stainless steel grid	301	118 – 258 (5 mV s^{-1})	0.5 M Na_2SO_4
Wang *et al.* [56]	Sol-gel	γ-MnO_2	80	15	5	Nickel foam	-	317 (100 mA g^{-1})	1 M LiOH
Xu *et al.* [57]	Reduction method	a-MnO_2	70	25	5	Nickel foam	171	298.7 (5 mA)	2 M KOH
Xu *et al.* [58]	Microemulsion	a-MnO_2	70	20	10	Stainless steel mesh connected to a nickel wire	145.7	246.2 (2 mV s^{-1})	1 M Na_2SO_4
Yuan *et al.* [59]	Interface synthesis	α- and γ-MnO_2	75	20	5	Graphite	239	285 (2 mV s^{-1})	1 M Na_2SO_4
Ragupathy *et al.* [60]	Chemical mixing	δ-MnO_2	75	20	5	Stainless steel	230	250 (0.5 mA cm^{-2})	0.1 M Na_2SO_4
Du *et al.* [61]	Anodic electrodeposition under supergravity field	γ-MnO_2	85	10	5	Nickel foam	127.71	277.9 (0.5 A g^{-1})	6 M KOH
Liu *et al.* [62]	Anodic electrodeposition under supergravity field	γ-MnO_2	80	15	5	Nickel foam	-	277.34 (0.5 A g^{-1})	6 M KOH

Dupont and Donne [63]	Anodic electrodeposition	α-MnO_2	75	15	10	Stainless steel rod	123.3	110 (25 mV s^{-1})	0.5 M Na_2SO_4
Tizfahm *et al.* [64]	Cathodic pulse electrodeposition and heat treatment	α- and γ-MnO_2	80	15	5	Nickel foam	-	182 (2 A g^{-1})	1 M Na_2SO_4
Bai *et al.* [65]	Hydrothermal	Birnessite MnO_2	80	15	5	Nickel foam	706.1 cm^3 g^{-1}	178 (1 A g^{-1})	0.5 M Na_2SO_4
Dupont *et al.* [66]	Anodic electrodeposition	γ-MnO_2	80	15	5	Stainless steel	33.5	45 (25 mV s^{-1})	0.5 M Li_2SO_4
Shivakumara *et al.* [67]	Coprecipitation	a-MnO_2	85	10	5	Stainless steel foil	232	290 (0.5 A g^{-1})	0.1 M $Ca(NO_3)_2.4H_2O$
Mahadi *et al.* [68]	Anodic pulse electrodeposition	α-MnO_2	80	10	10	Nickel foam	154.03	526.44 (0.5 A g^{-1})	0.5 M Na_2SO_4
Our work - $EMD_{(5,200)}$	Anodic electrodeposition	γ-MnO_2	75	15	10	Graphite	80.4	98 (1 mA cm^{-2}/ 1 A g^{-1})	2 M NaOH

3.6. Conclusion

In this chapter, EMD materials were synthesized via the galvanostatic electrodeposition method at varying synthesis conditions. Improving scientific understanding of the anodic electrodeposition of MnO_2 represents an opportunity to guide the electrowinning plant for scalable and economic production. We have used the existing knowledge and performed studies associated with different current densities (100 - 300 A m^{-2}) and deposition time durations (4 - 6 h) and reported their consequences on the microstructure and electrochemical behavior. The morphology of EMD deposited at lower current densities was spindle-like uniform and compact deposit, while a moss-like morphology was observed due to randomly deposited particles at higher current densities. From both physicochemical and electrochemical perspectives of the tested samples, the optimum process conditions were found for the EMD produced at 200 A m^{-2} for a 5 h deposition period. The specific capacitance observed for the $EMD_{(5,200)}$ was 98 F g^{-1} tested in the three-electrode cell in an aqueous NaOH electrolyte. The charge storage process of $EMD_{(5,200)}$ was quantitatively analyzed in detail. Surface redox (faradaic) reactions are found to be the primary charge storage mechanism. The faradaic contribution became lower with increasing scan rate while the capacitive contribution became predominant. For two-electrode, at a 2 mA current rate, the cell delivered 10 Wh kg^{-1} energy density and 2352 W kg^{-1} power density, comparable to the reported values. Therefore, the electrochemically synthesized manganese dioxide material could be prominent for energy storage.

3.7. References

[1] A. Biswal, B. Chandra Tripathy, K. Sanjay, T. Subbaiah, M. Minakshi, Electrolytic manganese dioxide (EMD): a perspective on worldwide production, reserves and its role in electrochemistry, RSC Adv. 5 (2015) 58255–58283.

[2] S. Devaraj, N. Munichandraiah, Effect of crystallographic structure of MnO_2 on its electrochemical capacitance properties, J. Phys. Chem. C. 112 (2008) 4406–4417.

[3] Y. Chabre, J. Pannetier, Structural and electrochemical properties of the proton / γ-MnO_2 system, Prog. Solid State Chem. 23 (1995) 1–130.

[4] K. Kordesch, M. Weissenbacher, Rechargeable alkaline manganese dioxide/zinc batteries, 51 (1994) 61–78.

[5] D.P. Dubal, W.B. Kim, C.D. Lokhande, Galvanostatically deposited Fe: MnO2 electrodes for supercapacitor application, J. Phys. Chem. Solids. 73 (2012) 18–24.

[6] R.K. Mishra, C.S. Prajapati, P.P. Sahay, Supercapacitive performance of electrochemically synthesized nanocrystalline MnO2 films using different plating solutions: A comparative study, J. Alloys Compd. 749 (2018) 172–179.

[7] A. Singh, D. Kumar, A. Thakur, N. Gupta, V. Shinde, B.S. Saini, R. Kaur, Galvanostatic deposition of manganese oxide films for super capacitive application and their fractal analysis, Ionics (Kiel). 27 (2021) 2193–2202.

[8] M.F. Dupont, S.W. Donne, Nucleation and growth of electrodeposited manganese dioxide for electrochemical capacitors, Electrochim. Acta. 120 (2014) 219–225.

[9] X. Dai, M. Zhang, J. Li, D. Yang, Effects of electrodeposition time on a manganese dioxide supercapacitor, RSC Adv. 10 (2020) 15860–15869.

[10] M. Zhang, Y. Chen, D. Yang, J. Li, High performance MnO_2 supercapacitor material prepared by modified electrodeposition method with different electrodeposition voltages, J. Energy Storage. 29 (2020).

[11] M. Zhang, D. Yang, J. Li, Supercapacitor performances of MnO_2 and MnO_2/ reduced graphene oxide prepared with various electrodeposition time, Vacuum. 178 (2020) 109455.

[12] M. Zhang, D. Yang, J. Li, Ultrasonic and NH_4^+ assisted Ni foam substrate oxidation to achieve high performance MnO_2 supercapacitor, Appl. Surf. Sci. 541 (2021) 148546.

[13] Y. Shi, M. Zhang, L. Zhang, X. Cui, X. Zhu, J. Zhao, D. Jin, D. Yang, J. Li, Reduced graphene oxide coated manganese dioxide electrode prepared by polyvinylpyrrolidone assisted electrodeposition, Vacuum. 199 (2022) 110925.

[14] R.K. Mishra, C.S. Prajapati, R.R. Shahi, A.K. Kushwaha, P.P. Sahay, Influence of electrodeposition modes on the electrochemical performance of MnO_2 films prepared using anionic MnO^{4-} (Mn^{7+}) precursor, Ceram. Int. 44 (2018) 5710–5718.

[15] M. Kazazi, Effect of electrodeposition current density on the morphological and pseudocapacitance characteristics of porous nano-spherical MnO_2 electrode, Ceram. Int. 44 (2018) 10863–10870.

[16] R.K. Mishra, C.S. Prajapati, P.P. Sahay, Supercapacitive performance of electrochemically synthesized nanocrystalline MnO_2 films using different plating solutions: A comparative study, J. Alloys Compd. 749 (2018) 172–179.

[17] S.H. Kazemi, M.A. Kiani, M. Ghaemmaghami, H. Kazemi, Nano-architectured MnO_2 Electrodeposited on the Cu-decorated Nickel Foam substrate as Supercapacitor Electrode with Excellent Areal Capacitance, Electrochim. Acta. 197 (2016) 107–116.

[18] C.J. Clarke, G.J. Browning, S.W. Donne, An RDE and RRDE study into the electrodeposition of manganese dioxide, Electrochim. Acta. 51 (2006) 5773–5784.

[19] A. Cross, A. Morel, A. Cormie, T. Hollenkamp, S. Donne, Enhanced manganese dioxide supercapacitor electrodes produced by electrodeposition, J. Power Sources. 196 (2011) 7847–7853.

[20] A. Biswal, B.C. Tripathy, T. Subbaiah, D. Meyrick, M. Minakshi, Electrodeposition of manganese dioxide: Effect of quaternary amines, J. Solid State Electrochem. 17 (2013) 1349–1356.

[21] R. Della Noce, S. Eugénio, T.M. Silva, M.J. Carmezim, M.F. Montemor, Electrodeposition: A versatile, efficient, binder-free and room temperature

one-step process to produce MnO_2 electrochemical capacitor electrodes, RSC Adv. 7 (2017) 32038–32043.

[22] X. Hu, X. Lin, Z. Ling, Y. Li, X. Fu, Fabrication and characteristics of galvanostatic electrodeposited MnO_2 on porous nickel from etched aluminium, Electrochim. Acta. 138 (2014) 132–138.

[23] C. Fong, B.J. Kennedy, M.M. Elcombe, A powder neutron diffraction study of and manganese dioxide and of $LiMn_2O_4$, Zeitschrift Für Krist. 209 (1994) 941–945.

[24] A. Biswal, B.C. Tripathy, D. Li, M. Minakshi, Electrodeposition of Pluronic F127 assisted rod-like EMD/carbon arrays for efficient energy storage, Dalt. Trans. 44 (2015) 16446–16457.

[25] E.D. Rus, G.D. Moon, J. Bai, D.A. Steingart, C.K. Erdonmez, Electrochemical Behavior of Electrolytic Manganese Dioxide in Aqueous KOH and LiOH Solutions: A Comparative Study, J. Electrochem. Soc. 163 (2016) A356–A363.

[26] H.W. Nesbitt, D. Banerjee, Interpretation of XPS Mn(2p) spectra of Mn oxyhydroxides and constraints on the mechanism of MnO_2 precipitation, Am. Mineral. 83 (1998) 305–315.

[27] M.C. Biesinger, B.P. Payne, A.P. Grosvenor, L.W.M. Lau, A.R. Gerson, R.S.C. Smart, Resolving surface chemical states in XPS analysis of first row transition metals, oxides and hydroxides: Cr, Mn, Fe, Co and Ni, Appl. Surf. Sci. 257 (2011) 2717–2730.

[28] M. Chigane, M. Ishikawa, Manganese oxide thin film preparation by potentiostatic electrolyses and electrochromism, J. Electrochem. Soc. 147 (2000) 2246–2251.

[29] A. Ramírez, P. Hillebrand, D. Stellmach, M.M. May, P. Bogdanoff, S. Fiechter, Evaluation of MnO_x, Mn_2O_3, and Mn_3O_4 Electrodeposited Films for the Oxygen Evolution Reaction of Water, J. Phys. Chem. C. 118 (2014) 14073–14081.

[30] R.K. Sharma, A.C. Rastogi, S.B. Desu, Manganese oxide embedded polypyrrole nanocomposites for electrochemical supercapacitor, Electrochim. Acta. 53 (2008) 7690–7695.

[31] D. Briggs, N. Fairley, Valence-band x-ray photoelectron spectroscopic studies of manganese and its oxides interpreted by cluster and band structure calculations, Surf. Interface Anal. 33 (2002) 274–282.

[32] Y. Zhao, C. Li, F. Li, Z. Shi, S. Feng, One-step synthesis of highly water-dispersible Mn3O4 nanocrystals, Dalt. Trans. 40 (2011) 583–588.

[33] M. Minakshi Sundaram, A. Biswal, D. Mitchell, R. Jones, C. Fernandez, Correlation among physical and electrochemical behaviour of nanostructured electrolytic manganese dioxide from leach liquor and synthetic for aqueous asymmetric capacitor, Phys. Chem. Chem. Phys. 18 (2016) 4711–4720.

[34] A. Cross, A. Morel, A. Cormie, T. Hollenkamp, S. Donne, Enhanced manganese dioxide supercapacitor electrodes produced by electrodeposition, J. Power Sources. 196 (2011) 7847–7853.

[35] J.B. Arnott, R.P. Williams, A.G. Pandolfo, S.W. Donne, Microporosity of heat-treated manganese dioxide, J. Power Sources. 165 (2007) 581–590.

[36] M. Dupont, A.F. Hollenkamp, S.W. Donne, Electrochemically active surface area effects on the performance of manganese dioxide for electrochemical capacitor applications, Electrochim. Acta. 104 (2013) 140–147.

[37] T. Brousse, M. Toupin, R. Dugas, L. Athouël, O. Crosnier, D. Bélanger, Crystalline MnO_2 as possible alternatives to amorphous compounds in electrochemical supercapacitors, J. Electrochem. Soc. 153 (2006) A2171.

[38] P.H. Emmett, S. Brunauer, The Use of Low Temperature van der Waals Adsorption Isotherms in Determining the Surface Area of Iron Synthetic Ammonia Catalysts, J. Am. Chem. Soc. 59 (1937) 1553–1564.

[39] Q. Qu, P. Zhang, B. Wang, Y. Chen, S. Tian, Y. Wu, R. Holze, Electrochemical performance of MnO_2 nanorods in neutral aqueous

electrolytes as a cathode for asymmetric supercapacitors, J. Phys. Chem. C. 113 (2009) 14020–14027.

[40] Q. Liu, J. Yang, R. Wang, H. Wang, S. Ji, Manganese dioxide core-shell nanostructure to achieve excellent cycling stability for asymmetric supercapacitor applications, RSC Adv. 7 (2017) 33635–33641.

[41] J. Yan, A. Sumboja, X. Wang, C. Fu, V. Kumar, P.S. Lee, Insights on the fundamental capacitive behavior: A case study of MnO_2, Small. 10 (2014) 3568–3578.

[42] J. Wang, J. Polleux, J. Lim, B. Dunn, Pseudocapacitive contributions to electrochemical energy storage in TiO2 (anatase) nanoparticles, J. Phys. Chem. C. 111 (2007) 14925–14931.

[43] M. Endo, T. Takeda, Y.J. Kim, K. Koshiba, K. Ishii, High Power Electric Double Layer Capacitor (EDLC's); from Operating Principle to Pore Size Control in Advanced Activated Carbons, Carbon Sci. 1 (2001) 117–128.

[44] M. Nakamura, M. Nakanishi, K. Yamamoto, Influence of physical properties of activated carbons on characteristics of electric double-layer capacitors, J. Power Sources. 60 (1996) 225–231.

[45] T. He, J. Nie, J. Ying, K. Cai, Investigation of Imbalanced Activated Carbon Electrode Supercapacitors, Int. J. Electrochem. 2015 (2015) 801217.

[46] A. Jänes, H. Kurig, E. Lust, Characterisation of activated nanoporous carbon for supercapacitor electrode materials, Carbon N. Y. 45 (2007) 1226–1233.

[47] K. Jurewicz, C. Vix-Guterl, E. Frackowiak, S. Saadallah, M. Reda, J. Parmentier, J. Patarin, F. Béguin, Capacitance properties of ordered porous carbon materials prepared by a templating procedure, J. Phys. Chem. Solids. 65 (2004) 287–293.

[48] J. Chmiola, G. Yushin, Y. Gogotsi, C. Portet, P. Simon, P.L. Taberna, Anomalous increase in carbon at pore sizes less than 1 nanometer, Science (80-.). 313 (2006) 1760–1763.

[49] S. Kaipannan, S. Marappan, Fabrication of 9.6 V High-performance Asymmetric Supercapacitors Stack Based on Nickel Hexacyanoferrate-derived $Ni(OH)_2$ Nanosheets and Bio-derived Activated Carbon, Sci. Rep. 9 (2019) 1–14.

[50] H.Y. Lee, J.B. Goodenough, Supercapacitor Behavior with KCl Electrolyte, J. Solid State Chem. 144 (1999) 220–223.

[51] M. Toupin, T. Brousse, D. Bélanger, Influence of microstucture on the charge storage properties of chemically synthesized manganese dioxide, Chem. Mater. 14 (2002) 3946–3952.

[52] Y.U. Jeong, A. Manthiram, Nanocrystalline Manganese Oxides for Electrochemical Capacitors with Neutral Electrolytes, J. Electrochem. Soc. 149 (2002) A1419.

[53] M. Toupin, T. Brousse, D. Bélanger, Charge storage mechanism of MnO_2 electrode used in aqueous electrochemical capacitor, Chem. Mater. 16 (2004) 3184–3190.

[54] T. Brousse, M. Toupin, R. Dugas, L. Athouël, O. Crosnier, D. Bélanger, Crystalline MnO_2 as Possible Alternatives to Amorphous Compounds in Electrochemical Supercapacitors, J. Electrochem. Soc. 153 (2006) A2171.

[55] A. Zolfaghari, F. Ataherian, M. Ghaemi, A. Gholami, Capacitive behavior of nanostructured MnO_2 prepared by sonochemistry method, Electrochim. Acta. 52 (2007) 2806–2814.

[56] X. Wang, A. Yuan, Y. Wang, Supercapacitive behaviors and their temperature dependence of sol-gel synthesized nanostructured manganese dioxide in lithium hydroxide electrolyte, J. Power Sources. 172 (2007) 1007–1011.

[57] M.W. Xu, D.D. Zhao, S.J. Bao, H.L. Li, Mesoporous amorphous MnO_2 as electrode material for supercapacitor, J. Solid State Electrochem. 11 (2007) 1101–1107.

[58] C. Xu, B. Li, H. Du, F. Kang, Y. Zeng, Electrochemical properties of

nanosized hydrous manganese dioxide synthesized by a self-reacting microemulsion method, J. Power Sources. 180 (2008) 664–670.

[59] C.Z. Yuan, B. Gao, L.H. Su, X.G. Zhang, Interface synthesis of mesoporous MnO_2 and its electrochemical capacitive behaviors, J. Colloid Interface Sci. 322 (2008) 545–550.

[60] P. Ragupathy, D.H. Park, G. Campet, H.N. Vasan, S.J. Hwang, J.H. Choy, N. Munichandraiah, Remarkable capacity retention of nanostructured manganese oxide upon cycling as an electrode material for supercapacitor, J. Phys. Chem. C. 113 (2009) 6303–6309.

[61] J. Du, G. Shao, X. Qin, G. Wang, Y. Zhang, Z. Ma, High specific surface area MnO_2 electrodeposited under supergravity field for supercapacitors and its electrochemical properties, Mater. Lett. 84 (2012) 13–15.

[62] S. Liu, Y. Liu, W. Song, J. Song, C. Wang, G. Shao, X. Qin, Flocky MnO_2/carbon nanotube composites electrodeposited under supergravity field for supercapacitors, J. Solid State Electrochem. 19 (2015) 1321–1329.

[63] M.F. Dupont, S.W. Donne, Separating the Faradaic and Non-Faradaic Contributions to the Total Capacitance for Different Manganese Dioxide Phases, J. Electrochem. Soc. 162 (2015) A5096–A5105.

[64] J. Tizfahm, M. Aghazadeh, M.G. Maragheh, M.R. Ganjali, P. Norouzi, F. Faridbod, Electrochemical preparation and evaluation of the supercapacitive performance of MnO_2 nanoworms, Mater. Lett. 167 (2016) 153–156.

[65] X. Bai, W. Zhu, W. Yao, T. Duan, Hydrothermal preparation of CS@MnO_2 with different morphologies for supercapacitor electrode materials, Mater. Lett. 210 (2018) 329–332.

[66] M.F. Dupont, M. Forghani, A.P. Cameron, S.W. Donne, Effect of electrolyte cation on the charge storage mechanism of manganese dioxide for electrochemical capacitors, Electrochim. Acta. 271 (2018) 337–350.

[67] S. Shivakumara, N. Munichandraiah, In-situ preparation of nanostructured α-

MnO_2/polypyrrole hybrid composite electrode materials for high performance supercapacitor, J. Alloys Compd. 787 (2019) 1044–1050.

[68] F. Mahdi, M. Javanbakht, S. Shahrokhian, Anodic pulse electrodeposition of mesoporous manganese dioxide nanostructures for high performance supercapacitors, J. Alloys Compd. 887 (2021) 161376.

Link to the next chapter

The electrodeposition conditions were investigated and optimized to synthesize the EMD via anodic electrodeposition in the previous chapter 3. The parameters were set to obtain optimal energy storage performance of EMD in supercapacitors. However, the determined specific capacitance of the pristine EMD was relatively lower to be utilized for any practical applications and should be improved. Thus, the established method in the previous chapter 3 has been followed in chapter 4 for further modifications in electrodeposited material to enhance its electrochemical performance.

In chapter 4, we have used a bio-polymer Alginic acid additive in the electrolytic bath studied at its varying concentrations to modify the EMD characteristics. The newly introduced molecular level interactions to the electrolyte species due to the addition of the bio-polymer were examined by computational modeling, which supported the experimental observations in the EMD deposits having varying morphologies. Compared to the pristine EMD in the hybrid capacitor, the bio-polymer modified EMD exhibited higher specific capacitance and energy densities, further improving its potential application in hybrid capacitors.

Chapter 4 Alginate biopolymer effect on the electrodeposition of manganese dioxide

This chapter is published as:

Alginate Biopolymer Effect on the Electrodeposition of Manganese Dioxide on Electrodes for Supercapacitors

Kethaki Wickramaarachchi, Manickam Minakshi Sundaram, David J. Henry, and Xiangpeng Gao

ACS Applied Energy Materials 2021 4 (7), 7040-7051

DOI: https://doi.org/10.1021/acsaem.1c01111

Impact factor: 6.024

ACS APPLIED ENERGY MATERIALS

www.acsaem.org Article

Alginate Biopolymer Effect on the Electrodeposition of Manganese Dioxide on Electrodes for Supercapacitors

Kethaki Wickramaarachchi, Manickam Minakshi Sundaram,* David J. Henry, and Xiangpeng Gao

Cite This: ACS Appl. Energy Mater. 2021, 4, 7040−7051 Read Online

ACCESS | Metrics & More | Article Recommendations | Supporting Information

ABSTRACT: Electrolytic manganese dioxide (EMD) synthesized from different electrolytic baths with varying biopolymer additive concentrations has been investigated for application as an electrochemical supercapacitor. Alginic acid, also termed "alginate", is a widely used biopolymer for various biological applications due to its physicochemical properties. Here, the EMD material synthesized with alginate crosslinking was introduced in the field of electrochemistry for supercapacitors. Different EMD and alginate composites were characterized to find the trade-off between the biopolymer content in the bath and the energy storage capability. Compared to the pristine EMD, the EMD composites at all of the alginate concentrations influenced both the physical and the electrochemical storage properties of the materials. The presence of alginate in the solution at higher concentrations altered the morphology from spindle-shaped to cactus-shaped with flutes. Rearranged morphology and enhanced particle size are attributed to the ability of the alginate to act as a template for binding the Mn^{2+} ions on the substrate in a relatively ordered and widely distributed manner. The EMD composite delivered 5 times higher capacitance (487 F g^{-1}) than the pristine EMD at a current density of 1 mA cm^{-2} in a three-electrode system using a 2 M NaOH aqueous electrolyte. When the EMD composite was coupled with activated carbon, the asymmetric device exhibited 52 F g^{-1} capacitance at a current density of 2 mA cm^{-2} while giving excellent capacitance retention (94%) over 5000 cycles. The molecular dynamics simulation model supported the influence of alginate on ion−polymer interactions in the electrolytic bath. The simulations showed that the alginate provides a template for binding Mn^{2+} ions in a relatively ordered manner. It could assist the EMD/Alg composite growth in a more favorable condition for energy storage applications.

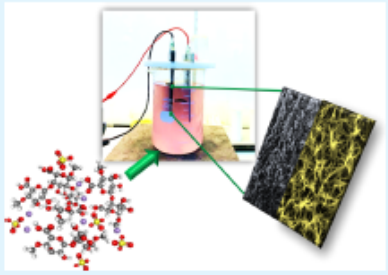

KEYWORDS: *manganese dioxide, electrodeposition, activated carbon, biopolymer, energy storage, alginate, molecular dynamics*

INTRODUCTION

High atmospheric levels of CO_2 and other greenhouse gases due to the significant use of fossil fuels are a concern with severe consequences to the earth. To enable a transition to clean energy utilizing renewable yet intermittent energy sources such as solar and wind power requires energy storage to guarantee consistent energy supplies. Recently, significant research has been focused on electrochemical energy devices for environmentally friendly operation and flexible energy storage to meet the supply and demand of electrical energy.

Among the available options, rechargeable batteries and electrochemical capacitors (ECs) are currently the best candidates. High specific energy density and power density are essential aspects of an efficient energy storage device accompanied by low-cost and environmentally friendly electrode materials. Supercapacitors (SCs) are a class of energy storage devices offering performance characteristics between ECs and rechargeable batteries.[1] Consequently, SCs have become widely accepted in energy management with their excellent combination of high-power delivery (5−10 kW kg^{-1}) and reasonable energy density capability (20−30 Wh kg^{-1}). In comparison, rechargeable batteries have larger energy densities (30−260 Wh kg^{-1}) but lower power values (0.1−5 kW kg^{-1}).[2]

Compared with the commonly investigated electrode materials for energy storage, manganese dioxide (MnO_2) cathode is abundant, eco-friendly, cost-effective, and used in both primary and secondary batteries available in the market.[3,4] More recently, there has been a dramatic increase in the research on manganese dioxides for SC applications as pseudocapacitive materials.[5−7] The SCs are classified as two types based on the charge storage reactions: (a) electric double-layer capacitors (EDLCs) employing non-faradic charge accumulation at an electrode−electrolyte interface, and (b) pseudocapacitors employing a faradic (charge transfer) redox reaction across the interface through a diffusion process

Received: April 16, 2021
Accepted: June 18, 2021
Published: July 4, 2021

ACS Publications © 2021 American Chemical Society

https://doi.org/10.1021/acsaem.1c01111
ACS Appl. Energy Mater. 2021, 4, 7040−7051

Author contribution

Contributor	Contribution (%)	Nature of contribution
Kethaki Wickramaarachchi	70	Conceptualization, experimentation, data collection, analysis and interpretation, drafting and critical revision of the manuscript.
Manickam Minakshi	30	Conceptualization, interpretation of data, critical revision of the manuscript.
David J. Henry		Theoretical insights and data interpretation.
Xiangpeng Gao		Critical revision of the manuscript.

4.1 Abstract

Electrolytic manganese dioxide (EMD) synthesized from different electrolytic baths with varying biopolymer additive concentrations has been investigated for application as an electrochemical supercapacitor. Alginic acid, also termed “alginate”, is a widely used biopolymer for various biological applications due to its physicochemical properties. Here, the EMD material synthesized with alginate crosslinking was introduced in the field of electrochemistry for supercapacitors. Different EMD and alginate composites were characterized to find the trade-off between the biopolymer content in the bath and the energy storage capability. Compared to the pristine EMD, the EMD composites at all of the alginate concentrations influenced both the physical and the electrochemical storage properties of the materials. The presence of alginate in the solution at higher concentrations altered the morphology from spindle-shaped to cactus-shaped with flutes. Rearranged morphology and enhanced particle size are attributed to the ability of the alginate to act as a template for binding the Mn^{2+} ions on the substrate in a relatively ordered and widely distributed manner. The EMD composite delivered 5 times higher capacitance (487 F g^{-1}) than the pristine EMD at a current density of 1 mA cm^{-2} in a three-electrode system using a 2 M NaOH aqueous electrolyte. When the EMD composite was coupled with activated carbon, the hybrid device exhibited 52 F g^{-1} capacitance at a current density of 2 mA cm^{-2} while giving excellent capacitance retention (94 %) over 5000 cycles. The molecular dynamics simulation model supported the influence of alginate on ion−polymer interactions in the electrolytic bath. The simulations showed that the alginate provides a template for binding Mn^{2+} ions in a relatively ordered manner. It could assist the EMD/Alg composite growth in a more favorable condition for energy storage applications.

4.2 Introduction

High atmospheric CO_2 and other greenhouse gases due to the significant use of fossil fuels are a concern with severe consequences to the earth. To enable a transition to clean energy utilizing renewable yet intermittent energy sources such as solar and wind power requires energy storage to guarantee consistent energy supplies. Recently,

significant research has been focused on electrochemical energy devices for environmentally friendly operation and flexible energy storage to meet the supply and demand of electrical energy. Rechargeable batteries and electrochemical capacitors (ECs) are currently the best candidates among the available options. High specific energy density and power density are essential aspects of an efficient energy storage device accompanied by low-cost and environmentally friendly electrode materials. Supercapacitors (SCs) are a class of energy storage devices offering performance characteristics between ECs and rechargeable batteries.[1] Consequently, SCs have become widely accepted in energy management with their excellent combination of high-power delivery (5 - 10 kW kg^{-1}) and reasonable energy density capability (20 - 30 Wh kg^{-1}). In comparison, rechargeable batteries have larger energy densities (30 - 260 Wh kg^{-1}) but lower power values (0.1 - 5 kW kg^{-1}).[2]

Compared with the commonly investigated electrode materials for energy storage, manganese dioxide (MnO_2) cathode is abundant, eco-friendly, cost-effective, and used in both primary and secondary batteries available in the market.[3,4] More recently, there has been a dramatic increase in the research on manganese dioxides for SC applications as pseudocapacitive materials.[5–7] The SCs are classified as two types based on the charge storage reactions: (a) electric double-layer capacitors (EDLCs) employing non-faradic charge accumulation at an electrode−electrolyte interface, and (b) pseudocapacitors employing a faradic (charge transfer) redox reaction across the interface through a diffusion process of charge storage ions. Manganese dioxide can be either natural (NMD) or synthesized via chemical methods (CMD) or by electrodeposition (EMD).[8–10] The electrolytic manganese dioxide has advantages over other types due to its low production cost, scalable production, electrochemical activity, and high purity.[11] Electrolytic manganese dioxide can be formed from the direct electrolysis of an aqueous bath containing manganese sulfate in sulfuric acid. Electrodeposition is a simple technique that could be conducted with moderate experimental conditions to tune the material properties such as particle size, density, and morphology,[12,13] which greatly influence the electrochemical energy storage properties.[14] Based on the applied voltage or current, the deposition techniques can be categorized as galvanostatic (GS), potentiostatic (PS), and cyclic voltammetry (CV). Despite the advantage of producing scalable EMD, the lack of structural stability for

the deposited EMD results in significant energy storage losses over long-term cycling when used as an electrode in SC applications. Therefore, additives/dopants are commonly introduced as foreign materials in the electrolytic bath to improve the surface morphology, electrochemical cyclability, structural stability, and flexibility of the deposited manganese dioxides.[15] To date, different composite electrodes of EMD with other metal dopants (Ni^{2+}, Co^{2+}, Fe^{2+}, Pb^{2+}, Zn^{2+}), polymers (chitosan, polyaniline, poly(o-phenylenediamine)), and surfactants (cetyltrimethylammonium bromide (CTAB), sodium n-dodecyl benzene sulfonate (SDBS), etc.) additives have been reported by many researchers.[16,17]

In this chapter, alginic acid crosslinked with EMD has been newly introduced, and its electrochemical properties were explored. This biopolymer is of interest in this chapter due to its excellent properties such as compatibility with hydrophobic and hydrophilic molecules, nontoxicity, tunable adhesiveness, and mechanical stability. A widely used natural polysaccharide, alginic acid (Figure 4.1), also termed “alginate”, is an anionic, biopolymer.

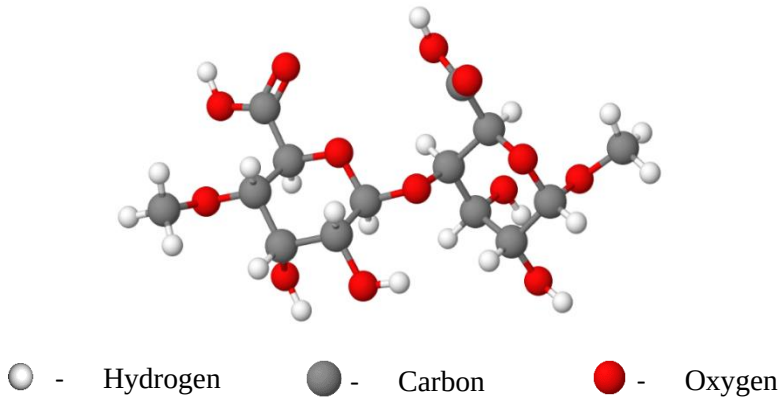

Figure 4.1 Chemical structure of the Alginic acid polymer.

Alginate is naturally created from brown algae, where it is present in the algae cell walls and intercellular spaces. It has an essential role in providing flexibility and strength to marine plants. Besides, alginate plays a pivotal part in several industrial applications such as biomedical, food, water treatment,[18] and catalysis[19] due to its biocompatibility, low toxicity, and relatively low cost.[20] The unique nature of alginate in facilitating film formation and spinning of fibers is also well known.[21] Alginate is a

block copolymer composed of (1,4)-linked β-D-mannuronate (M) and α-L-guluronate (G) residues. The G-blocks of alginate participate in intermolecular crosslinking with divalent cations, while M-blocks are responsible for the shape of the extended polymer chain. At a low pH, an increase in viscosity leads the alginate to undergo mild gelling, allowing for encapsulation of other species; for instance, Ca^{2+} can replace some of the H^+ and Na^+ in the alginate to form a calcium alginate gel. The molecule has highly reactive carboxylic acid groups that could be modified for various applications to act as functional materials. Therefore, the biopolymer alginate has been used as an additive in situ during the electrodeposition of manganese dioxide from the manganese sulfate electrolyte bath. The importance and originality of this chapter are that it explores the effect of alginate concentration on energy storage and cyclic stability through experimental analysis supported by molecular dynamics modeling. The molecular dynamics simulation was conducted to obtain further insights into the role of alginate in electrodeposition. Two different models were built of a fully protonated form and a model in which the carboxylic acids were deprotonated for comparison.

4.3. Materials and methods

4.3.1. Chemicals

All of the precursors and other chemicals used in the experiments were bought from commercial suppliers and used without further purification. Deionized (DI) water was used for solution preparation. $MnSO_4 \cdot H_2O$ (99.5 %), concentrated H_2SO_4 (98 %), and alginic acid as biopolymer additive were used as precursors in electrodeposition. Hereafter, the term “Alg” will be used to refer to alginic acid/alginate in this chapter.

4.3.2. Electrodeposition of MnO_2 with varied concentrations of Alg biopolymer

The concentrations of Mn^{2+} and H_2SO_4 used in the electrolytic bath were 0.9 and 0.25 M, respectively. Alginate is not readily dissolved in the electrolyte solution used in the experiment. Therefore, Alg was homogeneously dispersed in DI water by stirring. From a prepared stock solution, the appropriate amount of additive was added to the

electrolytic bath and stirred constantly throughout the experiment. The electrolytic solutions were prepared at different concentrations of Alg as 0.0, 0.1, 0.25, 0.5, and 1.0 g l^{-1}. The sample with a 0.0 g l^{-1} concentration of Alg is termed pristine EMD. Each sample was anodically deposited for 5 h on a lead (Pb) substrate with stainless steel (SS) stands as the cathode regardless of the additive concentration. A constant current of 200 A m^{-2} was applied, and the electrolytic bath was kept at 95 °C throughout the experiment. The electrolytic bath was covered with a poly(tetrafluoroethylene) (PTFE) lid to minimize evaporation, and the solution was continuously agitated to keep uniform conditions. At the end of the experiment, the Pb substrate was taken out and thoroughly washed with running DI water to remove entrained electrolyte and then kept in the oven for drying overnight. Later, the electrodeposited material was scraped off the electrode surface cautiously without damaging the anode electrode to avoid Pb particle contamination. The collected EMD flakes were further rinsed with DI water to make them electrolyte-free, and the resultant flakelike particles were dried in an oven at 80 °C for 12 h and termed "active material".

4.3.3. Material characterization

The surface morphology of the electrodeposited materials was observed by field emission scanning electron microscopy (FE-SEM, TESCAN CLARA). Mid-infrared (MIR) analysis was carried out at the infrared facility at the Australian Synchrotron, Melbourne. The beamline was coupled to a Bruker IFS 125/HR Fourier transform (FT) spectrometer. The data was acquired in single reflection diamond attenuated total reflection (ATR) transmission mode within 1970−400 cm^{-1} in the mid-IR using a Si:B photodetector. A background spectrum was first collected. Subsequently, the sample spectra were recorded with 50 scans and subtracted from the background spectrum. All data collection was performed using OPUS software version 8.0.19. X-ray diffraction was carried out to determine the crystal structure of the synthesized EMD samples using Cu Kα radiation (1.5418 Å) operated at 28 kV and 10 mA. Neutron diffraction data (NPD) were collected on the Echidna high-resolution powder diffractometer at the Open Pool Australian Lightwater (OPAL) facility located at the

Australian Nuclear Science and Technology Organisation (ANSTO), Australia. Data were collected in the 2θ range of 4 - 164° using 1.622 Å wavelength. The Rietveld refinement for NPD data was performed using crystallography data analysis software, GSAS-II. The surface area and pore structure of the EMD samples were characterized by adsorption−desorption isotherms of N2 at 77 K using the equipment ASAP 2010 MicroPore System (Micromeritics). The specific surface area was calculated by the Brunauer−Emmett−Teller (BET) method, and the pore volume vs. the pore diameter was determined by the Barrett−Joyner−Halenda (BJH) method.

4.3.4. Electrochemical (supercapacitor) studies

The synthesized EMD as active materials, either pristine EMD or EMD/Alg, was mixed with acetylene black and polyvinylidene difluoride (PVDF) binder in a mass ratio of 75:15:10 in N-methyl-2-pyrrolidone (NMP) solvent and made into a slurry for electrode coating. A 1 cm^2 area of a graphite current collector was coated and dried at 80 °C for 12 h. The active mass coated on the graphite was determined by weighing before and after the coating. Cyclic voltammetry (CV), galvanostatic charge-discharge (GCD), and electrochemical impedance spectroscopy (EIS) tests were carried out in a three-electrode system (half-cell measurements) with Hg/HgO reference and Pt wire counter electrodes in 2 M NaOH aqueous electrolyte using a BioLogic SP150 potentiostat. Half-cell measurements on CV and GCD were recorded at different sweep rates (2, 5, 10, and 20 mV s^{-1}) and current densities (0.5, 1, 2, and 3 mA cm^{-2}). EIS was performed for EMD/Alg single electrode at a frequency range of 10 mHz to 100 kHz with 10 mV amplitude. The impedance for real and imaginary parts was collected with ten points per decade for each frequency value. A hybrid capacitor comprising EMD/Alg coupled with activated carbon (AC) electrode was used to study the full-cell capacitance, cycling stability, and energy and power densities. The equations used in the calculation of specific capacitance from CV measurements ($C_{s,CV}$, Fg^{-1}), specific capacitance from GCD measurements ($C_{s,CD}$, Fg^{-1}), energy density (E, Wh kg^{-1}), and power density (P, W kg^{-1}) obtained from the charge−discharge data of half-cell, and full-cell capacitor studies are given by the equations 4.1 - 4.4.

$$C_{s,CV} = \int_{0}^{0.6} \frac{i\, dv}{2V_s m \Delta v} = \frac{Q}{m \Delta v} \quad (4.1)$$

$$C_{s,CD} = \frac{I\, \Delta t}{m\, \Delta v} \quad (4.2)$$

$$E = \frac{1}{2} C_{s,CD} \frac{\Delta v^2}{3.6} \quad (4.3)$$

$$P = \frac{E}{\Delta t} \times 3600 \quad (4.4)$$

4.3.5. Computational studies of the electrolyte solution in electrodeposition

Molecular dynamics simulations were performed to explore the nature of the interactions between the different species in the solution. The high molecular weight and low concentration of the Alg in the experiments meant that it was not possible to exactly recreate the experimental concentrations in the simulation, as this would have led to a computationally intractable simulation cell. However, the simulations used the experimental concentrations for Mn^{2+} (0.9 M), SO_4^{2-} (1.15 M), and H^+ (0.5 M), but the Alg was simulated by two fragments of polymer that were seven repeat units long, and the concentration was 1.5×10^{-4} M. The fully protonated form of Alg was used to represent the polymer at pHs below pKa (referred to as "Alg_p"). A second model was prepared in which the carboxylic acids were deprotonated (referred to as "Alg_{dp}"). The modeling framework for both the surface and molecules was developed using Materials Studio V 6.1.2. All species were represented by fully atomistic models. Each simulation was placed in a unit cell with dimensions $40.9 \times 40.9 \times 40.9$ Å^3 under 3D periodic boundary conditions.

The potential energy for each simulation was calculated using the COMPASS force field[22], which has previously been shown to perform well in describing the interactions between condensed hydrophilic and hydrophobic species.[23–25] Electrostatic interactions were calculated using the Ewald procedure, while van der Waals interactions were calculated with an atom-based procedure using a 12.50 Å cutoff, a spline width of 1.00 Å, a buffer of 0.50 Å, and a long-range tail correction. The modeled systems were initially energy minimized using the conjugate gradient procedure, with a convergence criterion of 0.04 kJ mol^{-1}. Molecular dynamics simulations were performed in the canonical ensemble (NVT, constant number of atoms (N), volume (V), and temperature (T)), equilibrated for 500 picoseconds (ps), followed by data acquisition for 4500 ps using 1.0 femtosecond (fs) time steps. The temperature was maintained at 298 K using the Andersen thermostat[26] with a collision ratio of 1.0.

4.4. Results and discussion

4.4.1. Physicochemical characterization

Morphology. The samples were first characterized by FESEM analysis to examine the morphologies of the EMD/Alg composites and compare them with the pristine EMD. The hierarchical structure of EMD is attributed to the electrodeposition synthesis of the MnO_2 material. The pristine EMD shows a small spindle-shaped particle (Figure 4.2A). However, in the magnified image (Figure 4.2B), ricelike grains associated with a star-shaped pattern branching out from the cluster of grains on the surface are seen. The FE-SEM images show that the grains have an average length of 100 - 150 nm with a width of 10 - 20 nm range. For the electrolytic bath with Alg added (EMD/Alg composite), both the shape and the thickness of the particles are changed (Figure 4.2 C−J). It is evident from the images that both pristine EMD and the EMD/Alg composites exhibit two different morphologies. The individual shape and thickness of the EMD particles changed significantly with the concentration of the Alg in the bath. At a lower concentration of 0.1 and 0.25 g l^{-1}, the Alg ions electrostatically interact with the surface of MnO_2, indicating the evolution in surface morphology (Figure 4.2

C−F) due to the biopolymer additive. At a concentration of 0.5 g l^{-1}, the increase in the thickness and elongation of the needlelike spines of the cactus-shaped (Figure 4.2G) particle indicates that the Alg is crosslinked onto the surface layer of electrodeposited MnO_2. The chelating interaction between the metal cation and the carboxylate groups seems viable in the gelation/crosslinking process. The magnified FE-SEM image for the EMD/Alg composites in Figure 4.2H shows cactus-shaped particles having flutes with an average length of 300 - 400 nm, which are well arranged to provide uninterrupted pathways for transporting ions to/from the electrolyte. However, agglomerated particles of nodule-shaped morphology have been observed for 1 g l^{-1} of Alg in the electrolytic bath. Therefore, Alg concentrations above the threshold (≥ 0.5 Alg) tend to cause more aggregation on the material surface (Figure 4.2I) because of the uncontrolled gelation (due to the competition of the carboxylic group with Mn^{2+} at a faster rate). The corresponding magnified image (Figure 4.2J) shows a porous morphology with no uniform gel structure and mechanical integrity. Overall, the results suggest that an excessive concentration of biopolymer additive can cause inhomogeneous distribution of particles and gel clogging issues resulting in inconsistent surface properties, which are not suitable for efficient storage applications, while the optimized amount (0.5 Alg) exhibits a more compact structure.

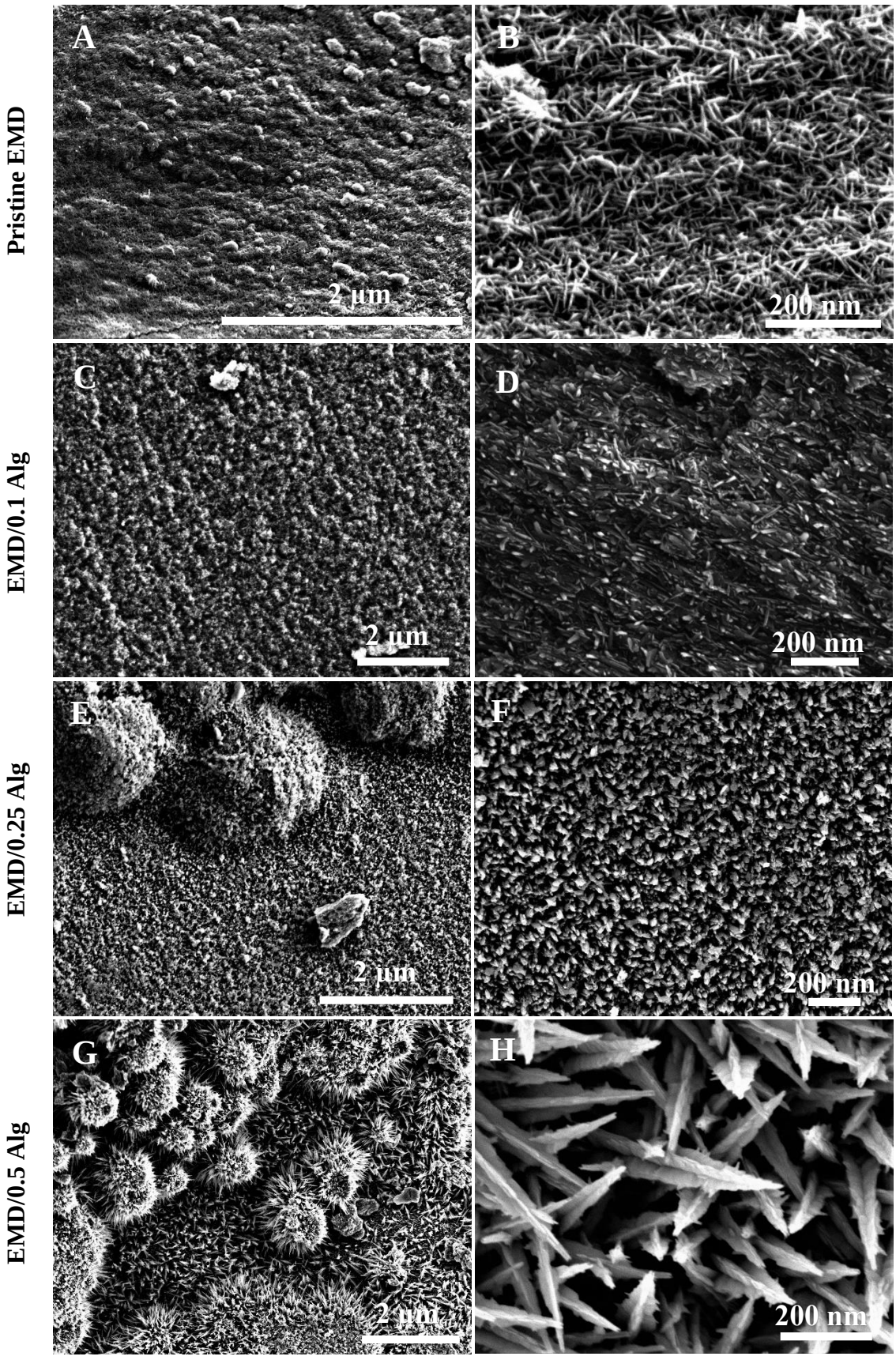
Pristine EMD
EMD/0.1 Alg
EMD/0.25 Alg
EMD/0.5 Alg
A
2 µm
B
200 nm
C
2 µm
D
200 nm
E
2 µm
F
200 nm
G
2 µm
H
200 nm

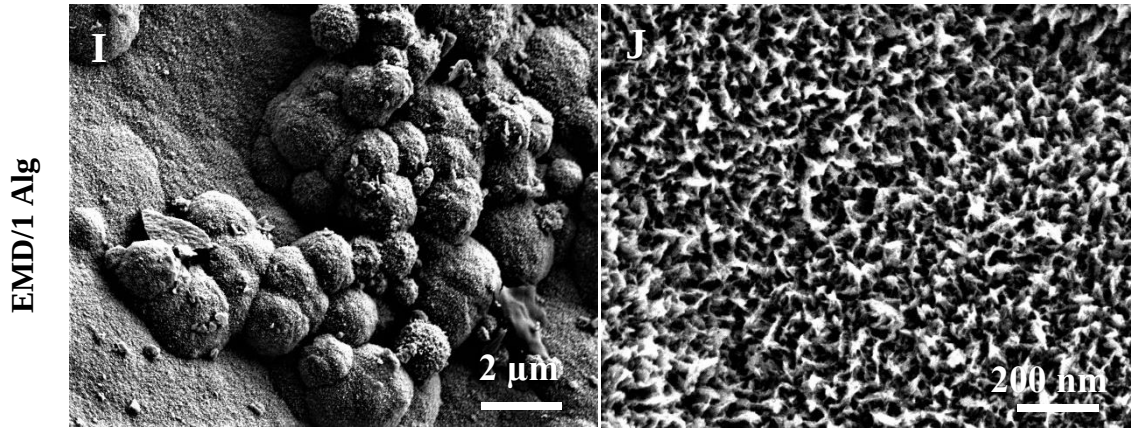

Figure 4.2 FESEM images for (A, B) pristine EMD, (C, D) EMD/0.1 Alg, (E, F) EMD/0.25 Alg, (G, H) EMD/0.5 Alg, and (I, J) EMD/1 Alg.

Structural analysis. Fourier transform infrared (FTIR) spectroscopy was used to analyze any functional groups present on the surface of the pristine EMD and EMD/Alg samples. The spectra obtained in the mid-infrared range of 500 - 1970 cm^{-1} is superimposed in Figure 4.3A. The highly intense absorption band appearing around the 575 cm^{-1} region for all samples represents the metal−oxygen Mn−O bond vibrations, indicating that a γ form of MnO_2 is present as expected. However, the observed bands in the range of 800 - 1100 cm^{-1} are slightly shifted to the higher frequency region for the EMD/Alg samples as compared to the pristine EMD sample. This may be due to the possible crosslinking of Alg with MnO_2. The overall intensity of the bands of the spectra of the Alg-added samples is increased with well-defined peaks at higher concentrations illustrating the strong interaction between MnO_2 and carboxylic anions. The strong and sharp band observed in the range of 800−1000 cm^{-1} can be attributed to the Mn−O−Mn bending vibrations of the MnO_6 octahedral in γ-MnO_2. The various shoulders observed between 900 and 1970 cm^{-1} can be assigned to the varying degrees of hydrogen bonding in the samples and the interactions between manganese and the carboxylic anions.[27,28] The band observed at 995 cm^{-1} may correspond to the stretching vibrations of the O-H groups.[29,30] The weakly formed doublet absorption around 1020 cm^{-1} in the EMD/Alg samples indicates that the surfaces of the EMD composites are rich in carboxyl groups, providing the possibilities for their further functionalization for energy storage activities.

Figure 4.3B shows the XRD patterns of pristine EMD compared with the EMD/Alg composites. Five diffraction peaks observed at 2θ values of 22, 37, 42, 56, and 67° can be adequately described as γ-MnO2 having a defective crystal phase. Chabre and Pannetier[31] explained that the EMD composites could be indexed by the orthorhombic unit cell structure. For comparison, the diffraction pattern of Alg for all concentrations has also been superimposed. The XRD spectrum of Alg exhibits broad diffuse diffraction peaks indicating its poor crystallinity. At a higher concentration of Alg in the electrolytic bath, the crystalline diffraction peak of EMD corresponding to a plane (110) was broadened, which could be due to the increment of crosslinking degree between the carboxylic group and Mn.

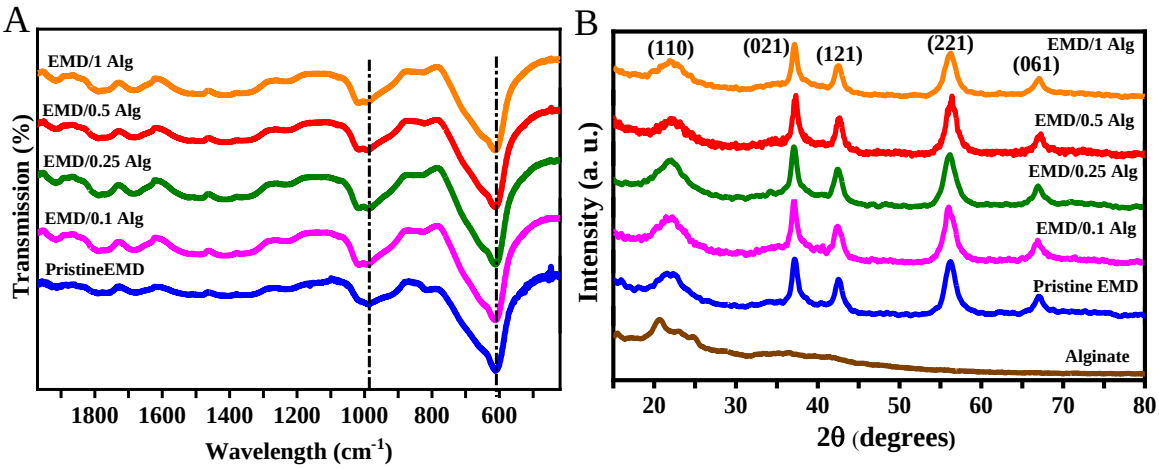

Figure 4.3 (A) Mid IR spectra and (B) XRD patterns of pristine EMD, EMD/0.1 Alg, EMD/0.25 Alg, EMD/0.5 Alg, and EMD/1 Alg as denoted along with the curves.

The EMD material (γ-MnO2) obtained from the optimized amount of Alg was further analyzed using neutron powder diffraction (NPD) data. This was to carry out a quantitative phase analysis based on the Rietveld refinement method. A comparison of the conventional XRD and NPD patterns of EMD/0.5 Alg is shown in Figure 4.4 A and B. Both patterns exhibit the features of structural disorder present in the electrodeposited material, which occurred due to the "De Wolff" disorder.[31] The Rietveld refinement was undertaken for the diffraction pattern (Figure 4.4B), which reveals that the EMD/0.5 Alg structure can be related to both the orthorhombic (Pnma) ramsdellite and tetragonal ($P4_2/mnm$) pyrolusite models. The parameters for the ramsdellite and pyrolusite phases were initially obtained from the database (American

Mineralogist Crystal Structure Database; AMCSD).[32,33] According to the refinement results, 0.42 of pyrolusite and 0.58 of ramsdellite fractions were present in the EMD material. The Rietveld refinement parameters were obtained using the lower-weighted profile R-factor (R_{wp}) of 0.0163, and the goodness of fit was 1.19. The refined unit cell parameters are provided in Table 4.1, while the atomic coordinates and displacement parameters are listed in Table 4.2. The data collected from previous studies for the pure pyrolusite and ramsdellite phases are also provided. Compared to the manganese oxide structures of ramsdellite and pyrolusite, EMD/0.5 Alg shows distortions in the unit cell parameters. The pyrolusite component is enlarged by 3.3 % along the a-axis, causing a volume expansion of 4.9 %. For the ramsdellite phase, a very little volume increase (0.07 %) is observed with axis expansion along a and b, while there is a contraction for c. It has been widely known that the degree of intergrowth of pyrolusite in ramsdellite varies with the synthesis conditions. This has been observed for the optimized biopolymer additive (EMD/0.5 Alg), which decreases the microtwinning by having a larger amount of pyrolusite in the crystalline ramsdellite phase.

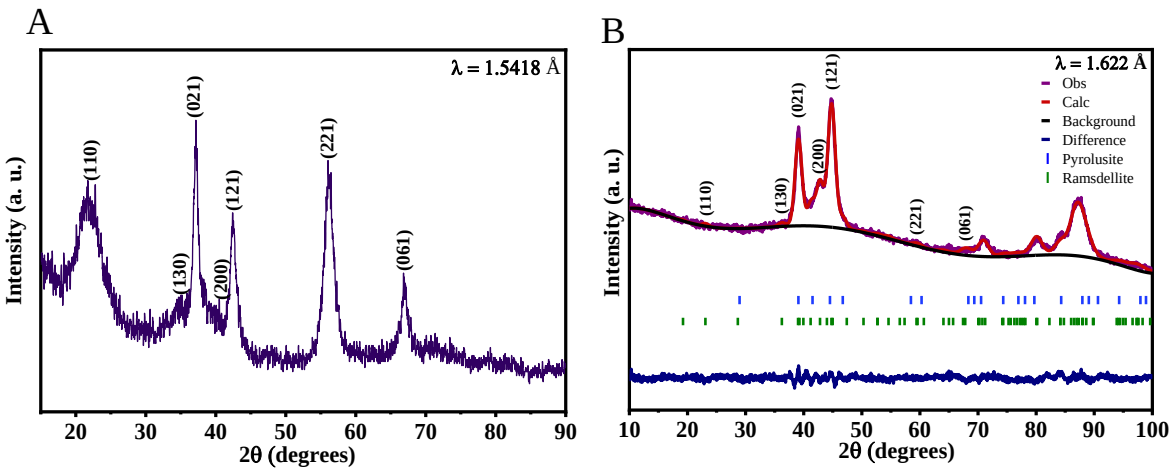

Figure 4.4 (A) X-ray diffraction pattern of EMD/0.5 Alg (γ-MnO_2), (B) Rietveld refinement profile using EMD/0.5 Alg data. Structural models for ramsdellite and pyrolusite are used as represented by green and blue vertical bars, respectively. Observed data are shown in purple, the calculated pattern in red, the background in black, and the difference between the observed and calculated in dark blue. The clearly observed reflections (021), (200), and (121) are labeled in black, the expected positions which are slightly seen, the (110), (130), and (221) reflections are also labeled.

Table 4.1 Unit cell parameters and volumes for ramsdellite and pyrolusite used in the Rietveld analysis.

Sample	a (Å)	b (Å)	c (Å)	V (Å^3)
Reported values for MnO_2 [32,34]				
Ramsdellite	9.3229	4.4533	2.8482	118.25
Pyrolusite	4.396	4.396	2.871	55.482
EMD/0.5 Alg				
Ramsdellite	9.6079	4.4152	2.7896	118.338
Pyrolusite	4.5403	4.5403	2.8222	58.178

Table 4.2 Atomic coordinates and thermal parameters for EMD/0.5Alg determined from NPD data analysis.[32,34]

Sample	Atom	x (Å)	y (Å)	z (Å)	U_{iso} (Å^2)
Reported values for MnO_2 [32,34]					
Ramsdellite	Mn1	0.1332	0.25	0.0258	0.0021
	O1	0.9655	0.25	0.7838	0.0041
	O2	0.2796	0.25	0.3201	0.0034
Pyrolusite	Mn1	0	0	0	-
	O1	0.30200	0.30200	0	-
EMD/0.5 Alg					
Ramsdellite	Mn1	0.1287	0.25	0.0207	0.015
	O1	0.9580	0.25	0.7689	0.011
	O2	0.2883	0.25	0.2938	0.007
Pyrolusite	Mn1	0	0	0	0.017
	O1	0.33260	0.33260	0	0.095

Nitrogen adsorption-desorption analyses were performed to examine the specific surface area, total pore volume, and pore diameter of the pristine EMD and EMD/Alg composites. EMD flakes were ground into powder and degassed before the Brunauer-Emmett-Teller (BET) analysis. The BET analyses of pristine EMD and EMD/Alg composites in Figure 4.5 show a type IV isotherm with an H2 hysteresis loop in the range 0.47 - 0.8 P/P_o according to the IUPAC classification.[35] The measured average pore sizes and pore volumes are presented in Table 4.3. The results indicate that the addition of Alg biopolymer has improved the surface area. The extent is larger for the optimized amount of Alg, which is EMD/0.5 Alg exhibiting 97.1 $m^2\ g^{-1}$ with an average pore diameter of 3.84 nm. The BET surface areas for electrodeposited EMD reported in the literature were in the range of 10 - 100 $m^2\ g^{-1}$.[36,37] The hysteresis loop at relative pressure closer to unity in the adsorption-desorption curves indicates the presence of mesopores in the material.[38] A significant increment of pore volume (from 0.1 $cm^3\ g^{-1}$ to 0.7 $cm^3\ g^{-1}$) in the particle diameter ranging from 2 to 6 nm has been observed from the curves obtained by Barret-Joyner-Halenda (BJH) method for EMD/0.5Alg composite as illustrated in Figure 4.5D.

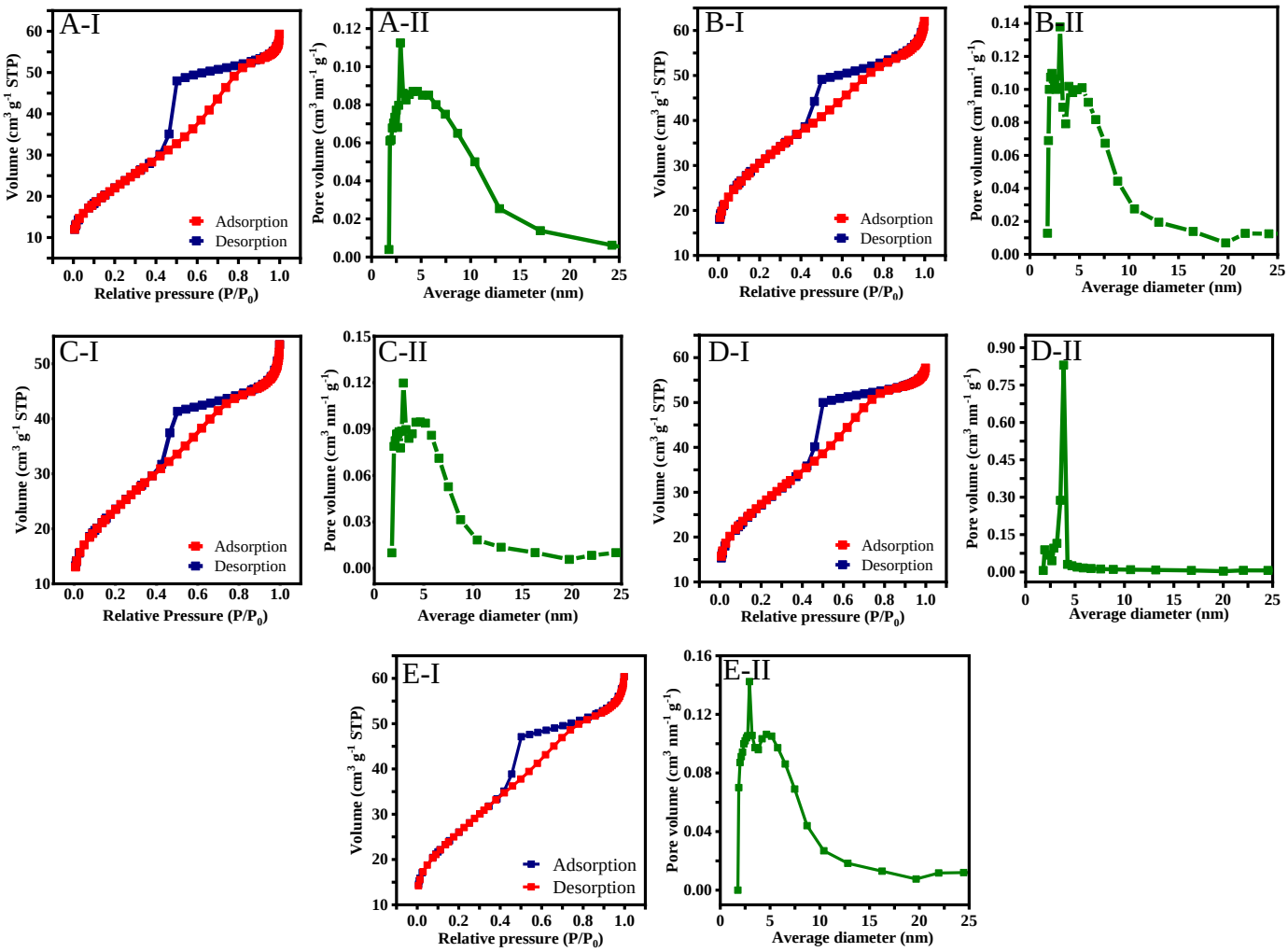

Figure 4.5 Nitrogen adsorption and desorption isotherms of (A-I, A-II) Pristine EMD, (B-I, B-II) EMD/0.1 Alg, (C-I, C-II) EMD/0.25 Alg, (D-I, D-II) EMD/0.5 Alg, (E-I, E-II) EMD/1 Alg.

Table 4.3 Surface area and pore size distribution values for the pristine EMD and EMD/Alg composites.

Sample	BET surface area ($m^2 g^{-1}$)	BJH adsorption average pore diameter (nm)	BJH Adsorption cumulative pore volume ($cm^3 g^{-1}$)
EMD	80.4	4.57	0.08
EMD/ 0.1 Alg	83.2	4.00	0.08
EMD/ 0.25 Alg	84.8	4.13	0.07
EMD/ 0.5 Alg	97.1	3.84	0.08
EMD/ 1 Alg	94.6	4.15	0.08

The high-resolution transmission electron microscopy (TEM) and the corresponding selected area electron diffraction (SAED) pattern in Figure 4.6 A and B shows the semicrystalline nature of the electrodeposited material. The γ-MnO2 structure of the EMD identified by the XRD and NPD patterns could be further confirmed by the diffraction rings obtained from the selected area electron diffraction (SAED) analysis. The TEM image of the powdered sample obtained after grinding the EMD flakes indicates the presence of nanograins within the EMD, typically of sizes ranging from 10 to 30 nm. High-angle annular dark-field scanning transmission electron microscopy (HAADF-STEM) image is shown in Figure 4.6C, and EDS mapping of the elements Mn, O, and C in the EMD/0.5 Alg sample is shown in Figure 4.6 D−F. This confirms the presence of the EMD composites. Compared to the HRTEM of pure EMD (Figure 4.6 G), slight changes could be observed, implying expansion of the lattice spacing in EMD/0.5 Alg in Figure 4.6 H and I. This could be related to the increments of unit cell volumes as obtained from the Reitveld refinement analysis of NPD data. Hence, the dependence of the lattice parameters could be attributed to the intercalation of polymer in the EMD structure.

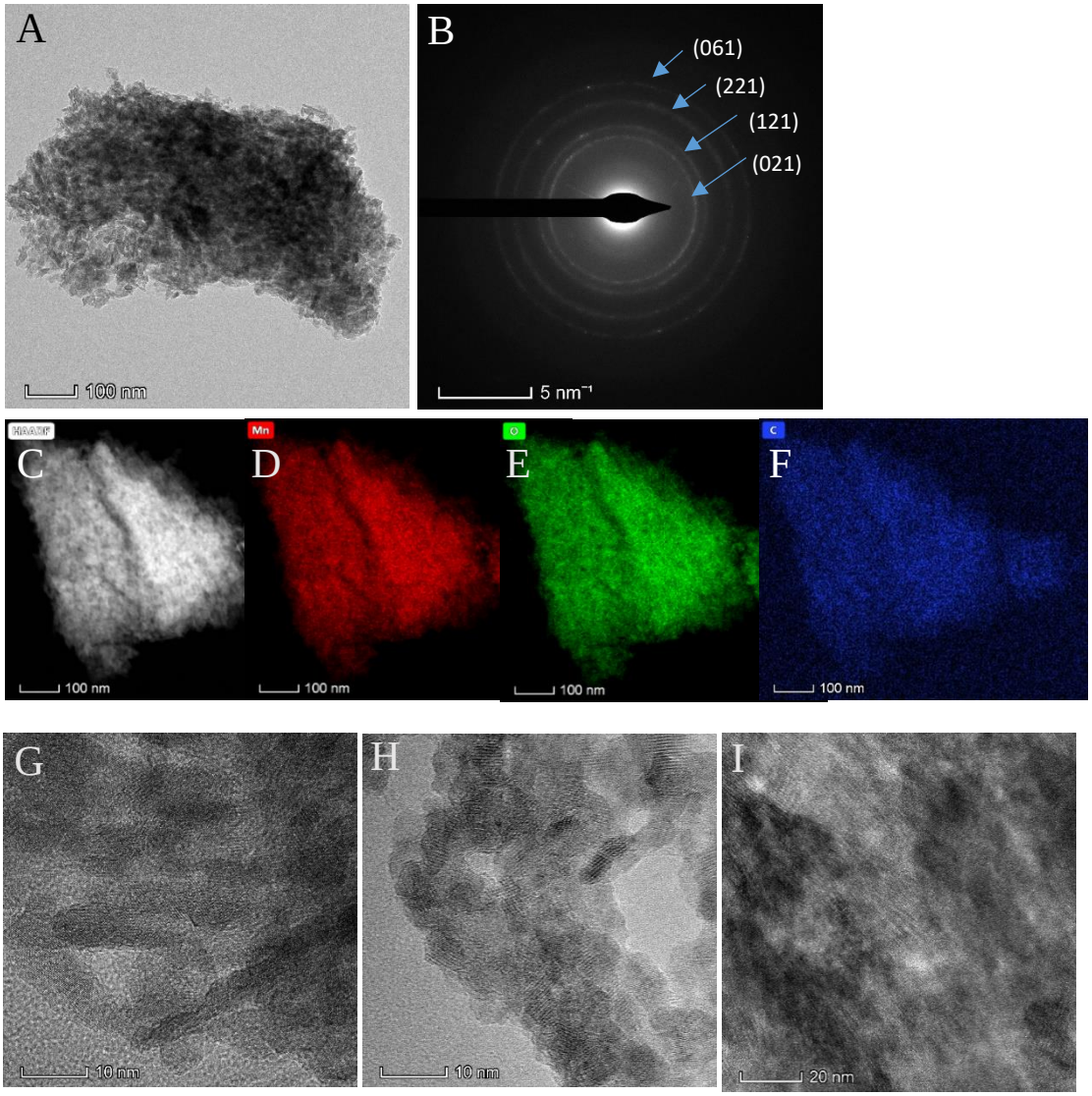

Figure 4.6 (A) Transmission electron microscopy (TEM) image, (B) Selected area electron diffraction image corresponding to image (a), (C) High angle annular dark-field (HAADF) – scanning transmission electron microscopy (STEM) images, and (D-F) Energy-dispersive x-ray spectroscopy (EDS) elemental mapping of EMD/0.5 Alg (G) High-resolution transmission electron microscopy (HRTEM) image of pristine EMD and (H, I) HRTEM images of EMD/0.5 Alg.

4.4.2. Electrochemical characterization

Electrochemical Characterization of the Single Electrode System. Capacitive Performance of the EMD/Alg Composites. CV and GCD tests were conducted to examine the electrochemical characteristics of the EMD samples. Figure 4.7 presents the CV and GCD profiles of the EMD samples at various concentrations of Alg (0, 0.1, 0.25, 0.5, and 1 g l^{-1}) individually at the potential range of 0-0.6 V in the sweep rates of 2-20 mV s^{-1} and current rate range of 0.5-3 mA, respectively. The CV curves in Figure 4.7 (A-I, B-I, C-I, D-I, E-I) show increased current response area under the curve for the EMD/Alg composites compared to the pristine EMD, thereby establishing beneficial charge storage properties. The current response increases with the increase in the concentration of Alg in the bath, but after the threshold (≥ 0.5 Alg), for 1 Alg, the current response decreases. Despite these, for all the biopolymer Alg concentrations, the CV curves invariably show cathodic (reduction) and anodic (oxidation) peaks during the analyses. The quasi-rectangular shape of the obtained peaks indicates that the charge storage mechanism involves charge transfer corresponding to being pseudocapacitive. For the EMD/0.5 Alg (Figure 4.7 D-I), the shape of the CV curve resembles or approaches electrochemical double layer (EDLC) behavior. The corresponding quasi-triangular shaped charge-discharge curves are shown in Figure 4.7 (A-II, B-II, C-II, D-II, E-II). The applied current rate (0.5 - 3 mA) is inversely proportional to the charge-discharge time, implying that at a lower current rate of 0.5 mA accumulation of ions from the electrolyte with the electrode interface gets longer, resulting in a longer discharge time. For the EMD/Alg composites, the IR drop of the discharge cycle is negligible, indicating the polymer is beneficial in reducing the IR drop and electrode resistance; this is further confirmed by EIS analysis (Figure 4.9). Among the concentrations studied, the EMD/0.5 Alg in Figure 4.7 D-II shows increased charge-discharge time, indicating a better charge storage mechanism for the EMD/Alg composites. However, at a higher concentration of Alg (1 Alg), the charge-discharge time gets similar to that of pristine EMD, suggesting the extensive aggregation of the carboxylic group with Mn cation led to poor behavior.

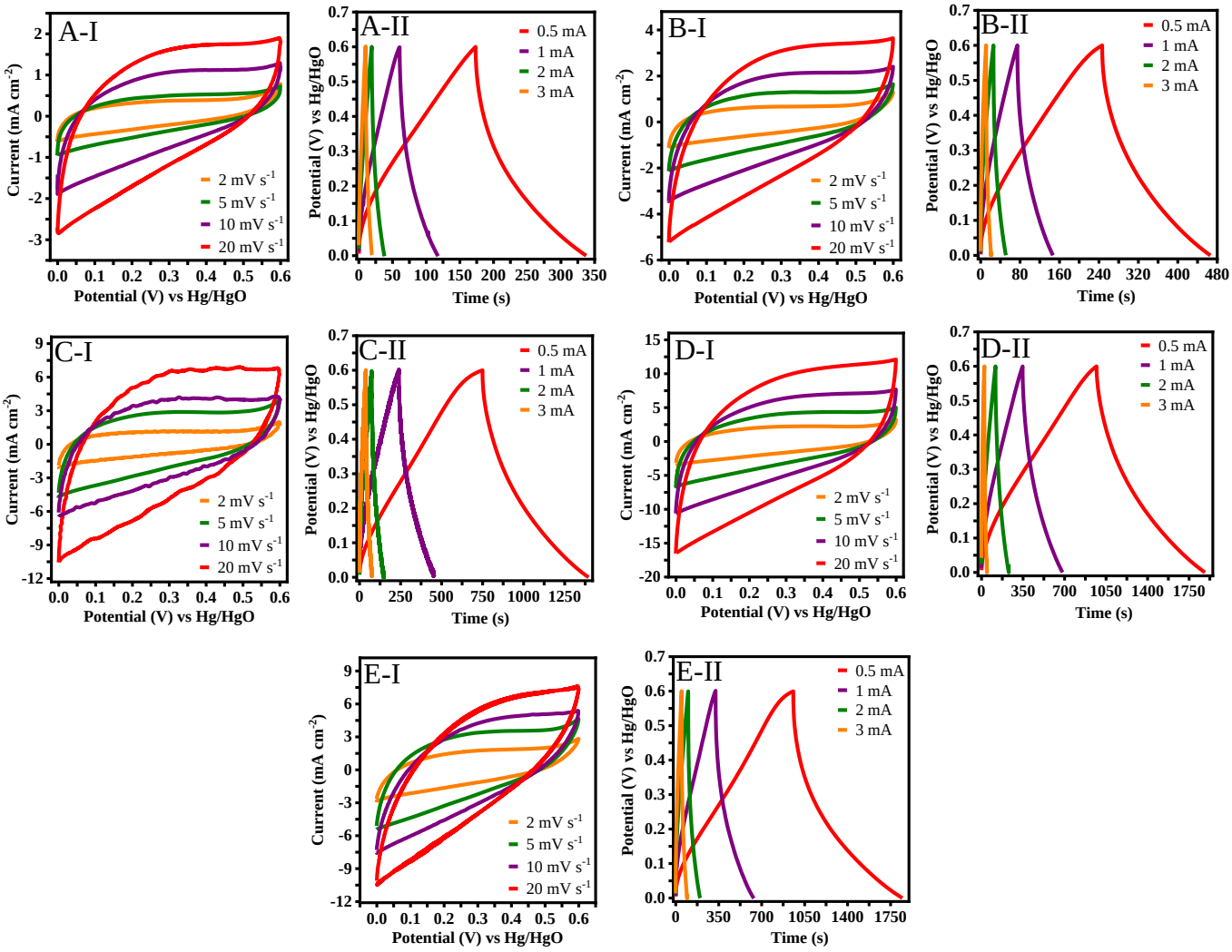

Figure 4.7 Cyclic voltammograms (CV) and galvanostatic charge-discharge (GCD) profiles of (A-I, A-II) pristine EMD, (B-I, B-II) EMD/0.1 Alg, (C-I, C-II) EMD/0.25 Alg, (D-I, D-II) EMD/5 Alg, (E-I, E-II) EMD/1 Alg and the bio polymer-modified EMD (Note. the axes scales are different for CV and GCD curves of each sample).

Based on the initial studies, we have chosen 10 mV s^{-1} sweep rate and 1 mA cm^{-2} current rate to compare the Alg concentrations to their energy storage performance. Figure 4.8 A and B show the CV and GCD curves of all Alg concentrations recorded at 10 mV s^{-1} and 1 mA cm^{-2}. CV curves have slightly deviated from the ideal rectangular shape for all of the concentrations, indicating faradic behavior corresponding to the pseudocapacitive nature of all samples. However, the EMD/0.5 Alg encloses the largest area of CV curves and the longest discharge time (exhibiting

near triangular curves), giving the best electrochemical capacitance performance among the studied Alg concentrations. The calculated specific capacitances from CV are 94, 145, 300, 489, and 434 F g^{-1} for EMD, EMD/0.1 Alg, EMD/0.25 Alg, EMD/0.5 Alg, and EMD/1 Alg, respectively. The Alg composite EMD/0.5 Alg exhibits superior values (about 5 times) compared to the pristine EMD, indicating an enhanced ion transport after crosslinking. For GCD results at 1 mA cm^{-2}, the specific capacitances obtained for EMD/0.1 Alg, EMD/0.25 Alg, EMD/0.5 Alg, and EMD/1 Alg are 95, 124, 364, 487, and 410 F g^{-1}, respectively. Figure 4.8C shows the specific capacitance variability at different Alg concentrations derived from GCD data conducted at 0.5, 1, 2, 3, and 5 mA current rates. The specific capacitances decline steadily with increasing current rates mainly affected by the shorter time for efficient charging and discharging. Thus, the fast-current flows do not access all of the available surface area and pores of the active material. Therefore, the higher current rates affect ion transportation at the electrode−solution interface by the low utilization of micropores, resulting in a short discharging time.[39,40] Figure 4.8D shows the variation of the specific capacitance with the increasing Alg concentrations. A significant improvement of the capacitance was obtained when the concentration varied from 0 to 0.5 g l^{-1}, showing the maximum capacitance of 487 F g^{-1} for 0.5 Alg. Following this, the capacitance decreases to 410 F g^{-1} for 1 Alg with a loss of ∼16 %.

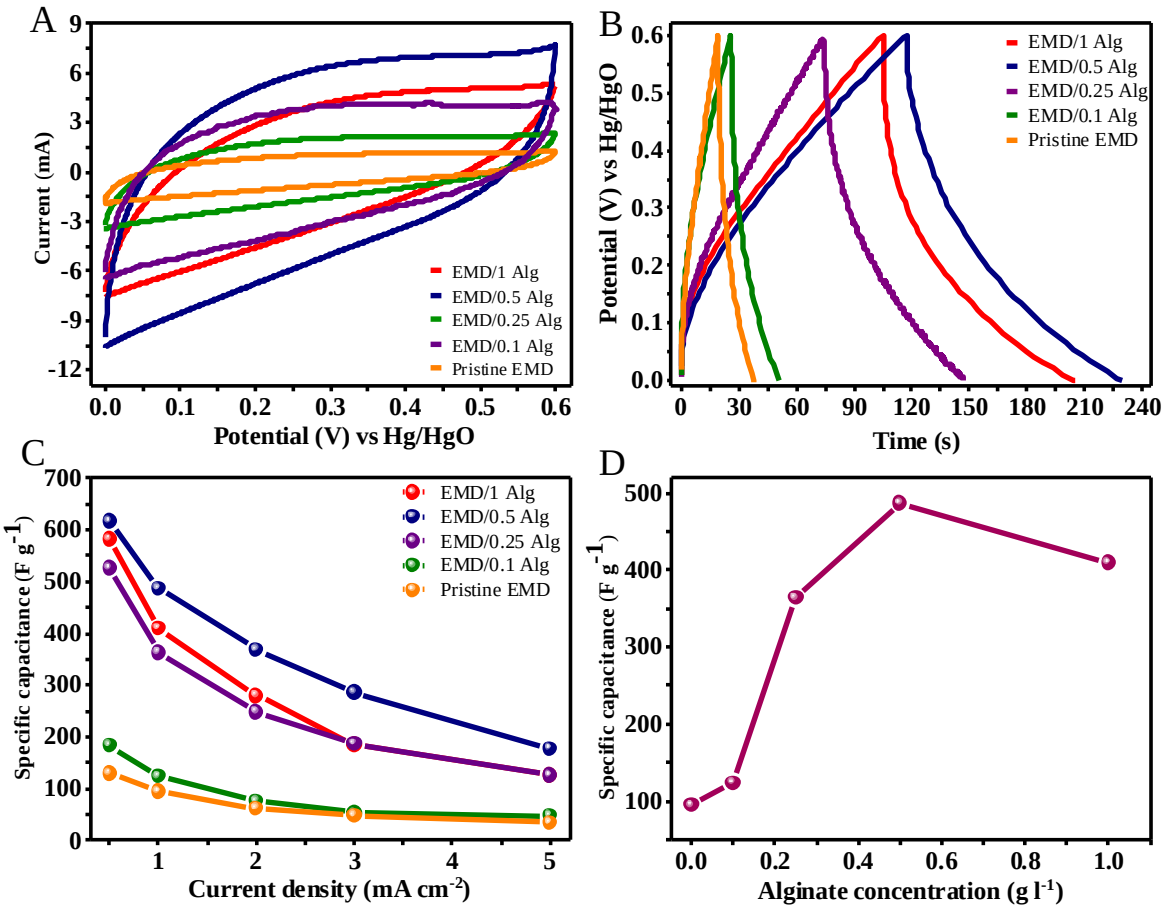

Figure 4.8 (A) CV at 10 mV s^{-1}, (B) CD at 1 mA cm^{-2}, (C) specific capacitance *vs.* current density at different Alg concentrations, (D) Specific capacitance calculated at 1 mA cm^{-2} at different concentrations of Alg (the trend lines connecting the data points in (C) and (D) are only for showing the pattern of the data points distribution).

To further understand the crosslinking process of the best performed EMD/0.5 Alg composites, their kinetics were studied through electrochemical impedance spectroscopy (EIS) measurements. The EIS measurements and fitted curves (Figure 4.9) closely agree with the experimental data collected before and after 1000 cycles in the three-electrode configuration. The equivalent circuit was built using the EC-Lab Z fit. The difference observed between the initial and after 1000 cycles is not significant. Typically, the Nyquist plot consists of a semicircle at high frequency, followed by a straight line. In the EMD/0.5 Alg, the Nyquist plot (Figure 4.9A) showed only a diffused semicircle at a high frequency that tails off linearly at lower frequencies. The

charge transfer resistance (R_{ct}) determined from the semicircle diameter is shown in Table 4.4. The ionic charge at the interface contributes to the ideal double-layer capacitance. However, the coated electrode surface roughness and porosity could produce overlapping double layers that caused deviations from the ideal capacitance. Therefore, the non-ideal capacitance is usually represented by a constant phase element [41–44] (CPE1 in Figure 4.9B), parallel to the charge transfer resistance R_{ct}.

When the protons and electrons are inserted into the EMD structure during the charge transfer, a diffusion component should also be considered for charge diffusion. At higher frequencies, the diffusion of charge (insertion and extraction) will occur considerably faster; therefore, the impact given to the impedance by diffusion will not be significant. At lower frequencies, the inserted electrons and ions tend to penetrate more depth; hence the mass transfer by diffusion would be the limiting factor in determining the impedance. This phenomenon is accounted for by the Warburg circuit element (W in Figure 4.9B). However, the structural disorder and porous surface of the crosslinked EMD will overrule the underlying assumption of Warburg impedance that is applied only to planar and semi-infinite diffusion of charge. This was compensated by the second constant phase element (CPE2 in Figure 4.9B) was included in the circuit in series with the Warburg element and R_{ct}. The values of the parameters according to modified Randle's circuit are shown in Table 4.4. Based on the results, only minimal changes have occurred for both R_s and R_{ct}. The 'n' is a number associated with the constant phase element CPE can vary between 0 to 1 ($0 \leq n \leq 1$). If the 'n' value is equal to 0, it shows the pure resistance, and if the value is 1, it is pure capacitance. According to 'n' parameters given by the model, the 'n_1' has a moderate value of about 0.6 while the 'n_2' is about 0.9 before and after charge-discharge cycling. The kinetic study concludes that crosslinked EMD seems to be stable for long-term cycling, and porosity enhances the ion transport for charge storage. The alginate acted as a template for binding the Mn^{2+} ions on the substrate in a relatively ordered and widely distributed manner that led to the enhancement of the capacitance. The biopolymer reduced the electrode−electrolyte interface resistance and improved the charge (ions, electrons) flow within the electrode.

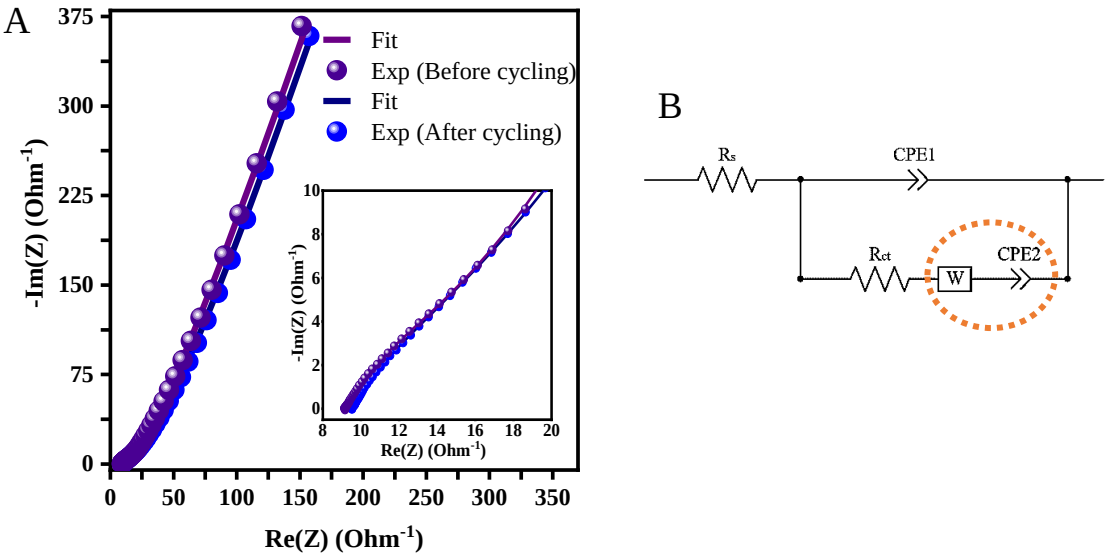

Figure 4.9 (A) Electrochemical impedance spectra of the EMD/0.5 Alg in 2M NaOH electrolyte for single electrode cell (before and after 1000 cycles) and fitted curve, (B) Equivalent circuit model employed in EIS analysis.

Table 4.4 Equivalent circuit parameters from the fitting using the modified Randles circuit.

	R_s (Ω)	R_{ct} (Ω)	σ^* (Ω $s^{0.5}$)	CPE1×10^3 (F s^{n_1-1})	n_1	CPE2×10^3 (F s^{n_2-1})	n_2
Before cycling	9.5	11.5	4.2	6.2	0.69	0.035	0.99
After cycling	9.8	10.1	4.4	5.9	0.67	0.030	0.94

Electrochemical characterization of the two-electrode system (hybrid capacitor). Commercially available activated carbon (AC) was used as the negative electrode in the two-electrode cell. CV and GCD analysis for activated carbon were performed in a negative potential range of -1 to 0 V at different sweep rates and current densities, as previously indicated in Figure 3.9 in chapter 3. The AC electrode clearly showed an EDLC behavior with perfect symmetrical charge-discharge curves. At a current

density of 1 mA cm^{-2}, the activated carbon exhibited a specific capacitance of 81 F g^{-1}. The hybrid device has been fabricated based on the best performed EMD/0.5 Alg (as the cathode) coupled with AC. The CV profiles for EMD/0.5 Alg and AC recorded at a similar scan rate (10 mV s^{-1}) (Figure 4.10) were found to have a working potential window of (+) 0.6 V and (−) 1 V, respectively. The AC electrode exhibited EDLC behavior, while the EMD/0.5 Alg composite exhibited pseudocapacitive behavior. Therefore, the potential window of the hybrid capacitor could be 1.6 V. To determine the safe operating voltage for the device, a two-electrode cell was tested at different voltages (Figure 4.11), and a mid-range of 1.4 V was found to be optimal. Considering the half-cell measurements of EMD and AC, the optimal mass ratio of the materials for the hybrid aqueous cell was calculated by the relationship as explained in equation 4.5.[45,46]

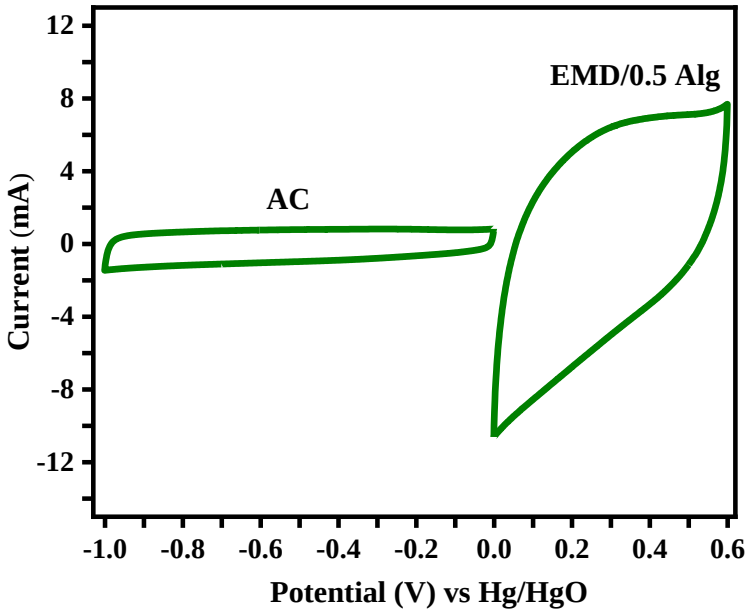

Figure 4.10 Cyclic voltammetry profiles of activated carbon (negative potential window -1 V) and EMD/0.5 Alg (positive potential window 0.6 V) at 10 mV s^{-1} scan rate.

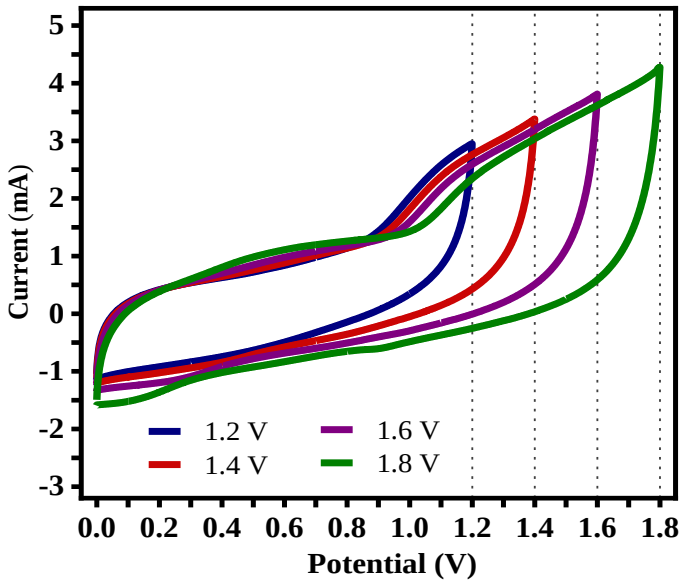

Figure 4.11 Cyclic voltammograms of the hybrid capacitor (EMD/0.5 Alg and AC) with increasing the operating voltage from 1.2 to 1.8 V at the scan rate of 10 mV s^{-1}.

$$\frac{m^+}{m^-} = \frac{C^-.\Delta E_m^-}{C^+.\Delta E_m^+} \qquad (4.5)$$

where, C^+, m^+, ΔE_m^+ and C^-, m^-, ΔE_m^- are specific capacitances, masses, and safe operation potential window of the positive and the negative electrodes. The electrode mass ratio was determined as 0.30.

Typical CV and GCD profiles of the fabricated EMD/0.5 Alg *vs.* AC are shown in Figure 4.12. The CV curve (Figure 4.12A) shows two distinct regions, EDLC at a lower potential and a diffused redox characteristic at a higher potential. Even at higher sweep rates, the shape of the CV profiles is intact, indicating that the material can sustain fast charge kinetics. The storage mechanism is related to the intercalation of alkali metal cations (Na^+ ions in the electrolyte) into the EMD electrode during reduction and deintercalation upon oxidation. As no clear redox peaks are observed, the battery-type intercalation mechanism is ruled out.[34] However, a charge transfer reaction occurs at a higher voltage between 1.2 and 1.4 V, resulting in the reduction of surface pseudocapacitance. The charge-discharge profiles for EMD/0.5 Alg *vs.* AC at a voltage window of 1.4 V tested at different current rates are shown in Figure 4.12B. The cell is reversible, and the shape of the curves is more symmetrical at higher current

rates with no obvious IR drop. At a lower current rate of 2 mA, an inflection in the charge curve at 1.2 V is observed, and the discharge process is not fully reversible. The discharge cell capacitances calculated at 1, 2, 3, 4, 5, and 6 mA cm^{-2} were 52, 50, 45, 41, 38, and 35 F g^{-1}. The EMD synthesized at an optimized Alg concentration enhanced the charging kinetics, where pores acted as the ion reservoir and facilitated ion transport. The long-cycling performance of EMD/0.5 Alg versus AC at 2 mA cm^{-2} is shown in Figure 4.12C for over 5000 cycles. The capacitance retention of the cell as a function of cycle number and its Coulombic efficiency can be inferred from this plot. At the end of 5000 cycles, 94 % of the initial capacitance was retained, confirming the excellent stability of the cell within the tested voltage range. The observed superior performance could be attributed to the unique structure and mesoporous nature of the EMD/0.5 Alg. The energy and power densities of the hybrid capacitor (EMD/0.5 Alg versus AC) were calculated and displayed in the Ragone plot in Figure 4.12D, compared with the reported literature for other electrodeposited manganese oxides. At increasing applied currents of 1, 2, 3, 4, 5, 6, and 7 mA cm^{-2}, the cell delivered the following power, energy densities (14, 500), (14, 1000), (12, 1500), (11, 2009), and (10, 2533), respectively. Despite the lower capacitance obtained from the hybrid capacitor, the maximum energy density is 14 Wh g^{-1} (at 1 mA cm^{-2}). This value is noticeably better than the values reported for EMD in hybrid cells in the literature.[45,46]

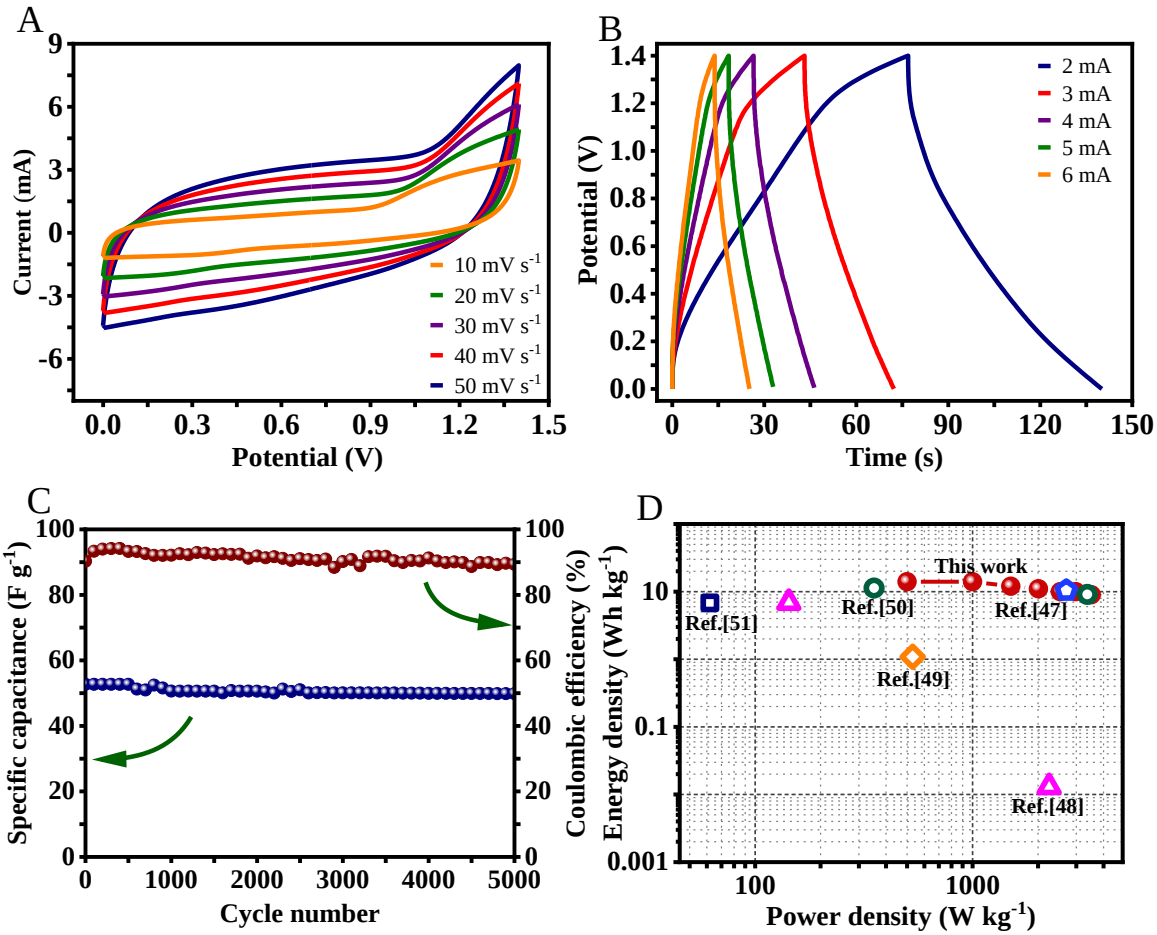

Figure 4.12 (A) CV and (B) GCD profiles of hybrid capacitor in aqueous 2 M NaOH electrolyte at 1.4 V cell voltage, (C) capacitance retention and coulombic efficiency over 5000 cycles (D) energy and power densities of the hybrid capacitor with increasing applied current densities; 1, 2, 3, 4, 5, 6, 7 mA cm^{-2} (Ref: [47–51]).

4.4.3. Simulation results

In this section, the model results are presented, which were carried out to examine the electrolyte, the medium of the electric circuit formed between the anode and the cathode. The model evaluates the ion-polymer interactions, distribution, and influence on manganese dioxide/polymer composite electrodeposition.

The images in Figure 4.13 A and B show the arrangement of the deprotonated Alg (pink), Mn^{2+} (purple), and sulfate ions (yellow/red) at the end of the simulation. Water molecules have been hidden in these pictures to make the location of other species easier to see. Although there is some clustering of the Mn^{2+} and SO_4^{2-} ions, quite a

few Mn^{2+} ions are distributed around the deprotonated Alg polymers. This likely improves the distribution of the Mn^{2+} ions and modifies the way in which these are deposited in the final structure. At pHs below the pKa of the Alg, the carboxylate groups of the polymer are protonated and there is less attraction of the Mn^{2+} ions. This is evident in the images in Figure 4.13 C and D, where there is a wider dispersion of the Mn^{2+} ions throughout the simulation cell.

Figure 4.13 A-E describes the average separation between different species during the simulations that provides some measure of the level of interaction between these species. The Mn^{2+} ions are dispersed throughout the simulation cell. As can be seen in Figure 4.13A, there is a peak at 4.0 Å, indicating that this is the closest that these ions approach one another during all of the simulations. The peaks are more intense for the systems with Alg, indicating a higher probability of the ions being at this separation than the solution without the Alg. However, there is little difference in the separation between Mn^{2+} ions for the two pHs investigated. The Mn^{2+} ions are well solvated in all of the simulations. There is very little difference in the interactions between water and Mn^{2+} with a Mn/O distance of 2.8 Å for the first solvation shell. The peak is slightly more intense in the system with no Alg because there is no Alg present to interact with the Mn^{2+} ions. The analysis of the interactions between the Mn^{2+} ions and the oxygen atoms of the carboxylate groups of the Alg polymers is shown in Figure 4.13C. The Mn^{2+} ions are strongly attracted to the deprotonated carboxylate groups (Alg above pKa), as shown by the large peak at 2.6 Å. The two oxygen atoms of the carboxylate are equivalent in the deprotonated state, and therefore, there is only a single plot for this interaction. In the protonated state (pH below pKa), the two oxygen atoms of the carboxylates are not equivalent. These are designated Alg_p_Mn^{2+}/-CO for the carbonyl oxygen atom and Alg_p_Mn^{2+}/-COH for the acidic (-OH) oxygen atom. The interaction of Mn^{2+} with the protonated carboxylate groups is much weaker, as shown by the smaller peaks in the plot (Figure 4.13C). Interaction between Mn^{2+} and the acidic oxygen atom is favored over the carbonyl oxygen, but as noted, this interaction is much weaker than the interaction with the deprotonated carboxylates.

The interaction between Mn^{2+} and the alcohol groups of the Alg polymers is quite strong. This is particularly the case for the simulation with the deprotonated Alg. It should be noted that the alcohol groups in this set are not deprotonated, but the strong

electrostatic attraction between Mn^{2+} and -RCO_2 brings the metal ions close to the polymer, and this increases the probability of interaction with the alcohol groups. This same interaction is present in the protonated polymer simulations but is weaker (Alg_p_Mn^{2+}/-OH in Figure 4.13D). Naturally, there is a strong electrostatic attraction between Mn^{2+} and SO_4^{2-} in solution (Figure 4.13E). The interactions are largely unaffected by the charge state of the polymer. The plots indicate that the average separation between Mn^{2+} and SO_4^{2-} is 2.5 Å. There is evidence of the solvated Mn^{2+} and SO_4^{2-} clustering in the simulations. It seems likely from these simulations that the Alg provides a template for binding the Mn^{2+} ions in a relatively ordered manner that may assist in the growth of the EMD/Alg composite in a more favorable condition for storage applications.

Based on the foregoing discussion, the underlying mechanism of the EMD deposition is proposed. The results suggest that the ionic species in the electrolytic bath are uniformly dispersed in the presence of the alginic acid polymer. The Mn^{2+} divalent cations attract the carboxylic surface functional groups in the electrolyte via ionic interactions and crosslinking, which influenced the morphology of the EMD deposits. Increasing the polymer concentrations in the electrolyte improved the crosslinking density; however, the optimized value is found to be 0.5 g l^{-1}. Above this threshold, the aggregate morphology seen on the EMD surface led to lower energy storage.

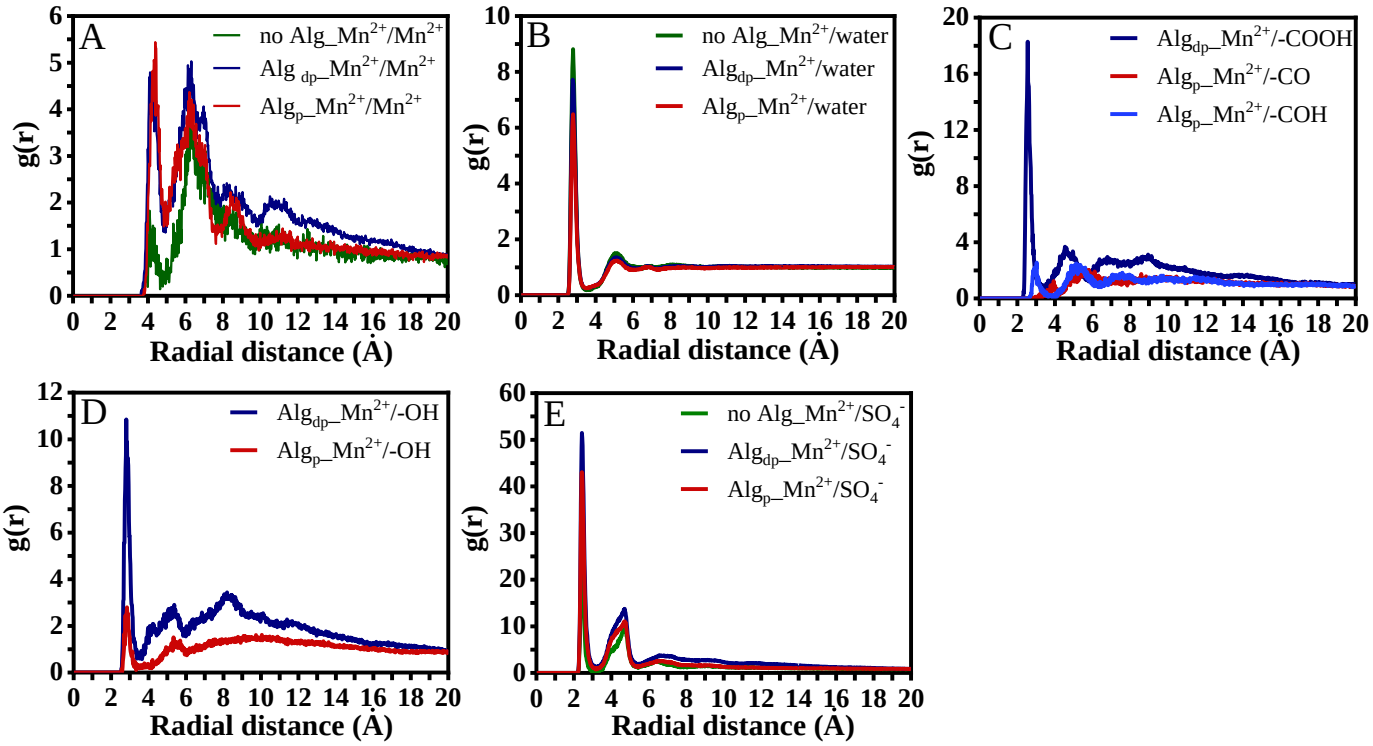

Figure 4.13 Average separation between different species in the absence and presence of Alg (protonated (Alg_p) and deprotonated (Alg_{dp})) in the electrolyte bath: (A) Mn^{2+} ions, (B) Mn^{2+} ions and water, (C) Mn^{2+} ions and carboxylate groups of Alg polymer, (D) Mn^{2+} ions and alcohol groups, (E) Mn^{2+} and SO_4^{2-} ions.

4.5. Conclusion

Manganese dioxide was synthesized by anodic electrodeposition with varied concentrations of alginate (Alg) biopolymer additive. The process is scalable, cost-effective, and environmentally friendly. Here, we have reported the structural, surface, morphological, and electrochemical properties of the hierarchical structure of Alg crosslinked with EMD. Cacti-shaped flutelike EMD nanomaterial with tunable porosity was obtained for the EMD/0.5 Alg concentration. Compared to the pristine EMD, the EMD/0.5 Alg exhibits an excellent specific capacitance of 487 F g^{-1} for a single electrode study, which is 5 times higher than that of the pristine EMD. A practical hybrid capacitor device was fabricated using the EMD/0.5 Alg //activated carbon, which gave the specific energy of 14 Wh kg^{-1} and specific power of 500 W kg^{-1} at a 1 mA current rate. The Alg crosslinked with EMD cathode favors a more

diffusion-free pseudocapacitance-like charge storage mechanism. In addition, the interactions between ions and polymer species (Mn^{2+}, OH^{-}, H^{+}, SO_4^{2-}, Alg polymer) in the electrolytic bath were fully comprehended by molecular modeling. It clearly depicted the advantages of Alg in the electrolytic bath with its tailorable architecture for assembling the EMD on the anode substrate and enhancing its physicochemical and electrochemical properties. Using the facile electrodeposition method inherited from chapter 3 was rewarded with an attractive material for energy storage. Clearly, there exists the potential of using the natural biopolymer Alg for developing composites by combining its functional framework with active materials to be used in future energy storage devices.

4.6. References

(1) Zhang, Y.; Mei, H. xin; Cao, Y.; Yan, X. hua; Yan, J.; Gao, H. li; Luo, H. wei; Wang, S. wen; Jia, X. dong; Kachalova, L.; Yang, J.; Xue, S. chang; Zhou, C. gang; Wang, L. xia; Gui, Y. hai. Recent Advances and Challenges of Electrode Materials for Flexible Supercapacitors. *Coord. Chem. Rev.* **2021**, *438*, 213910.

(2) Cloud, M. What is the Energy Density of a Lithium-Ion Battery? https://www.fluxpower.com/blog/what-is-the-energy-density-of-a-lithium-ion-battery.

(3) Chou, S.; Cheng, F.; Chen, J. Electrodeposition Synthesis and Electrochemical Properties of Nanostructured γ-MnO_2 Films. *J. Power Sources* **2006**, *162* (1), 727–734.

(4) Biswal, A.; Tripathy, B. C.; Li, D.; Minakshi, M. Electrodeposition of Pluronic F127 Assisted Rod-like EMD/Carbon Arrays for Efficient Energy Storage. *Dalt. Trans.* **2015**, *44* (37), 16446–16457.

(5) Yuan, X.; Zhang, Y.; Yan, Y.; Wei, B.; Qiao, K.; Zhu, B.; Cai, X.; Chou, T. W. Tunable Synthesis of Biomass-Based Hierarchical Porous Carbon Scaffold@MnO_2 Nanohybrids for Asymmetric Supercapacitor. *Chem. Eng. J.* **2020**, *393*, 121214.

(6) Dupont, M. F.; Forghani, M.; Cameron, A. P.; Donne, S. W. Effect of Electrolyte Cation on the Charge Storage Mechanism of Manganese Dioxide for Electrochemical Capacitors. *Electrochim. Acta* **2018**, *271*, 337–350.

(7) Wei, F.; Cui, X.; Chen, W.; Ivey, D. G. Phase-Controlled Synthesis of MnO_2 Nanocrystals by Anodic Electrodeposition: Implications for High-Rate Capability Electrochemical Supercapacitors. *J. Phys. Chem. C* **2008**, *112* (38), 15075–15083.

(8) Minakshi, M.; Singh, P.; Issa, T. B.; Thurgate, S.; De Marco, R. Lithium Insertion into Manganese Dioxide Electrode in MnO_2/Zn Aqueous Battery Part II. Comparison of the Behavior of EMD and Battery Grade MnO_2 in Zn|MnO_2| Aqueous LiOH Electrolyte. *J. Power Sources* **2004**, *138* (1–2), 319–322.

(9) Zhang, Y.; Yao, Q. Q.; Gao, H. L.; Zhang, L. Sen; Wang, L. Z.; Zhang, A. Q.; Song, Y. H.; Wang, L. X. Synthesis and Electrochemical Performance of MnO_2/BC Composite as Active Materials for Supercapacitors. *J. Anal. Appl. Pyrolysis* **2015**, *111*, 233–237.

(10) Zhang, Y.; Yao, Q. qian; Gao, H. li; Wang, L. xia; Wang, L. zhen; Zhang, A. qin; Song, Y. hua; Xia, T. chi. Synthesis and Electrochemical Properties of Hollow-Porous MnO_2-Graphene Micro-Nano Spheres for Supercapacitor Applications. *Powder Technol.* **2014**, *267*, 268–272.

(11) Takehara, H.; Yoshihiro, N.; Shimizugawa, R.; Tsutomu, K.; Murai, T.; Takahashi, F.; Takahashi, K. Electrolytic Manganese Dioxide and Method of Manufacturing the Same. EP 0 751 241 A1, 1997.

(12) Zhang, Y.; Chang, C. rong; Jia, X. dong; Huo, Q. yuan; Gao, H. li; Yan, J.; Zhang, A. qin; Ru, Y.; Mei, H. xin; Gao, K. zheng; Wang, L. zhen. Morphology-Dependent $NiMoO_4$/Carbon Composites for High Performance Supercapacitors. *Inorg. Chem. Commun.* **2020**, *111* (October 2019), 107631.

(13) Zhang, Y.; Chang, C. rong; Jia, X. dong; Cao, Y.; Yan, J.; Luo, H. wei; Gao, H. li; Ru, Y.; Mei, H. xin; Zhang, A. qin; Gao, K. zheng; Wang, L. zhen. Influence of Metallic Oxide on the Morphology and Enhanced

Supercapacitive Performance of $NiMoO_4$ Electrode Material. *Inorg. Chem. Commun.* **2020**, *112* (October 2019), 107697.

(14) Yan, W.; Ayvazian, T.; Kim, J.; Liu, Y.; Donavan, K. C.; Xing, W.; Yang, Y.; Hemminger, J. C.; Penner, R. M. Mesoporous Manganese Oxide Nanowires for High-Capacity, High-Rate, Hybrid Electrical Energy Storage. *ACS Nano* **2011**, *5* (10), 8275–8287.

(15) Minakshi, M.; Mitchell, D. R. G.; Prince, K. Incorporation of TiB_2 Additive into MnO_2 Cathode and Its Influence on Rechargeability in an Aqueous Battery System. *Solid State Ionics* **2008**, *179* (9–10), 355–361.

(16) Biswal, A.; Chandra Tripathy, B.; Sanjay, K.; Subbaiah, T.; Minakshi, M. Electrolytic Manganese Dioxide (EMD): A Perspective on Worldwide Production, Reserves and Its Role in Electrochemistry. *RSC Adv.* **2015**, *5* (72), 58255–58283.

(17) Wei, W.; Cui, X.; Chen, W.; Ivey, D. G. Manganese Oxide-Based Materials as Electrochemical Supercapacitor Electrodes. **2011**, *40*, 1697–1721.

(18) Kim, S.; Alauzun, J. G.; Louvain, N.; Brun, N.; Stievano, L.; Boury, B.; Monconduit, L.; Mutin, P. H. Alginic Acid Aquagel as a Template and Carbon Source in the Synthesis of $Li_4Ti_5O_{12}$/C Nanocomposites for Application as Anodes in Li-Ion Batteries. *RSC Adv.* **2018**, *8* (57), 32558–32564.

(19) Behar, S.; Gonzalez, P.; Agulhon, P.; Quignard, F.; Swierczynski, D. New Synthesis of Nanosized Cu-Mn Spinels as Efficient Oxidation Catalysts. *Catal. Today* **2012**, *189* (1), 35–41.

(20) Lee, K. Y.; Mooney, D. J. Alginate: Properties and Biomedical Applications. *Prog. Polym. Sci.* **2012**, *37* (1), 106–126.

(21) Liling, G.; Di, Z.; Jiachao, X.; Xin, G.; Xiaoting, F.; Qing, Z. Effects of Ionic Crosslinking on Physical and Mechanical Properties of Alginate Mulching Films. *Carbohydr. Polym.* **2016**, *136*, 259–265.

(22) Sun, H.; Ren, P.; Fried, J. R. The COMPASS Force Field: Parameterization and Validation for Phosphazenes. *Comput. Theor. Polym. Sci.* **1998**, *8* (1–2),

229–246.

(23) Henry, D. J.; Evans, E.; Yarovsky, I. Classical Molecular Dynamics Study of [60]Fullerene Interactions with Silica and Polyester Surfaces. *J. Phys. Chem. B* **2006**, *110* (32), 15963–15972.

(24) Henry, D. J.; Lukey, C. A.; Evans, E.; Yarovsky, I. Theoretical Study of Adhesion between Graphite, Polyester and Silica Surfaces. *Mol. Simul.* **2005**, *31* (6–7), 449–455.

(25) Shaw, L. A.; Yiapanis, G.; Henry, D. J.; MacLaughlin, S.; Evans, E.; Yarovsky, I. Surface Crosslinking Effects on Contamination Resistance of Functionalised Polymers. *Soft Matter* **2013**, *9* (6), 1798–1806.

(26) Andersen, H. C. Molecular Dynamics Simulations at Constant Pressure and/or Temperature. *J. Chem. Phys.* **1980**, *72* (4), 2384–2393.

(27) Fernandes, J. B.; Desai, B. D.; Kamat Dalal, V. N. Studies on Chemically Precipitated Mn(IV) Oxides-II. *Electrochim. Acta* **1983**, *28* (3), 309–315.

(28) Julien, C.; Massot, M. Spectroscopic Studies of the Local Structure in Positive Electrodes for Lithium Batteries. *Phys. Chem. Chem. Phys.* **2002**, *4* (17), 4226–4235.

(29) Abbas, H.; Nasser, S. A. Hydroxyl as a Defect of the Manganese Dioxide Lattice and Its Applications to the Dry Cell Battery. *J. Power Sources* **1996**, *58* (1), 15–21.

(30) Biswal, A.; Tripathy, B. C.; Subbaiah, T.; Meyrick, D.; Minakshi, M. Electrodeposition of Manganese Dioxide: Effect of Quaternary Amines. *J. Solid State Electrochem.* **2013**, *17* (5), 1349–1356.

(31) Chabre, Y.; Pannetier, J. Structural and Electrochemical Properties of the Proton/γ-MnO_2 System. *Prog. Solid State Chem.* **1995**, *23* (1), 1–130.

(32) Wyckoff, R. W. G. Crystal Structures. In *Crystal structures*; Interscience Publishers, New York, 1963; Vol. 1.

(33) Post, J. E.; Heaney, P. J. Neutron and Synchroton X-Ray Diffraction Study of the Structures and Dehydration Behaviors of Ramsdellite and “Groutellite.”

Am. Mineral. **2004**, *89* (7), 969–975.

(34) C., F.; J., K. B.; M., E. M. A Powder Neutron Diffraction Study of and Manganese Dioxide and of $LiMn_2O_4$. *Zeitschrift für Krist.* **1994**, *209* (001), 941–945.

(35) Sing, K. S. W. Reporting Physisorption Data for Gas/Solid Systems. *Pure Appl. Chem.* **1982**, *54* (11), 2201–2218.

(36) Cross, A.; Morel, A.; Cormie, A.; Hollenkamp, T.; Donne, S. Enhanced Manganese Dioxide Supercapacitor Electrodes Produced by Electrodeposition. *J. Power Sources* **2011**, *196* (18), 7847–7853.

(37) Arnott, J. B.; Williams, R. P.; Pandolfo, A. G.; Donne, S. W. Microporosity of Heat-Treated Manganese Dioxide. *J. Power Sources* **2007**, *165* (2), 581–590.

(38) Biswal, A.; Tripathy, B. C.; Li, D.; Minakshi, M. Electrodeposition of Pluronic F127 Assisted Rod-like EMD/Carbon Arrays for Efficient Energy Storage. *Dalt. Trans.* **2015**, *44*, 16446–16457.

(39) Poonguzhali, R.; Shanmugam, N.; Gobi, R.; Senthilkumar, A.; Viruthagiri, G.; Kannadasan, N. Effect of Fe Doping on the Electrochemical Capacitor Behavior of MnO_2 Nanocrystals. *J. Power Sources* **2015**, *293*, 790–798.

(40) Kim, B. K.; Sy, S.; Yu, A.; Zhang, J. Electrochemical Supercapacitors for Energy Storage and Conversion. In *Handbook of Clean Energy Systems*; John Wiley & Sons, Ltd, 2015.

(41) Ross Macdonald, J. Note on the Parameterization of the Constant-Phase Admittance Element. *Solid State Ionics* **1984**, *13* (2), 147–149.

(42) Schelder, W. Theory of the Frequency Dispersion of Electrode Polarization. Topology of Networks with Fractional Power Frequency Dependence. *J. Phys. Chem.* **1975**, *79* (2), 127–136.

(43) Arnott, J. B.; Donne, S. W. Examining Manganese Dioxide Graphite Connectivity in Alkaline Electrolytes. *J. Electrochem. Soc.* **2007**, *154* (8), A776.

(44) Bailey, M. R.; Donne, S. W. Electrochemical Impedance Spectroscopy Study

into the Effect of Titanium Dioxide Added to the Alkaline Manganese Dioxide Cathode. **2011**, *158* (7), A802–A808.

(45) Ruiz-Rosas, R. *Design of Hybrid Asymmetric Capacitors in Aqueous Electrolyte Using ZTC and Ultraporous Activated Carbons Diseño de Condensadores Asimétricos Híbridos En Electrolito Acuso Mediante ZTC y Carbones Activados Utraporosos*; 2015.

(46) Peng, C.; Zhang, S.; Zhou, X.; Chen, G. Z. Unequalisation of Electrode Capacitances for Enhanced Energy Capacity in Asymmetrical Supercapacitors. *Energy Environ. Sci.* **2010**, *3* (10), 1499–1502.

(47) Jafta, C. J.; Nkosi, F.; Le Roux, L.; Mathe, M. K.; Kebede, M.; Makgopa, K.; Song, Y.; Tong, D.; Oyama, M.; Manyala, N.; Chen, S.; Ozoemena, K. I. Manganese Oxide/Graphene Oxide Composites for High-Energy Aqueous Asymmetric Electrochemical Capacitors. *Electrochim. Acta* **2013**, *110*, 228–233.

(48) Beyazay, T.; Eylul Sarac Oztuna, F.; Unal, U. Self-Standing Reduced Graphene Oxide Papers Electrodeposited with Manganese Oxide Nanostructures as Electrodes for Electrochemical Capacitors. *Electrochim. Acta* **2019**, *296*, 916–924.

(49) Rafique, A.; Massa, A.; Fontana, M.; Bianco, S.; Chiodoni, A.; Pirri, C. F.; Hernández, S.; Lamberti, A. Highly Uniform Anodically Deposited Film of MnO_2 Nanoflakes on Carbon Fibers for Flexible and Wearable Fiber-Shaped Supercapacitors. *ACS Appl. Mater. Interfaces* **2017**, *9* (34), 28386–28393.

(50) Xu, H.; Hu, X.; Yang, H.; Sun, Y.; Hu, C.; Huang, Y. Flexible Asymmetric Micro-Supercapacitors Based on Bi_2O_3 and MnO_2 Nanoflowers: Larger Areal Mass Promises Higher Energy Density. *Adv. Energy Mater.* **2015**, *5* (6), 1–7.

(51) He, Y.; Chen, W.; Li, X.; Zhang, Z.; Fu, J.; Zhao, C.; Xie, E. Freestanding Three-Dimensional Graphene/MnO_2 Composite Networks as Ultralight and Flexible Supercapacitor Electrodes. *ACS Nano* **2013**, *7* (1), 174–182.

Link to the next chapter

The role of the bio-polymer Alginic acid (Alg) in the electrolytic bath when used at different concentrations to synthesize EMD for supercapacitors was studied in the previous chapter 4. Further design and synthesis of EMD can be explored, broadening its potential application as a pseudocapacitive electrode in the energy storage field. Surfactants usually play a significant role in controlling morphologies and particle sizes, thus changing material properties. Unlike the polymers, it has been demonstrated by the researchers that the surfactants can get adsorbed on the metal surface and reduce the interfacial tension between solid and liquid. Therefore, in chapter 5, we prepared the EMD using various surfactants with different molecular structures and, adding them into the electrolytic bath for electrodeposition. The influence of the surfactants that occurred due to their physisorption/chemisorption on the Pb anode surface on the anchoring of the MnO_2 particles has been investigated using molecular modeling. The suitability and optimal concentrations of the surfactants on the EMD material electrochemical performance were also explored in chapter 5.

Chapter 5 Surfactant-mediated electrodeposition of manganese dioxide

This chapter is published as:

Surfactant-mediated electrodeposition of a pseudocapacitive manganese dioxide a twofer

Kethaki Wickramaarachchi, Manickam Minakshi Sundaram, David J. Henry

Journal of Energy Storage 2022 55 (A), 105403

DOI: https://doi.org/10.1016/j.est.2022.105403

Impact factor: 8.907

Journal of Energy Storage 55 (2022) 105403

Contents lists available at ScienceDirect

Journal of Energy Storage

journal homepage: www.elsevier.com/locate/est

Research papers

Surfactant-mediated electrodeposition of a pseudocapacitive manganese dioxide a twofer

Kethaki Wickramaarachchi, Manickam Minakshi Sundaram *, David Henry

College of Science, Health, Engineering and Education, Murdoch University, WA 6150, Australia

ARTICLE INFO

Keywords:
Electrolytic
Manganese dioxide
Cationic
Surfactants
Energy storage
Molecular dynamics

ABSTRACT

Electrochemical energy storage is one of the most promising ways of storing energy from intermittent, renewable sources. To meet the needs, the development of scalable, earth-abundant, chemically stable, and environmentally friendly electrode materials is crucial. This work presents four cationic surfactant-mediated manganese sulfate electrolytic solutions used for the synthesis of electrolytic manganese dioxide (EMD) to produce scalable material that satisfies the pre-requisites desired for supercapacitor applications. The influence of the surfactant molecular structure, its concentration, and its interaction in the electrolytic sulfate bath was studied, which opens up new possibilities for the fabrication of the supercapacitor electrode. The performance of three surfactants (Tetradecyltrimethylammonium bromide, Didodecyldimethylammonium bromide, Benzyldodecyldimethylammonium bromide) was benchmarked against the widely used Cetyltrimethylammonium bromide under identical conditions. The surfactants were chosen based on their different head groups and hydrocarbon chains. Benzyldodecyldimethylammonium bromide-assisted EMD (EMD/B-AB) in a single-electrode device showed improved capacitance of 602 F g^{-1} (at 1 mA cm^{-2}) over the other surfactant-mediated samples. The molecular dynamics simulations indicated that the electrodeposition of manganese dioxide is highly influenced by B-AB, as it adsorbs with the aryl group planar to the Pb surface. The appropriate concentration of B-AB surfactant in the bulk solution appears to be incorporated into the EMD deposit due to their hydrophobic nature and controlled nucleation and established improved pseudocapacitive performance to score a twofer. The asymmetric capacitor of EMD/B-AB_{30} vs. porous activated carbon exhibited a high specific capacitance of 91 F g^{-1}, with an energy density of 32.4 Wh kg^{-1} for a corresponding power density of 971 W kg^{-1}.

1. Introduction

Sustainable, clean, low-cost production and highly efficient energy technologies to store and supply energy are one of the most significant concerns in today's world. Presently, various types of electrochemical energy systems such as lithium-ion batteries (LIBs), electrochemical capacitors (ECs), metal-O_2 batteries (Zn-O_2; Li—O_2), and fuel cells are primarily used in the applications of portable electronics, hybrid electric vehicles, smart grids, and other rechargeable electronic devices [1,2]. Therefore, innovative materials chemistry is more appealing than ever for the means of continual improvement of high-power energy sources.

A number of surfactants exist with unparalleled potential in various industrial applications such as detergents, medicines, cosmetics, pharmaceuticals, corrosion inhibitors, wetting agents, and electrochemical devices [3]. Surfactants are organic compounds with opposing polarities, a head group with the affinity for polar phases and a tail group that attracts the non-polar phases, showing their amphiphilic nature. This unique structure of surfactants can be used to reduce the surface and interfacial tension [4]. Surfactant-mediated synthesis of materials plays a critical role in optimizing particle properties. The limitations of preparing stable dispersions in nanotechnology have been addressed by using amphiphilic surfactants as stabilizers to disperse hydrophobic inorganic nanomaterials such as carbon nanotubes [5], graphene [6], etc. Using surfactants as additives can alter the atomic surface arrangements, active sites and affect the chemisorption/physisorption process of the electrochemical energy storage materials [7–10]. The functions of the surfactants, when present in electrolytic baths, differ with their properties of electron density and the shape of adsorbate orbitals. Physisorption and chemisorption at the electrode substrate (Pb in this work) may take place depending on the properties of the surfactants. Adding surfactants to the electrolyte solution affects the kinetics and the electrodeposition mechanism. Surfactants can be

* Corresponding author.
E-mail address: m.minakshi-sundaram@murdoch.edu.au (M.M. Sundaram).

https://doi.org/10.1016/j.est.2022.105403
Received 24 January 2022; Received in revised form 8 July 2022; Accepted 26 July 2022
Available online 3 August 2022
2352-152X/© 2022 Elsevier Ltd. All rights reserved.

Author contribution

Contributor	Contribution (%)	Nature of contribution
Kethaki Wickramaarachchi	70	Conceptualization, experimentation, data collection, analysis and interpretation, drafting and critical revision of the manuscript.
Manickam Minakshi	30	Conceptualization, interpretation of data, critical revision of the manuscript.
David J. Henry		Theoretical insights and data interpretation.

5.1. Abstract

Electrochemical energy storage is one of the most promising ways of storing energy from intermittent, renewable sources. To meet the needs, the development of scalable, earth-abundant, chemically stable, and environmentally friendly electrode materials is crucial. This chapter presents four cationic surfactant-mediated manganese sulfate electrolytic solutions used for the synthesis of electrolytic manganese dioxide (EMD) to produce scalable material that satisfies the prerequisites desired for supercapacitor applications. The influence of the surfactant molecular structure, its concentration, and its interaction in the manganese sulfate electrolytic bath was studied, which opens up new possibilities for the fabrication of the supercapacitor electrode. The performance of three surfactants (Tetradecyltrimethylammonium bromide, Didodecyldimethylammonium bromide, Benzyldodecyldimethylammonium bromide) was benchmarked against the widely used Cetyltrimethylammonium bromide under identical conditions. The surfactants were chosen based on their different head groups and hydrocarbon chains. Benzyldodecyldimethylammonium bromide-assisted EMD (EMD/B-AB) in a three-electrode system showed improved capacitance of 602 F g^{-1} (at 1 mA cm^{-2}) over the other surfactant-mediated samples. The molecular dynamics simulations indicated that the electrodeposition of manganese dioxide is highly influenced by B-AB, as it adsorbs with the aryl group planar to the Pb surface. The appropriate concentration of B-AB surfactant in the bulk solution appears to be incorporated into the EMD deposit due to their hydrophobic nature and controlled nucleation and established improved pseudocapacitive performance to score a twofer. The hybrid capacitor of EMD/B-AB_{30} *vs*. porous activated carbon exhibited a high specific capacitance of 91 F g^{-1}, with an energy density of 32.4 Wh kg^{-1} for a corresponding power density of 971 W kg^{-1}.

5.2. Introduction

Sustainable, clean, low-cost production and highly efficient energy technologies to store and supply energy are one of the most significant concerns in today's world. Presently, various types of electrochemical energy systems such as lithium-ion batteries (LIBs), electrochemical capacitors (ECs), metal-O_2 batteries (Zn-O_2; Li-O_2),

and fuel cells are primarily used in the applications of portable electronics, hybrid electric vehicles, smart grids, and other rechargeable electronic devices [1,2]. Therefore, innovative materials chemistry is more appealing than ever for the means of continual improvement of high-power energy sources.

A number of surfactants exist with unparalleled potential in various industrial applications, such as detergents, medicines, cosmetics, pharmaceuticals, corrosion inhibitors, wetting agents, and electrochemical devices [3]. Surfactants are organic compounds with opposing polarities, a head group with an affinity for polar phases and a tail group that attracts the non-polar phases, showing their amphiphilic nature. This unique structure of surfactants can be used to reduce surface and interfacial tension [4]. Surfactant-mediated synthesis of materials plays a critical role in optimizing particle properties. The limitations of preparing stable dispersions in nanotechnology have been addressed by using amphiphilic surfactants as stabilizers to disperse hydrophobic inorganic nanomaterials such as carbon nanotubes [5], graphene [6], etc. Using surfactants as additives can alter the atomic surface arrangements, active sites and affect the chemisorption/physisorption process of the electrochemical energy storage materials [7–10]. The functions of the surfactants, when present in electrolytic baths, differ with their properties of electron density and the shape of adsorbate orbitals. Physisorption and chemisorption at the electrode substrate (Pb in this chapter) may take place depending on the properties of the surfactants. Adding surfactants to the electrolyte solution affects the kinetics and the electrodeposition mechanism. Surfactants can be adsorbed additives that can get adsorbed onto the electrode and reduce the mean free path for lateral diffusion of the ions when the element/compound diffuses to find the position with the lowest potential energy to deposit on the electrode [11].

In this chapter, we have employed four different surfactants (Figure 5.1) as additives in the electrolytic bath to study their influence and the relationship with the molecular structure to the electrodeposited manganese dioxide (EMD) characteristics. The surfactant-modified EMD was analyzed to explore its applicability in hybrid capacitor devices. The three quaternary ammonium-based surfactants (Figure 5.1 A-C), namely, Benzyldodecyldimethylammonium bromide, Didodecyldimethylammonium bromide, Tetradecyltrimethylammonium bromide, are labeled as (B-AB), (D-AB), (T-AB), respectively have not been researched widely for energy storage applications. The

quaternary ammonium-based surfactants are structured with at least one hydrophobic alkyl chain bonded to a positively charged nitrogen atom. Therefore, these surfactants have been chosen to study due to the fact that the different chain lengths and character of head groups, which can assist in structure-directing EMD formation. The surfactants are expected to control the disproportionation and hydrolysis reactions of the Mn^{2+} ions at the electrode-electrolyte interface. With their hydrophobic chains, surfactants can also help extend the operating voltage of the capacitor due to hydrophobic thin films incorporated in the electrode, which shifts the water electrolysis region [12]. The performance of the relatively new cationic surfactants is benchmarked against the well-known Cetyltrimethylammonium bromide (C-AB) (Figure 5.1D) [13–15] and pristine EMD. Previous studies reported that the adsorption of cationic and nonionic surfactants is greater than that of anionic surfactants [16]. Notably, there is hardly any report on the use of EMD when the cationic surfactants are varied in terms of the head group and the molecular chain for supercapacitor application. In this chapter, each cationic surfactant was tested at similar concentrations to compare the performances.

Herein, we demonstrate a significant improvement in capacitor activity and stability of surfactant-mediated EMD by tuning the interfacial tensions between solid and liquid phases, improving the dispersion stability, and controlling the geometry of the electrodeposited MnO_2. The use of extremely small amounts of surfactants to influence the EMD microstructural properties was another advantage compared to using metal elements or polymer additives. Compared to C-AB, the T-AB-assisted EMD was in a similar range of performance with slightly higher values for EMD/C-AB, which could be related to the surfactant chain length. Similar behaviors have also been reported elsewhere [17,18]. D-AB has double chains (with relatively shorter individual chain lengths), which are strongly adsorbed and well-performed at lower concentrations. The D-AB reached its critical micelle concentration (CMC) within the chosen concentrations, and EMD/D-AB performance decreased when surpassing the CMC value. When the micelles are formed, they can saturate the electrode surface with one or more surfactant layers, and the interactions between them could also be significant. This phenomenon can affect the Mn^{2+} ion reaction, creating an additional electrostatic barrier at the substrate for EMD deposition and promoting surfactant incorporation in EMD. Among the chosen surfactants, the presence of B-AB in the electrolytic bath helped improve the EMD material properties. This can be attributed to the B-AB

molecular structure with the aryl group bonded to the hydrophilic head group that enhanced the molecular assembling of the EMD particles. We have also explored the effect of B-AB orientation on the Pb substrate and compared it with the C-AB and pristine EMD, as shown in molecular simulation. To the best of our knowledge, there is no evidence in the literature for such a study using both experimental and computational work to explore the influence of surfactant in the electrodeposited material. The EMD/B-AB led to improved microstructure in contact with the electrolyte and improved storage properties (capacitance) among all the materials. A hybrid capacitor was fabricated using best performed EMD material (EMD/B-AB_{30}), and activated carbon (MS-AC) [19] showed higher energy and power densities comparable to the recently reported literature for the asymmetric/hybrid capacitors. To this end, the findings on the orientation of the B-AB on the Pb substrate surface with the effect of the aromatic ring in the alkyl chain provide new insight into enhancing the pseudocapacitive properties of EMD for supercapacitors.

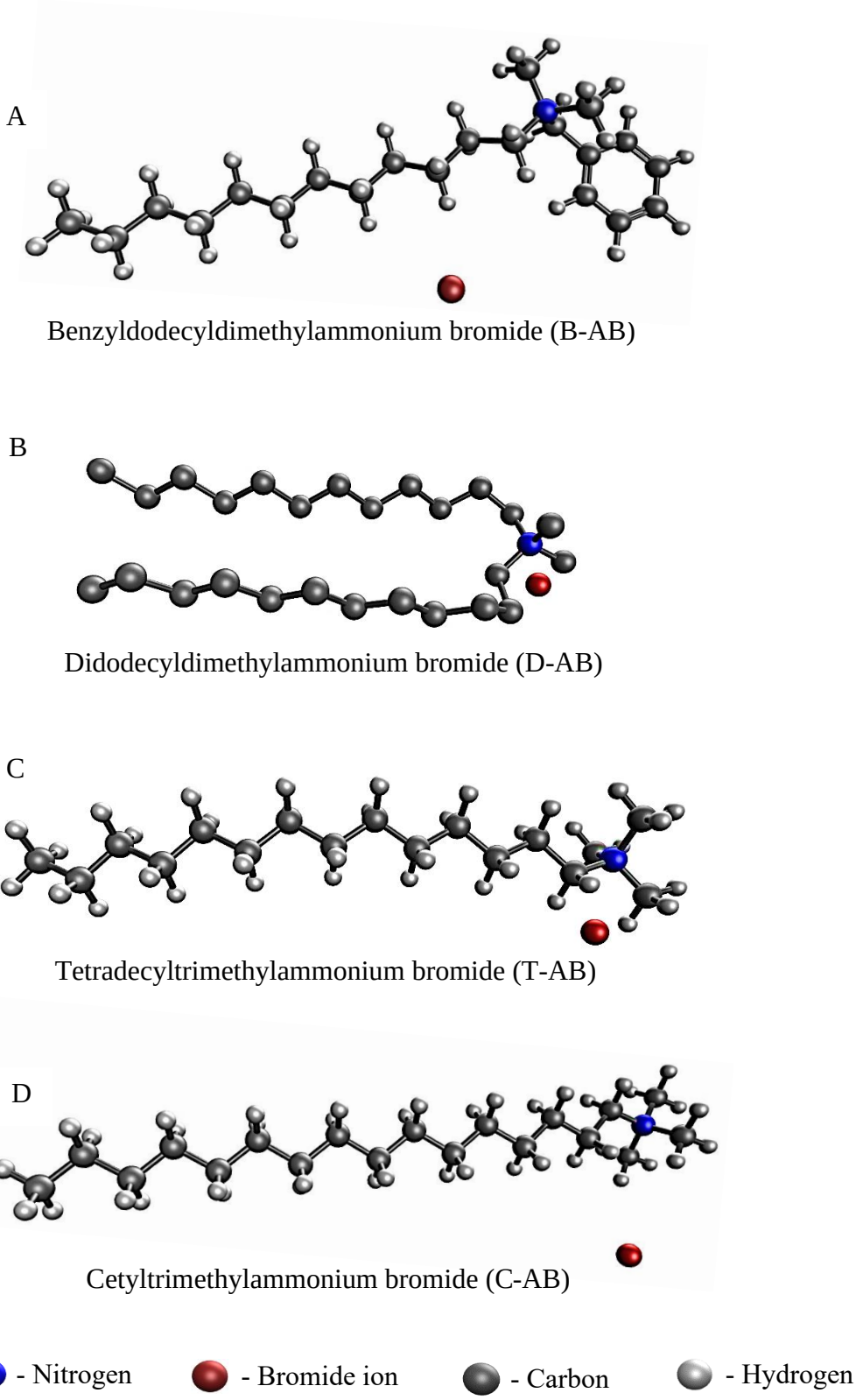

Figure 5.1 Molecular structures of the surfactants used in the electrodeposition.

5.3. Materials and methods

5.3.1. Electrode material synthesis

Manganese dioxide material was deposited on a lead (Pb) anode substrate, where Stainless Steel (SS) was used as the cathode (Figure 5.2). An aqueous solution of acidic (0.25 M H_2SO_4) manganese sulfate (0.9 M of Mn^{2+}) was used as the electrolyte bath. Pristine EMD was synthesized from the surfactant-free electrolyte, and each surfactant was homogeneously dispersed in the electrolyte to synthesize the surfactant-mediated EMD. The electrodeposition was carried out galvanostatically at an applied current of 200 A m^{-2} at 95 ± 2 ºC for 5 h. Then the anode was removed from the bath, rinsed with deionized (DI) water, and kept in the oven for drying overnight. Later, the deposited material was scraped from the substrate cautiously without damaging it to avoid Pb particle contamination. The EMD flakes were rinsed with DI water, dried in the oven at 80 °C for 12 h, and termed as an active material for supercapacitor studies.

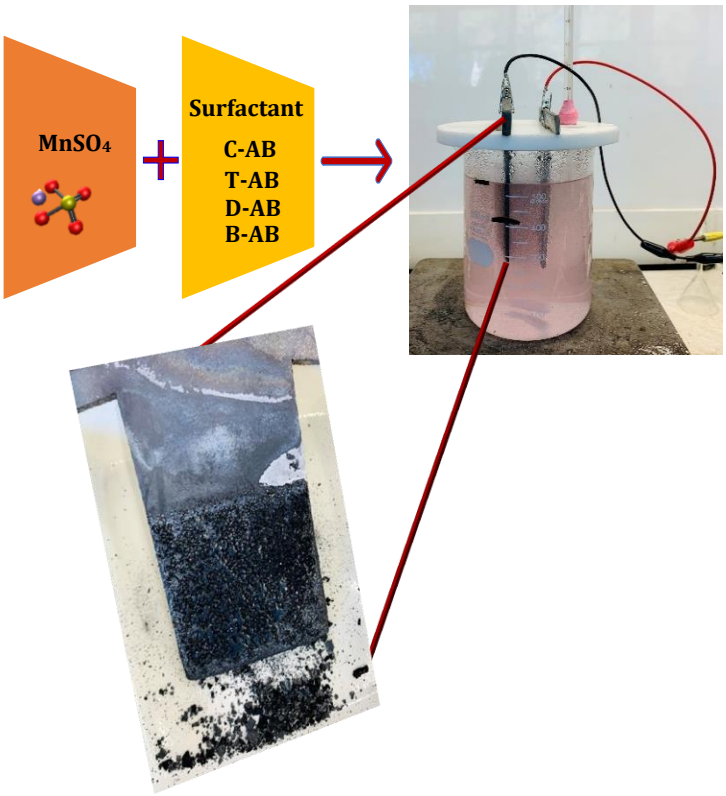

Figure 5.2 Electrodeposition of manganese dioxide on Pb electrode using manganese sulfate and surfactant electrolyte solution. The magnified image shows EMD deposited on the Pb electrode hanger bar and the scraped particles suitable for characterization.

5.3.2. Physicochemical characterization

The crystallinity of the synthesized material was characterized using a GBC Emma X-ray diffractometer using Cu Kα radiation (λ = 1.5418 Å) operated at 28 kV and 10 mA. Mid-infrared (MIR) analysis was carried out at the infrared facility at the Australian Synchrotron, Melbourne. The beamline was coupled to a Bruker IFS 125/HR Fourier transform (FT) spectrometer. The data was acquired in single reflection diamond attenuated total reflection (ATR) transmission mode within 1970 - 400 cm^{-1} in the mid-IR using Si:B photodetector. The data was collected using OPUS software version 8.0.19. The microstructure and the surface morphology of the materials were investigated using field emission scanning electron microscopy (FE-SEM, Tescan Clara). Transmission electron microscope observations (TEM) observations were performed by FEI Talos FS200X G2. The surface area and pore analysis of the

synthesized samples were conducted by the N_2 adsorption-desorption isotherms at 77 K using ASAP 2010 MicroPore System (Micromeritics).

5.3.3. Electrochemical characterization

The active material, acetylene black and polyvinylidene difluoride (PVDF) binder, were mixed in a mass ratio of 75:15:10, respectively, in N-methyl-2-pyrrolidone (NMP) solvent and made into a slurry. The graphite current collector was coated with the slurry and dried at 80 °C for 12 hours. Electrochemical measurements of all the EMD electrodes were taken using a three-electrode configuration (half-cell measurements) in an aqueous 2 M NaOH electrolyte, with a Hg/HgO reference electrode and a platinum (Pt) wire counter electrode.

The best-performed materials were identified after analyzing the physicochemical and electrochemical characterization of different electrodes in the three-electrode system. The two surfactants that showed promising results in the preliminary studies were selected for further experiments while varying at different concentrations. Finally, the highly performed electrode material was chosen to study the hybrid capacitor (two-electrode system) performance that comprised of surfactant-mediated EMD (EMD/B-AB_{30}) *vs*. in-house synthesized biomass-derived activated carbon (MS-AC) [19]. The masses of the EMD/B-AB_{30} and MS-AC used in the hybrid capacitor are 0.5 mg and 1.3 mg, respectively, calculated using equation 3.4 in chapter 3. The hybrid capacitor was evaluated by CV and GCD tests within the potential range of 0-1.6 V. The equations used to calculate the specific capacitance (F g^{-1}), energy density (Wh kg^{-1}), and power density (W kg^{-1}) from GCD measurements are explained in chapter 3 (equation 3.5 - 3.7).

5.4. Computational modeling

Molecular dynamics (MD) simulations were performed to explore the nature of the interactions between the different species in solution and a lead substrate. Two surfactants, benzyl dodecyl dimethylammonium bromide (B-AB) and cetyltrimethylammonium bromide (C-AB) (Figure 5.1 A and D), were investigated using the MD simulations. The low concentration of the surfactants in the experiments

meant that it was not possible to exactly recreate the experimental concentrations in the simulation. However, the simulations used the experimental concentrations for Mn^{2+} (0.9 M), SO_4^{2-} (1.15 M), and H^+ (0.5 M), but the surfactants were simulated at a concentration of 1.5 x 10^{-4} M. The Pb surface was modeled using a crystalline lead structure cleaved along the 1 0 0 planes. The modeling framework for the molecules was developed using Materials Studio 2017 R2. All species were represented by fully atomistic models. Each simulation was placed in a unit cell with dimensions 39.6 x 39.6 x 90.0 Å under 3D periodic boundary conditions.

The potential energy for each simulation was calculated using the COMPASS force field, which has previously been shown to perform well in describing the interactions between condensed hydrophilic and hydrophobic species [20–22]. Electrostatic interactions were calculated using the Ewald procedure, while van der Waal's interactions were calculated with an atom-based procedure using a 12.50 Å cutoff, a spline width of 1.00 Å, a buffer of 0.50 Å, and a long-range tail correction. The modeled systems were initially energy minimized using the conjugate-gradient procedure, with a convergence criterion of 0.04 kJ mol^{-1}. Molecular dynamic simulations were performed in the canonical ensemble (NVT, constant number of atoms (*N*), volume (*V*), and temperature (*T*)), equilibrated for 500 picoseconds (ps), followed by data acquisition for 9500 ps using 2.0 femtosecond (fs) time steps. The "Fix bond" option was selected to improve the computational efficiency that constrained C-H and O-H bond lengths during the simulation. The coordinates of the lead atoms of the substrate were also constrained during the simulation. The temperature was maintained at 298 K using the Andersen thermostat [23] with a collision ratio of 1.0.

5.5.Results and discussion

5.5.1. Physicochemical characterization

Morphology. Manganese dioxide flakes were electrodeposited on the Pb anode in the absence and presence of surfactants at various concentrations while keeping the other parameters constant to make a meaningful comparison. Regardless of the presence of surfactants, black MnO_2 flakes were visibly deposited on the Pb substrate invariably.

Figure 5.3 shows the surface morphologies of the pristine EMD (absence of surfactant) and EMD/surf (surfactant-mediated EMD) with 30 mg l^{-1} surfactant concentration. Figure 5.3 gives the surface morphologies of EMD/surf with 15 mg l^{-1}. The pristine EMD in Figure 5.3A shows spindle-shaped aggregated particles in a net-like assembly. A compacted nature of the micro-sized particles is visible. With the introduction of surfactants, the surface morphologies of the surfactant-mediated EMD have shown in Figure 5.3 B-E. The FESEM images have not markedly changed for EMD/T-AB_{30} (Figure 5.3B) against the well-known EMD/C-AB_{30} (Figure 5.3C) and pristine EMD (Figure 5.3A) except for the particle shape. The aggregated arrangement remains while a small change is observed as the particle shapes have been shown to form tiny rod-like shapes compared to the pristine EMD. Interestingly, for EMD/D-AB (Figure 5.3D) and EMD/B-AB (Figure 5.3E), the surface morphology has been dramatically changed with an emerged nanoscale texture. This shows stronger adsorption of D-AB and B-AB onto the EMD surface compared to that of T-AB and C-AB counterparts. The D-AB bearing the double hydrocarbon chains and the B-AB with a longer chain and larger head group strongly influenced the surface modification of the EMD. According to Figure 5.3D, adding D-AB (30 mg l^{-1}) into the electrolytic bath led to the formation of prickly sow-thistle flower-like morphology. When the B-AB was introduced, the morphology evolved with composed particles representing Romanesco broccoli-like surface morphology (Figure 5.3E). The adsorption of D-AB and B-AB on the EMD surface has also reduced the particle size by limiting the growth compared to the pristine EMD. The fine branches appeared like the rootlets on the modified surface increased the surface area of the EMD/D-AB and EMD/B-AB, as evidenced by the BET surface area values. Overall, Figure 5.3 clearly emphasizes the effect of the surfactants depending on their molecular structures on forming nucleation and film growth during deposition. The presence of the well-defined shaped nanoparticles enhances the surface area and pores, which in turn influences its pseudocapacitive properties through fast ion transport toward high capacitance.

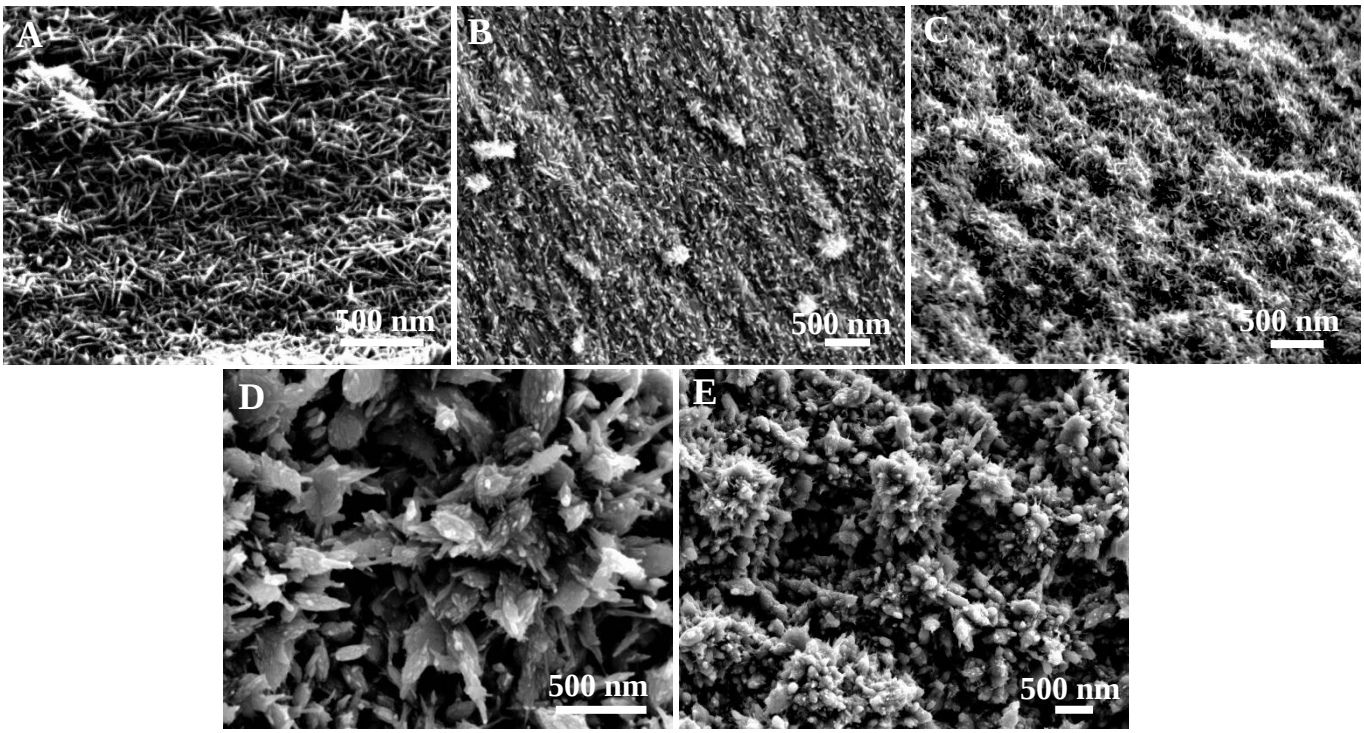

Figure 5.3 Field emission scanning electron microscope (FESEM) images of the EMD synthesized in the absence (A) pristine EMD and presence of the surfactants (B- E) at the concentration of 30 mg l^{-1} in the electrolytic bath; (B) EMD/T-AB_{30}, (C) EMD/C-AB_{30}, (D) EMD/D-AB_{30}, and (E) EMD/B-AB_{30}.

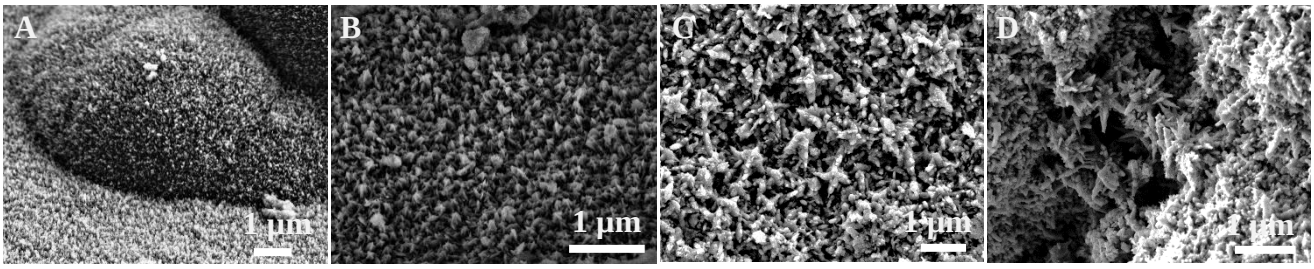

Figure 5.4 Field emission scanning electron microscope (FESEM) images of the EMD synthesized in the presence of the surfactants at the concentration of 15 mg l^{-1} in the electrolytic bath; (A) EMD/T-AB_{15}, (B) EMD/C-AB_{15}, (C) EMD/D-AB_{15}, and (D) EMD/B-AB_{15}.

Further characterization of EMD samples in a TEM confirms the nanostructured material. Figure 5.5 represents the TEM images obtained after pipetting 3 - 5 µl of the powdered form of EMD dispersed in ethanol onto a TEM grid. The TEM images of the pristine EMD are compared with surfactant-mediated EMD/D-AB_{30} and EMD/B-AB_{30} in Figure 5.5 A-C, respectively, confirming the presence of nanoparticles. For EMD/B-AB_{30} (Figure 5.5C), several ultrafine nanoparticles have a uniform distribution of shapes and sizes and are densely packed, whereas they are less defined for both EMD/D-AB_{30} (Figure 5.5B) and pristine EMD (Figure 5.5A). The inclusion of B-AB in the electrolytic bath passivates the layer with the fine surfactant clusters embedded in EMD nanocrystals, which made the deposition more resistant to aggregate and refined the grain structure. The deposition mechanism of EMD initiates anodically upon applying a voltage to the Pb electrode immersed in the electrolyte solution. With the continuation of electrodeposition, more surfactant molecules tend to get adsorbed onto the EMD surface. The presence of B-AB molecules provided by large electrostatic attraction with the ions due to their larger head groups highly influences the growth process, controlling the assembly of particles within the deposited material. The surfactants may have controlled the deposition mechanisms (disproportionation and hydrolysis reactions in chapter 3) initiated by the Mn^{2+} ions by stabilizing the Mn^{3+} ions at the Pb interface, providing sufficient time to react and deposit as MnO_2. This can limit prospective portions of MnOOH deposition. The selected area electron diffraction (SAED) pattern for EMD/D-AB (inset of Figure 5.5B) and EMD/B-AB (inset of Figure 5.5C) indicate the semicrystalline nature of the EMD materials. The high resolution-TEM was employed for EMD/D-AB (Figure 5.5D) and EMD/B-AB (Figure 5.5E) to gain further insights. The corresponding high-angle annular dark-field scanning transmission electron microscopy (HAADF-STEM) images and energy-dispersive x-ray spectroscopy (EDS) mapping revealed the homogenous distribution of Mn and O in both samples confirming the successful formation of EMD deposits.

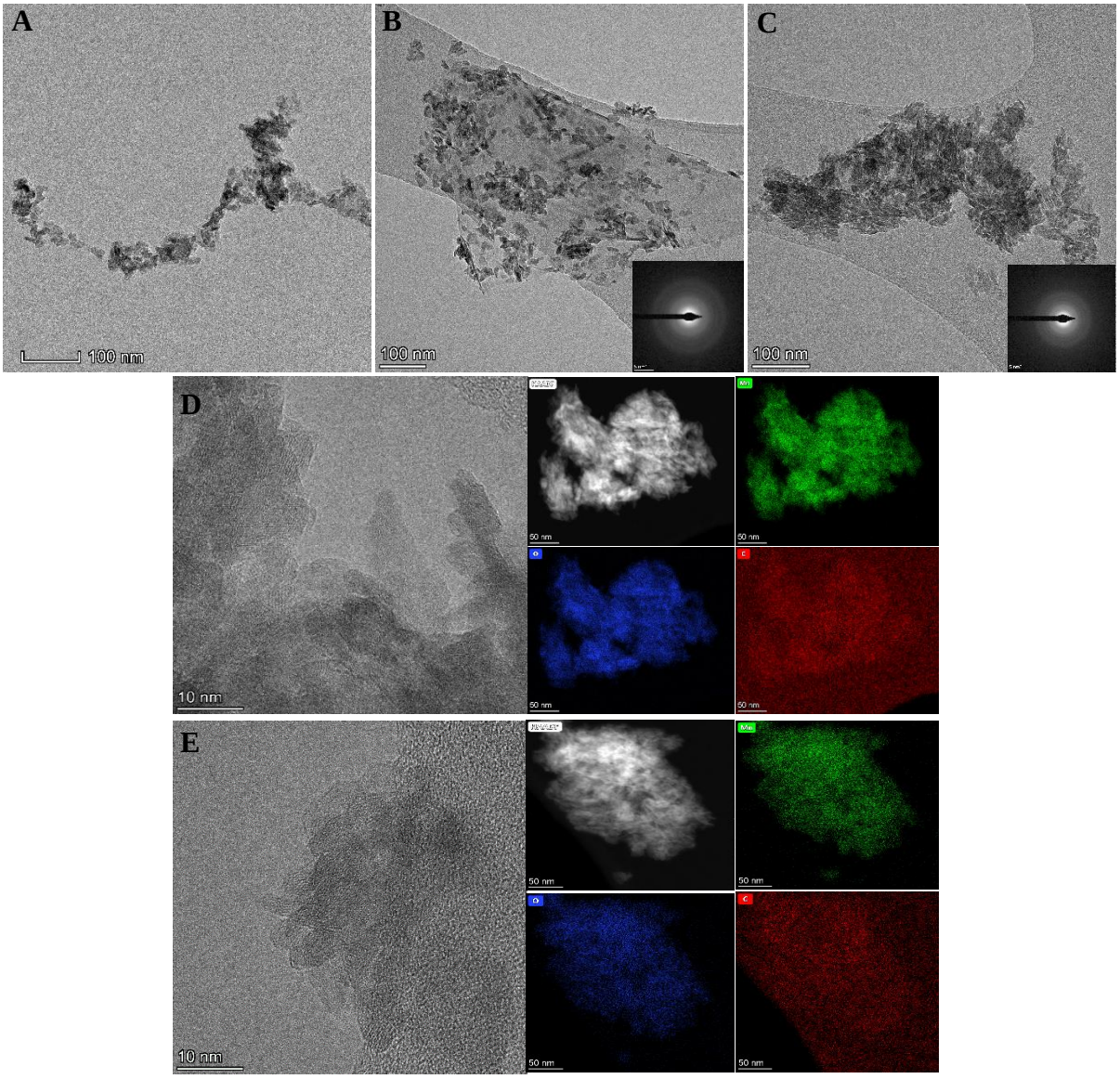

Figure 5.5 Transmission electron microscope (TEM) images of (A) Pristine EMD, (B) EMD/D-AB_{30}, and (C) EMD/B-AB_{30}. High-resolution transmission electron microscopy (HR-TEM) image, the corresponding High angle annular dark-field (HAADF) - scanning transmission electron microscopy (STEM) images, and energy-dispersive x-ray spectroscopy (EDS) elemental mapping images of (D) EMD/D-AB_{30}, and (E) EMD/B-AB_{30}.

XRD and IR analyses. Figure 5.6A presents the X-ray diffraction (XRD) patterns of the EMD materials to reveal their crystal structure. All the observed X-ray diffraction peaks are identified as the orthorhombic gamma (γ) phase of MnO_2 without any detectable impurities. Surfactant-mediated EMD samples did not show any significant

variation in the peak intensities implying the crystallographic orientations are like that of pristine EMD. As the surfactant concentrations used for the electrochemical synthesis are a meager amount, it is undeniable that no significant changes visibly occur in the crystal structure. Therefore, all the profiles can be indexed to the orthorhombic γ-MnO_2 (JCPDS card no. 65-1298), which is favorable for electrochemical energy storage performance. The broad diffraction peaks, which is a characteristic nature of EMD, suggest the semicrystalline nature of the samples. The semicrystalline nature of the nanoparticles has also been confirmed by high-resolution TEM studies. To analyze any presence of surface functional groups on the electrodeposited surface, mid-IR spectra are employed, and the spectra in the region 500-1970 cm^{-1} are shown in Figure 5.6B for pristine EMD and chosen surfactant-mediated EMD materials. The broad peak observed for all the samples around 600 cm^{-1} is the characteristic absorption band of γ-MnO_2 as expected for this material, which corresponds to the stretching collision of H-O-H [24,25]. The absorption band ~995 cm^{-1} is attributed to the bending vibrations of the O-H groups combined with the Mn atoms [26,27]. Additionally, shoulder peaks between 900-1970 cm^{-1} can be assigned to varying degrees of hydrogen and Mn bonding in the samples [28,29], representing the surface -OH groups for EMD particles. All these facts point to the importance of molecular structure and length of chain for the chosen surfactant, and its introduction in the electrolytic bath leads to a larger concentration of nanoparticles and its size and arrangement but with only subtle changes in the structure on the atomic level.

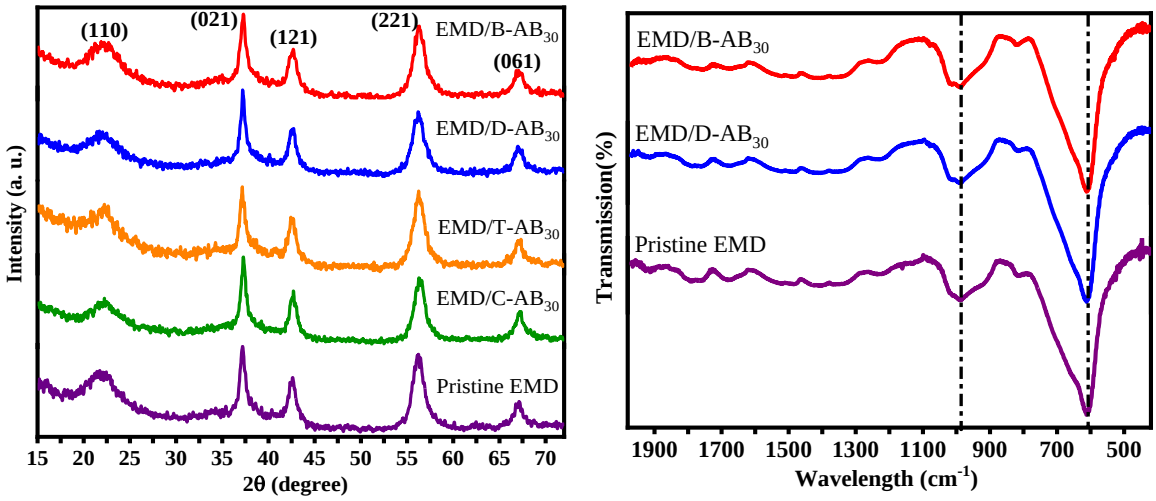

Figure 5.6 (A) X-ray diffraction (XRD) patterns and (B) Mid-IR spectra of EMD synthesized in the absence (pristine) and presence of the surfactants (labeled in the respective figures) at the concentration of 30 mg l^{-1} in the electrolytic bath.

Surface area and pore distribution analyses. Figure 5.7 shows the nitrogen adsorption-desorption isotherms and pore size distribution analysis of the pristine EMD compared with the surfactant-mediated EMD synthesized at a similar surfactant concentration (30 mg l^{-1}). The surface area and pore analysis values are tabulated in Table 5.1. All the curves exhibit a type IV isotherm with an H2 hysteresis loop, implying the presence of mesoporous samples. The measured BET surface area of the pristine EMD, EMD/T-AB, and EMD/C-AB is arrayed in a similar range (~80 m^2 g^{-1}), while the EMD/D-AB and EMD/B-AB exhibit relatively higher values ~100 m^2 g^{-1}. Compared to pristine EMD, the surfactant-added electrolytic bath could stabilize the particles at smaller sizes uniformly, resulting in an improved surface area that is more pronounced for EMD/D-AB and EMD/B-AB. This can be attributed to the double chain length of the D-AB, which effectively reduces the interfacial tension at the electrolyte/substrate when compared to that of T-AB and C-AB [30] counterpart surfactants. A similar contribution also applies to B-AB, in addition to that, it has a polar head group bonded to an aryl group that is inclined to get adsorbed onto a particle surface during deposition. Therefore, the B-AB could be more influential on the reactions of Mn^{4+} at the substrate and the conformation of MnO_2 on the surface. The well-developed mesopores of EMD/B-AB originated from the way of refining the

grain structure, as evidenced in the microscopy analysis. During the electrodeposition process, a rough surface was initially built upon the Pb surface, accompanied by nucleation. In the absence of surfactants, it is difficult to scrape off the EMD materials from the substrate. However, in the presence of the B-AB, the EMD deposits can be easily scraped from the substrate due to reduced interfacial tension. This simple and cost-effective protocol will further eliminate the Pb contamination in the EMD and make the production scalable. However, an excess amount of surfactant would disrupt the EMD structure therefore, the concentration is optimized. The aromaticity and the electronic structure stemming from the surfactant-mediated EMD would facilitate the electrochemical performance discussed in the subsequent section.

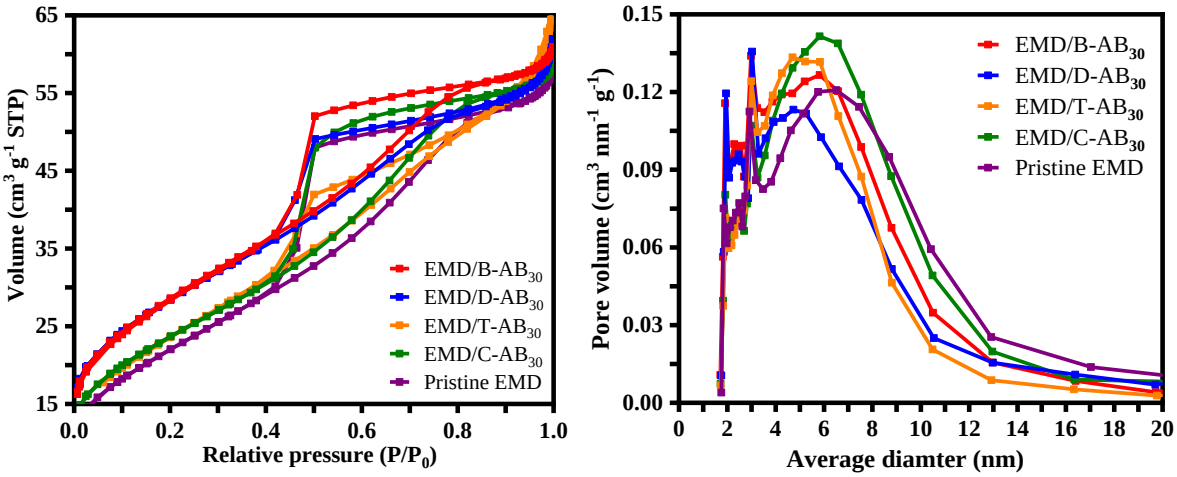

Figure 5.7 Nitrogen adsorption and desorption isotherms of EMD synthesized in the absence (pristine) and presence of the surfactants (labeled in the respective figures) at the concentration of 30 mg l^{-1} in the electrolytic bath and the corresponding surface area and pore analysis data.

Table 5.1 Surface area and pore analysis data of pristine EMD and EMD/surf materials.

Sample	BET surface area ($m^2\ g^{-1}$)	BJH average pore diameter (nm)
EMD/B-AB_{30}	103.1	3.96
EMD/D-AB_{30}	99.5	3.95
EMD/T-AB_{30}	83.2	3.76
EMD/C-AB_{30}	84.6	4.19
Pristine EMD	80.5	4.31

5.5.2. Electrochemical characterization: Three-electrode system (Half-cell measurements)

The electrochemical profiles of the surfactant-mediated EMD materials were characterized by the typical three-electrode system and compared against the pristine EMD. The three-electrode configuration comprises EMD as the working electrode, Pt as the counter, and Hg/HgO serving as a reference electrode. Figure 5.8 A and B show the cyclic voltammetry (CV) curves related to all the EMD materials in the absence and presence of surfactants at a 10 mV s^{-1} scan rate. The CV curves show no clear redox peaks in each curve, indicating the typical pseudocapacitor nature of the electrodeposited MnO_2 material. It suggests the rapid intercalation/deintercalation of Na^+ ions into the material. Accordingly, two charge storage mechanisms can be proposed in the reaction, R(5.1) and R(5.2).

$$MnO_2 + Na^+ + e^- \leftrightarrow MnOONa \qquad \text{R(5.1)}$$

$$(MnO_2)_{surface} + Na^+ + e^- \leftrightarrow (MnO_2 - Na)_{surface} \qquad \text{R(5.2)}$$

The shape of the CVs remains the same for all the samples studied, implying the electrochemical process is identical. However, the area of the CV curve increased for all the surfactant-mediated EMD deposits against the pristine EMD, resulting in enhanced specific capacitance. The extent of the area under the CV curve was found

to be higher for EMD/D-AB and EMD/B-AB samples. Figure 5.8 C and D shows the corresponding galvanostatic charge-discharge (GCD) profiles, where the applied current rate was 1 mA cm^{-2}. When tested at 1 mA cm^{-2} current, the electrodes exhibited specific capacitances of 98, 110, 126 ,128, 133, 180, 274, 564, 602 for pristine EMD, EMD/T-AB_{15}, EMD/C-AB_{15}, EMD/T-AB_{30}, EMD/C-AB_{30}, EMD/D-AB_{15}, EMD/D-AB_{30}, EMD/B-AB_{15}, EMD/B-AB_{30}, respectively. Figure 5.8E presents the rate performance tested at different current densities of 0.5, 1, 2, 3, 4, 5 mA cm^{-2} (1, 2, 4, 6, 8, 10 A g^{-1} respectively). Overall, increasing the current decreases the specific capacitance, which is expected as there is only less time available for ion transfer at higher current densities. The B-AB-modified EMD materials delivered the best performance among the samples studied, while the D-AB-modified EMD also exhibited considerable improvement. The obtained specific capacitance is comparable to the high rate performances recently reported for electrolytic manganese dioxide capacitors in the literature, 489.7 [31], 526.44 [32], 458 [33], 170 [34] F g^{-1}. Even at the higher current rates, the EMD/B-AB and EMD/D-AB sustained to provide higher capacitances than the pristine EMD (Figure 5.8E). Further comparisons of CV, GCD, and EIS performance of the EMD materials are given in Figure 5.9. Capacitances delivered from each electrode material at a 1 mA cm^{-2} current rate were evaluated in Figure 5.8F. Based on the performances shown in Figure 5.8F, EMD/B-AB_{15} and EMD/B-AB_{30} tested at two different concentrations were found to be superior, having the highest values of 564 F g^{-1} and 602 F g^{-1}, respectively. The presence of D-AB surfactants also shows some potential, but the available capacitance for EMD/D-AB is half to that of EMD/B-AB and twice the amount to that of the pristine EMD. To further demonstrate the function of the EMD/B-AB and EMD/D-AB, additional experiments were conducted at their varying concentrations, and to get more insights, simulations have been performed at the molecular level. The summarized results of EMD/B-AB are illustrated in Figure 5.10, and EMD/D-AB are in Figure 5.11.

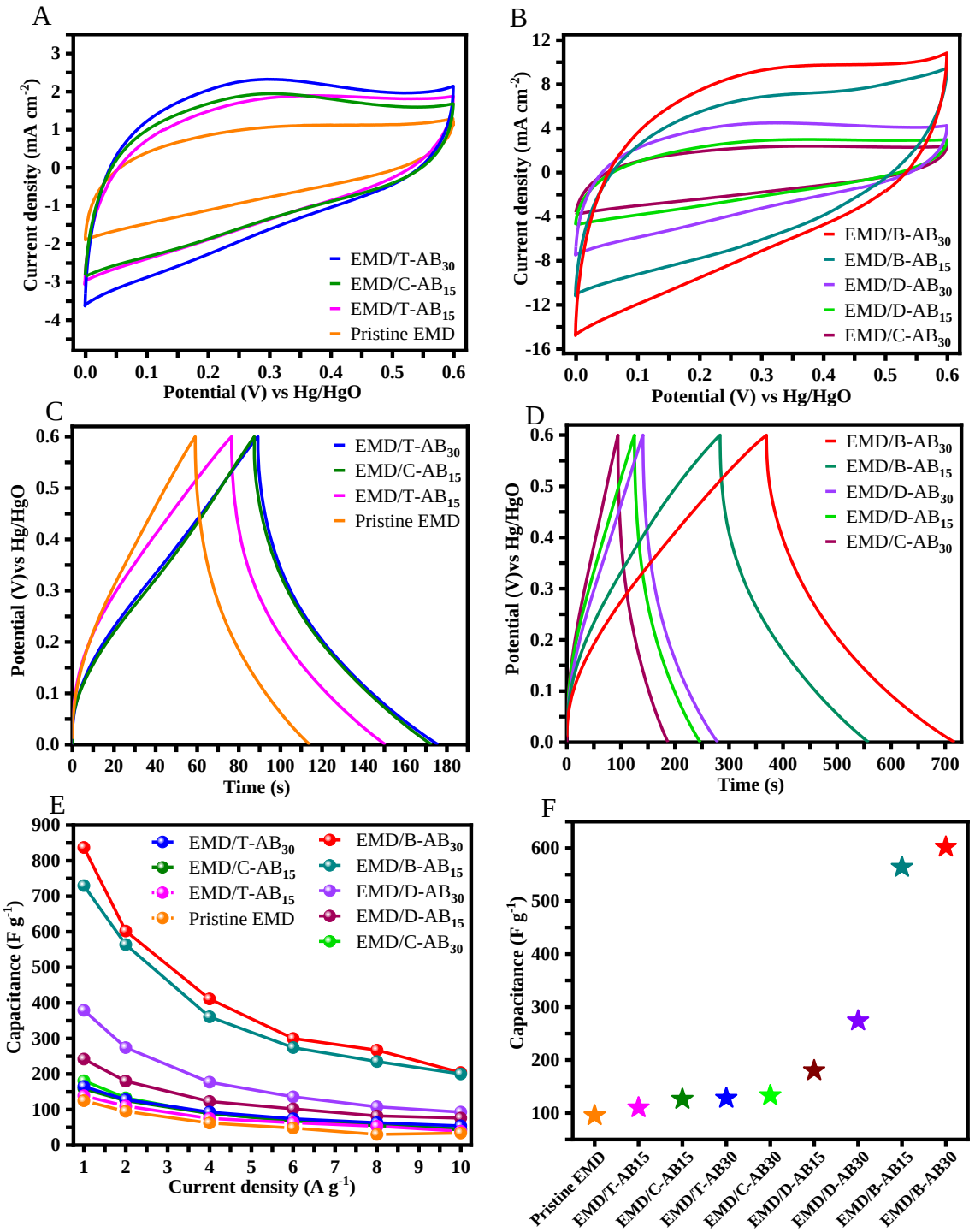

Figure 5.8 (A-B) Cyclic voltammetry at 10 mV s^{-1} scan rate, (C-D) galvanostatic charge-discharge curves at 1 mA current rate; (E) rate performance of all the samples (the trend lines connecting the data points are only for showing the data points distribution pattern), (F) obtained capacitance value of EMD synthesized in the absence (pristine), and presence of the surfactants (labeled in the respective figures) at the concentration 15 and 30 mg l^{-1} in the electrolytic bath.

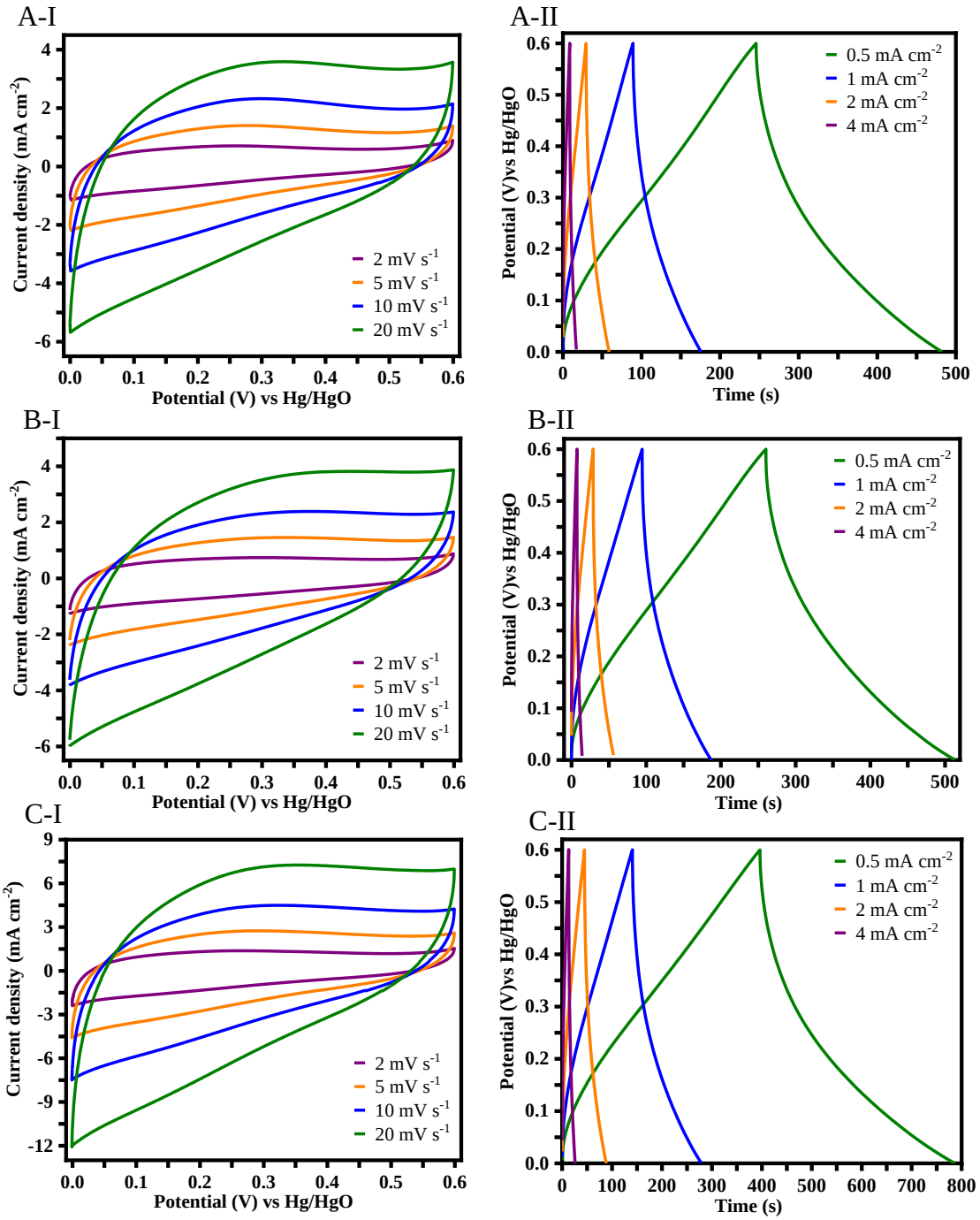
A-I
Current density (mA cm-2)
Potential (V) vs Hg/HgO
2 mV s-1
5 mV s-1
10 mV s-1
20 mV s-1
A-II
Potential (V)vs Hg/HgO
Time (s)
0.5 mA cm-2
1 mA cm-2
2 mA cm-2
4 mA cm-2
B-I
Current density (mA cm-2)
Potential (V) vs Hg/HgO
2 mV s-1
5 mV s-1
10 mV s-1
20 mV s-1
B-II
Potential (V)vs Hg/HgO
Time (s)
0.5 mA cm-2
1 mA cm-2
2 mA cm-2
4 mA cm-2
C-I
Current density (mA cm-2)
Potential (V) vs Hg/HgO
2 mV s-1
5 mV s-1
10 mV s-1
20 mV s-1
C-II
Potential (V)vs Hg/HgO
Time (s)
0.5 mA cm-2
1 mA cm-2
2 mA cm-2
4 mA cm-2

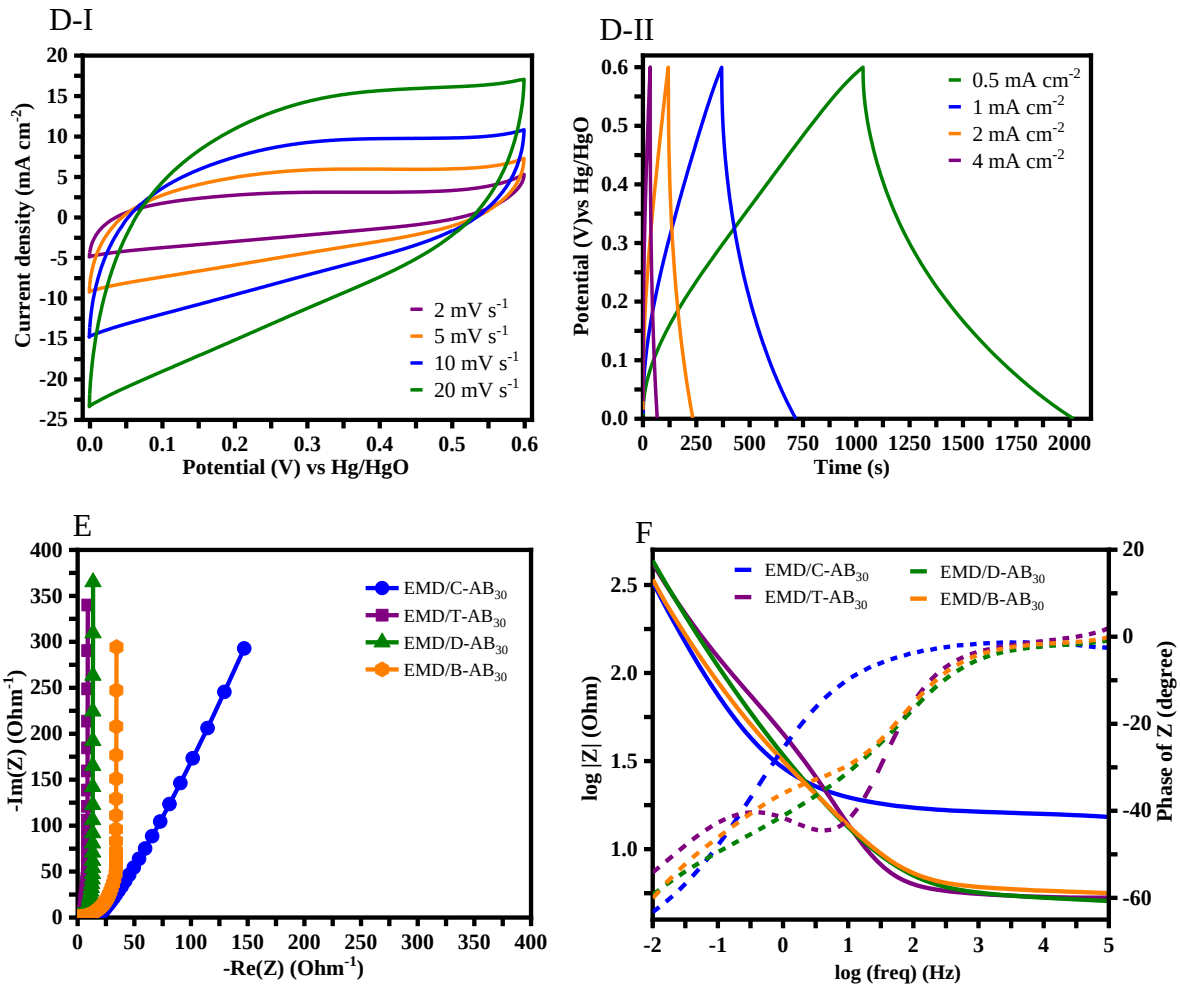

Figure 5.9 Cyclic voltammetry and Galvanostatic charge-discharge (GCD) curves of (A-I, A-II) EMD/T-AB$_{30}$, (B-I, B-II) EMD/C-AB$_{30}$, (C-I, C-II) EMD/D-AB$_{30}$, (D-I, D-II) EMD/B-AB$_{30}$, (E) Electrochemical impedance spectroscopy and (F) Bode impedance diagrams of EMD/T-AB$_{30}$, EMD/C-AB$_{30}$, EMD/D-AB$_{30}$, EMD/B-AB$_{30}$ samples.

Figure 5.10 summarizes the electrochemical performances and the physicochemical characteristics of EMD/B-AB with varying concentrations, i.e., 15, 30, and 60 mg l^{-1}. The CV curves of the EMD/B-AB at various concentrations (Figure 5.10A) show the areas of the curved surface around 0.3 V *vs*. Hg/HgO increase with the increase in concentration from 15 - 60 mg l^{-1}. To elaborate further, the corresponding GCD curves (Figure 5.10B) of the samples with increasing concentrations showed a quasi-triangular shape representing a longer discharge time than the charging time with an inflection at a voltage of around 0.2 V, indicating pseudocapacitive properties. The

specific capacitance of the EMD/B-AB demonstrated 564 F g^{-1} (at 1mA cm^{-2}) at 15 mg l^{-1} surfactant concentration. After doubling the concentration to 30 mg l^{-1}, the capacitance improved to 602 F g^{-1}. When the concentration was further increased to 60 mg l^{-1}, the calculated capacitance was reduced to 582 F g^{-1}. Figure 5.10C represents the GCD curves related to the half-cell at different currents. The specific capacitance values for 30 mg l^{-1} (EMD/B-AB_{30}) at 1, 2, 4, 6, 8, 10 A g^{-1} were 837, 602, 411, 300, 267, 204 F g^{-1}. Figure 5.10C indicates the current rate performance curve of an EMD/B-AB sample is feasible for higher current rate performance. Overall, the study of the EMD/B-AB sample with varying concentrations suggests that increasing the concentrations of the surfactants in the electrolytic bath over the threshold value (30 mg l^{-1}) would lower the energy values as the surfactant can passivate the layers covering the MnO_2 particles. Therefore, it concludes that the maximal specific capacitances of EMD synthesized in the presence of B-AB can be reached at a concentration within the range of 30 - 60 mg l^{-1}. At higher concentrations, the solubility of the B-AB surfactant reaches its limit while reaching its critical micelle concentration (CMC). The concentrations used in work in this chapter are lower than the CMC (5.3 × 10^{-3} mol l^{-1}) [35] of the B-AB surfactant. This is explained due to agglomerative formations (Figure 5.10D), the enhanced size of the mesopores (Figure 5.10F) rather than any structural influence as evidenced in the XRD (Figure 5.10E) for surfactant-mediated EMD at concentrations 15 - 60 mg l^{-1}.

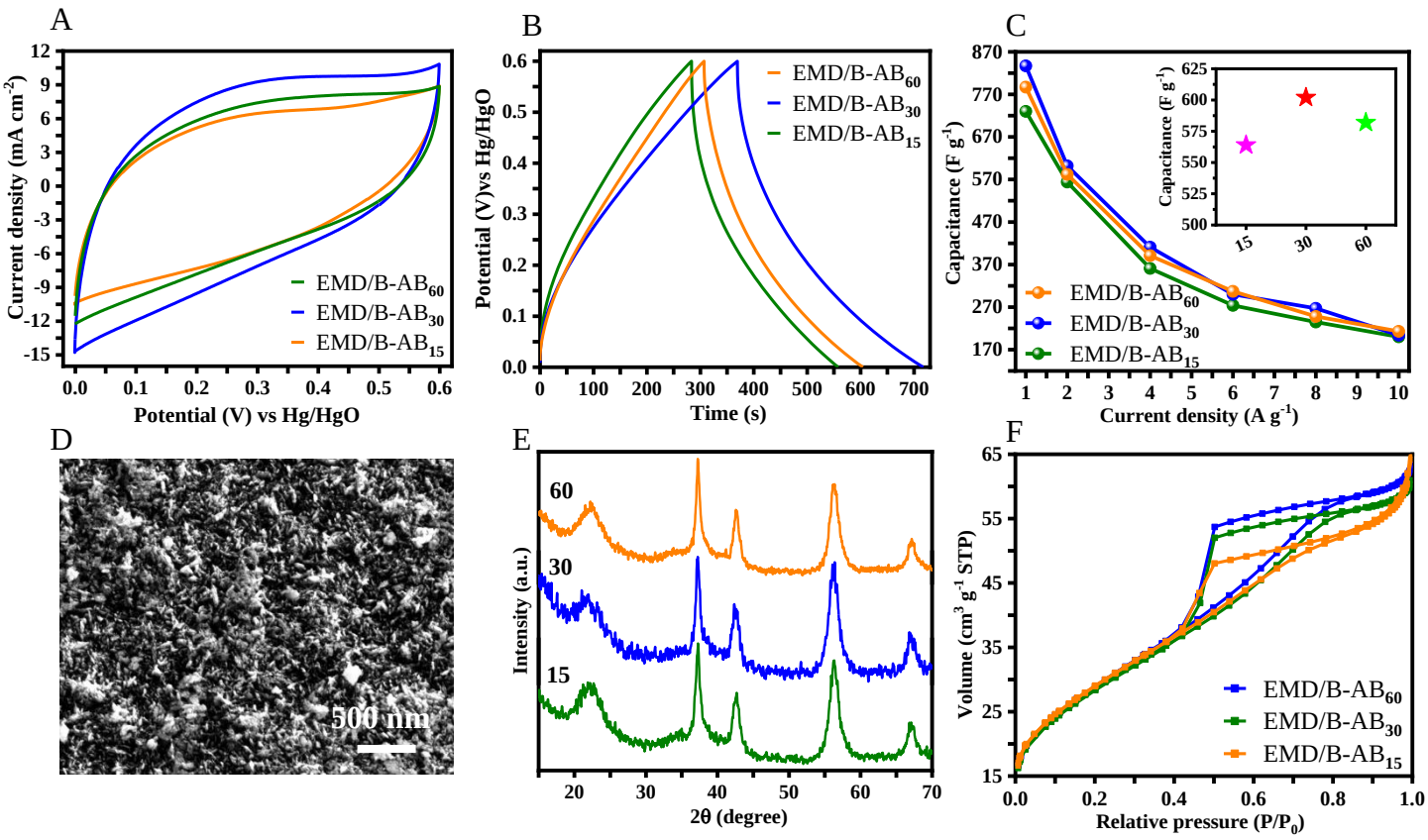

Figure 5.10 (A) Cyclic voltammetry (CV), (B) Galvanostatic charge-discharge (GCD), (C) specific capacitances at 1 mA (2 A g^{-1}), (D) FESEM of EMD/B-AB_{60}, (E) Xray diffraction (XRD), (F) Nitrogen adsorption desorption isotherms of B-AB with varying surfactant concentration (15, 30, 60 mg l^{-1}) in the electrolyte solution.

The EMD/D-AB materials at varying concentrations followed a similar trend can be seen in Figure 5.11. Comparatively, EMD/D-AB_{60} (Figure 5.11A) is occupied with more clusters due to it marginally exceeds its maximum limit of critical micelle concentration (CMC) of 1.5×10^{-4} mol l^{-1} in the solution [36] hence the adsorption density has been increased. This decrease in capacitance could be due to the increased adsorption of micelles onto nano EMD particles creating concentrated defect regions. Hence, the capacitance at the final concentration (120 F g^{-1} at 60 mg l^{-1}) was ~33% lower compared to its result at the initial concentration (180 F g^{-1} at 15 mg l^{-1}).

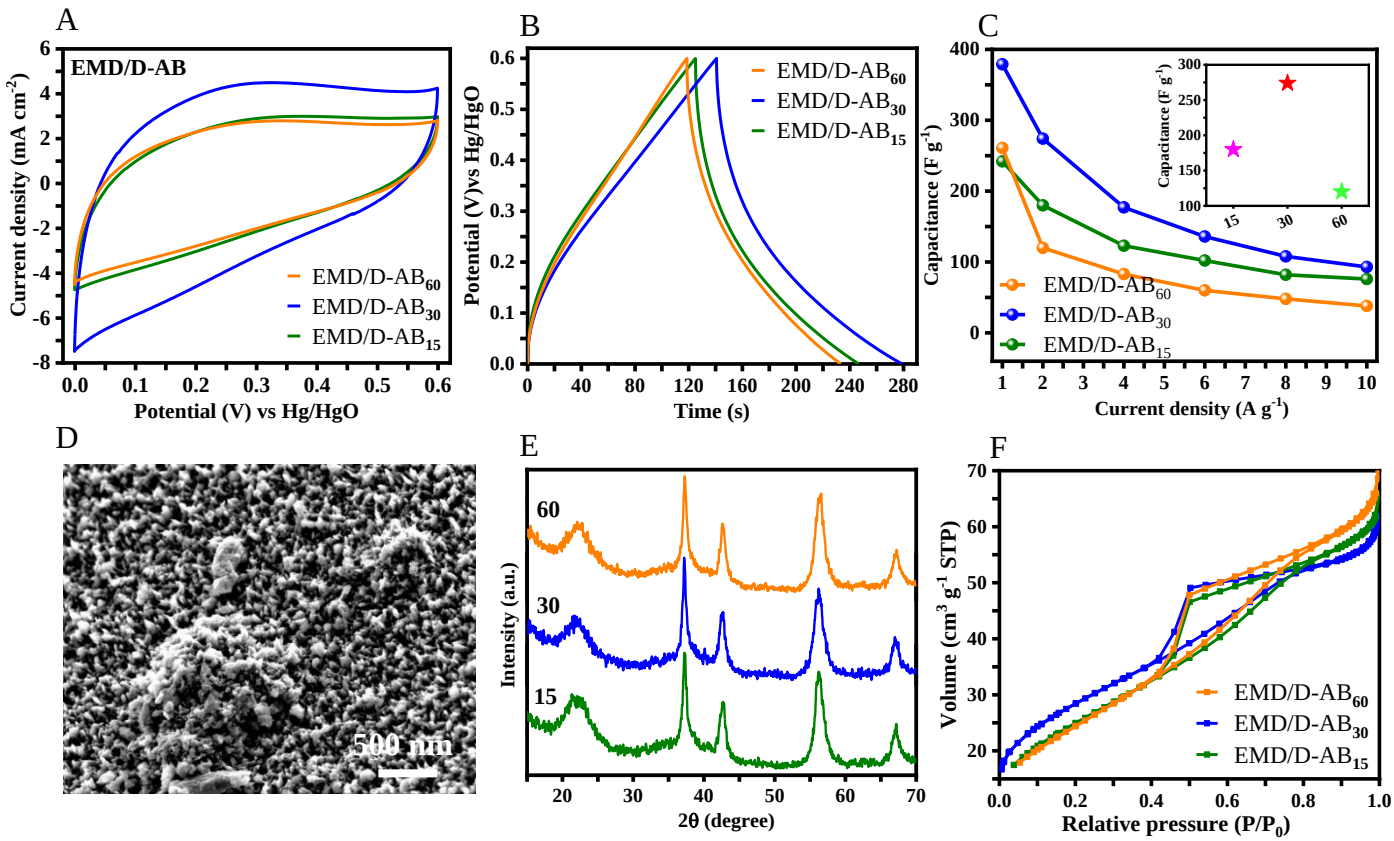

Figure 5.11 (A) Cyclic voltammetry (CV), (B) Galvanostatic charge-discharge (GCD), (C) specific capacitances at 1 mA (2 A g^{-1}), (D) FESEM of EMD/D-AB_{60}, (E) Xray diffraction (XRD), (F) Nitrogen adsorption desorption isotherms of D-AB with varying concentrations (15, 30, 60 mg l^{-1}) surfactant in the electrolyte solution.

5.5.3. Simulation results

According to the physicochemical characteristics, the surfactant adsorption and manganese dioxide electrodeposition were controlled by electrostatic and hydrophobic interactions of the surfactants at the surface/electrolyte interface. It demonstrated that the adsorption of T-AB and C-AB have resulted in morphology that is qualitatively alike. This is simply due to their slightly different molecular structures; thus, the driving force for adsorption are quite similar. Further, the B-AB was more effective in improving both the physicochemical and electrochemical properties of EMD exhibiting pseudocapacitive properties. This was studied in the molecular dynamics (MD) simulation to get insights into its activity at the Pb substrate compared to the pristine EMD and EMD/C-AB. The MD simulations reveal that the surfactants form a film adsorbed at the electrode surface via van der Waals and electrostatic interactions

when the Pb substrate is immersed in the solution (Figure 5.12). As in Figure 5.12A, the B-AB adsorbs with the aryl group planar to the Pb surface and the hydrophobic tail oriented parallelly to the metal surface. Once the B-AB molecule is in contact with the surface, it remains fixed in this orientation. This excludes manganese ions from the Pb surface at the specific points of contact for the B-AB, and therefore nucleation occurs around the molecule. The B-AB molecule interactions were compared with the C-AB and pristine EMD in Figures 5.12 B and C. The C-AB molecule also adsorbs parallel to the Pb surface but shows more freedom of movement across the surface, and this will likely disturb nucleation around the molecule and affect the growth of the manganese dioxide particles. During the electrodeposition, the surfactants in the bulk solution are incorporated into the deposit due to their hydrophobic nature; therefore, it may modulate nucleation. However, at higher concentrations of the surfactant, it is prone to form more surface aggregates which eventually saturate the surface.

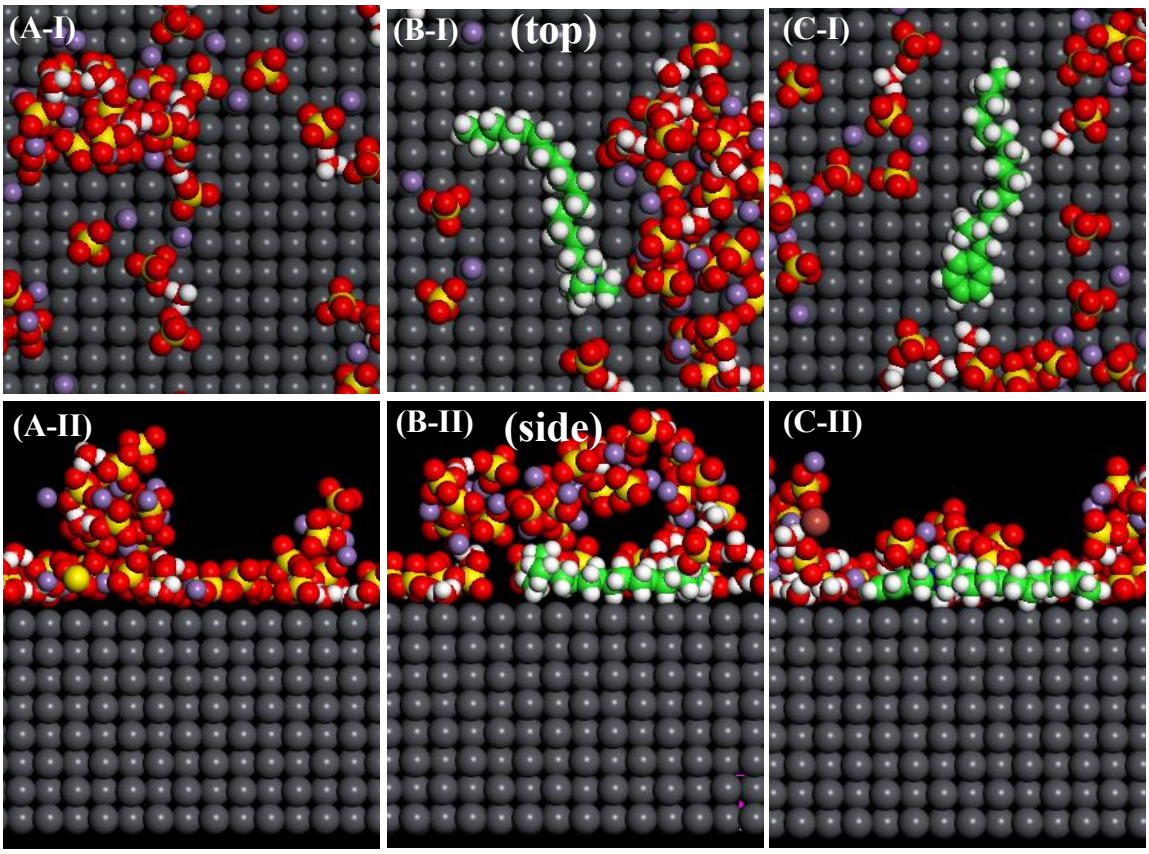

Figure 5.12 Top and side views of the equilibrium arrangements of molecules for simulations of (A) Pristine EMD (no surfactant), (B) C-AB system, and (C) B-AB system. Pb atoms are depicted in grey, Mn purple, O red, S yellow, H white, C green, and Br (brown). Water molecules have been hidden for clarity.

5.5.4. Hybrid capacitor performance (EMD/B-AB$_{30}$ *vs.* MS-AC)

Based on the three-electrode configuration studies, the best-performed EMD/B-AB$_{30}$ electrode has been chosen for a two-electrode system. The EMD/B-AB$_{30}$ electrode was coupled with a porous Mango seed-derived carbon material which was in-house synthesized (in chapter 6) and exhibited a specific capacitance of 135 F g^{-1} [19]. The operating voltage of the hybrid device is determined by both the chemistry of the electrode materials and the electrochemical kinetics of the electrolyte. The electrodes used in this work showed single electrode potential windows of 0.6 V for EMD (positive) and 1 V for the MS-AC (negative) electrode. Therefore, the capacitor voltage is calculated as the potential difference between positive and negative electrodes, which is 1.6 V for the hybrid capacitor discussed in this chapter. The hybrid

device has been evaluated for its suitability at varying potential windows (1.4, 1.5, 1.6, 1.7, 1.8 V) through CV and GCD measurements. The electrochemical performances at different operating potentials are shown in Figure 5.13. The results show that the capacitor is reversibly exhibiting a quasi-rectangular shape at a higher voltage. This has also been evidenced in the CV curves, a deviated rectangular-shaped curve is more obvious at higher potential implying 1.6 V is a safe operating window. The study illustrates the material is safe for a higher potential window exhibiting a pseudocapacitive in nature.

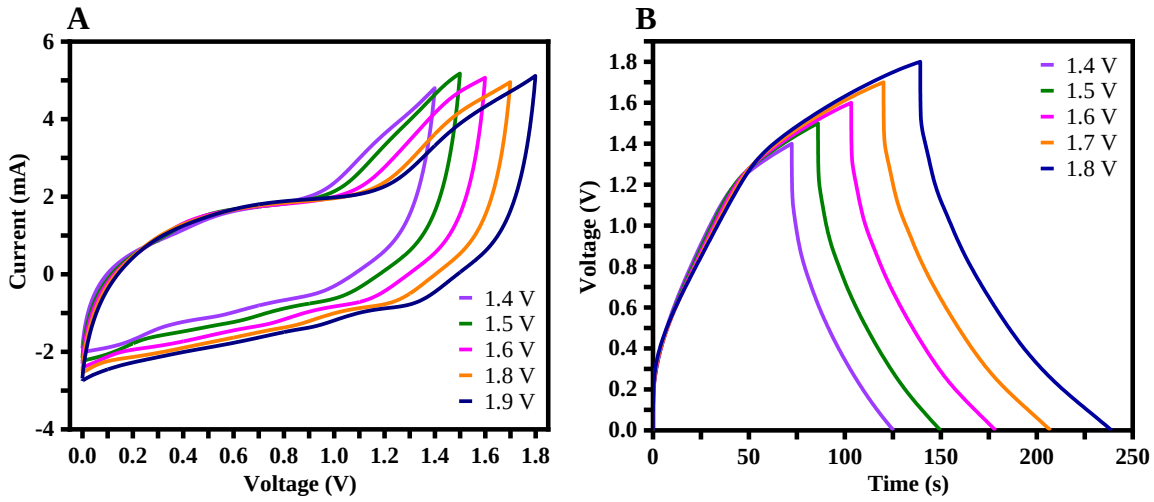

Figure 5.13 Performance of the asymmetric capacitor at different potential windows (1.4, 1.5, 1.6, 1.7, 1.8 V) (A) Cyclic voltammetry (CV), (B) Galvanostatic charge-discharge (GCD) curves.

The CV curves of the hybrid capacitor obtained at 5, 10, 20, 30, and 40 mV s^{-1} scan rates exhibit a near rectangular-shaped curve which is a characteristic of pseudocapacitors, as shown in Figure 5.14A. The corresponding GCD curves shown in Figure 5.14B are tested at a constant current of 2, 3, 4, 5, and 6 mA within an optimal voltage window of 1.6 V, preserving the asymmetric nature of the charge-discharge curves. The specific capacitance values were calculated as 91, 76, 65, 57, 48 F g^{-1} at 2, 3, 4, 5, and 6 mA cm^{-2}. Figure 5.14C shows the long-term stability tested for 10000 cycles at a current density of 5 mA cm^{-2}. After 10000 cycles, the capacitance was decreased from 57 to 36 F g^{-1}. However, the couloumbic efficiency was more than 95 % suggesting excellent reversibility after long cycling contributed by the modulated nucleation resulting from the B-AB surfactant. The Ragone plot in Figure

5.14D shows that the EMD/B-AB_{30} *vs*. MS-AC hybrid capacitor delivered a high performance comparable with the recently reported literature [37–42]. The device exhibits a specific capacitance of 91 F g^{-1} at 2 mA cm^{-2} (1 A g^{-1}) and an outstanding energy density of 32.4 Wh kg^{-1} at a power density of 971 W kg^{-1}. A further illustration of the electrochemical properties of similar systems published in the literature in comparison to our work is given in Table 5.2.

The full cell also shows markedly lower equivalent series resistance (Rs) and charge transfer resistance (R_{ct}), implying higher electrical conductivity as suggested by the electrochemical impedance spectroscopy (EIS) results (Figure 5.14E). A diffused semicircle at high frequencies, which linearly tails off at lower frequencies, is noticed. The bulk electrolyte resistance, R1, before and after cycling were 11.5 Ω and 11.9 Ω, respectively. The charge transfer resistance, R2, corresponds to the sum of the electrolyte resistance in the porous electrode structure and resistance at the electrode/current collector interface, which was 2.4 Ω before cycling and decreased to 2.0 Ω at the end of cycling [43]. The Warburg impedance element, W2, and the capacitor element C2 are the responses of a non-ideal and non-homogeneous system, elaborating the deviations of ideal Warburg diffusion impedance. The Q2 represents the actual cell capacitance [44]. All parameter values are given in Table 5.3. These results conclude that the faster ion transport at the electrode surface for the surfactant-mediated sample contributes to the improved pseudocapacitive performance.

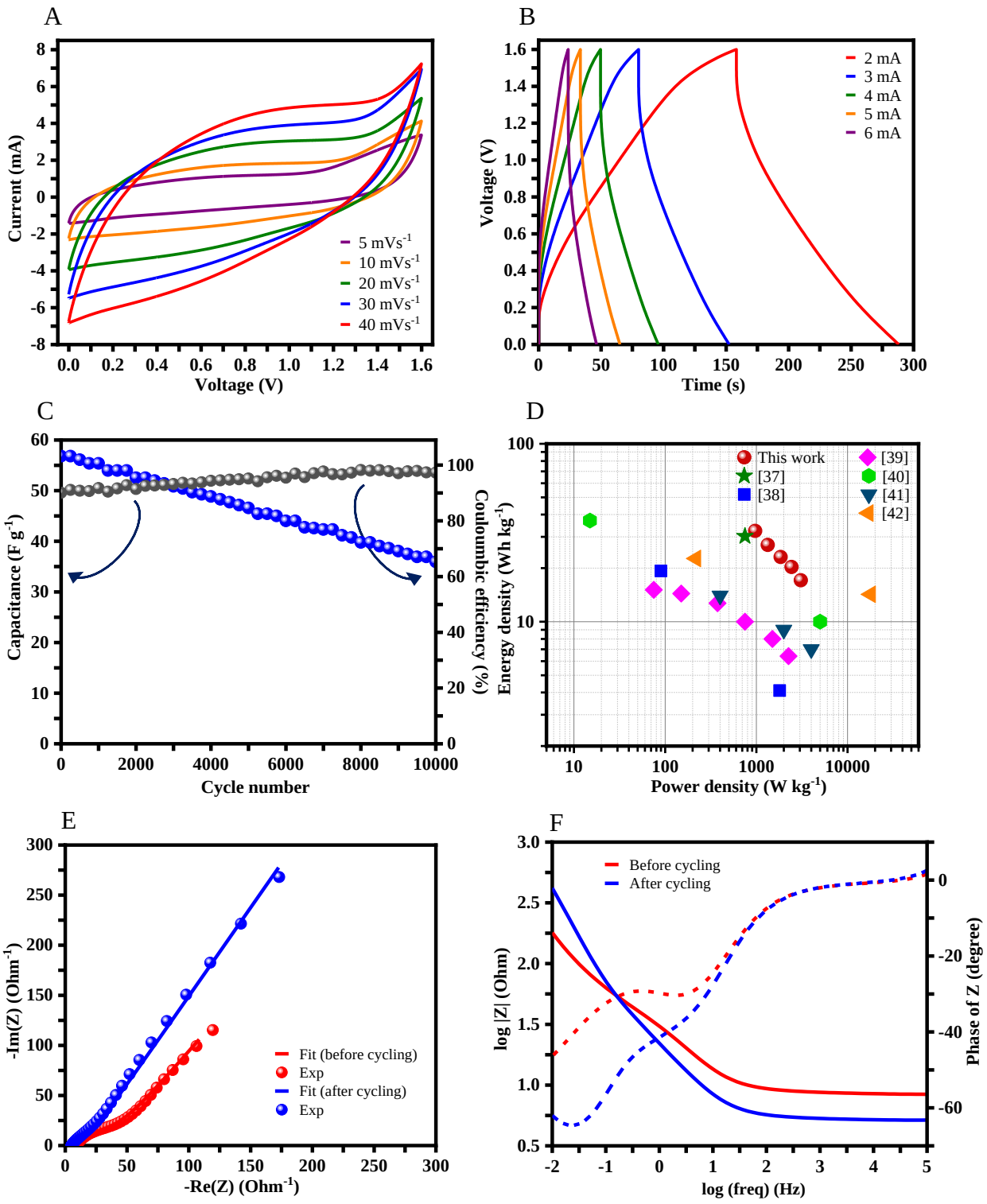

Figure 5.14 (A) CV and (B) GCD profiles of hybrid capacitor in an aqueous 2 M NaOH electrolyte at 1.6 V cell potential, (C) long-term stability and coulombic efficiency over 2000 cycles, (D) Ragone plot for energy and power density comparison between the EMD/B-AB$_{30}$ *vs.* MS-AC and the asymmetric/hybrid capacitors reported in the literature [38–43], (E) Nyquist plots and fitted curves

(inset: equivalent circuit model), and (F) Bode impedance curves before and after cycling.

Table 5.2 Comparison of the hybrid capacitor performance carried out in this chapter with similar asymmetric/hybrid systems reported in the literature.

Ref.	**Electrodes**		**Electrolyte**	**Voltage (V)**	**Current density ($A\ g^{-1}$)**	**C_{sp} ($F\ g^{-1}$)**	**E_{sp} ($Wh\ kg^{-1}$)**	**P_{sp} ($W\ kg^{-1}$)**
	Positive (cathode)	Negative (anode)						
Wang *et al.* [37]	CoNiFe-LDH/CNFs-0.5	Activated carbon	6 M KOH	1.6	1	84.9	30.2	~750
Pei *et al.* [45]	nano-Co_3O_4/CoS	RHC	2 M KOH	1.4	1	-	22	-
Rathore *et al.* [38]	Vanadium telluride/C	Activated carbon	1 M Na_2SO_4	1.8	0.1	42.8	19.3	89.9
							4.1	1800
Yan *et al.* [39]	NiS/MoS_2	Activated carbon	3 M KOH	1.5	0.1	48.4	15.1	75
					0.2	46	14.4	150
					0.5	40.5	12.7	375
					1	32.1	10.0	750
					2	25.6	8	1500
					3	20.5	6.4	2250
Morenghi *et al.* [40]	Ni-decorated graphene	Pure graphene	3.5 M KOH	1.5	0.04	-	37	15
					10	-	10	5000
Siwek *et al.*[41]	$MnOx@NiCo_f$	Carbon cloth	1 M Na_2SO_4	1.5	-	-	14	400
							9	2000
							7	4000
Li *et al.* [42]	MXene/PANI	Activated carbon	7 M KOH	1.2	0.5	-	22.67	217
					20		14.25	17900
Our work	EMD/B-AB_{30}	MS-AC	2 M NaOH	1.6	1	91	32.4	971

C_{sp} - specific capacitance
E_{sp} - specific energy
P_{sp} - specific power

Table 5.3 Equivalent circuit parameters determined from the EIS data.

	R1 (Ω)	**R2 (Ω)**	**Q2 × 10^3 (F s^{a-1})**	**a1**	**Q3 × 10^3 (F s^{a-1})**	**a3**
Before cycling	8.8	27.8	0.012	0.65	0.042	0.61
After cycling	5.2	10.7	0.010	0.88	0.020	0.67

5.6. Conclusion

The surfactant-mediated electrodeposition of MnO_2 demonstrates how significantly the electrochemical performance of a MnO_2 can change despite similar bulk characteristics. EMD materials have been synthesized using an aqueous $MnSO_4$ solution in the absence and presence of four cationic surfactants in the bath. The results from XRD suggest the presence of surfactant has no significant changes in the crystal structure, however, the FE-SEM and TEM analyses showed a variation in the morphologies of the obtained EMD deposits. It was revealed that the effect of surfactants on the nanostructured MnO_2 performance is highly correlated to their molecular geometries, possessing different hydrocarbon chain lengths and head groups, which are desired to manipulate the surface morphology and the surface area. Among the studied surfactants, Benzyldodecyldimethylammonium bromide (B-AB) has been found to provide improved specific capacitance of 602 F g^{-1} at 1 mA current rate compared to that of the other surfactants (T-AB, D-AB, C-AB) examined. The best performance of EMD/B-AB has been evidenced by the molecular dynamics simulation. It provides stability for nucleation and growth due to its unique molecular structure. The hybrid capacitor EMD/B-AB_{30} *vs.* MS-AC delivered a specific capacitance of 91 F g^{-1} and an energy density of 32 Wh kg^{-1} at a power density of 971 W kg^{-1}, also exhibiting excellent cycling stability. Overall, the work in this chapter shows that even with small additives used in the electrodeposition, it is feasible to tune the properties, a crucial characteristic for an energy storage electrode, and improve the performance of the electrochemical capacitors.

5.7. References

[1] A.L.M. Reddy, S.R. Gowda, M.M. Shaijumon, P.M. Ajayan, Hybrid nanostructures for energy storage applications, Advanced Materials. 24 (2012) 5045–5064.

[2] A. Manthiram, A. Vadivel Murugan, A. Sarkar, T. Muraliganth, Nanostructured electrode materials for electrochemical energy storage and conversion, Energy Environ Sci. 1 (2008) 621–638.

[3] S.M. Shaban, J. Kang, D.H. Kim, Surfactants: Recent advances and their applications, Composites Communications. 22 (2020) 100537.

[4] F. Zhang, S. Li, Q. Zhang, J. Liu, S. Zeng, M. Liu, D. Sun, Adsorption of different types of surfactants on graphene oxide, J Mol Liq. 276 (2019) 338–346.

[5] M.C. Hersam, Progress towards monodisperse single-walled carbon nanotubes, Nanoscience and Technology: A Collection of Reviews from Nature Journals. (2009) 3–10.

[6] A.A. Green, M.C. Hersam, Solution phase production of graphene with controlled thickness via density differentiation, Nano Lett. 9 (2009) 4031–4036.

[7] F. Sarf, Metal Oxide Gas Sensors by Nanostructures, Gas Sensors. (2020) 1–17.

[8] H. Zhang, Y. Wang, C. Liu, H. Jiang, Influence of surfactant CTAB on the electrochemical performance of manganese dioxide used as supercapacitor electrode material, J Alloys Compd. 517 (2012) 1–8.

[9] A. Biswal, B.C. Tripathy, T. Subbaiah, D. Meyrick, M. Ionescu, M. Minakshi, Effect of non-ionic surfactants and its role in K intercalation in electrolytic manganese dioxide, Metallurgical and Materials Transactions E. 1 (2014) 226–238.

[10] L. Hongtao, X. Zichen, Z. Lina, Z. Zhiqiang, X. Li, The effects of different surfactants on the morphologies and electrochemical properties of MoS_2 /reduce graphene oxide composites, Chem Phys Lett. 716 (2019) 6–10.

[11] M. Paunovic, M. Schlesinger, Effect of Additives, in: Fundamentals of Electrochemical Deposition, The Electrochemical Society, 1998: pp. 167–186.

[12] E.N. Schulz, E.P. Schulz, P.C. Schulz, Electrochemistry of Surfactants, in: R. Najjar (Ed.), Application and Characterization of Surfactants, 2nd ed., IntechOpen, London, 2017.

[13] S.M. Senthil Kumar, K. Chandrasekara Pillai, Cetyltrimethyl ammonium bromide surfactant-assisted morphological and electrochemical changes in electrochemically prepared nanoclustered iron(III) hexacyanoferrate, Journal of Electroanalytical Chemistry. 589 (2006) 167–175.

[14] W. Li, M. Zhang, J. Zhang, Y. Han, Self-assembly of cetyl trimethylammonium bromide in ethanol-water mixtures, Frontiers of Chemistry in China. 1 (2006) 438–442.

[15] K. Liu, H. Qi, R. Dong, R. Shivhare, M. Addicoat, T. Zhang, H. Sahabudeen, T. Heine, S. Mannsfeld, U. Kaiser, Z. Zheng, X. Feng, On-water surface synthesis of crystalline, few-layer two-dimensional polymers assisted by surfactant monolayers, Nat Chem. 11 (2019) 994–1000.

[16] N. Yekeen, M.A. Manan, A.K. Idris, A.M. Samin, Influence of surfactant and electrolyte concentrations on surfactant Adsorption and foaming characteristics, J Pet Sci Eng. 149 (2017) 612–622.

[17] S.M. Shaban, I. Aiad, M.M. El-Sukkary, E.A. Soliman, M.Y. El-Awady, One step green synthesis of hexagonal silver nanoparticles and their biological activity, Journal of Industrial and Engineering Chemistry. 20 (2014) 4473–4481.

[18] A.A. Abd-Elaal, N.M. Elbasiony, S.M. Shaban, E.G. Zaki, Studying the corrosion inhibition of some prepared nonionic surfactants based on 3-(4-hydroxyphenyl) propanoic acid and estimating the influence of silver nanoparticles on the surface parameters, J Mol Liq. 249 (2018) 304–317.

[19] W.A.M.K.P. Wickramaarachchi, M. Minakshi, X. Gao, R. Dabare, K.W. Wong, Hierarchical porous carbon from mango seed husk for electro-chemical energy storage, Chemical Engineering Journal Advances. 8 (2021) 100158.

[20] D.J. Henry, E. Evans, I. Yarovsky, Classical molecular dynamics study of [60]fullerene interactions with silica and polyester surfaces, Journal of Physical Chemistry B. 110 (2006) 15963–15972.

[21] D.J. Henry, C.A. Lukey, E. Evans, I. Yarovsky, Theoretical study of adhesion between graphite, polyester and silica surfaces, Mol Simul. 31 (2005) 449–455.

[22] L.A. Shaw, G. Yiapanis, D.J. Henry, S. MacLaughlin, E. Evans, I. Yarovsky, Surface crosslinking effects on contamination resistance of functionalised polymers, Soft Matter. 9 (2013) 1798–1806.

[23] H.C. Andersen, Molecular dynamics simulations at constant pressure and/or temperature, J Chem Phys. 72 (1980) 2384–2393.

[24] H. Abbas, S.A. Nasser, Hydroxyl as a defect of the manganese dioxide lattice and its applications to the dry cell battery, J Power Sources. 58 (1996) 15–21.

[25] K. Wickramaarachchi, M.M. Sundaram, D.J. Henry, X. Gao, Alginate Biopolymer Effect on the Electrodeposition of Manganese Dioxide on Electrodes for Supercapacitors, ACS Appl Energy Mater. 4 (2021) 7040–7051.

[26] K.M. Racik, K. Guruprasad, M. Mahendiran, J. Madhavan, T. Maiyalagan, M.V.A. Raj, Enhanced electrochemical performance of MnO_2/NiO nanocomposite for supercapacitor electrode with excellent cycling stability, Journal of Materials Science: Materials in Electronics. 30 (2019) 5222–5232.

[27] M. Zheng, H. Zhang, X. Gong, R. Xu, Y. Xiao, H. Dong, X. Liu, Y. Liu, A simple additive-free approach for the synthesis of uniform manganese monoxide nanorods with large specific surface area, Nanoscale Res Lett. 8 (2013) 1–7.

[28] J.B. Fernandes, B.D. Desai, V.N. Kamat Dalal, Studies on chemically precipitated Mn(IV) oxides-II, Electrochim Acta. 28 (1983) 309–315.

[29] C. Julien, M. Massot, Spectroscopic studies of the local structure in positive electrodes for lithium batteries, Physical Chemistry Chemical Physics. 4 (2002) 4226–4235.

[30] S.K. Mehta, S. Kumar, S. Chaudhary, K.K. Bhasin, Effect of cationic surfactant head groups on synthesis, growth and agglomeration behavior of ZnS nanoparticles, Nanoscale Res Lett. 4 (2009) 1197–1208.

[31] D. Gong, H. Tong, J. Xiao, T. Li, J. Liu, Y. Wu, X. Chen, J. Liu, X. Zhang, Self-standing manganese dioxide/graphene carbon nanotubes film electrode for

symmetric supercapacitor with high energy density and superior long cycling stability, Ceram Int. 47 (2021) 33020–33027.

[32] F. Mahdi, M. Javanbakht, S. Shahrokhian, Anodic pulse electrodeposition of mesoporous manganese dioxide nanostructures for high performance supercapacitors, J Alloys Compd. 887 (2021) 161376.

[33] Y. Shi, M. Zhang, D. Yang, J. Li, Study on preparation of high performance manganese dioxide supercapacitor by cyclic voltammetry, Ionics (Kiel). 27 (2021) 4521–4529.

[34] A. Singh, D. Kumar, A. Thakur, N. Gupta, V. Shinde, B.S. Saini, R. Kaur, Galvanostatic deposition of manganese oxide films for super capacitive application and their fractal analysis, Ionics (Kiel). 27 (2021) 2193–2202.

[35] J. Harkot, B. Jańczuk, Surface and volume properties of dodecylethyldimethylammonium bromide and benzyldimethyldodecylammonium bromide. I. Surface properties of dodecylethyldimethylammonium bromide and benzyldimethyldodecylammonium bromide, J Colloid Interface Sci. 331 (2009) 494–499.

[36] L.R. Griffin, K.L. Browning, C.L. Truscott, L.A. Clifton, J. Webster, S.M. Clarke, A comparison of didodecyldimethylammonium bromide adsorbed at mica/water and silica/water interfaces using neutron reflection, J Colloid Interface Sci. 478 (2016) 365–373.

[37] F. Wang, S. Sun, Y. Xu, T. Wang, R. Yu, H. Li, High performance asymmetric supercapacitor based on Cobalt Nickle Iron-layered double hydroxide/carbon nanofibres and activated carbon, Sci Rep. 7 (2017) 1–11.

[38] H.K. Rathore, M. Hariram, M.K. Ganesha, A.K. Singh, D. Das, M. Kumar, K. Awasthi, D. Sarkar, Charge storage mechanism in vanadium telluride/carbon nanobelts as electroactive material in an aqueous asymmetric supercapacitor, J Colloid Interface Sci. 621 (2022) 110–118.

[39] J. Yan, S. Wang, Y. Chen, M. Yuan, Y. Huang, J. Lian, J. Qiu, J. Bao, M. Xie, H. Xu, H. Li, Y. Zhao, Smart in situ construction of NiS/MoS_2 composite nanosheets

with ultrahigh specific capacity for high-performance asymmetric supercapacitor, J Alloys Compd. 811 (2019) 151915.

[40] A. Morenghi, S. Scaravonati, G. Magnani, M. Sidoli, L. Aversa, R. Verucchi, G. Bertoni, M. Riccò, D. Pontiroli, Asymmetric supercapacitors based on nickel decorated graphene and porous graphene electrodes, Electrochim Acta. 424 (2022) 140626.

[41] K.I. Siwek, S. Eugénio, I. Aldama, J.M. Rojo, J.M. Amarilla, A.P.C. Ribeiro, T.M. Silva, M.F. Montemor, Tailored 3D Foams Decorated with Nanostructured Manganese Oxide for Asymmetric Electrochemical Capacitors, J Electrochem Soc. 169 (2022) 020511.

[42] Y. Li, P. Kamdem, X.J. Jin, Hierarchical architecture of MXene/PANI hybrid electrode for advanced asymmetric supercapacitors, J Alloys Compd. 850 (2021) 1–9.

[43] B.A. Mei, O. Munteshari, J. Lau, B. Dunn, L. Pilon, Physical Interpretations of Nyquist Plots for EDLC Electrodes and Devices, Journal of Physical Chemistry C. 122 (2018) 194–206.

[44] M. Singh, K. Manoli, A. Tiwari, T. Ligonzo, C. Di Franco, N. Cioffi, G. Palazzo, G. Scamarcio, L. Torsi, The double layer capacitance of ionic liquids for electrolyte gating of ZnO thin film transistors and effect of gate electrodes, J Mater Chem C Mater. 5 (2017) 3509–3518.

[45] D. Pei, J. Bao, Y. Li, Y. Li, H. Wang, H. Lu, Z. Wang, Three-dimensional Co_3O_4/CoS hierarchical nanoneedle arrays electrode grown on nickel foam for high-performance asymmetric capacitors, J Energy Storage. 51 (2022) 104483.

Link to the next chapter

Electrodeposited MnO_2 studied in the previous chapters 3 to 5 was found to be a potential positive electrode in hybrid capacitor applications. Usually, the carbon materials are used as the negative electrodes in hybrid capacitors since they tend to have better cycling stability and rate capability. Therefore, developing and designing advanced carbon electrodes with higher surface area, surface morphology, and hierarchical pore structure is essential. On the other hand, the usual synthesis of carbon materials using fossil fuel resources is unsustainable and harmful to the environment.

Biomass waste is a cheap, abundant, and environmentally friendly precursor and can be a realistic alternative to currently used carbon precursors. Recently, various biomass precursors have been investigated by several researchers. In chapter 6, we studied the synthesis of activated carbon (AC) from Mango seed (MS) husk collected from Western Australia. We were interested in seeing how the MS husk-derived carbon inherits the porous structure from its precursor and its effectiveness in fabricating the carbon electrodes. In this chapter, the synthesis was conducted in a two-step process of carbonization and activation. The influence of the activation temperature was also studied here on developing the porous network within the AC materials. The physicochemical, electrochemical, and theoretical findings encouraged using the MS husk-derived AC to fabricate the hybrid capacitors are discussed in chapter 6.

Chapter 6 Hierarchical porous carbon from Mango seed husk for electrochemical energy storage

This chapter is published as:

Hierarchical porous carbon from mango seed husk for electrochemical energy storage

W A M Kethaki Pabasara Wickramaarachchi, Manickam Minakshi, Xiangpeng Gao, Rukshima Dabare, Kok Wai Wong

Chemical Engineering Journal Advances 2021 (8), 100158
DOI: https://doi.org/10.1016/j.ceja.2021.100158

Chapter 6. Hierarchical porous carbon from Mango seed husk for electrochemical energy storage

Chemical Engineering Journal Advances 8 (2021) 100158

Contents lists available at ScienceDirect

Chemical Engineering Journal Advances

journal homepage: www.sciencedirect.com/journal/chemical-engineering-journal-advances

Hierarchical porous carbon from mango seed husk for electro-chemical energy storage

W.A.M. Kethaki Pabasara Wickramaarachchi [a], Manickam Minakshi [a,*], Xiangpeng Gao [a], Rukshima Dabare [b], Kok Wai Wong [b]

[a] College of Science, Health, Engineering and Education
[b] Information Technology, College of Arts, Business, Law and Social Sciences, Murdoch University, WA 6150, Australia

ARTICLE INFO

Keywords:
Mango seed husk
Biomass activated carbon
Activation temperature
Energy storage
Machine learning modeling

ABSTRACT

Bio-waste valorization of Mango Seed (MS) husk to Activated Carbon (AC) was conducted via carbonization followed by chemical activation using KOH for sustainable supercapacitor material. Various physicochemical techniques were used to characterise both MS husk and AC, while electrochemical techniques were used to assess the energy storage capability. Carbonized MS husk was activated at four different temperatures 800, 900, 1000, and 1100 °C. Optimal activation temperature was found to be 1100 °C resulting in a hierarchical porous structure, possessing the highest specific surface area 1943 $m^2 g^{-1}$ and average pore volume 0.397 $cm^3 g^{-1}$, the critical parameters for their energy storage performance. In a three-electrode configuration, the MS-AC sample synthesized at 1100 °C (MS-AC 1100) exhibited a maximum specific capacitance of 135 F g^{-1} at 5 mA cm^{-2} with the energy density of 19 Wh kg^{-1} at the power density of 1077 W kg^{-1}, which is higher than the commercially available AC. The MS-AC 1100 delivered 97% of the capacitance when increasing the current densities from 2 to 10 mA cm^{-2}. The capacitance retention is 100% at 5 mA cm^{-2} with 1000 cycles. Moreover, Machine Learning (ML) models are used to identify the non-linear pattern for predicting the AC capacitance using various input parameters. Out of the four ML models considered in this work, the Multi-Layer Perceptron (MLP) model outperformed the other models to better correlate the predicted data and the experimental measurements. This study demonstrates the economic perspective of repurposing MS husk bio-waste to a low-cost super-capacitor electrode material and developing high-performance carbon materials to aid the integration of renewable energy into electricity systems.

1. Introduction

The viability of using cost-effective energy storage materials to alleviate renewable penetration level for the reasons of decarbonizing electricity production is a critical issue that remains unsolved due to a multi-disciplinary problem encompassing areas such as materials science, chemical engineering, and electrochemistry. The ever-growing energy demand is being addressed by the "energy mix" developing clean and sustainable energy substitutions for fossil fuels, such as solar, wind, and tide as weather dependent renewable resources [1]. Therefore, the inherent attribute of these resources being intermittent, and variable has become a significant limitation for balancing the demand and supply of the societal energy requirement [2]. Thus, efficient energy storage has become one of the greatest challenges in the 21st century that can provide us a range of services, and its economic rationale is predominantly application dependent. Consequently, the batteries and capacitors play a vital role as electrochemical energy storage systems but have different characteristics and applications.

The electrochemical capacitors, also known as super-capacitors, are much more efficient than the conventional capacitors [3]. The two distinct categories of super-capacitors are electrochemical double layer capacitors (EDLC) and pseudo-capacitors. Comparatively, pseudo-capacitors exhibit higher specific capacitances than the EDLCs. A super-capacitor cell consists of highly conductive two electrodes (positive and negative) that are physically apart in an electrolyte with mobile ionic species. Upon applying a voltage across these electrodes, the cations and anions accumulated and adsorbed at the two electrodes [3]. The ion adsorption is highly reversible and leads to high specific capacitance, power density and excellent cycling stability. Unlike the batteries, the super-capacitors store charge not only through diffusion of

* Corresponding author.
E-mail address: minakshi@murdoch.edu.au (M. Minakshi).

https://doi.org/10.1016/j.ceja.2021.100158
Received 29 March 2021; Received in revised form 16 July 2021; Accepted 25 July 2021
Available online 27 July 2021
2666-8211/© 2021 The Author(s). Published by Elsevier B.V. This is an open access article under the CC BY-NC-ND license (http://creativecommons.org/licenses/by-nc-nd/4.0/).

Author contribution

Contributor	Contribution (%)	Nature of contribution
Kethaki Wickramaarachchi	70	Conceptualization, experimentation, data collection, analysis and interpretation, drafting and critical revision of the manuscript.
Manickam Minakshi	30	Conceptualization, interpretation of data, critical revision of the manuscript.
Xiangpeng Gao		Critical revision of the manuscript.
Rukshima Dabare		Theoretical insights and data interpretation.
Kok Wai Wong		Theoretical insights and data interpretation.

6.1. Abstract

Bio-waste valorization of Mango seed (MS) husk to Activated Carbon (AC) was conducted via carbonization followed by chemical activation using KOH for sustainable supercapacitor material. Various physicochemical techniques were used to characterize MS husk and AC, while electrochemical techniques were used to assess the energy storage capability. Carbonized MS husk was activated at four different temperatures 800, 900, 1000, and 1100 °C. The optimal activation temperature was found to be 1100 °C resulting in a hierarchical porous structure, possessing the highest specific surface area of 1943 $m^2\ g^{-1}$ and average pore volume of 0.397 $cm^3\ g^{-1}$, the critical parameters for their energy storage performance. In a three-electrode configuration, the MS-AC sample synthesized at 1100 °C (MS-AC 1100) exhibited a maximum specific capacitance of 135 F g^{-1} at 5 mA cm^{-2} with the energy density of 19 Wh kg^{-1} at the power density of 1077 W kg^{-1}, which is higher than the commercially available AC. The MS-AC 1100 delivered 97 % of the capacitance when increasing the current densities from 2 to 10 mA cm^{-2}. The capacitance retention is 100 % at 5 mA cm^{-2} with 1000 cycles. Moreover, Machine Learning (ML) models are used to identify the non-linear pattern for predicting the AC capacitance using various input parameters. Out of the four ML models considered in this chapter, the Multi-Layer Perceptron (MLP) model outperformed the other models in correlating the predicted data and the experimental measurements. This chapter demonstrates the economic perspective of repurposing MS husk bio-waste into a low-cost supercapacitor electrode material and developing high-performance carbon materials to aid the integration of renewable energy into electricity systems.

6.2. Introduction

The viability of using cost-effective energy storage materials to alleviate renewable penetration levels for decarbonizing electricity production is a critical issue that remains unsolved due to a multi-disciplinary problem encompassing areas such as materials science, chemical engineering, and electrochemistry. The ever-growing energy demand is being addressed by the ‘energy mix’ developing clean and

sustainable energy substitutions for fossil fuels, such as solar, wind, and tide, as weather-dependent renewable resources [1]. Therefore, the inherent attribute of these resources being intermittent and variable has become a significant limitation for balancing the demand and supply of the societal energy requirement [2]. Thus, efficient energy storage has become one of the greatest challenges in the 21st century that can provide us with a range of services, and its economic rationale is predominantly application-dependent. Consequently, the batteries and capacitors play a vital role as electrochemical energy storage systems but have different characteristics and applications.

The electrochemical capacitors, also known as supercapacitors, are much more efficient than the conventional capacitors [3]. The two distinct categories of supercapacitors are electrochemical double-layer capacitors (EDLC) and pseudo-capacitors. Comparatively, pseudo-capacitors exhibit higher specific capacitances than the EDLCs. A supercapacitor cell consists of highly conductive two electrodes (positive and negative) that are physically apart in an electrolyte with mobile ionic species. Upon applying a voltage across these electrodes, the cations and anions accumulated and adsorbed at the two electrodes [3]. The ion adsorption is highly reversible and leads to high specific capacitance, power density, and excellent cycling stability. Unlike the batteries, the super-capacitors store charge not only through the diffusion of ions into the bulk material but also store/release charge at the interface. Despite this, available energy density is significantly low, explaining that no single technology excels in all characteristics. Nevertheless, with these complementary features, the electrochemical capacitors could couple with batteries in need of high-power requirements.

Addressing waste management via reducing, reusing, and recycling waste is crucial for sustainable development to accelerate the transition from a linear economy to a circular economy. Huge efforts have been made to convert waste into functional materials, especially carbon-based electrodes, for supercapacitor applications. Among the available different forms of carbon, such as carbon nanotubes [4], graphene [5], graphene oxide [6], porous carbon [7] and their composites [8], etc., activated carbon has been a versatile electrode for storing ions [9,10]. This is due to their high production cost, process complexity, environmental degradation, and unsustainability,

limiting the other forms of carbon from wider applications. Utilizing the biomass materials and their derivatives, including renewable crops and animal residues, to produce AC for storing energy can be regarded as less environmentally polluting, cheaper, and sustainable. Every year, about 146 billion tons of waste are generated by crop yields, which should be used wisely without being directly sent to landfills [11]. A number of studies have reported repurposing various natural sources/waste, such as algae, catkins, rice, orange peel, sugar cane bagasse, rice stem, wheat straw, coconut shell, almond, etc., as biomass precursors for storing energy efficiently [12].

The intrinsic microstructural characteristics and chemical compositions of the biomass materials varied from one to another. Generally, it possesses a 3D framework that is mostly stable and would be inherited by the carbon material after the thermochemical conversion [13–15]. Besides being a carbon-rich material, biomass possibly contains other elements such as H, O, N, S, and some traceable amounts of Ca, K, Mg, Na, and Si minerals [16,17]. When these minerals naturally exist in the original sample, they can act as self-activating agents and cause the direct conversion to porous carbon with no further activation step required. Otherwise, the synthesis process can be of two steps with carbonization followed by physical or chemical activation conducted in an inert environment. Chemical activation is the most economically feasible approach due to the shorter processing time and higher yield of activated carbon [18]. In the chemical activation method, the pyrolyzing of the sample is generally carried out at a temperature > 400 °C, then mixed with an activating agent (KOH, NaOH, $CaCl_2$, $ZnCl_2$, H_3PO_4, K_2CO_3) to generate highly porous structures, and finally heated in a protective atmosphere (Ar, N_2) at a temperature commonly lies in the range of 500 - 800 °C [19].

Herein, a series of KOH-activated carbon materials have been synthesized using MS husk as the biomass waste precursor. A 35 - 60 % of the Mango fruit comprises Mango seed, the kernel protected by a thick husk, and the outer skin is discarded as waste [20]. The MS husk has less commercial value than the Mango seed kernel and is disposed to the environment. Australia discards Mango seeds about 60,000 tonnes per year, causing significant waste disposal [21]. The waste Mango seeds collected from the Western Australia region are of interest in this chapter for converting the thick-husk biomass precursor into activated carbon (AC) for energy storage applications.

Moreover, MS husk is a natural, abundant, and low-cost lignocellulosic biomass that offers an inexpensive and excellent carbon source. Therefore, the options for the valorization of this waste pave the way for sustainable and renewable carbon-rich resources than synthetic precursors for future energy storage [18]. Several studies reported on Mango seed-derived activated carbon but were limited to the applications such as wastewater treatment and adsorbent in the adsorption cooling system [18,22]. The research to date on sustainable biomass material has not yet investigated the MS husk-derived activated carbon as an electrode for supercapacitor application along with effective material designing.

Therefore, in this chapter, the MS husk-derived activated carbon (MS-AC) is reported for supercapacitor applications. Experimental data are used to establish Machine Learning (ML) models for predicting the energy storage performance of the synthesized AC samples. ML tools are a powerful approach to obtaining a quantitative understanding of the relationship between input and output variables. Importantly, it reduces the time and cost of repetitive experiments for optimizing synthesis parameters and increases the efficiency of discovering new materials [23]. For instance, an investigation with promising results could be more effective if guided by computational modeling to design the material further to obtain desirable material properties. It is predominant with the current transition to clean and renewable energy storage applications, where ML would undoubtedly play a critical role in material designing. In material science, it has been proven to predict band gaps, dielectric constants, thermodynamic stability, chemical reactions, etc. [24]. It has already shown its superior capability over conventional DFT simulations compared to when it is guided by ML-based methods [25]. The results indicated that ML-based approaches could significantly accelerate the over guess-and-check research paradigm initially conducted in the past [23,25]. In order to study the carbon electrodes as supercapacitor materials, most researchers have utilized inputs only based on physical properties and established good correlations [26,27]. In the study conducted by Dongale *et al.* [28], the cyclic voltammetric behavior of the samples was predicted using potential and current density as inputs. With this inspiration from the published literature, ML methods have been used for the work in this chapter to study the influence of material synthesis conditions, structural and electrochemical features on the MS electrode

performance. we have attempted to evaluate the chemical and physical aspects of MS husk-derived AC and compare the raw MS husk precursor characteristics that inherit the final product. The role of carbonization and activation temperature of the MS husk are investigated. This chapter summarizes material synthesis, physicochemical characterization, electrochemical characterization, and ML model that predicts the capacitance nearly within their experimental uncertainty. Using MS husk bio-waste as the starting precursor for AC synthesis and simulating its properties and behaviors would be decisive steps forward, contributing to developing new materials by advancing from laboratory to industry.

6.3. Experimental

6.3.1. Conversion of biomass to activated carbon

The waste mango seeds were washed and kept in the oven at 80 °C to dry appropriately. Then the MS kernels and the thick husks were separated from the raw mango seeds. The separated MS husks were cleaned and dried in the oven at 60 °C for 24 h, ground into small particles, and screened through a 350 µm mesh sieve (steps 1 and 2 are shown in Figure 6.1). The powder was put into a tubular furnace heated to reach 600 °C with a heating rate of 5 °C min^{-1} and kept for 3 h in an N_2 atmosphere with a nitrogen flow rate of 1 l min^{-1}. Carbonized (biochar) sample and the KOH (85.0 % min, chem-supply) taken 1:3 ratio were mixed in a solution. The mixture was dried and put into the tubular furnace and heated at 5 °C min^{-1} with 1 h keeping time for activation at four different temperatures of 800, 900, 1000, and 1100 °C in the presence of inert N_2 gas at the same flow rate. The product is shown in Figure 6.1 (step 3). After carbonization and activation, the samples were cooled to room temperature naturally in an inert atmosphere. The excess base in the AC was neutralized by acid treatment with 1 M HCl (32 %) followed by washing with deionized water until pH was neutral ≈ 7. Then, the sample was dried in the oven at 60 °C for 12 h. For performance comparison, commercial AC is purchased from Calgon carbon, USA.

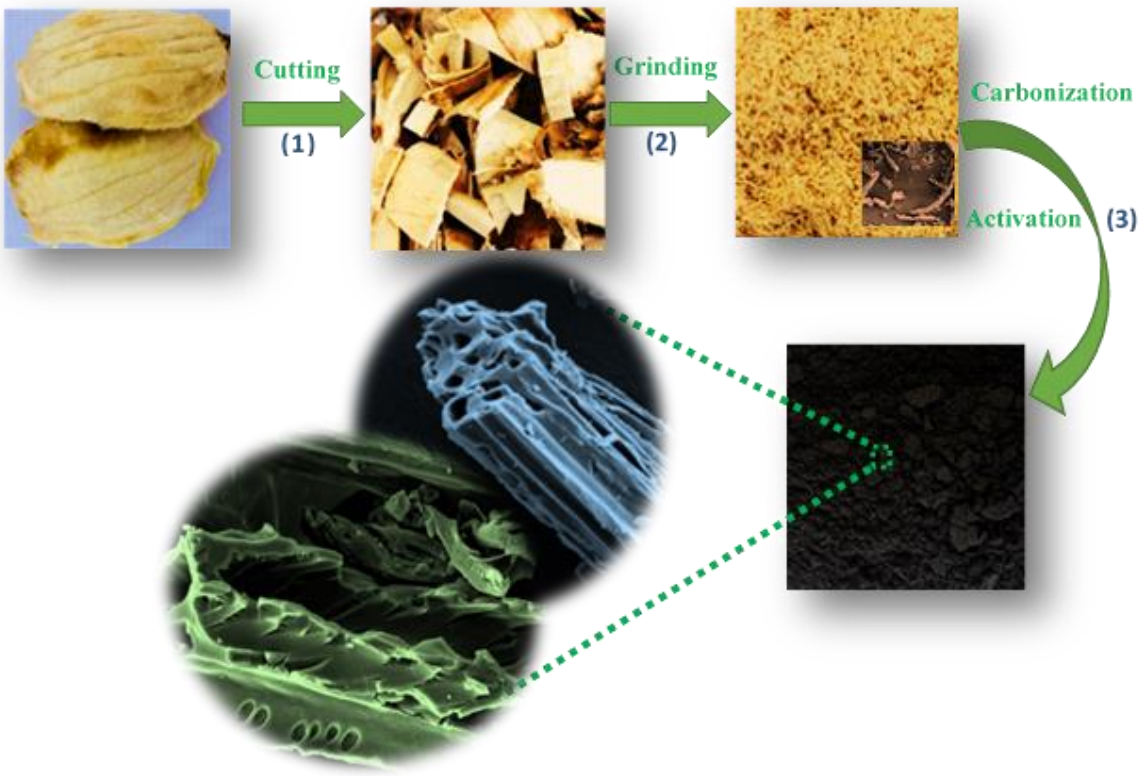

Figure 6.1 Schematic representation shows various steps to convert Mango seed (MS) husk biomass to activated carbon (AC).

6.3.2. Physicochemical characterization

Microstructural analysis of the synthesized materials was carried out by Field Emission Scanning Electron Microscopy (FESEM, TESCAN CLARA). Surface area and pore analysis (SAPA) of the samples was carried out by N_2 adsorption-desorption isotherms at 77 K. The obtained specific surface area was calculated by Brunauer-Emmett-Teller (BET) method, while the pore volume *vs.* the pore diameter was determined by Barrett-Joyner-Halenda (BJH) method. X-ray diffraction (X-ray powder diffractometer, EMMA) and the Raman spectroscopy (high-resolution WITec Alpha 300RA+ system with a 532 nm Ar laser) were used for structural analysis. Elemental analysis was carried out to identify the carbon and other elements (O, H, N, S) in the raw precursor and the AC.

6.3.3. Electrochemical characterization

MS-derived AC (MS-AC active material), acetylene black, and PVDF binder in a mass ratio of 75: 15: 10 were mixed in a slurry using N-Methylpyrrolidone (NMP) as a solvent for electrode coating. 1 cm^2 area of a graphite current collector was coated with approximately 1 mg of the material using the slurry coating method and dried at 80 °C for 12 h to evaporate the solvent. The active mass coated on graphite was determined by the mass weighing before and after coating. Cyclic Voltammetry (CV), Galvanostatic Charge-Discharge (GCD), and electrochemical impedance spectroscopy (EIS) tests were carried out in a three-electrode system (half-cell measurements). MS-AC working electrode, Pt wire counter electrode, and Hg/HgO reference electrode in 2M NaOH aqueous electrolyte were used in the electrochemical cell connected to Biologic SP-150 potentiostat. Half-cell measurements on CV and GCD were carried out for practical purposes at different scan rates (5 - 50 mV s^{-1}) and current densities (2 - 10 mA cm^{-2}). EIS was performed at a frequency range of 10 mHz to 100 kHz with a 5 mV bias voltage. A symmetric capacitor fabricated with two MS-AC electrodes was used to study the full cell capacitance, energy, and power densities. The equations (3.5 -3.7) in chapter 3 were used to calculate the specific capacitance ($C_{s,CD}$, F g^{-1}), energy density (E, Wh kg^{-1}), and power density (P, W kg^{-1}) obtained from charge-discharge data in two-electrode/three-electrode configurations.

6.4. Machine Learning (ML) models

6.4.1. Regression modeling using ML

ML tasks can be either supervised, semi-supervised or unsupervised. Supervised learning tasks are provided with a set of data and some associated labels. In opposition, unsupervised tasks do not require labels to execute tasks [29]. Most of the supervised tasks fall into two categories, either classification or prediction. The problem concerned in this chapter is to identify the relationship between the inputs and the outputs or estimate a mapping function from input variables to a continuous output variable. Therefore, the predictive regression modeling was selected as the ML

model's task. The quantity that is predicted from these ML models is capacitance. The inputs used to predict the capacitance are activation temperature, surface area, I_D/I_G, pore-volume, average pore diameter, and current density.

Four popular ML models, namely, Linear Regression model (LR) [30], Support Vector Regression model (SVR) [31], Decision Tree regression (DT) [32], and a Multi-Layer Perceptron model (MLP) [33], were used and compared in this chapter. LR is commonly used when predicting the variable's value based on another variable's value, while a linear relationship can be found between them [34]. LR is a fast prediction technique and easy to implement. However, a simple linear regression might not perform well for cases where the relationship between the input and output becomes non-linear. Hence, other regression algorithms such as SVR, DT, and MLP are also used. SVR is a regression technique for solving regression estimation problems using an extended concept of Support Vector Machines (SVM) [35]. Thus, SVRs have a strongly non-linear approximation ability using kernel tricks, and the data are separated using different planes or lines. In the DT regression model, data is split along the predictor axes into subsets with similar dependent variable values [36]. Therefore, the process can be represented by a decision tree that can be used to make predictions from newly observed data. MLPs are a type of Artificial Neural Network (ANN) with hidden layers between the inputs and outputs. MLPs can provide a general framework for representing non-linear functional mappings between input variables and a set of output variables [37]. Each hidden layer and the output layer of MLPs consist of computational nodes with activation functions that can compute complex non-linear problems. In addition, the MLP learning process adjusts the weighted connections between nodes until the best solution is reached.

The four ML models, LR, SVR, DT, and MLP, were built using the Sci-Kit-learn package in Python. LR, SVR, and DT use the default settings given in the Sci-Kit-learn package. The MLP regressor was built using two hidden layers with 10 and 5 nodes each. The activation function used is 'ReLu' (Rectified Linear Unit), and the solver used is 'lbfgs' (Limited-memory Broyden-Fletcher-Goldfarb-Shanno). The MLP was trained for a maximum iteration of 2500. The 5 - fold cross cross-validation scheme is applied to all the ML models. From the experimental data, 80% is used for training, and the rest is used for testing the ML models. Hence, it assures that a

different set of test data and training data is used to predict each simulation run which provides the average of the 5 - fold simulation as the final result.

6.4.2. Comparison matrices

Results of the 5 - fold simulations are presented using three evaluation metrics. The correlation coefficient R^2 as given in equation (6.1), Mean Squared Error (MSE) as given in equation (6.2), and Mean Absolute Error (MAE) as given in equation (6.3) are used to benchmark the model accuracy in capacitance predictions.

$$R^2 = 1 - \frac{\sum_{i=1}^{n}(y_i - u_i)^2}{\sum_{i=1}^{n}(y_i - \bar{u})^2} \quad (6.1)$$

$$MSE = \frac{\sum_{i=1}^{n}(y_i - u_i)^2}{n} \quad (6.2)$$

$$MAE = \sqrt{\frac{\sum_{i=1}^{n}|y_i - u_i|}{n}} \quad (6.3)$$

where n, y_i, u_i, $\bar{u}$ are the number of data points, the value calculated from ML, the experimental value, and the average of all experimental data, respectively. To identify the best ML model, it should show the highest R^2, which would reach 1 for a perfect fit, whereas the MSE and an MAE should be lower. The smaller the MSE and MAE are, the closer the predicted and actual values.

6.5. Physicochemical characterization of the MS-derived biomass

Microstructural analysis. Figure 6.2 A-B shows the FESEM images of the raw MS husk as a precursor for synthesizing activated carbon. The microstructural images of the MS husk raw precursor in Figure 6.2 A-B illustrate a twisted shape, a typical characteristic of the precursor. Apart from this, no other clear evidence of forming a well-defined porous network is evident before being subjected to thermochemical conversion. However, a substantial change in morphology is seen as a function of

temperatures in Figure 2 C-J, which arises after removing the volatile components from the MS husk via lignocellulosic biomass decomposition. During the carbonization, the moisture content from the lignin is removed, and the inorganic compounds produce volatile products that undergo condensation resulting in the porous framework. Figure 2 C-J shows the evolution of cleavage, channels, and formation of pores, which have been grown on the twisted structure with increasing activation temperature. The initial twisted structure of the MS husks is preserved during its thermal degradation, implying that the physiological function of the MS husks was able to inherit the porous architecture originating from the precursor [38]. Compared to the commercial AC in Figure 6.2 K-L, the morphology of the MS-AC surfaces (Figure 6.2 C-J) are different in their shapes and sizes. The MS-AC samples exhibit more open channels, and porous networks evolved through carbonization and activation. The cracks and pores generated after carbonization facilitated KOH to flow into the interior of the carbonized materials. As a function of the increase in temperature, the pores on the surface become more prominent (Figure 6.2 G-J) with improved pore volume. This created better pathways that help to reduce the flow resistance and allow for efficient ion transportation from the electrolyte into the bulk material during charging-discharging. On the other hand, samples activated at a lower temperature, MS-AC 800 (Figure 6.2 C-D), displayed more cracks with short tunnels and fissures within them. Randomly arranged macro-pores ranging from a few hundred nanometers to microns are seen on the surfaces. At the same time, a combination of 2D and 3D morphologies can be observed for the MS-AC 1100 (Figure 6.2 I-J) that could synergistically improve the material performance. The TEM images (Figure 6.3) further confirm randomly distributed highly porous carbon layers indicating the disordered structure of MS-AC 1100. A few other regions of the TEM (Figure 6.3C) show graphite sheets-like morphology.

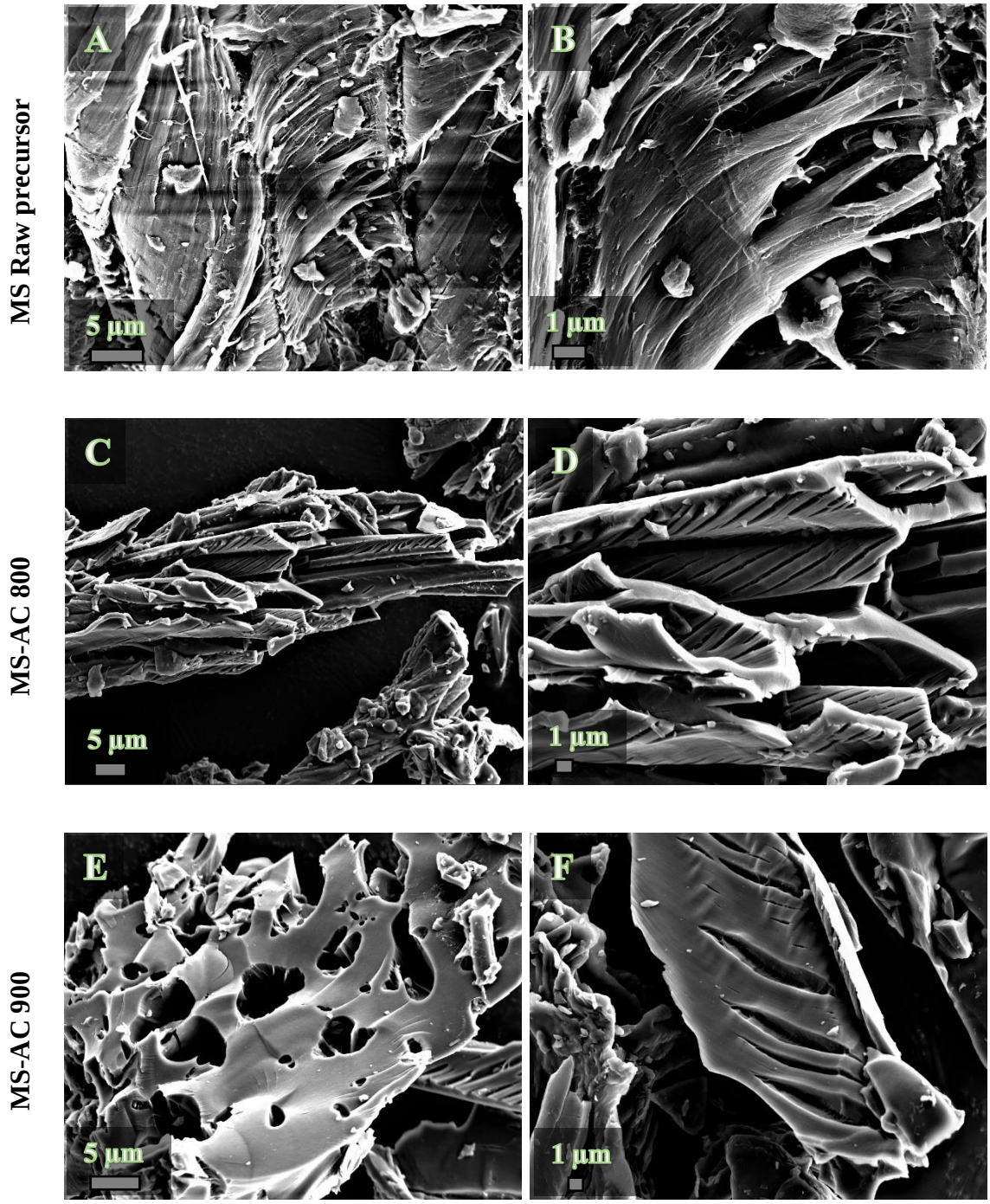
MS Raw precursor
A
5 µm
B
1 µm
MS-AC 800
C
5 µm
D
1 µm
MS-AC 900
E
5 µm
F
1 µm

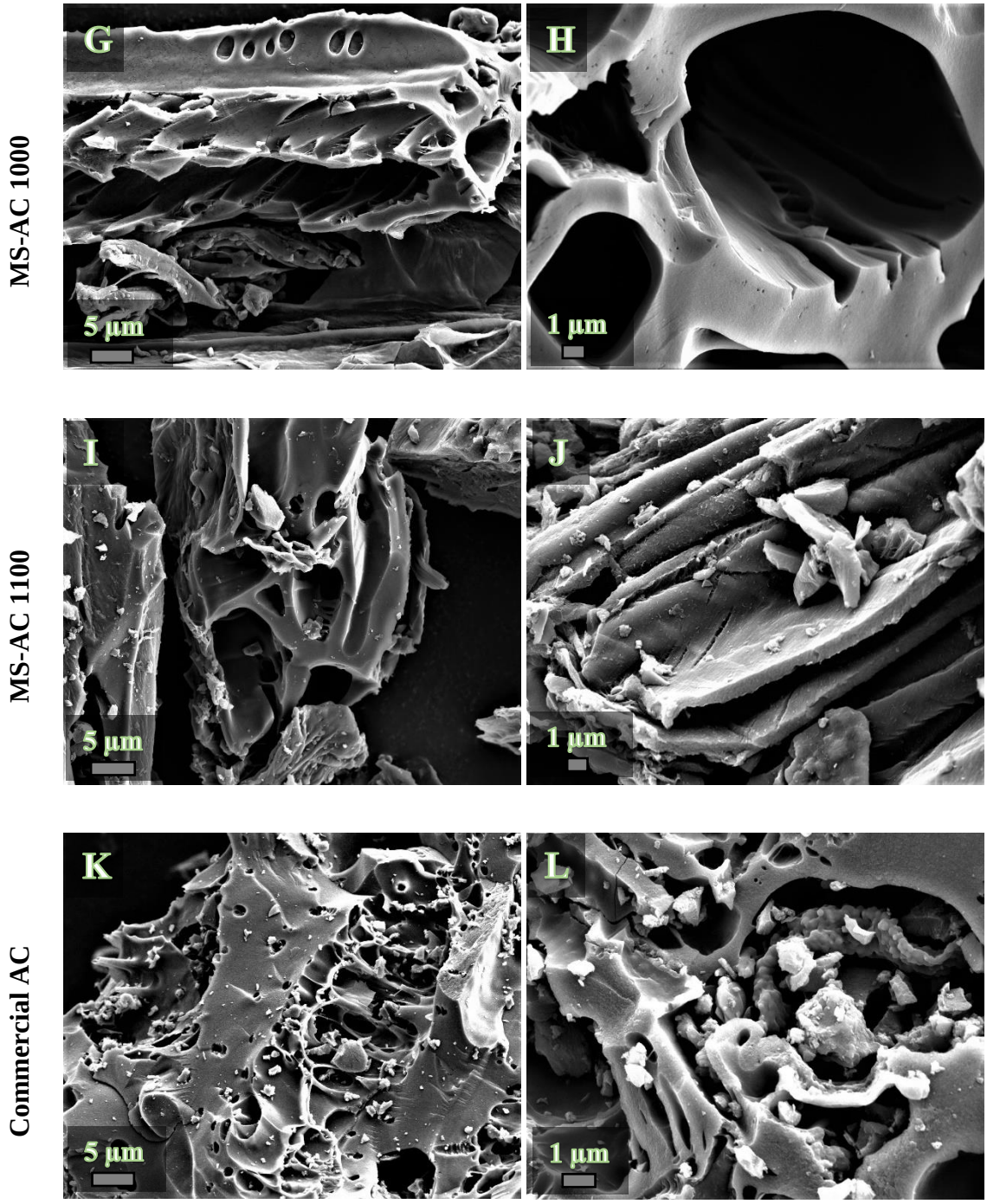

Figure 6.2 Field-emission Scanning Electron Micrographs (FE-SEM) of Mango seed (MS) husk derived AC materials. (A-B) MS raw precursor, (C-D) MS-AC 800, (E-F) MS-AC 900, (G-H) MS-AC 1000, (I-J) MS-AC 1100, and (K-L) Commercial AC.

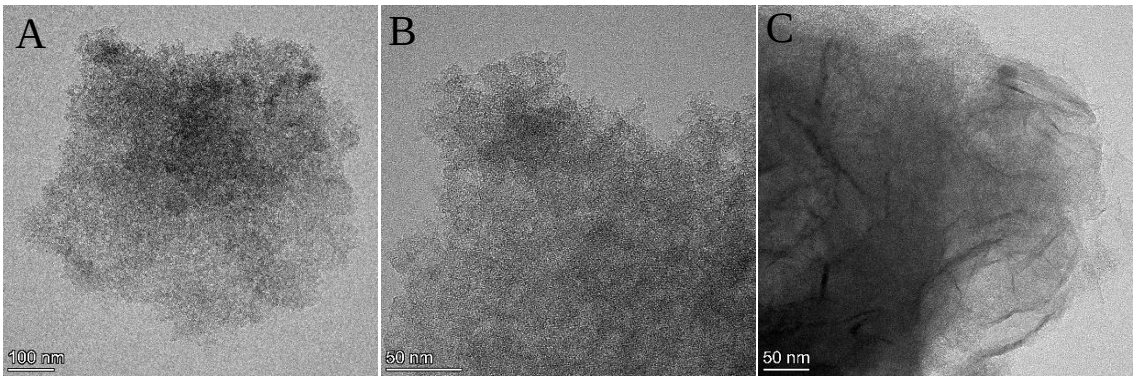

Figure 6.3 (A, B, C) TEM images of MS-AC 1100.

The plausible activating mechanism for KOH activation can be as follows. The pore network in the material is created by the redox reactions between KOH and carbon. The intermediate compounds such as CO_2 and H_2O participate in gasification reactions (physical activation), resulting in the formation of pores. The metallic 'K' produced during the reactions intercalating into the carbon lattice cause lattice expansion, which is removed by washing the sample after activation. Subsequently, the relevant spaces are occupied by the micro-pores leading to a hierarchical pore structure [39]. When the activation temperature increases from 800 - 1100 °C, a lower yield has been observed in the AC samples but results in a highly porous form. The pore volume occupied by the micro-pores has been increased, leading to a well-defined hierarchical porous architecture as the critical parameter for energy storage applications.

Pore structure analysis. Figure 6.4A shows Nitrogen adsorption-desorption curves of four MS-derived biomass samples. The BET surface area, cumulative pore volume, and diameter for the samples activated at different temperatures are compared with commercially available activated carbon in Table 6.1. According to the IUPAC classification, all the isotherms (Figure 6.4A) can be categorized as type-IV isotherms. In all the isotherm curves, primary adsorption occurs at a relative pressure of less than 0.1 and shows an almost horizontal plateau at higher relative pressures except for MS-AC 1100 (red plot in Figure 6.4A). This indicates that compared to MS-AC 1100, the other samples possess a considerable portion of micro-pores but have narrow pore size distribution [40]. The pore size distributions shown in Figure 6.4B are generally alike

for those samples synthesized at 800, 900, and 1000 °C, but the pore volume obtained for MS-AC 1100 is significantly high. This is consistent with the hysteresis (Figure 6.4A) becoming more clearly visible in the samples with increasing activation temperature suggesting high porosity. Hysteresis starts to occur for pores wider than ~ 4 nm. Therefore, the MS-AC 1100 contains a higher amount of mesopores with larger pore sizes, leading to hysteresis behavior. The type H4 hysteresis loop, typical for micro-mesopore carbon, is seen in the relative pressure range of 0.4 to 1.0. This represents that different pore shapes exist in the carbon lattice though there is no effect of pore-blocking/percolation that often occurs due to more complex pore structures [41,42]. Based on the pore size distribution, all the samples are rich in mesopores and micro-pores. Meso-pores in the MS-AC samples can store the electrolyte, reduce the electrolyte diffusion distance, and supply the electrolyte for quick storage/release of ions.

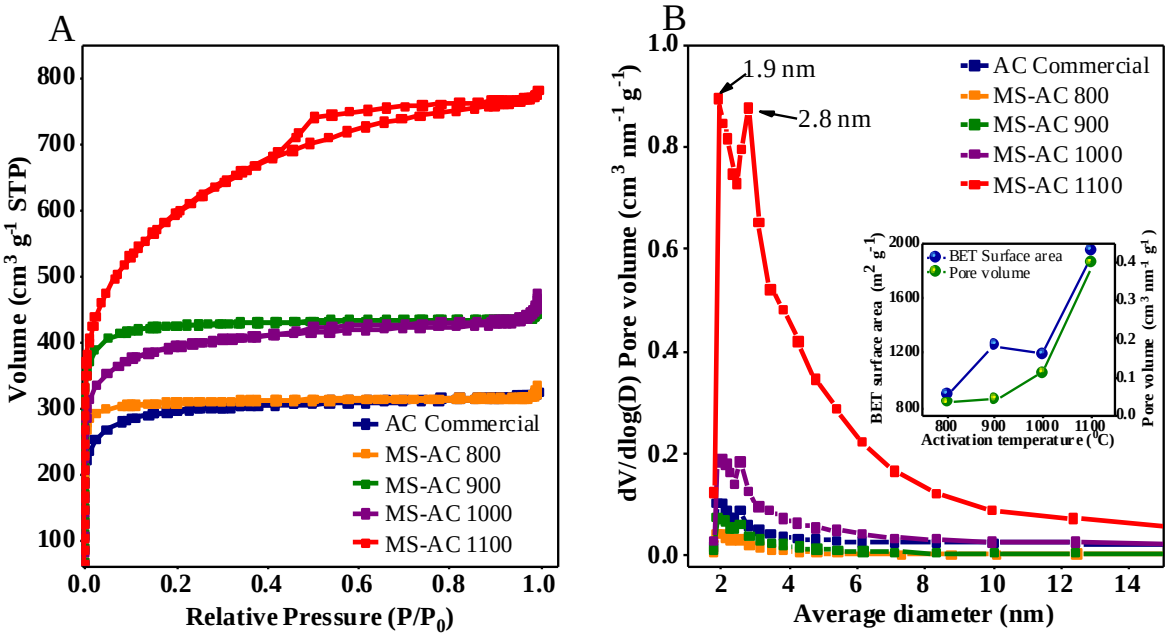

Figure 6.4 BET nitrogen adsorption-desorption hysteresis loops of MS-AC activated at different temperatures along with commercially activated carbon shown for comparison, and (right) pore size distribution profiles (effect of activation temperature on surface area and pore volume are shown in the inset profile).

From Table 6.1, it can be inferred that both the BET surface area and the average pore volume estimated for MS-AC 1100 are superior to those of MS-AC activated at lower temperatures. Therefore the pore structure presented by MS-AC 1100 is suitable for ideal supercapacitor material having considerable amounts of the micro (< 2 nm), meso (2–50 nm), and macro (>50 nm) pore types [43]. Overall, it is concluded that at increased activation temperature, the material possesses micro-meso-macropores with heteroatoms residues for creating defects on activated materials resulting in turbostratic carbons.

Table 6.1 BET surface area analysis of MS-derived materials compared with commercial AC.

Sample	**BET surface area (m^2 g^{-1})**	**BJH Adsorption average pore diameter (nm)**	**BJH Adsorption cumulative pore volume (cm^3 g^{-1})**
Commercial AC	879.84	3.7048	0.0556
MS-AC 800	899.31	7.5227	0.0341
MS-AC 900	1256.29	5.2089	0.0429
MS-AC 1000	1190.17	4.6473	0.1135
MS-AC 1100	1943.75	3.1553	0.3970

Structural and spectral analysis. The XRD profiles of MS raw precursor carbonized at 600 °C and activated at different temperatures are compared with commercially available activated carbon in Figure 6.5A. For the raw precursor, the primary diffraction peak is located in the region of 22° (with the h k l indices 002), and a shoulder is seen between 16° and 18° are attributed to the cellulose component in the biomass precursor. Correspondingly, the presence of diffused diffraction peak confirms the semi-crystalline nature of biomass [44]. During the heat treatments of carbonization and activation at different temperatures, the semi-crystalline biomass has been transformed to amorphous carbon as in the XRD profiles of MS-AC in Figure 6.5. Thus, MS-AC samples activated until 900 °C show visibly reduced peak intensity but with peak broadening. Overall, when the activated temperature is increased from

800 to 1000 °C, broad peaks become less visible. This could be due to the fact that the splitting effect of KOH on partially crystalline cellulose converted the carbon into activated carbon with no pronounced order [45]. The broadened peak labeled in the regions 25° (002) and at around 43° (100) could attribute to the amorphous carbon [40,46], which is quite comparable to that of peaks seen for commercially available AC.

FTIR was used to analyze the transformation of the functional groups during the conversion from the raw MS husk to biochar and then to the activated carbon. The collected FTIR spectra is shown in Figure 6.5B. Any biomass can have a typical and complex lignocellulosic structure. In this case, untreated MS husk exhibits several functional groups such as alkene, aromatic, ketone, hydroxyl, and carboxyl functional groups common for lignocellulosic raw materials. The peaks in the region between 1000 and 1400 cm^{-1} (with vertical bars) show the presence of functional groups such as C-O and C-H, characteristic of the cellulose constituent. The peaks in the 1210 - 1230 cm^{-1} region are attributed to the aromatic phenyl group C-O. The carbon-carbon double bond C=C in the alkene functional group was evident from the absorption band at the 1654 cm^{-1} region [18], which indicates the aromatic nature of lignin in the precursor. Moreover, the IR peak at 2915 cm^{-1} (2800 - 3000 cm^{-1}) is ascribed to the C-H stretching vibration of aliphatic carbon in the lignocellulosic component. The hydrogen-bonded O-H stretching vibration in methyl groups of lignin/water in the biomass precursor is correlated to the band at 3318 cm^{-1}, as shown in Figure 6.5B [47,48]. During the carbonization, intensities of the C-O-C absorption bands corresponding to the cellulose and hemicelluloses components have been decreased and almost less defined. Most of the elements (O, H) have been removed from the raw biomass structure as volatile substances during the thermal treatment. Further, upon alkali (KOH) treatment, the volatile components of MS husk are mostly removed, as evidenced by the disappearance of corresponding bands [18,48]. The remaining carbon atoms create cross-links and form graphitic and turbostratic carbon [49].

Unlike FTIR, the Raman analysis provides vibrational information and information on the electronic features through the electron-phonon coupling that gives insights into defects and doping through the intensities and widths of the Raman peaks. The Raman spectra of the MS husk-derived carbon activated at different temperatures are

compared with commercially available activated carbon are shown in Figure 6.5C. The characteristic peaks of commercially available AC corresponding to the D-band and G-band can be seen at 1337 cm^{-1} and 1582 cm^{-1}. In the case of the MS-AC at different temperatures, corresponding peaks are seen at 1338 cm^{-1} and 1577 cm^{-1}, implying the nature of AC is similar. The presence of the D band in the material infers the structural defect while the G band corresponds to the degenerate in-plane high-frequency excitation (E_{2g}) phonon at the Brillouin zone center. An ideal defect-free carbon will not show the D peak [50]. The lower relative intensity of the G peak compared to the D peak indicates a highly defective nature in the carbon lattice [51–53]. The intensity of the D band relative to that of the G band increases with the amount of disorder. Its intensity ratio (I_D/I_G) has often been used to characterize the defective nature of the material. The calculated intensity ratios of D and G peaks are 1.02 for commercial AC, while 0.98, 0.95, 0.67, and 0.97 for MS-AC 800, 900, 1000, and 1100, respectively. Additionally, the 2D band is also seen for the samples synthesized at higher temperatures, indicating a second order of the D band, commonly reported for the graphene stacked layer. The results suggest that all the samples combine turbostratic and graphitic carbon. The highest degree of graphitization is shown for the MS-AC activated at 1000 and 1100 °C. The material's inherent structure may have contributed to suppressing the deformation of the carbon lattice, and the increased inter-planar distance due to distinct process conditions could also lower the defect density than the commercial AC.

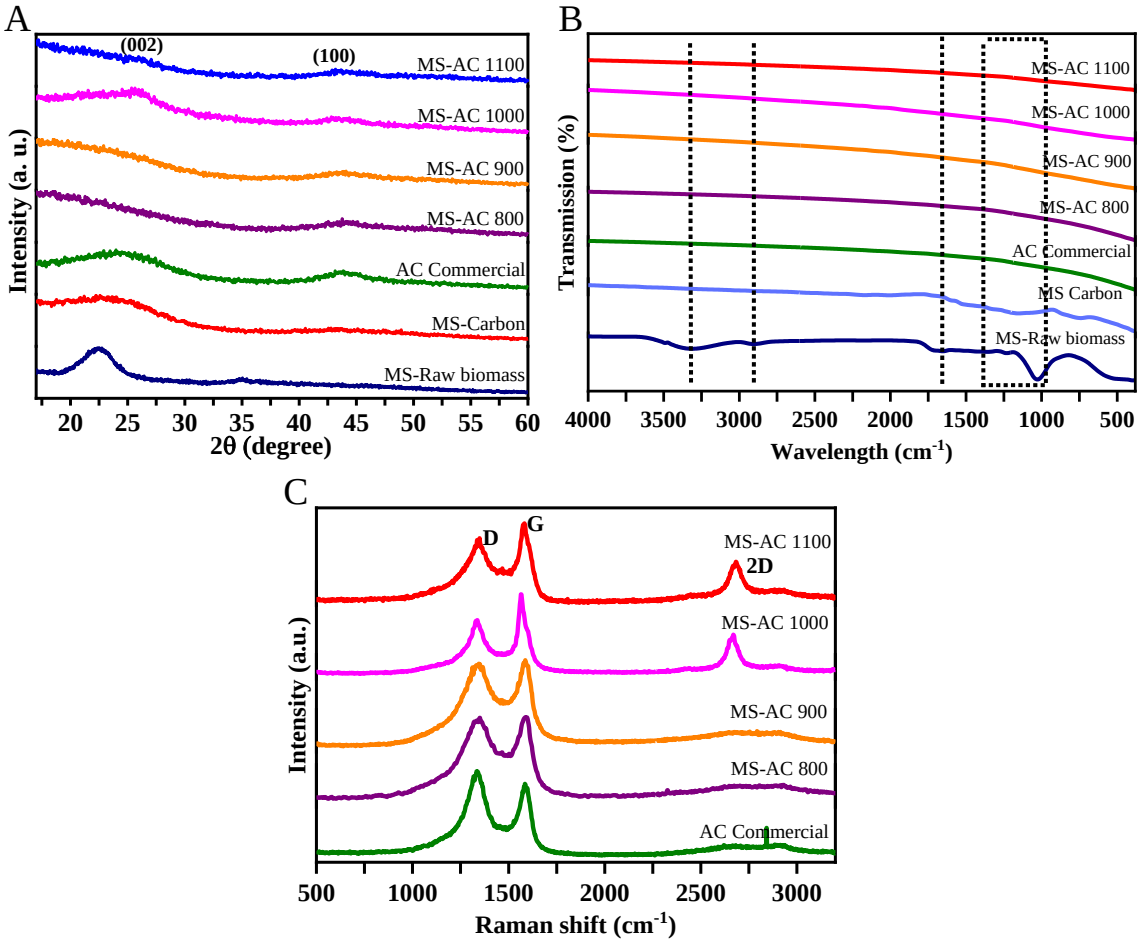

Figure 6.5 (A) X-ray diffraction patterns, (B) Mid and near infra-red (IR) spectra, and (C) Raman spectra of MS husk derived materials. Samples are labeled in the individual plots. Sample activated at a higher temperature (MS-AC 1100) shows an amorphous carbon in Figure 6.5 A-B and with the evolution of the 2D band in Figure 6.5C.

Elemental analysis. The raw precursor comprises various elements, mainly C, H, O, N, and S. Additionally, heteroatoms can exist in organic biomass materials. The O, H and C, N, S analysis was carried out to find the inbuilt percentage of elements in the MS raw precursor and MS-AC materials. The results are tabulated in Table 6.2. The thermochemical treatment has significantly increased the carbon content in the materials. It is ~1.9 times higher in the MS-AC 1100 compared to the initial amount in the raw MS husk. In contrast, the oxygen percentage has drastically decreased during the process, which is ~20 times less than before the treatment. This is due to

the removal of oxygen functional groups, which is consistent with the FTIR results. Content of 0.2 % S has been identified for the raw precursor. However, after heating the precursor at a high temperature (MS-AC 1100), the corresponding EDS analysis (Table 6.2) did not show any presence of 'S' in the material. This could be due to the volatile content that presents on the shell, which was transformed into a vapor at the given temperature [54]. Moreover, the EDS results in Figure 6.6 confirm the presence of C and O as major elements in MS-AC 1100, illustrating that this profoundly enhances the electrochemical performance in supercapacitors.

Table 6.2 Elemental analysis of the raw precursor and samples activated at different temperatures.

Elements (%)	C	H	N	S	O
MS- Raw biomass	49.8	7.4	-	0.2	42.6
MS-AC 800	92.7	1.0	-	-	6.3
MS-AC 900	93.5	0.9	-	-	5.6
MS-AC 1000	96.0	-	-	-	4.0
MS-AC 1100	98.0	-	-	-	2.0

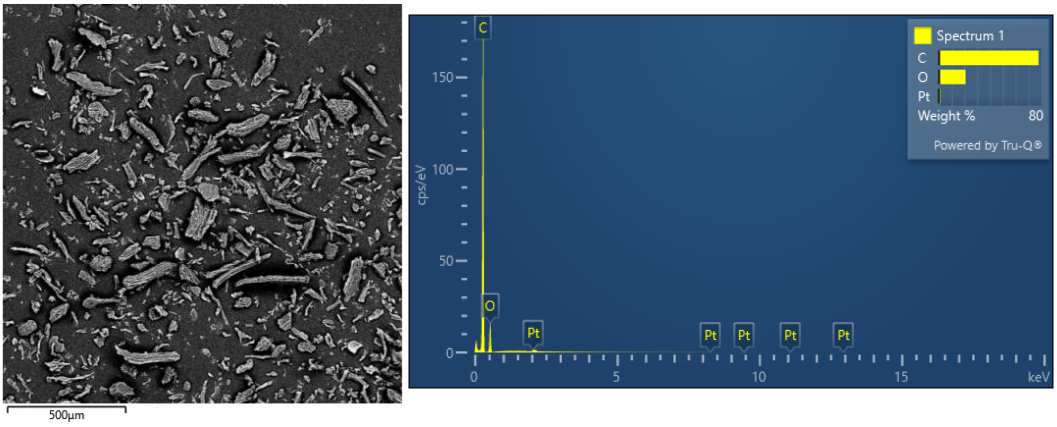

Figure 6.6 EDS mapping and the respective spectra of the MS-AC 1100 sample.

6.6. Electrochemical characterization of the MS-derived biomass (three-electrode configuration)

As explained in the previous sections, the physical parameters of the biomass converted to activated carbon play a key role in increasing the electrochemically accessible area of the carbon electrode for charge storage [55]. To verify this, the electrochemical studies of MS-derived AC were carried out through CV and GCD experiments in an aqueous electrolyte 2 M NaOH at a potential window of 1 V in the negative region. Most of the work reported in the literature [13,56] on producing AC is electrochemically tested using either an acidic electrolyte (1 M H_2SO_4) or highly basic electrolyte (6 M KOH) solutions. Generally, the concentration of the electrolyte also affects the capacitance performance. It has been widely accepted that better ionic diffusion has been observed when the H^+ is present in the acidic electrolytes, which improves the EDLC behavior. In contrast, the extreme conditions of a strong pH acid/base cause disadvantages such as increased corrosion rate of the current collectors and metals in the system [57]. Compared with the alkaline cations such as Na^+ and K^+, the factors such as low ion diffusivity and large ionic radius will limit the energy/power densities obtained by the K^+ ion capacitors. Though Li and Na have similar chemical properties, the resources and abundance of Na are unmatched by Li, which should be considered for future developments. Therefore, our goal is to examine the biomass material using 2 M NaOH as an emerging electrolyte for capacitors to overcome these issues reported [58].

The CV and GCD profiles of MS-AC at different temperatures are compared with commercially available AC. The corresponding plots at different scan rates and current densities are shown in Figure 6.7. Regardless of the physicochemical nature of the samples derived from the biomass, all the CV curves (Figure 6.7 A-I to E-I) show a quasi-rectangular shape without any redox peaks indicating that the material is in the proximity of the typical rectangular shape, characteristic of the EDLC behavior [59,60]. However, based on the nature of the sample, the area under the curve varies; in other words, the current response differs significantly. The performance characteristics of the MS-derived AC samples are superior to that of the commercially available AC sample. The samples are further verified by the GCD technique, which

shows a perfect symmetry while displaying a triangular shape of typical capacitive material (Figure 6.7 A-II to E-II) involving reversible adsorption and desorption of ions during the discharge and charge processes, respectively. With increasing scan rate (to 40 mV s^{-1}) and current density (to 6 mA), CV curves still exhibit a quasi-rectangular shape, and GCD curves also show nearly linear slopes indicating an excellent rate-independency on energy storage. It can be further supported by very low resistive voltage losses (no apparent Ohmic losses seen at GCD profiles) stem from the resistance between the active material and the current collector and the electrolyte resistance across the electrode surface. The specific capacitance values calculated at 5 mA cm^{-2} for all the samples are presented in Table 6.3. The specific capacitance values of MS-AC activated at 800, 900, 1000, and 1100 °C correspond to 86, 98, 118, and 135 F g^{-1} at 5 mA cm^{-2}. Under identical conditions, the obtained specific capacitance for the commercially available activated carbon measured at the laboratory is found to be 78 F g^{-1}. These results suggest that the MS-derived biomass converted to AC exceeds the storage capacity, and the value is much higher for MS-AC 1100. The effect of elemental composition and defects observed for MS-AC 1100 through physicochemical studies appears to be suitable for facilitating OH^- ion transportation and interfacial chemical reactions that result in higher specific capacitance. For MS-AC1100 having a range of pore distribution was found more efficient for storing/releasing ions during the electrochemical process. It helps mitigate the high viscous force issue with the NaOH electrolyte, resulting in a good rate capability. The hierarchical porous network displayed in Figure 6.2 I-J inherited from the Mango seed with husk after thermal treatment served as a channel for ion percolation in bulk to enhance the available specific capacitances.

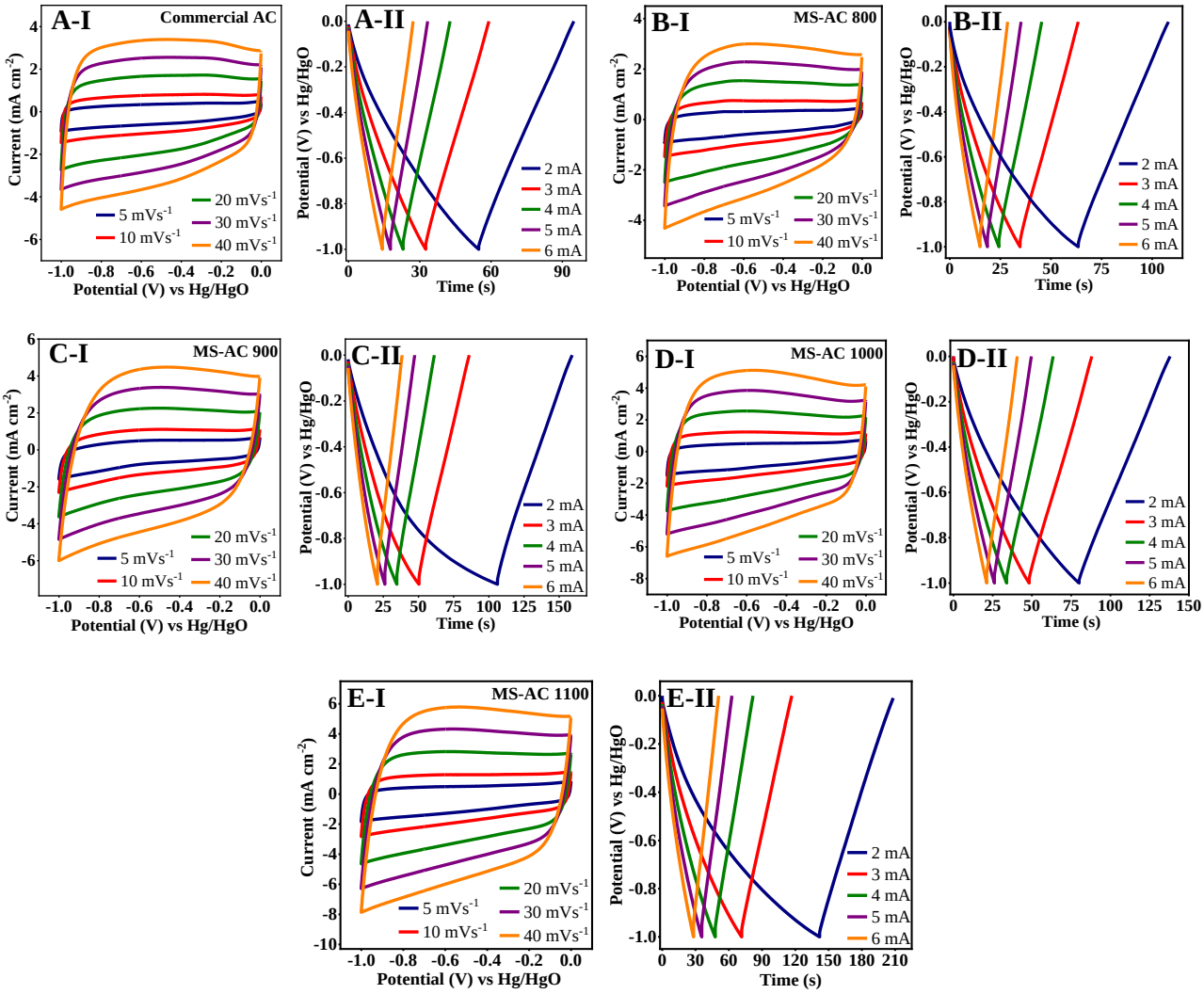

Figure 6.7 (A-I, B-I, C-I, D-I, E-I) Cyclic Voltammograms (CV), and (A-II, B-II, C-II, D-II, E-II) galvanostatic charge-discharge (GCD) curves in a three-electrode configuration of MS husk derived AC at different sweep rates and applied currents tested in 2 M NaOH electrolyte. Samples are labeled in the individual plots.

Table 6.3 The storage properties of MS-derived AC compared with commercial AC (tested at a current density of 5 mA cm^{-2} in 2 M NaOH aqueous electrolyte).

Active material	F g^{-1}
Commercial AC	78
MS-AC 800	86
MS-AC 900	98
MS-AC 1000	118
MS-AC 1100	135

To compare the electrochemical performance characteristics of the MS-AC samples activated at different temperatures, CV and GCD profiles are superimposed in Figure 6.8 A-B. Among the samples studied at different temperatures of 800 - 1100 °C, MS-AC 1100 performs superior, as expected from the previously discussed parameters such as surface area and pore analysis. The specific capacitances of the MS-AC calculated as a function of the current density (2 to 10 mA cm^{-2}) from their GCD curves are displayed in Figure 6.8C. The rate performance capacitances of the samples were very high, except the MS-AC 800 shows an initial capacitance of 90 F g^{-1} with a small decline (10 %) with increasing current density from 2 to 10 mA cm^{-2}. The fissured structure observed in Figure 6.2 C-D for MS-AC 800 limits the passage of ions and hence the lower capacitance. The specific capacitance as a function of activated temperature further confirms that the procured surface area is proportional to maximizing the storage capacitance. Higher surface area and pore volume in porous material create more active sites and transport ions to promote the electrochemical reaction. The cycling stability and the coulombic efficiency over 1000 cycles were tested for the best-performed sample MS-AC 1100 sample, and the long-term cycling data is shown in Figure 6.8D. The capacitance retention is almost 100 % even after consecutive cycles of 1000 with an excellent coulombic efficiency. MS-AC 1100 electrode delivered an energy density of 19 Wh $kg^{-1,}$ with a 1077 W kg^{-1} power density. The EIS was carried out on MS-AC 1100, and the Nyquist plots for this sample are displayed in Figure 6.8E with curve fitting and the equivalent circuit shown in the

inset. The EIS analysis helps gain a fundamental understanding of the behavior of electrode/electrolyte interface, electrolyte bulk properties, and their impact on the electrochemical performance bringing a valid conclusion to MS-AC 1100 compared to other counterparts. The inset in Figure 6.8E shows a curve representing a semicircle in the high-frequency region, a Warburg line in the intermediate frequency region, and an almost vertical line in the low-frequency region. The plots were fitted into a model using Z-fit in EC Lab using the modified Randle's equivalent circuit. The five elements in the circuit represent interfacial resistance (R_s), Constant Phase Element (CPE), charge transfer resistance (R_{ct}), Warburg component (Z_w), and capacitance (C). The intercept of the semicircular arc of the plot with the real axis gives the R_s. The R_s value for before and after cycling were found to be 2.09 and 2.05 Ω, respectively, giving an indication of a slight increment of ions and electron transfer rates. R_s is a combination of electrolyte ionic resistance, intrinsic resistance of the electrode material, and contact resistance at the interface of the electrode material and the current collector. R_{ct}, the charge transfer resistance at the electrode surface is about 0.24 Ω (1st cycle) and 0.21 Ω (1000^{th} cycle), exhibiting an efficient charge transfer through more electrolyte penetration into the electrode. The straight line with the 45° slope illustrates the resistance for electrolyte ion diffusion into the electrode, as a typical characteristic of porous carbon which is denoted by the Warburg parameter. The small diameter of the semicircular arch and a shorter Warburg portion can be occurred due to a fast charge transfer and ion diffusion supported by a well-arranged pore structure of the MS-AC 1100 material [56,61,62]. In the low-frequency region, the curve has become more vertical, displaying a low ionic diffusion resistance that causes an enhanced capacitive performance through faster ionic diffusion through the electrode material, which can be attributed to the higher surface area and porous nature [48]. Therefore, the EIS study confirms that at the activated temperature of 1100 °C, the intrinsic properties of the material best suit the electrochemical performance. An in-depth analysis of the material from its chemical engineering and electrochemistry perspectives is crucial to elucidate the relationship between biomass and supercapacitor applications. The variation of obtained specific capacitances at various current densities is shown in Figure 6.8F and is comparable in terms of the delivered capacitance to that of the similar carbon materials reported in the literature.

Table 6.4 depicts the information on the range of biomass precursors reported on converting to AC, activating agents used for conversion, and electrochemical studies of some of the AC materials referring to the work found in the literature have been compared with the results obtained for MA-AC in this chapter. Figure 6.8D shows the capacitance performance with a range of biomass precursors reported [63–66]. To assess the structural integrity of the sample, FE-SEM and TEM images for the biomass carbon (MS-AC 1100) before and after cycling have now been performed and shown in Figure 6.9. The morphological features of the biomass were retained for the material went through several cycling. This indicates that the structure of the biomass is intact.

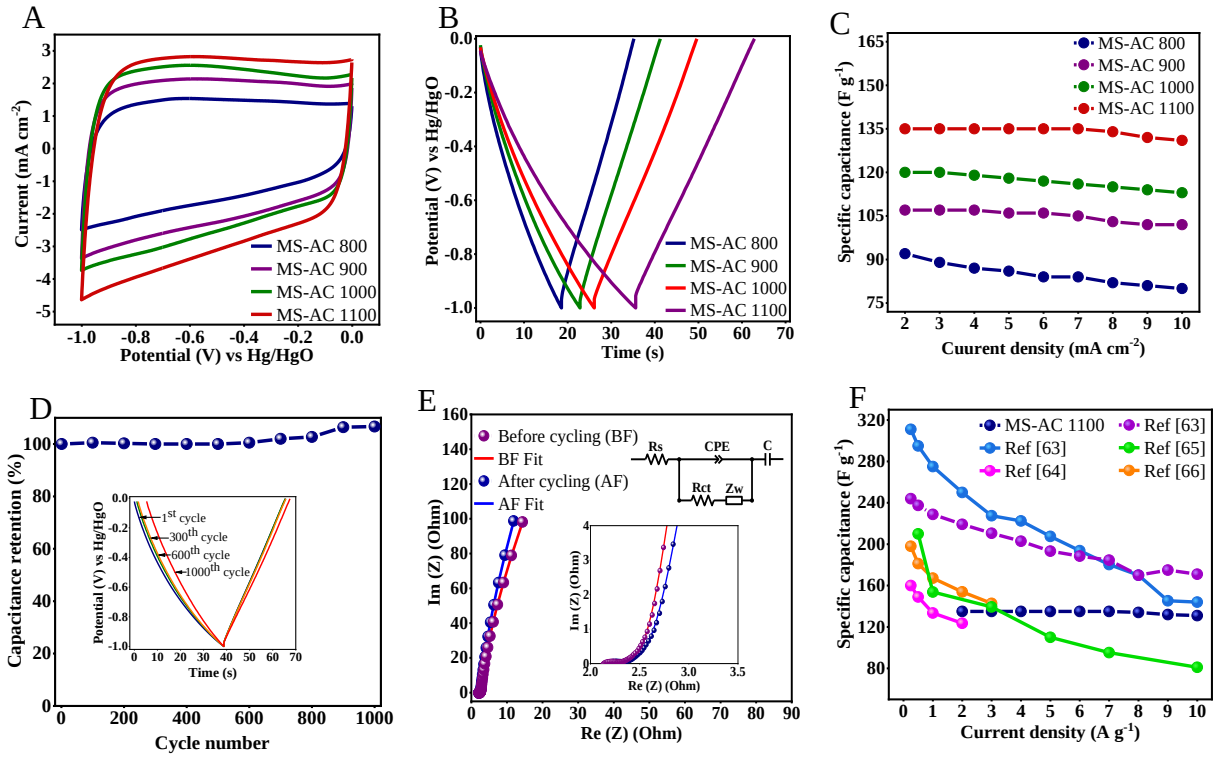

Figure 6.8 Electrochemical profiles of MS-derived material. (A) CV plots at a sweep rate of 20 mV s^{-1}, (B) GCD plots at 5 mA cm^{-2} current density, and (C) variation of specific capacitance of MS-derived materials activated at different temperatures, (D) Capacitance retention tested for MS-AC 1100 (GCD curves compared at 1st and 1000th cycles), (E) Nyquist plots and the fitted curves before and after cycling of MS-AC 1100 (Nyquist plots and the fitted curves for narrow region shown in the inset), (F) comparison of specific capacitances of MS-AC 1100 with previous works reported in the literature [63–66].

Table 6.4 The electrochemical properties of biomass-based carbon derived from various precursors compared with our work.

No.	Biosource	Activating agent	Electrolyte	Current density	Specific capacitance ($F\ g^{-1}$)	Ref.
1	Banana fibres	$ZnCl_2$ KOH	1 M Na_2SO_4	0.5 A g^{-1}	74 66	[67]
2	Coffee endocarp	CO_2 KOH	1 M H_2SO_4	10 mA (~ 0.2 A g^{-1})	176 69	[68]
3	Wheat straw	KOH	6 M KOH	0.5 A g^{-1}	226.2	[69]
4	Macadamia nutshell	KOH	1 M Na_2SO_4	1 A g^{-1}	231	[70]
5	Shrimp shell	KOH	6 M KOH	0.5 A g^{-1}	239	[71]
6	Rice straw	KOH	6 M KOH	1 A g^{-1}	337	[72]
7	**Mango seed husk**		**2 M NaOH**	**2 A g^{-1}**	**135**	**our work**

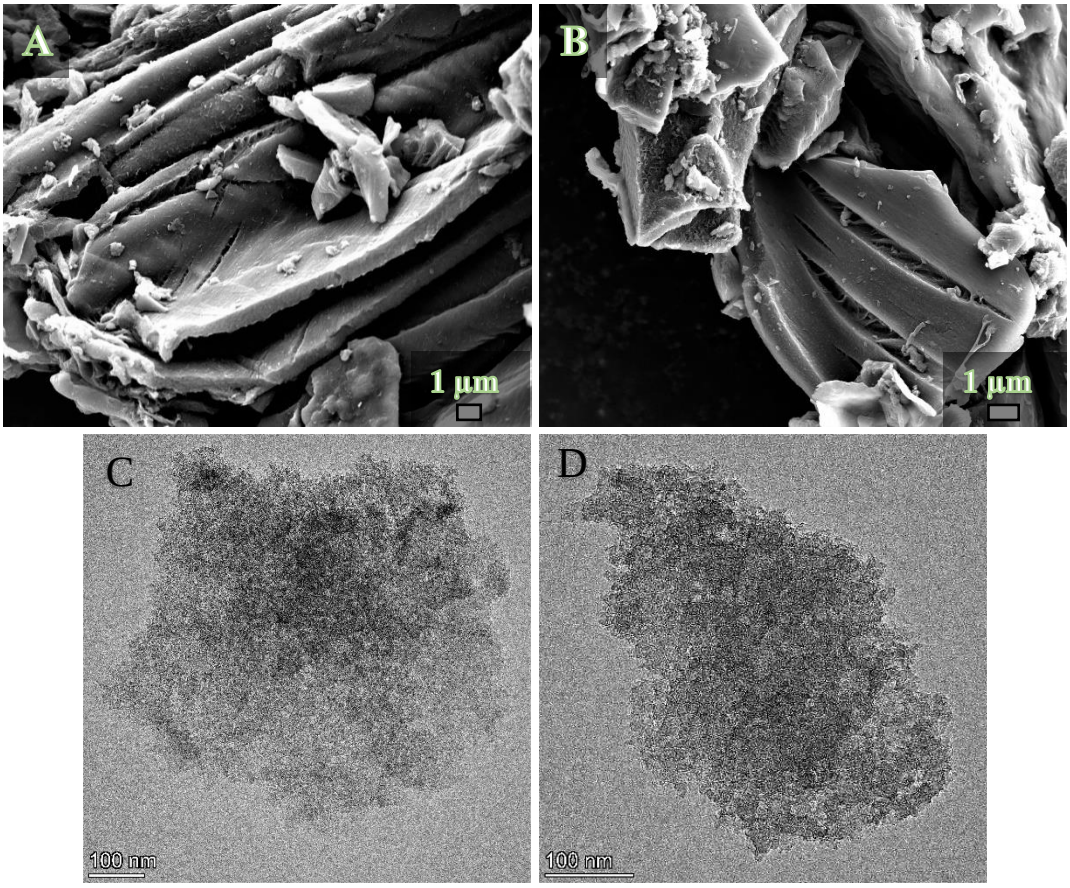

Figure 6.9 Comparison of the microstructures for MS-AC 1100 before and after cycling. FE-SEM and TEM micrographs (A, C) before cycling and (B, D) after cycling.

6.6.1. Machine learning model for predicting specific capacitance in MS-derived biomass

The experimental results (in sections 6.5.1 and 6.5.2) can provide an indication of the influences on the capacitance values from a range of different parameters. However, a clear and quantified relationship would be difficult to achieve by capturing the correlation between experimental inputs and outputs. Furthermore, most existing methods are time-consuming and tedious as they mostly incorporate a trial-and-error approach. Therefore, ML modeling tools were utilized to provide a fast and effective alternative for predicting the capacitance of activated carbon materials. The MLP architecture for modeling experimental data sets for MS-AC is given in Figure 6.10.

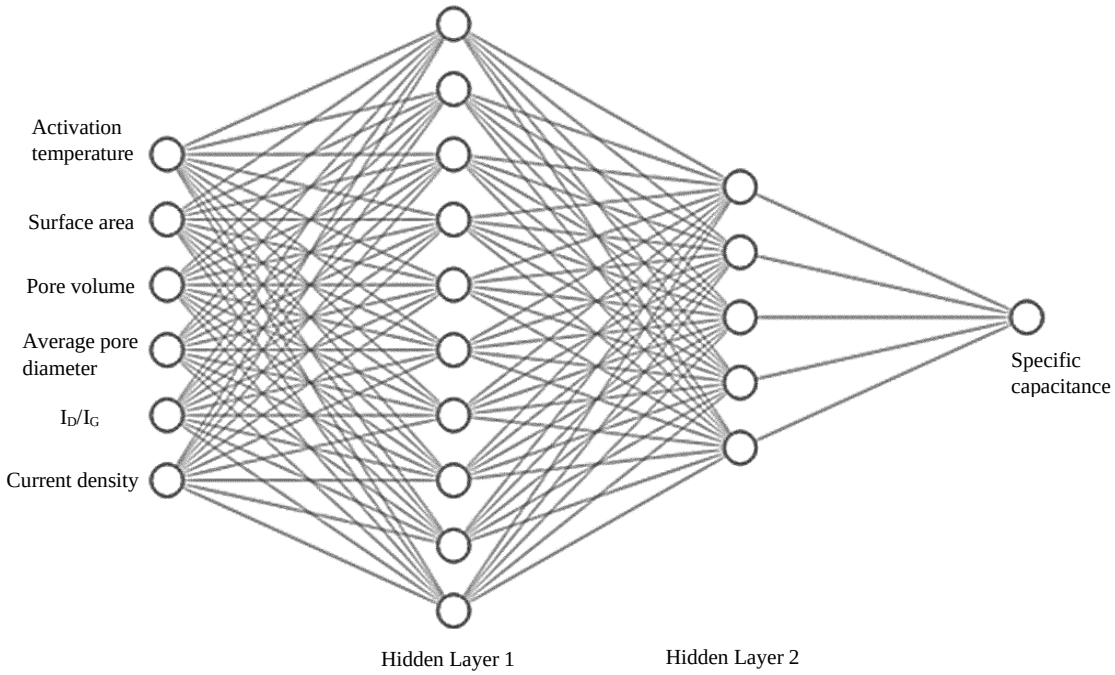

Figure 6.10 MLP model architecture showing input and output shapes with two hidden layers.

Pearson Correlation Coefficient was calculated between the variables to provide a general statistical overview of the dataset. In Figure 6.11, the dark red color squares represent a positive correlation, dark blue represents a negative correlation, and light colors represent no correlation. According to Figure 6.11, it can be concluded that most variables do not hold any strong relationships with each other. It further implies that the relationship between the variables cannot be explained through a simple linear function. The results in Table 6.5 present the R^2, MSE, and MAE values relevant for each model (DT, LR, SVM, and MLP as explained in the method section) simulated in this chapter.

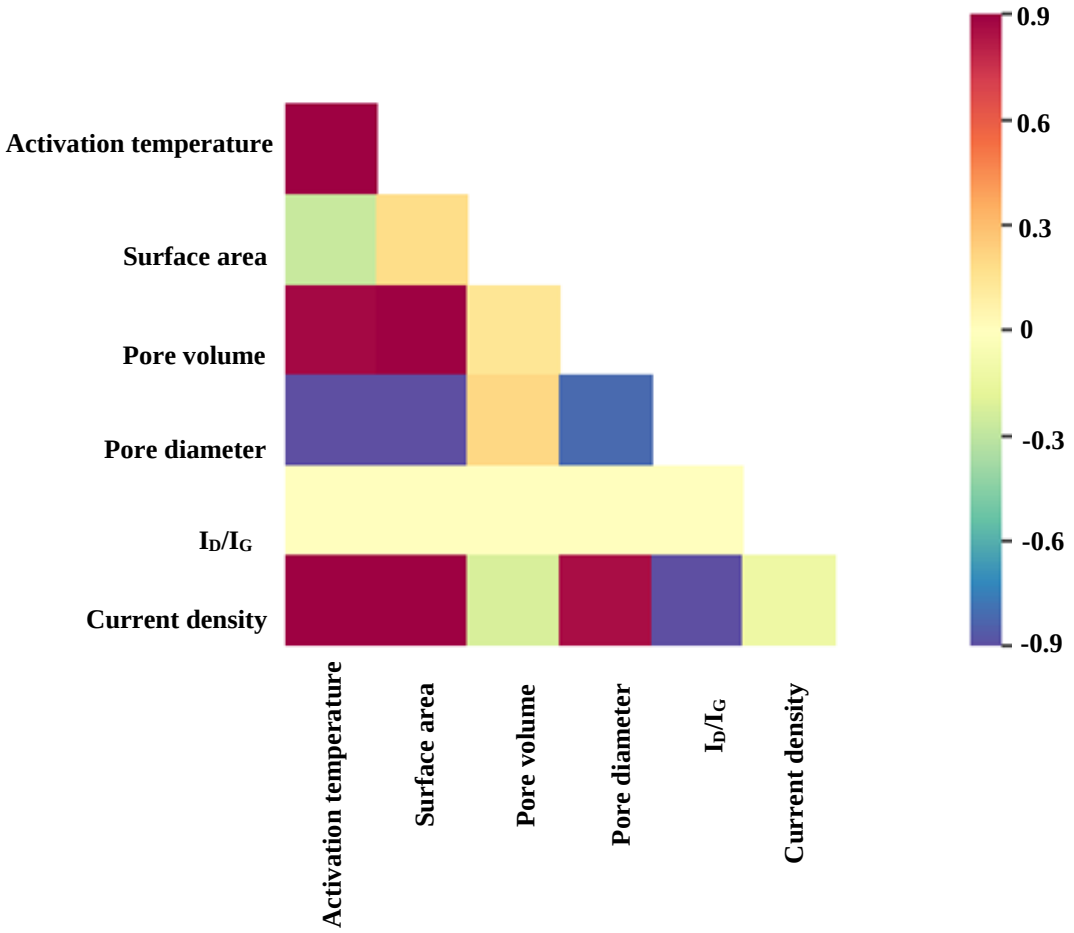

Figure 6.11 Pearson correlation coefficient matrix for the parameters influencing the supercapacitive properties showing non-linear relation.

Table 6.5 Obtained values of statistical criteria for ML models training.

ML Model	R^2	MSE	MAE
DT	0.9427	18.0816	3.3248
LR	0.9759	7.5854	2.1133
SVR	0.9856	4.5308	1.6989
MLP	0.9868	4.1651	1.5741

Figure 6.12 (A-D) depicts the specific capacitance values predicted by each model for all the MA-AC samples. Among the four ML methods, the largest deviation was observed for the DT model with the lowest R^2 and highest MSE and MAE. The reason

for this behavior is that the DT model classifies a dataset into branch-like segments and builds an inverted tree-like structure which causes the similar data items to fall into one branch of the DT. The other three models, LR, SVM, and MLP provided better fittings compared to DT.

For the MLP model, the R^2 value is 0.9868, MSE is 4.1651, and MAE is 1.5741 indicating the highest accuracy level of model predictions. It gives the best fitting in Figure 6.12 (D), with only a marginal difference between the model and experimental results. Therefore, MLP gives superior results to other ML models considered in this chapter. Due to the hidden layers and their connections between each node of MLP, the non-linear relationship between the inputs and the output can be correctly modeled. This leads to precise results by MLP predictions on unseen data. Therefore, From the results presented in Table 6.5 and Figure 6.12, it can be concluded that the model can overcome the complexity of understanding the non-linear relationship between the various inputs (synthesis conditions, physical and electrochemical parameters) and the output (electrode's energy storage performance). Overall, it suggests that ML modeling can be utilized for better experimental design to avoid cumbersome trial and error in experiments on material performance optimization tasks. Furthermore, the ML models can overcome the challenge of physics-based modeling that is primarily valid for the systems at or near equilibrium. Thus, the ML models can be utilized to build correlations between inputs and outputs regardless of the physical condition [36].

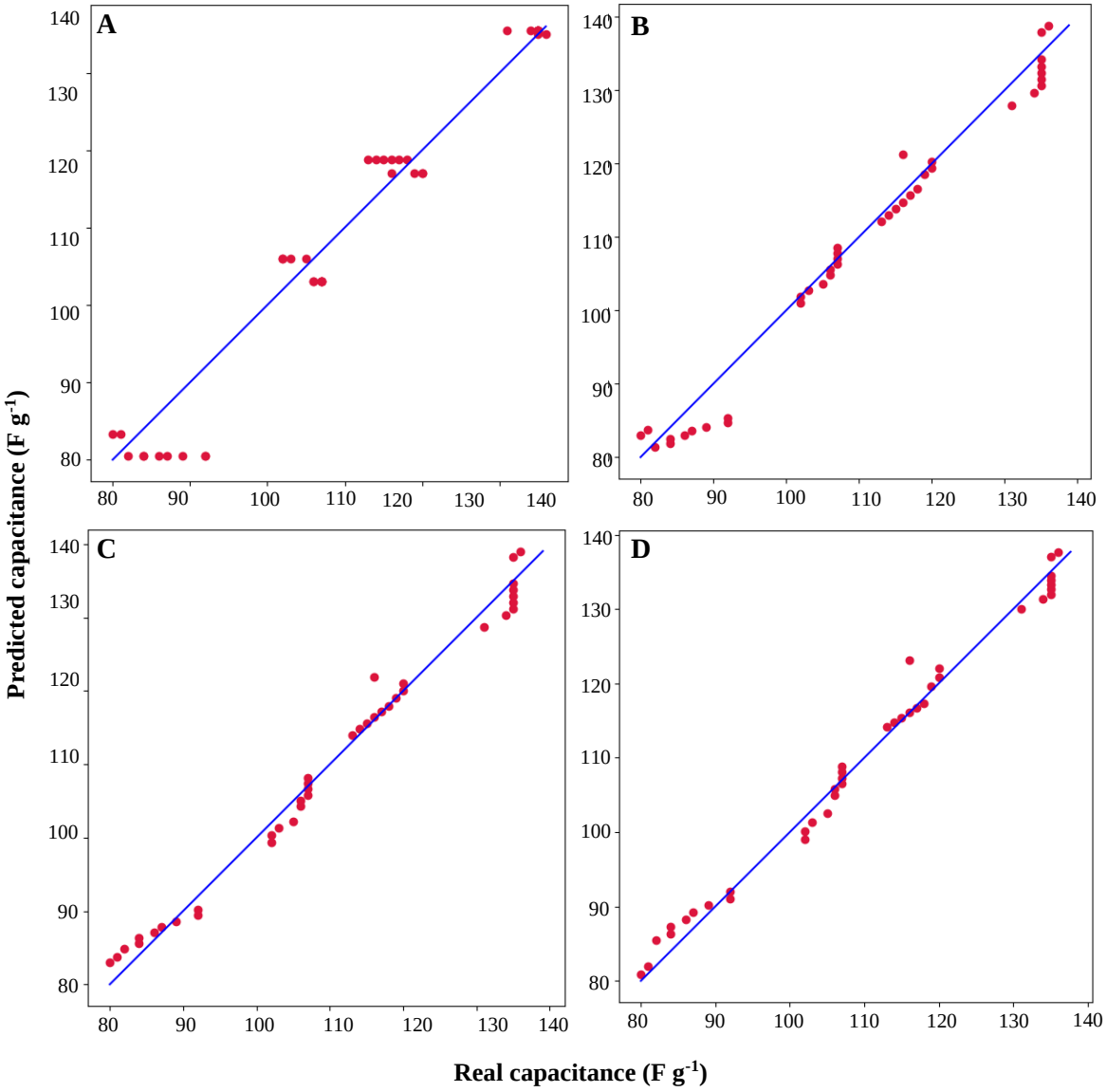

Figure 6.12 Statistical performance of each ML model representing the correlation between the predicted specific capacitance (F g^{-1}) (y-axis) and the real experimental specific capacitance (F g^{-1}) (x-axis) for MS husk-derived AC samples: (A) Decision tree regression (DT) (B) Linear regression (LR), (C) Support vector regression (SVR), (D) Multilayer Perceptron (MLP), the solid line gives the perfect correlation between model and experiment.

6.6.2. Symmetric cell (MS-AC 1100 *vs.* MS-AC 1100) performance of the MS-derived AC (two-electrode configuration)

Figure 6.13 illustrates the CV and GCD profiles of the symmetric cell conducted in a two-electrode configuration using MS-AC 1100 material. The tests were carried out in the potential range of 1 V in a 2 M NaOH aqueous electrolyte. The results of the CV and GCD profiles are consistent with that of the three-electrode configuration (discussed in section 6.5.2) attributed to ion adsorption due to the presence of hierarchical porous carbon electrode that resulted in EDLC behavior. CV curves at different scan rates from 20 to 100 mV s^{-1} are displayed in Figure 6.13A, and GCD plots are shown in Figure 6.13B at current densities from 5 to 10 mA. The specific capacitance measured at the lowest current density of 2 mA cm^{-2} (~1 A g^{-1}) was 54 F g^{-1}, which decreased to 33 F g^{-1} at the highest current density 10 mA cm^{-2} (~5 A g^{-1}). The trend of the specific capacitance as a function of current density is given in Figure 6.13C, and the symmetric cell is stable for high-rate discharge. Consequently, the specific energy density and power density calculated based on the specific capacitance values are given in the Ragone plot in Figure 6.13D. At low current loads, the energy density has been achieved up to 8 Wh kg^{-1} by the symmetric supercapacitor cell, demonstrating considerably higher energy storage, which was lowered to 4.7 Wh kg^{-1} of 10 mA cm^{-2}. As shown in Figure 6.13D, the calculated energy density of the cell is comparable to those reported in the literature [64,72–77].

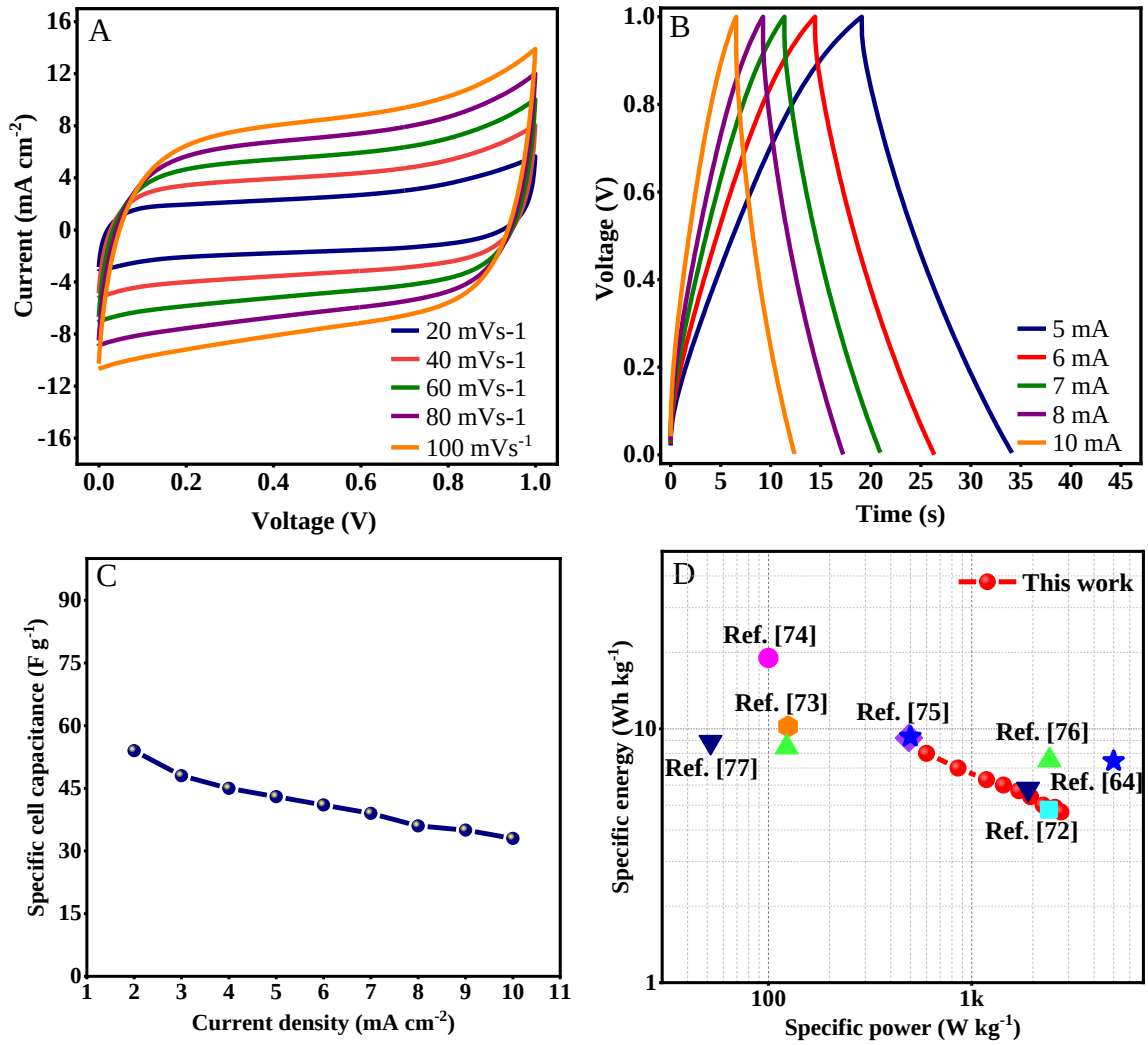

Figure 6.13 (A) Cyclic Voltammograms (CV) and (B) galvanostatic charge-discharge curves in a two-electrode configuration (symmetric cell) of MS-AC 1100 in 2 M NaOH electrolyte at different sweep rates and applied currents shown in the respective plots, (C) Variation of specific capacitance with current density, and (D) Ragone plot of MS-AC 1100 sample [64,72–77].

6.7. Conclusion

The bio-waste valorization of Mango seed (MS) husk has been conducted via carbonization and chemical activation. The optimized temperature is found to be 1100 °C for the preparation of activated carbon (AC) as supercapacitor electrode material.

MS husk is a clean and affordable source, and repurposing the bio-waste was found to be promising for developing sustainable porous carbon materials to be applied in super-capacitors applications.

Activation temperature of the MS husk improved the physical parameters of the carbon, such as surface area, pore-volume, and the graphitic orientation of the AC, which are determining factors for improved storage performance. N_2 adsorption/ desorption experiments and Raman analysis show that the MS-AC 1100 exhibited the best physical properties. Likewise, the electrochemical performance of this material delivers 135 F g^{-1} specific capacitance at 5 mA cm^{-2} (2 A g^{-1}) and ~100 % cyclability over 1000 cycles and is found to be superior to those of the temperatures studied and commercially available AC material. The electrochemical behavior revealed that the formation of the electric double-layer is the primary charge storage while the pseudo-capacitance phenomenon is negligible. MS-AC 1100 was also studied using a two-electrode symmetric configuration, and the assembled symmetric cell shows energy density up to 8 Wh kg^{-1} under the applied current loads. Four Machine Learning (ML) algorithms were used to establish quantitative correlations between synthesis parameters, and the structural and electrochemical features of MS-AC materials to predict specific capacitances. Among the tested ML models, MLP can well capture (highest R^2 score ~ 0.99) the capacitance dependence on considered inputs. ML modeling addresses one of the biggest challenges in theoretical modeling in developing correlations for the systems at non-equilibrium conditions that produce significant gaps in theoretical and experimental investigations. Higher quality results are obtained through a significant acceleration of simulation time beyond the trial-and-error research conducted through conventional experiments and models. Providing more experimental inputs and data sets can offer a significant advantage as every new data point added would improve the ML correlations statistics. The expected energy storage targets could be achieved by using the reverse engineering mechanism to find the ideal experimental parameters.

In conclusion, the hierarchical porous carbon derived from MS husk has the potential to be utilized in symmetric/asymmetric capacitors as a contribution to the efforts to develop new carbon-based electrodes. The work presented in this chapter also demonstrates an approach of combining experimental data and ML algorithms to

provide insights into the accelerated development of designing carbon materials for future energy storage applications.

6.6. References

[1] S. Hatfield-Dodds, H. Schandl, D. Newth, M. Obersteiner, Y. Cai, T. Baynes, J. West, P. Havlik, Assessing global resource use and greenhouse emissions to 2050, with ambitious resource efficiency and climate mitigation policies, J. Clean. Prod. 144 (2017) 403–414.

[2] S. Chu, A. Majumdar, Opportunities and challenges for a sustainable energy future, Nature. 488 (2012) 294–303.

[3] M. Salanne, B. Rotenberg, K. Naoi, K. Kaneko, P.L. Taberna, C.P. Grey, B. Dunn, P. Simon, Efficient storage mechanisms for building better supercapacitors, Nat. Energy. 1 (2016) 16070 (2016).

[4] Z. Niu, H. Dong, B. Zhu, J. Li, H.H. Hng, W. Zhou, X. Chen, S. Xie, Highly stretchable, integrated supercapacitors based on single-walled carbon nanotube films with continuous reticulate architecture, Adv. Mater. 25 (2013) 1058–1064.

[5] C. Liu, Z. Yu, D. Neff, A. Zhamu, B.Z. Jang, Graphene-based supercapacitor with an ultrahigh energy density, Nano Lett. 10 (2010) 4863–4868.

[6] M.P. Down, S.J. Rowley-Neale, G.C. Smith, C.E. Banks, Fabrication of Graphene Oxide Supercapacitor Devices, ACS Appl. Energy Mater. 1 (2018) 707–714.

[7] W. Du, Z. Zhang, L. Du, X. Fan, Z. Shen, X. Ren, Y. Zhao, C. Wei, S. Wei, Designing synthesis of porous biomass carbon from wheat straw and the functionalizing application in flexible, all-solid-state supercapacitors, J. Alloys Compd. 797 (2019) 1031–1040.

[8] R.R. Salunkhe, J. Lin, V. Malgras, S.X. Dou, J.H. Kim, Y. Yamauchi, Large-scale synthesis of coaxial carbon nanotube/$Ni(OH)_2$ composites for

asymmetric supercapacitor application, Nano Energy. 11 (2015) 211–218.

[9] H. Wan, X. Hu, From biomass-derived wastes (bagasse, wheat straw and shavings) to activated carbon with three-dimensional connected architecture and porous structure for Li-ion batteries, Chem. Phys. 521 (2019) 108–114.

[10] G. Wang, H. Wang, X. Lu, Y. Ling, M. Yu, T. Zhai, Y. Tong, Y. Li, Solid-state supercapacitor based on activated carbon cloths exhibits excellent rate capability, Adv. Mater. 26 (2014) 2676–2682.

[11] S. Gillet, M. Aguedo, L. Petitjean, A.R.C. Morais, A.M. Da Costa Lopes, R.M. Łukasik, P.T. Anastas, Lignin transformations for high value applications: Towards targeted modifications using green chemistry, Green Chem. 19 (2017) 4200–4233.

[12] H. Yang, S. Ye, J. Zhou, T. Liang, Biomass-derived porous carbon materials for supercapacitor, Front. Chem. 7 (2019) 1–17.

[13] P. Cheng, T. Li, H. Yu, L. Zhi, Z. Liu, Z. Lei, Biomass-Derived Carbon Fiber Aerogel as a Binder-Free Electrode for High-Rate Supercapacitors, J. Phys. Chem. C. 120 (2016) 2079–2086.

[14] B. Liu, Y. Liu, H. Chen, M. Yang, H. Li, Oxygen and nitrogen co-doped porous carbon nanosheets derived from Perilla frutescens for high volumetric performance supercapacitors, J. Power Sources. 341 (2017) 309–317.

[15] Q. Zhang, K. Han, S. Li, M. Li, J. Li, K. Ren, Synthesis of garlic skin-derived 3D hierarchical porous carbon for high-performance supercapacitors, Nanoscale. 10 (2018) 2427–2437.

[16] D. Kang, Q. Liu, J. Gu, Y. Su, W. Zhang, D. Zhang, “Egg-Box”-Assisted Fabrication of Porous Carbon with Small Mesopores for High-Rate Electric Double Layer Capacitors, ACS Nano. 9 (2015) 11225–11233.

[17] Z. Wang, H. Guo, F. Shen, G. Yang, Y. Zhang, Y. Zeng, L. Wang, H. Xiao, S. Deng, Biochar produced from oak sawdust by Lanthanum (La)-involved pyrolysis for adsorption of ammonium (NH_4^+), nitrate (NO_3^-), and phosphate (PO_4^{3-}), Chemosphere. 119 (2015) 646–653.

[18] A. Dzigbor, A. Chimphango, Production and optimization of NaCl-activated carbon from mango seed using response surface methodology, Biomass Convers. Biorefinery. 9 (2019) 421–431.

[19] K.R. Thines, E.C. Abdullah, N.M. Mubarak, M. Ruthiraan, Synthesis of magnetic biochar from agricultural waste biomass to enhancing route for waste water and polymer application: A review, Renew. Sustain. Energy Rev. 67 (2017) 257–276.

[20] G.C. Braga, P.S. Melo, K.B. Bergamaschi, A.P. Tiveron, A.P. Massarioli, S.M. de Alencar, Extraction yield, antioxidant activity andphenolics from grape, mango and peanut agro-industrial by-products, Ciência Rural. 46 (2016) 1498–1504.

[21] Seeds of success: Students use mango seed waste to create skin care products, (n.d.). https://news.csu.edu.au/latest-news/seeds-of-success-students-use-mango-seed-waste-to-create-skin-care-products.

[22] R.C. de Andrade, R.S.G. Menezes, R.A. Fiuza-Jr, H.M.C. Andrade, Activated carbon microspheres derived from hydrothermally treated mango seed shells for acetone vapor removal, Carbon Lett. 31 (2020) 779-783.

[23] D.H. Barrett, A. Haruna, Artificial intelligence and machine learning for targeted energy storage solutions, Curr. Opin. Electrochem. 21 (2020) 160–166.

[24] K. Min, B. Choi, K. Park, E. Cho, Machine learning assisted optimization of electrochemical properties for Ni-rich cathode materials, Sci. Rep. 8 (2018) 1–7.

[25] A.D. Sendek, E.D. Cubuk, E.R. Antoniuk, G. Cheon, Y. Cui, E.J. Reed, Machine Learning-Assisted Discovery of Solid Li-Ion Conducting Materials, Chem. Mater. 31 (2019) 342–352.

[26] H. Farsi, F. Gobal, Artificial neural network simulator for supercapacitor performance prediction, Comput. Mater. Sci. 39 (2007) 678–683.

[27] J. Wang, Z. Li, S. Yan, X. Yu, Y. Ma, L. Ma, Modifying the microstructure of

algae-based active carbon and modelling supercapacitors using artificial neural networks, RSC Adv. 9 (2019) 14797–14808.

[28] T.D. Dongale, P.R. Jadhav, G.J. Navathe, J.H. Kim, M.M. Karanjkar, P.S. Patil, Development of nano fiber MnO2 thin film electrode and cyclic voltammetry behavior modeling using artificial neural network for supercapacitor application, Mater. Sci. Semicond. Process. 36 (2015) 43–48.

[29] S. Rogers, M. Girolami, A First Course of Machine Learning, 2nd ed., Chapman and Hall/CRC, 2016.

[30] G.U. Yule, On the Theory of Correlation, R. Stat. Soc. 60 (1897) 812–854.

[31] H. Drucker, C.J. Burges, L. Kaufman, A. Smola, V. Vapnik, Support vector regression machines. Advances in neural information processing systems, in: Adv. Neural Inf. Process. Syst., 1996: pp. 155–161.

[32] M. Xu, P. Watanachaturaporn, P.K. Varshney, M.K. Arora, Decision tree regression for soft classification of remote sensing data, 97 (2005) 322–336.

[33] F. Rosenblatt, Principles of neurodynamics perceptions and the theory of brain mechanisms, Cornell Aeronautical Laboratory, INC. Buffalo 21, New York, 1961.

[34] D.C. Montgomery, E.A. Peck, G.G. Vining, Introduction to Linear Regression Analysis, 5th ed., Wiley, 2012.

[35] L. Wan, M. Zeiler, S. Zhang, Y. LeCun, R. Fergus, Regularization of Neural Networks using DropConnect, in: Proc. 30th Int. Conf. Mach. Learn., 2013: pp. 1058–1066.

[36] M. Zhou, A. Gallegos, K. Liu, S. Dai, J. Wu, Insights from machine learning of carbon electrodes for electric double layer capacitors, Carbon N. Y. 157 (2020) 147–152.

[37] C.M. Bishop, Neural Networks for Pattern Recognition, OXFORD University press, 1995.

[38] J. Li, Y. Gao, K. Han, J. Qi, M. Li, Z. Teng, High performance hierarchical

porous carbon derived from distinctive plant tissue for supercapacitor, Sci. Rep. 9 (2019) 1–11.

[39] J. Wang, S. Kaskel, KOH activation of carbon-based materials for energy storage, J. Mater. Chem. 22 (2012) 23710–23725.

[40] Q. Wang, Q. Cao, X. Wang, B. Jing, H. Kuang, L. Zhou, A high-capacity carbon prepared from renewable chicken feather biopolymer for supercapacitors, J. Power Sources. 225 (2013) 101–107.

[41] I.A.W. Tan, A.L. Ahmad, B.H. Hameed, Adsorption isotherms, kinetics, thermodynamics and desorption studies of 2, 4, 6-trichlorophenol on oil palm empty fruit bunch-based activated carbon, J. Hazard. Mater. 164 (2009) 473–482.

[42] M. Thommes, K. Kaneko, A. V Neimark, J.P. Olivier, F. Rodriguez-reinoso, J. Rouquerol, K.S.W. Sing, Physisorption of gases, with special reference to the evaluation of surface area and pore size distribution (IUPAC Technical Report), Pure Appl. Chem. 87 (2015) 1051–1069.

[43] P. Hao, Z. Zhao, J. Tian, H. Li, Y. Sang, G. Yu, H. Cai, H. Liu, C.P. Wong, A. Umar, Hierarchical porous carbon aerogel derived from bagasse for high performance supercapacitor electrode, Nanoscale. 6 (2014) 12120–12129.

[44] J. Liu, Q. Wang, S. Wang, D. Zou, K. Sonomoto, Utilisation of microwave-NaOH pretreatment technology to improve performance and l-lactic acid yield from vinasse, Biosyst. Eng. 112 (2012) 6–13.

[45] L.W. Lai, M. Ibrahim, N.M. Rahim, E.F. Hashim, M.Z. Ya'cob, I. Ani, J. Akhtar, Study on Composition, Structural and Property Changes of Oil palm Frond Biomass under Different Pretreatments, Cellul. Chem. Technol. 50 (2016) 951–959.

[46] K. Subramani, N. Sudhan, M. Karnan, M. Sathish, Orange Peel Derived Activated Carbon for Fabrication of High-Energy and High-Rate Supercapacitors, ChemistrySelect. 2 (2017) 11384–11392.

[47] Q. Liu, S. Wang, Y. Zheng, Z. Luo, K. Cen, Mechanism study of wood lignin

pyrolysis by using TG-FTIR analysis, J. Anal. Appl. Pyrolysis. 82 (2008) 170–177.

[48] M. Demir, A.A. Farghaly, M.J. Decuir, M.M. Collinson, R.B. Gupta, Supercapacitance and oxygen reduction characteristics of sulfur self-doped micro/mesoporous bio-carbon derived from lignin, Mater. Chem. Phys. 216 (2018) 508–516.

[49] L. Wang, Y. Zheng, Q. Zhang, L. Zuo, S. Chen, S. Chen, H. Hou, Y. Song, Template-free synthesis of hierarchical porous carbon derived from low-cost biomass for high-performance supercapacitors, RSC Adv. 4 (2014) 51072–51079.

[50] A.C. Ferrari, D.M. Basko, Raman spectroscopy as a versatile tool for studying the properties of graphene, Nat. Nanotechnol. 8 (2013) 235–246.

[51] H. Kim, J. Cho, S.Y. Jang, Y.W. Song, Deformation-immunized optical deposition of graphene for ultrafast pulsed lasers, Appl. Phys. Lett. 98 (2011) 2009–2012.

[52] A.C. Ferrari, J.C. Meyer, V. Scardaci, C. Casiraghi, M. Lazzeri, F. Mauri, S. Piscanec, D. Jiang, K.S. Novoselov, S. Roth, A.K. Geim, Raman spectrum of graphene and graphene layers, Phys. Rev. Lett. 97 (2006) 1–4.

[53] G. Eda, G. Fanchini, M. Chhowalla, Large-area ultrathin films of reduced graphene oxide as a transparent and flexible electronic material, Nat. Nanotechnol. 3 (2008) 270–274.

[54] W. Kiciński, M. Szala, M. Bystrzejewski, Sulfur-doped porous carbons: Synthesis and applications, Carbon N. Y. 68 (2014) 1–32.

[55] J. Scheers, S. Fantini, P. Johansson, A review of electrolytes for lithium-sulphur batteries, J. Power Sources. 255 (2014) 204–218.

[56] L. Peng, Y. Liang, H. Dong, H. Hu, X. Zhao, Y. Cai, Y. Xiao, Y. Liu, M. Zheng, Super-hierarchical porous carbons derived from mixed biomass wastes by a stepwise removal strategy for high-performance supercapacitors, J. Power Sources. 377 (2018) 151–160.

[57] B.K. Kim, S. Sy, A. Yu, J. Zhang, Electrochemical supercapacitors for energy storage and conversion, in: Handb. Clean Energy Syst., John Wiley & Sons, Ltd, 2015.

[58] P. Cai, K. Zou, X. Deng, B. Wang, M. Zheng, L. Li, H. Hou, G. Zou, X. Ji, Comprehensive Understanding of Sodium-Ion Capacitors: Definition, Mechanisms, Configurations, Materials, Key Technologies, and Future Developments, Adv. Energy Mater. 11 (2021) 1–56.

[59] M.A. Garakani, S. Bellani, V. Pellegrini, R. Oropesa-Nuñez, A.E.D.R. Castillo, S. Abouali, L. Najafi, B. Martín-García, A. Ansaldo, P. Bondavalli, C. Demirci, V. Romano, E. Mantero, L. Marasco, M. Prato, G. Bracciale, F. Bonaccorso, Scalable spray-coated graphene-based electrodes for high-power electrochemical double-layer capacitors operating over a wide range of temperature, Energy Storage Mater. 34 (2021) 1–11.

[60] G. Wang, L. Zhang, J. Zhang, A review of electrode materials for electrochemical supercapacitors, Chem. Soc. Rev. 41 (2012) 797–828.

[61] S. Lei, L. Chen, W. Zhou, P. Deng, Y. Liu, L. Fei, W. Lu, Y. Xiao, B. Cheng, Tetra-heteroatom self-doped carbon nanosheets derived from silkworm excrement for high-performance supercapacitors, J. Power Sources. 379 (2018) 74–83.

[62] A.A. Mohammed, C. Chen, Z. Zhu, Low-cost, high-performance supercapacitor based on activated carbon electrode materials derived from baobab fruit shells, J. Colloid Interface Sci. 538 (2019) 308–319.

[63] H. Yin, B. Lu, Y. Xu, D. Tang, X. Mao, W. Xiao, D. Wang, A.N. Alshawabkeh, Harvesting capacitive carbon by carbonization of waste biomass in molten salts, Environ. Sci. Technol. 48 (2014) 8101–8108.

[64] X. Li, W. Xing, S. Zhuo, J. Zhou, F. Li, S.Z. Qiao, G.Q. Lu, Preparation of capacitor's electrode from sunflower seed shell, Bioresour. Technol. 102 (2011) 1118–1123.

[65] I.I. Misnon, N.K.M. Zain, R.A. Aziz, B. Vidyadharan, R. Jose,

Electrochemical properties of carbon from oil palm kernel shell for high performance supercapacitors, Electrochim. Acta. 174 (2015) 78–86.

[66] X. Hong, K.S. Hui, Z. Zeng, K.N. Hui, L. Zhang, M. Mo, M. Li, Hierarchical nitrogen-doped porous carbon with high surface area derived from endothelium corneum gigeriae galli for high-performance supercapacitor, Electrochim. Acta. 130 (2014) 464–469.

[67] V. Subramanian, C. Luo, A.M. Stephan, K.S. Nahm, S. Thomas, B. Wei, Supercapacitors from activated carbon derived from banana fibers, J. Phys. Chem. C. 111 (2007) 7527–7531.

[68] J.M.V. Nabais, J.G. Teixeira, I. Almeida, Development of easy made low cost bindless monolithic electrodes from biomass with controlled properties to be used as electrochemical capacitors, Bioresour. Technol. 102 (2011) 2781–2787.

[69] G. Gou, F. Huang, M. Jiang, J. Li, Z. Zhou, Hierarchical porous carbon electrode materials for supercapacitor developed from wheat straw cellulosic foam, Renew. Energy. 149 (2020) 208–216.

[70] X. Yan, Y. Jia, L. Zhuang, L. Zhang, K. Wang, X. Yao, Defective Carbons Derived from Macadamia Nut Shell Biomass for Efficient Oxygen Reduction and Supercapacitors, ChemElectroChem. 5 (2018) 1874–1879.

[71] A.K. Mondal, K. Kretschmer, Y. Zhao, H. Liu, H. Fan, G. Wang, Naturally nitrogen doped porous carbon derived from waste shrimp shells for high-performance lithium ion batteries and supercapacitors, Microporous Mesoporous Mater. 246 (2017) 72–80.

[72] S. Liu, Y. Zhao, B. Zhang, H. Xia, J. Zhou, W. Xie, H. Li, Nano-micro carbon spheres anchored on porous carbon derived from dual-biomass as high rate performance supercapacitor electrodes, J. Power Sources. 381 (2018) 116–126.

[73] D. Wang, Y. Min, Y. Yu, Facile synthesis of wheat bran-derived honeycomb-like hierarchical carbon for advanced symmetric supercapacitor applications,

J. Solid State Electrochem. 19 (2014) 577–584.

[74] A. Bello, N. Manyala, F. Barzegar, A.A. Khaleed, D.Y. Momodu, J.K. Dangbegnon, Renewable pine cone biomass derived carbon materials for supercapacitor application, RSC Adv. 6 (2016) 1800–1809.

[75] S. Qu, J. Wan, C. Dai, T. Jin, F. Ma, Promising as high-performance supercapacitor electrode materials porous carbons derived from biological lotus leaf, J. Alloys Compd. 751 (2018) 107–116.

[76] X. Han, H. Jiang, Y. Zhou, W. Hong, Y. Zhou, P. Gao, R. Ding, E. Liu, A high performance nitrogen-doped porous activated carbon for supercapacitor derived from pueraria, J. Alloys Compd. 744 (2018) 544–551.

[77] W. Zhang, M. Zhao, R. Liu, X. Wang, H. Lin, Hierarchical porous carbon derived from lignin for high performance supercapacitor, Colloids Surfaces A Physicochem. Eng. Asp. 484 (2015) 518–527.

Link to the next chapter

Moving from one biomass precursor to another varies the intrinsic microstructural characteristics and chemical compositions of the biomass materials. Therefore, the research should be conducted to select the potential precursors from diverse biomass and their design to optimize the electrochemical performance for capacitor application.

In chapter 7, we have chosen to study the AC derived from Grape marc (GM) as a potential precursor. Grape marc is a by-product of the renowned wine industry in Australia, and it has a relatively rich lignin component. The synthesis of the AC has been carried out using single-step carbonization and activation, also in two steps similar to that in chapter 6. The activating power of different activating agents and the effect of Nitrogen (N) dopant on developing a porous AC framework have been studied. The synthesized N-doped AC exhibited comparatively superior electrochemical performance. Theoretical density functional theory (DFT) studies were carried out to examine the chemistry of AC in the absence and presence of the dopant bonded to carbon structure. Insights into machine learning have been given to develop a theoretical model beneficial for predicting the capacitive properties of carbon materials.

Chapter 7 Repurposing the Grape marc for the fabrication of supercapacitors with theoretical and machine learning models

This chapter is published as:

Repurposing N-Doped Grape Marc for the Fabrication of Supercapacitors with Theoretical and Machine Learning Models

Kethaki Wickramaarachchi, Manickam Minakshi, S. Assa Aravindh, Rukshima Dabare, Xiangpeng Gao, Zhong-Tao Jiang, Kok Wai Wong

Nanomaterials 2022, 12, 1847
DOI: https://doi.org/10.3390/nano12111847

Impact factor: 5.719

nanomaterials

MDPI

Article

Repurposing N-Doped Grape Marc for the Fabrication of Supercapacitors with Theoretical and Machine Learning Models

Kethaki Wickramaarachchi [1], Manickam Minakshi [1,*], S. Assa Aravindh [2], Rukshima Dabare [1], Xiangpeng Gao [1], Zhong-Tao Jiang [1] and Kok Wai Wong [1]

[1] College of Science, Health, Engineering & Education, Murdoch University, Perth, WA 6150, Australia; kethaki.wickramaarachchi@murdoch.edu.au (K.W.); rukshima_mech@yahoo.com (R.D.); x.gao@murdoch.edu.au (X.G.); z.jiang@murdoch.edu.au (Z.-T.J.); k.wong@murdoch.edu.au (K.W.W.)

[2] Nano and Molecular Systems Research Unit, University of Oulu, Pentti Kaiteran Katu 1, 90570 Oulu, Finland; assa.sasikaladevi@oulu.fi

* Correspondence: minakshi@murdoch.edu.au; Tel.: +61-89-3602017

Abstract: Porous carbon derived from grape marc (GM) was synthesized via carbonization and chemical activation processes. Extrinsic nitrogen (N)-dopant in GM, activated by KOH, could render its potential use in supercapacitors effective. The effects of chemical activators such as potassium hydroxide (KOH) and zinc chloride ($ZnCl_2$) were studied to compare their activating power toward the development of pore-forming mechanisms in a carbon electrode, making them beneficial for energy storage. GM carbon impregnated with KOH for activation (KAC), along with urea as the N-dopant (KAC_{urea}), exhibited better morphology, hierarchical pore structure, and larger surface area (1356 m^2 g^{-1}) than the GM carbon activated by $ZnCl_2$ (ZnAC). Moreover, density functional theory (DFT) investigations showed that the presence of N-dopant on a graphite surface enhances the chemisorption of O adsorbates due to the enhanced charge-transfer mechanism. KAC_{urea} was tested in three aqueous electrolytes with different ions (LiOH, NaOH, and $NaClO_4$), which delivered higher specific capacitance, with the NaOH electrolyte exhibiting 139 F g^{-1} at a 2 mA current rate. The NaOH with the alkaline cation Na^+ offered the best capacitance among the electrolytes studied. A multilayer perceptron (MLP) model was employed to describe the effects of synthesis conditions and physicochemical and electrochemical parameters to predict the capacitance and power outputs. The proposed MLP showed higher accuracy, with an R^2 of 0.98 for capacitance prediction.

Keywords: biomass carbon; winery waste; density functional theory; nitrogen doping; activating agent; energy storage; machine learning

Citation: Wickramaarachchi, K.; Minakshi, M.; Aravindh, S.A.; Dabare, R.; Gao, X.; Jiang, Z.-T.; Wong, K.W. Repurposing N-Doped Grape Marc for the Fabrication of Supercapacitors with Theoretical and Machine Learning Models. *Nanomaterials* **2022**, *12*, 1847. https://doi.org/10.3390/nano12111847

Academic Editor: Byoung-Suhk Kim

Received: 3 May 2022
Accepted: 26 May 2022
Published: 27 May 2022

Publisher's Note: MDPI stays neutral with regard to jurisdictional claims in published maps and institutional affiliations.

Copyright: © 2022 by the authors. Licensee MDPI, Basel, Switzerland. This article is an open access article distributed under the terms and conditions of the Creative Commons Attribution (CC BY) license (https://creativecommons.org/licenses/by/4.0/).

1. Introduction

Carbon-based electrode materials are suitable for energy storage applications because they possess attractive features such as excellent chemical and thermal stability, high electrical conductivity, and a large surface area [1]. Various carbonaceous materials—such as activated carbon (AC), carbon nanotubes (CNTs), carbon aerogels, graphene, ordered mesoporous carbon, carbon composites, etc. [2,3]—have been widely reported for their double-layer capacitive behavior and potential applications in supercapacitor devices. Among the carbonaceous materials reported in the literature for electrodes, AC is the most widely used, due to its high surface area and moderate production cost [4]. The synthesis routes of the other carbon materials, with high cost and difficulties of scaling-up, are not readily successful for practical implementation. Even though graphene-related allotropes of carbon have emerged as highly conductive materials, challenges exist in formulating single-layer graphene and reducing graphene layer aggregation, limiting their

Author contribution

Contributor	Contribution (%)	Nature of contribution
Kethaki Wickramaarachchi	70	Conceptualization, experimentation, data collection, analysis and interpretation, drafting and critical revision of the manuscript.
Manickam Minakshi	30	Conceptualization, interpretation of data, critical revision of the manuscript.
S. Assa Aravindh		Theoretical insights and data interpretation.
Rukshima Dabare		Theoretical insights and data interpretation.
Xiangpeng Gao		Critical revision of the manuscript.
Zhong-Tao Jiang		Procured funding.
Kok Wai Wong		Theoretical insights and data interpretation.

7.1. Abstract

Porous carbon derived from Grape marc (GM) was synthesized via carbonization and chemical activation processes. Extrinsic nitrogen (N)-dopant in GM, activated by KOH, could render its potential use in supercapacitors effective. The effects of chemical activators such as potassium hydroxide (KOH) and zinc chloride ($ZnCl_2$) were studied to compare their activating power toward the development of pore-forming mechanisms in a carbon electrode, making them beneficial for energy storage. GM carbon impregnated with KOH for activation (KAC), along with urea as the N-dopant (KACurea), exhibited better morphology, hierarchical pore structure, and larger surface area (1356 $m^2\ g^{-1}$) than the GM carbon activated by $ZnCl_2$ (ZnAC). Moreover, density functional theory (DFT) investigations showed that the presence of N-dopant on a graphite surface enhances the chemisorption of O adsorbates due to the enhanced charge-transfer mechanism. KACurea was tested in three aqueous electrolytes with different ions (LiOH, NaOH, and $NaClO_4$), which delivered higher specific capacitance, with the NaOH electrolyte exhibiting 139 F g^{-1} at a 2 mA current rate. The NaOH with the alkaline cation Na^+ offered the best capacitance among the electrolytes studied. A multilayer perceptron (MLP) model was employed to describe the effects of synthesis conditions and physicochemical and electrochemical parameters to predict the capacitance and power outputs. The proposed MLP showed higher accuracy, with an R^2 of 0.98 for capacitance prediction.

7.2. Introduction

Carbon-based electrode materials are suitable for energy storage applications because they possess attractive features such as excellent chemical and thermal stability, high electrical conductivity, and a large surface area [1]. Various carbonaceous materials such as activated carbon (AC), carbon nanotubes (CNTs), carbon aerogels, graphene, ordered mesoporous carbon, carbon composites, etc. [2,3] have been widely reported for their double-layer capacitive behavior and potential applications in supercapacitor devices. Among the carbonaceous materials reported in the literature for electrodes,

AC is the most widely used due to its high surface area and moderate production cost [4]. The synthesis routes of the other carbon materials, with high cost and difficulties of scaling up, are not readily successful for practical implementation. Even though graphene-related allotropes of carbon have emerged as highly conductive materials, challenges exist in formulating single-layer graphene and reducing graphene layer aggregation, limiting their use in commercial applications. The nature of the carbon precursor and the processing method highly influence the derived carbon properties, such as pore size distribution, surface functional groups, and structure. Typically, the surface area and pore size are the key factors contributing to electrochemical performance, resulting in a higher power density [5].

Conventionally, AC is produced from fossil resources such as coal [6], petroleum coke [7], and coal tar [8], which provide larger surface areas for the carbon material. Finding green and renewable energy sources has become essential with the rising scarcity of non-renewable fossil fuels, increasing environmental pollution, and climate change. In recent years, biomass materials have been considered an eco-friendly alternative to produce porous carbon, replacing conventional AC precursors [9]. In particular, using biomass waste to produce carbon materials for energy storage can yield value-added products and address challenging waste disposal problems [10]. Various studies in the literature have shown the exemplary designs and competitive electrochemical performances of biomass-based low-cost carbons compared with conventional AC [11–13]. Various biomass resources such as sugarcane [10], rice husk [14], fishbone [15], garlic skin [16], wheat straw [17], etc., have been employed to prepare AC electrodes. Biomass can inherit its pore structure or develop porous or layered structures, depending on the carbonization and physical/chemical activation parameters [18]. The carbonization and activation processes are the main steps involved in synthesizing AC. They control structural and textural factors such as morphology, specific surface area, pore size distribution, pore-volume, etc., which determine the performance of the carbon electrode in energy storage applications.

On the other hand, environmentally friendly biomass precursors with green approaches to synthesizing porous carbon materials are also emerging and can provide pragmatic improvements in the sustainable processing of energy-storing materials. Goldfarb *et al.* authors [19] proposed an integrated process for extracting biofuel from the

pyrolysis of pistachio nutshells and impregnating it with KOH activation processes to produce activated carbon. This integrated process increased the biofuel yield by up to 25 %, and the AC was used for electrochemical capacitor studies. McNair *et al.* [20] reported green binders (γ-valerolactone) and solvents (i.e., cellulose acetate, carboxymethyl cellulose) as alternatives for replacing the conventional solvents (N-methyl-2-pyrrolidone; NMP) and binders (fluorinated, such as PVDF) for membrane capacitive deionization electrodes with enhanced capacitive performance. They aimed to reduce the environmental impacts and chemical consumption used in electrode processing. All of these studies concluded that sustainable biomass electrodes could be biodegradable.

Australia is a very competitive wine-producing country that produces ~1.2 billion liters of wine per year for domestic and global sales, using ~1.73 million metric tons of wine grape crush, yielding ~0.5 million tons of GM, which requires safe disposal [21]. The. The waste disposal of winery residues (otherwise termed “Grape marc”) includes onsite dumping and settling in ponds while producing tartaric acid, low-quality wine and ethanol, and animal feed, as well as composting off-site [22]. However, proper approaches to recovering the GM to produce value-added products are yet to be developed. For instance, waste dumping provides an economical means of waste disposal but causes environmental impacts, including spreading pests and diseases [23]. After extracting tartrate or ethanol, the waste streams remain and must be treated to prevent groundwater pollution and foul odors. In such cases, the thermal conversion of the GM into valuable products such as biochar, energy, or chemical feedstock is an alternative in terms of both environmental and economic benefits [24]. GM consists largely of lignin, which possesses a 3D network structure and higher density than other lignocellulosic biomass [1]. Thus, it can be a promising feedstock for energy storage applications. With this advantage, I aimed to exploit GM, a free and sustainable material collected from Australian wineries to produce AC. To the best of our knowledge, repurposing of GM as a precursor with extrinsic nitrogen (N)-dopant has not been reported for the fabrication of supercapacitors.

Considering the wide range of biomass precursors available and the number of synthesis conditions, it is much more beneficial to develop a proper design protocol to choose the appropriate precursors and the experimental conditions to obtain optimized

electrode performance. This drives the demand to focus on state-of-the-art technologies that could assist in the design, development, and discovery of novel materials. Compared to the traditional models and algorithms, machine learning (ML) technologies have great potential to address the challenges in optimizing energy storage materials [25]. The synthesis conditions such as carbonizing temperature, hold time duration, activation temperature, and doping amounts strongly influence the decomposition kinetics, determining the pore-formation mechanisms of the produced carbon. The physicochemical parameters, such as the morphology and structure of a porous material, differ with the type of raw precursor and the synthesis conditions. In addition, the electrolyte type and testing conditions also affect the electrochemical performance. Therefore, it is customary to note that many parameters are involved in tailoring the energy and power densities of the energy storage materials, and it is difficult to rationalize these parameters through experimental work [26–28]. From one of our works stated in chapter 6, it was found that the multilayer perceptron (MLP) model can deliver highly accurate predictions of capacitance [29]. Hence, the MLP model was employed in this chapter, and the model predictions were compared by varying the inputs to predict the specific capacitance and power. In summary, in this chapter, we investigated the production of AC from Australian GM with N-dopant for capacitor applications, using parameter-extensive experimental work and a DFT model to elaborate on the effects of the N-dopant. As a time- and cost-effective method, the ML technique was applied to predict capacitance and power delivered by the AC materials.

7.3. Materials and methods

7.3.1. Materials

GM collected from a local winery consisting of Grape marc and stalks. The as-received GM was washed with deionized water, dried at 60 °C in an oven for ~24 h, ground and sieved to a size fraction of < 350 µm, and then used as the precursor for AC. Urea and dried GM were mixed before carbonization and activation to synthesize the N-doped

carbon. ACS-grade potassium hydroxide (KOH) and zinc chloride ($ZnCl_2$) supplied by Sigma-Aldrich were used as activating agents in the chemical activation process.

7.3.2. Synthesis of GM-derived N-doped AC

The diagram in Figure 7.1 gives a complete view of GM-derived AC using varying synthesis conditions, showing that the synthesis routes are slightly different for KOH and $ZnCl_2$ activation. Powdered GM was placed in a tubular furnace and then heat-treated at 600 °C for 3 h in an N_2 atmosphere for carbonization. Carbonized GM was mixed with the activating agent (KOH or $ZnCl_2$) in a solution with a mass ratio of 1:3. The mixture was kept in the oven at 80 °C overnight for dehydration. Then, the dried mixture was transferred into a crucible and activated at 800 °C for 1 h in an N_2 atmosphere. The carbon activated by KOH was termed KAC, while that activated by $ZnCl_2$ was called $ZnAC_1$. This process went through two steps: carbonization followed by activation processes. The above conditions were identical to synthesizing the nitrogen-doped carbon, except that fertilizer urea was repurposed as a nitrogen additive. Urea and dried GM were mixed at a 1:1 ratio before carbonization. The AC product was termed N-doped activated carbon (KAC_{urea}). The AC was synthesized using the one-step activation method at 450 °C, with $ZnCl_2$ activation termed $ZnAC_2$.

After the activation process of each sample, it was allowed to cool down naturally to ambient temperature. Then, the samples were washed with HCl and DI water until the pH of the filtrate became neutral. Thoroughly washed AC was dried in the oven at 105 °C for 12 h and used for further analysis.

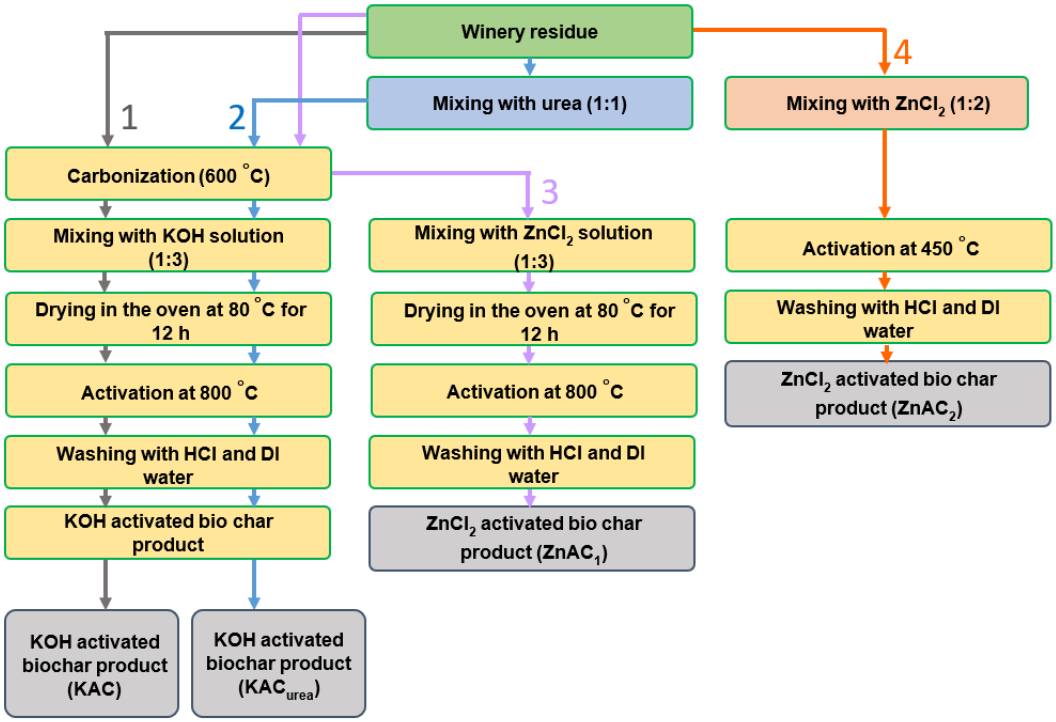

Figure 7.1 Flow diagram of the synthesis conditions followed in producing activated carbon (AC).

7.3.3. Characterization of materials

The surface morphology of the GM and its derived AC materials was investigated via field-emission scanning electron microscopy - energy-dispersive spectroscopy (FESEM–EDS, TESCAN CLARA). X-ray diffraction (XRD) analysis was conducted (X-ray powder diffractometer, GBC Emma Theta) using Cu Kα radiation (λ = 1.5418 Å) operated at 28 kV and 10 mA. The surface functional groups of the prepared ACs were detected by Fourier-transform infrared (FTIR) spectroscopy. The spectra were recorded from 4000 to 400 cm^{-1}. The Raman spectra of the AC materials were recorded via a high-resolution Raman spectrometer (WITec Alpha 300RA+), and microscopy was carried out using a high-resolution system with a 532 nm Nd:YAG laser. The surface area and pore structure were characterized by nitrogen (N_2) adsorption-desorption isotherms at 77 K, using the surface area and pore analysis (SAPA) instrument (micromeritics, TriStar II Plus).

Synthesized AC materials, acetylene black, and PVDF binder were mixed at a mass ratio of 75: 15: 10 in a slurry using N-methyl-2-pyrrolidone (NMP) solvent for electrode coating. The graphite current collector (1 cm^2 area) was coated with ~3 mg mass loading using the slurry coating method and then dried at 80 °C for 12 h. The active mass coated on the graphite was determined by the mass weighing before and after coating. Cyclic voltammetry (CV), galvanostatic charge-discharge (GCD), and electrochemical impedance spectroscopy (EIS) tests were carried out in a three-electrode system (half-cell measurements) with Hg/HgO as one reference (for the alkaline electrolytes), Ag/AgCl as another reference (for the salt electrolytes), and a Pt wire counter electrode using a Bio-logic SP-150 potentiostat. CV measurements were carried out at different scan rates of 5 - 60 mV s^{-1}, GCD tests were conducted at different current densities of 2 - 6 mA cm^{-2}, and EIS was performed at a frequency range of 10 mHz to 100 kHz, with 10 mV amplitude. The equations used to calculate the specific capacitance (C_{sp}, F g^{-1}), energy density (E, Wh kg^{-1}), and power density (P, W kg^{-1}) using GCD data are given in chapter 3 in equation (3.5)-(3.7).

7.3.4. Density functional theory (DFT) calculations

DFT simulations were performed using the Vienna Ab initio Simulation Package (VASP) [30]. A graphite bilayer was simulated using the supercell approach. A kinetic energy cutoff of 450 eV was used to explain the plane waves included in the basis set. The exchange and correlation interactions were expanded using the projector-augmented wave (PAW) [31] within the Perdew-Burke-Ernzerhof functional (PBE). To describe the semi-empirical corrections, DFT-D3 formalism was used [32] within the general gradient approximation (GGA). A 3 × 3 × 1 bilayer graphite was simulated, and a vacuum region of 15 Å was employed along the Z direction to avoid interaction between the repeating images. A Monkhorst Pack k-grid of 9 × 9 × 1 was used for the Brillouin zone integration [33]. The energy and force convergence criteria were set to 10^{-6} eV and 10^{-3} eV/Å, respectively.

7.3.5. Multilayer perceptron (MLP) model

The MLP model better extracts the correlations between inputs and outputs to predict the electrochemical performance of the energy storage carbon [29,34]. Therefore, an MLP model with three hidden layers was employed to predict the specific capacitance and power density from the collected data. Figure 7.2 presents the ML model architecture, consisting of three hidden layers with 40, 60, and 15 nodes. The majority of the datasets were created from this chapter, with the remainder sourced from experiments conducted for chapter 6. Thus in this chapter, 100 datasets were used based on in-house experiments conducted to synthesize waste-derived AC biomass. The electrochemical data were collected from the three-electrode experiments to better understand each electrode's performance with changing current rates. The model effectively distinguishes between the different samples when many sample features are included as inputs. Firstly, to quantitatively determine the effects of the inputs, the MLP model employed used 6 input parameters, as in chapter 6. Then, the number of input parameters was expanded to 21 to increase the parameter contribution for capacitance prediction, and the accuracy of the models was compared. To characterize the porous carbon from different biomass precursors, we postulate it is important to consider surface area, micropore volume, average pore diameter, and surface morphology properties. The more inputs to identify and differentiate the properties of the materials make the predictions more robust [35]. The effect of the changed current rate has also been considered in this chapter as an electrochemical feature. The current rate directly affects the integral capacitance measured from the GCD curves, which generally decreases with an increasing rate. As another determining factor of the capacitance, the electrolyte properties, the hydrated radius of the ions, ion conductivity, and mobility have also been included as inputs. Thus 21 input parameters were considered as inputs for the MLP model. MLP model was built using the Scikit-learn package in Python. The relu' and 'linear' activation functions are used for the model, and the optimizer used is 'adam'. The MLP was trained for a maximum iteration of 2500 for this model. Out of the experimental data, 80 % was used for training, and 20 % was used to test the MLP model. The 5 - fold cross-validation splits the data into 5 equal-sized blocks and one block for testing and the other blocks for

training for the model [36]. The results presented in this section consider the average of those 5 - fold cross-validation. The coefficient of determination (R^2 in equation (6.1) in chapter 6), mean squared error (MSE in equation (6.2) in chapter 6), and mean absolute error (MAE in equation (6.3) in chapter 6) were used as the evaluation metrics to determine the model's accuracy [34]. In general, the R^2 value should be close to 1 for a perfect fit for the regression models, while the MSE and MAE values should be close to 0 to indicate fewer errors in fitting the data. The smaller the MSE and the MAE, the closer the predicted and the actual experimental data. The key inputs employed in the MLP model are given in Table 7.1.

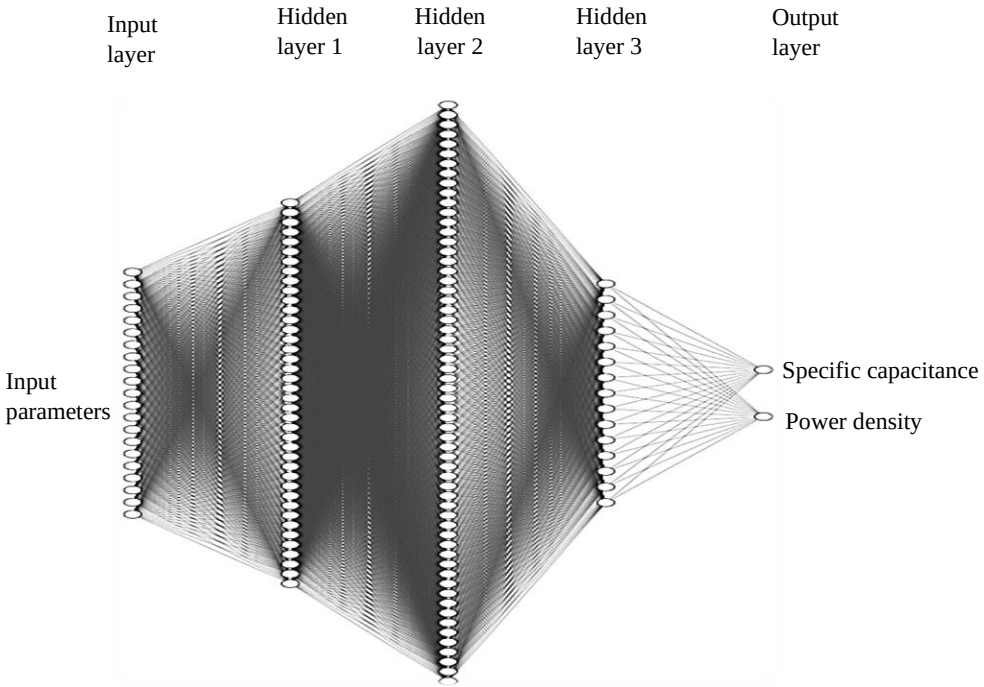

Figure 7.2 MLP model architecture correlating the inputs with specific capacitance and the power density.

Table 7.1 Summary of inputs and outputs used for MLP model.

Inputs	Outputs
Activating agent type	
Dopant % in the precursor	
Carbonization temperature	
Carbonization time	
Activation temperature	
Activation time	
Porosity fraction	
Surface average pore size	Specific capacitance
BET surface area	
Micropore area	Power density
External surface area	
Micropore volume	
BJH average pore diameter	
Electrolyte type	
Cation hydrated ionic radius	
Anion hydrated ionic radius	
Cation ionic conductivity	
Anion ionic conductivity	
Cation ionic mobility	
Anion ionic mobility	
Current rate	

7.4. Results and discussion

7.4.1. Physicochemical characterization of the GM-derived N-doped AC materials

Morphology analyses. Figure 7.3 shows the surface morphologies of the GM and its derived AC materials. Globular particles with a fibrous structure were observed on the surface of the dried GM (Figure 7.3 A-C). No visible pores were observed on the

surface. After carbonization and subsequent activation with KOH, the KAC demonstrated a porous structure due to the removal of hemicellulose and cellulose. Twisted-shaped particles with irregular sizes varying from the sub-micrometer scale to tens of micrometers were also observed (Figure 7.3 D-F). Interestingly, for KAC_{urea}, Figure 7.3 G-I shows a flattened-shaped morphology with well-distributed porosity and an interpore connection. The decomposition of N-functionalities from the urea-mixed GM evolved into gaseous species around 520 °C [37], increasing the defect sites and mesopores of KAC_{urea} compared to KAC, as visible in Figure 7.3 D-F. In the case of the $ZnCl_2$ activating agent, $ZnAC_1$ (Figure 7.3 J-L) showed a stacked granular morphology with a very low number of pores on the surface. In comparison, $ZnAC_2$ (Figure 7.3 M-O) shows large cavities on the surface with some small pores embedded.

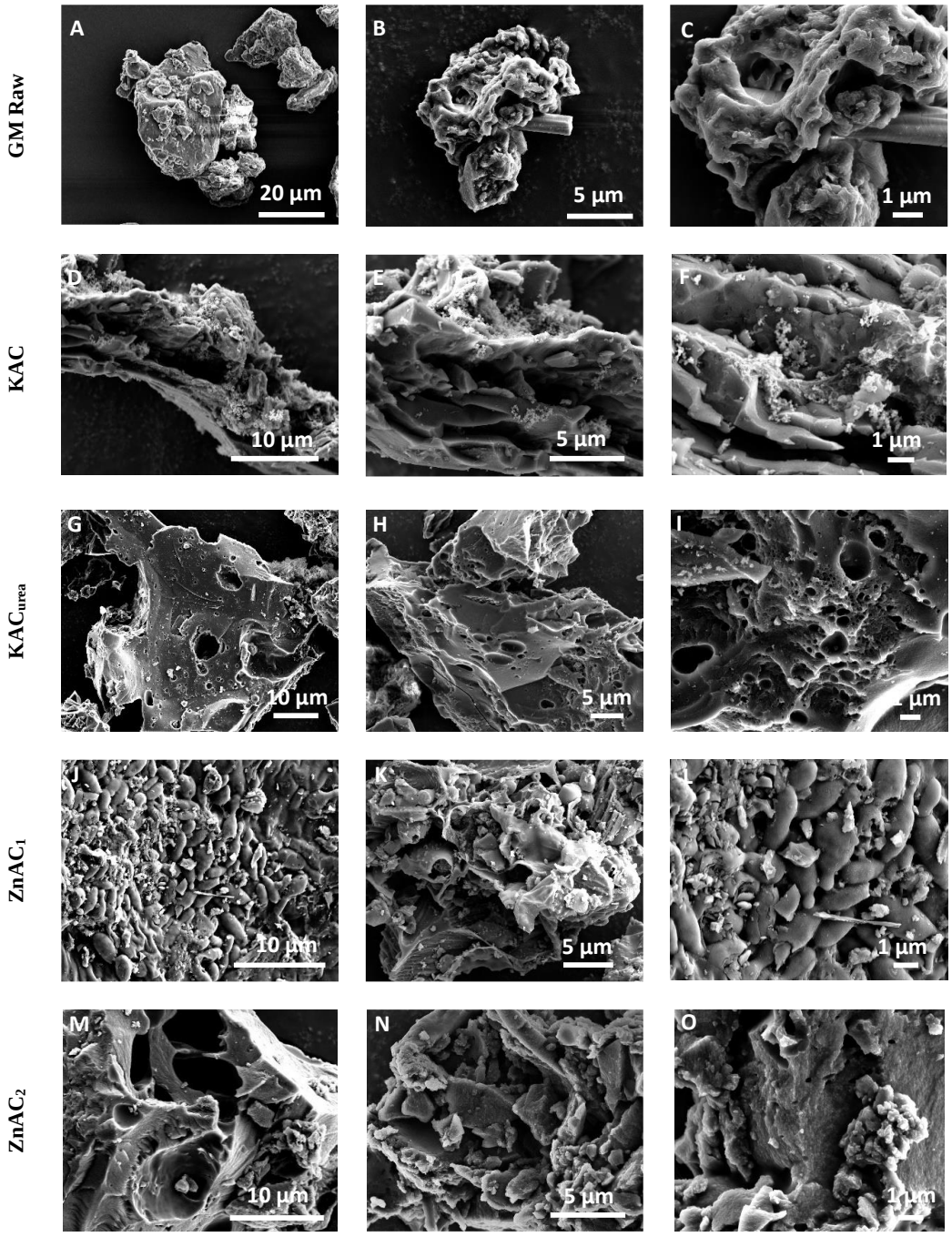

Figure 7.3 FESEM images of (A-C) GM precursor before any heat treatment, (D-F) KAC, (G-H) KAC_{urea}, (J-L) $ZnAC_1$ (M-O) $ZnAC_2$.

The SEM image (Figure 7.4A) and EDS elemental mapping (Figure 7.4 B-D) for KAC_{urea} illustrate the element distribution on the AC surface. Figure 7.4B illustrates a substantial amount of carbon present in the sample. The urea in the GM precursor embedded the nitrogen within the carbon structure, as seen in Figure 7.4D. The microstructure of KAC_{urea} was examined using TEM, as shown in Figure 7.5 A and B. The HRTEM image (Figure 7.5B) reveals the amorphous structure of KAC_{urea}, which is consistent with reported work on hard carbon synthesized via pyrolysis of carbonaceous precursors such as pomelo peels, banana stems, and corn cobs [38,39]. This further demonstrates that the elements present in the materials are similar to the previously observed SEM and EDS images in Figure 7.4.

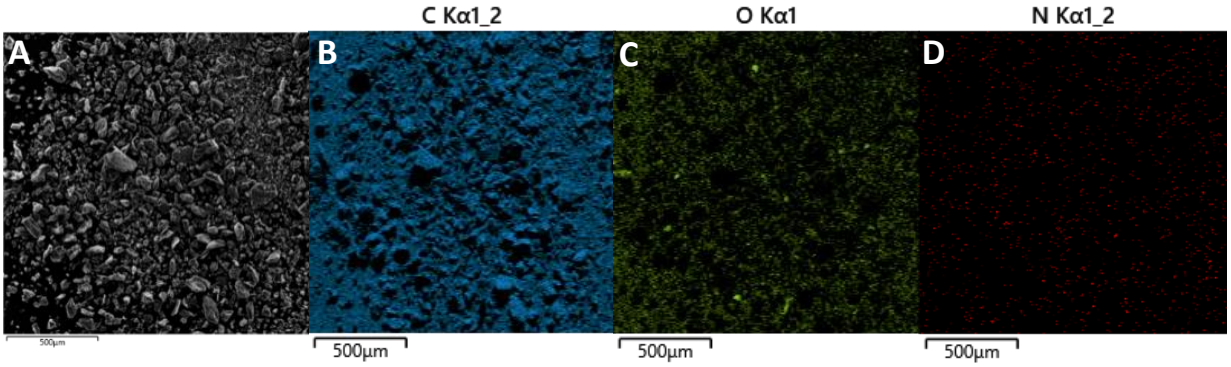

Figure 7.4 SEM coupled with EDS of KAC_{urea} (A) electron image, (B, C, D) elemental mapping of 'C', 'O' and 'N' respectively.

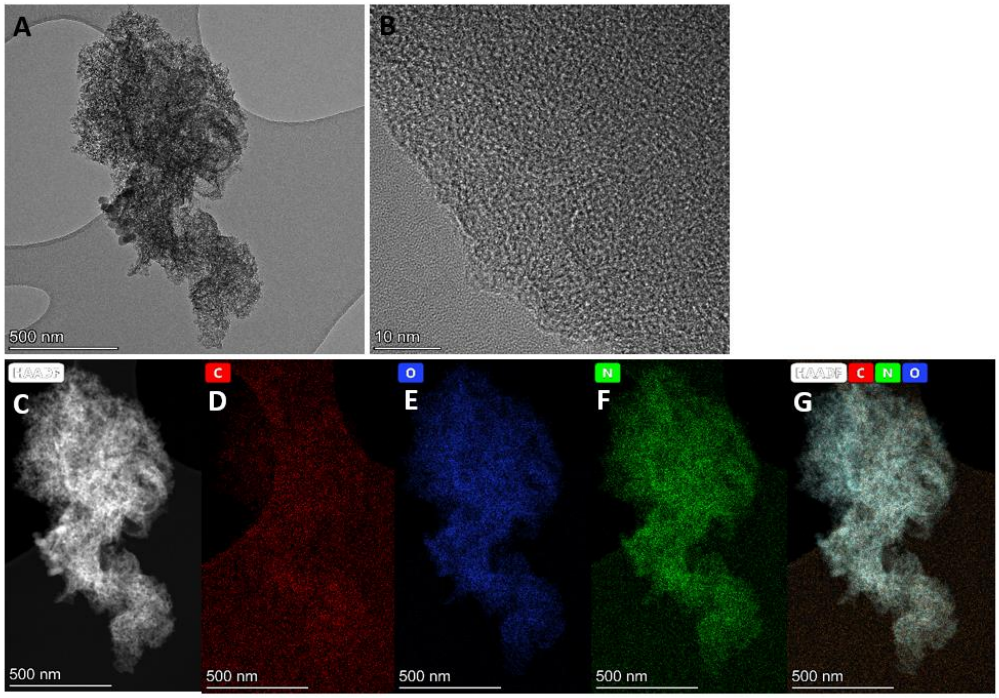

Figure 7.5 (A) Low-resolution TEM, (B) High-resolution TEM images, (C) High-angle annular dark-field (HAADF)-scanning transmission electron microscopy (STEM) image, and (D-G) Energy-dispersive X-ray spectroscopy (EDS) elemental mapping of KAC_{urea}.

Structural and spectral analyses. The XRD patterns of the GM-derived AC materials using different activating agents are given in Figure 7.6A. All of the samples exhibited two characteristic broad diffraction peaks of turbostratic carbon (t-carbon) positioned around 25° and 44°. The diffraction peak at around 25° was attributed to the disordered (amorphous) carbon corresponding to the 002 crystal plane. The peak at 44° was indexed to the 100 plane of graphitized carbon [40]. In contrast to $ZnAC_1$ and $ZnAC_2$, the KAC and KAC_{urea} samples showed a slight shift in the 002 peak to a lower angle, positioned around 22° in the XRD pattern. This implies that the 'K' penetration in carbon occurs during the KOH activation and induces higher interlayer spacing of (002) d_{002}. The higher d-spacing increases the number of active sites for the electrolyte ion (adsorption-desorption) interaction during charging/discharging. The broader peak seen in the KAC_{urea} indicates that the highly amorphous nature of the sample comes from the N-functionalities on its surface. For $ZnAC_1$, the 002 peak was well defined

and intense, implying a crystalline material supported by the morphology seen in the FESEM images discussed earlier. By contrast, the $ZnAC_2$ sample, which was carbonized and activated at a lower temperature of 450 °C, showed less crystallinity. These observations suggest that the KOH activation gives a more disordered crystal structure and is relatively suitable for energy storage performance.

A qualitative analysis of functional groups in the GM-derived AC materials was carried out via FTIR spectroscopy in the mid-and near-IR regions (Figure 7.6B). The FTIR curves of all AC spectra were similar. A broader band observed around 3400 cm^{-1} could be attributed to the O-H stretching vibration of hydroxyl functional groups [41]. This was very likely caused by the dehydration of GM during the carbonization process. The position of the bands shifted to a lower wavenumber as the carbonization temperature increased for $ZnAC_1$ compared to $ZnAC_2$. This could be due to the disruption of H-bonds established by OH groups. The peak at 1600 cm^{-1} was related to the C=C stretching of aromatic rings and C=O conjugated with the aromatic rings [42]. The peak around 960 cm^{-1} could be associated with stretching vibration of C-C or C-H groups [43]. Overall, the oxygen-containing moieties, including C=O functionalities on the surface of GM-derived AC materials, may significantly contribute to capacitive performance [44].

The structure, defects, and disordered nature of the carbon materials could be determined by Raman spectroscopy. The Raman spectra for GM-derived AC materials using different activating agents and N-dopants are shown in Figure 7.6C. The D-band around 1345 cm^{-1} was related to the sp^3 carbon sites, indicating that the defect peak arises due to the A1g mode of vibration. The nearby peak around 1580 cm^{-1} represents the G-band related to the sp^2 carbon sites and indicates the graphitic peak [45]. The graphitic peak was observed because of the E2g mode of vibration and relevant stretching of the C-C carbon bond. The D and G band intensity (I_D/I_G) ratio was inversely proportional to the in-plane crystallite sizes of the AC [45]. The I_D/I_G values of 0.99, 0.99, and 1.01 for KAC_{urea}, KAC, and $ZnAC_1$, respectively but not the 0.97 for $ZnAC_2$, indicated good graphitic crystallinity. For a non-defective carbon material, I_D/I_G should be equal to zero. The calculated I_D/I_G values for the AC samples imply that all four samples had defects in the graphitic carbon, with an amorphous character. Validations such as the shift in 2θ of XRD towards the lower angle and higher I_D/I_G

ratio suggest increased interplanar spacing and a high disorder level due to KOH activation.

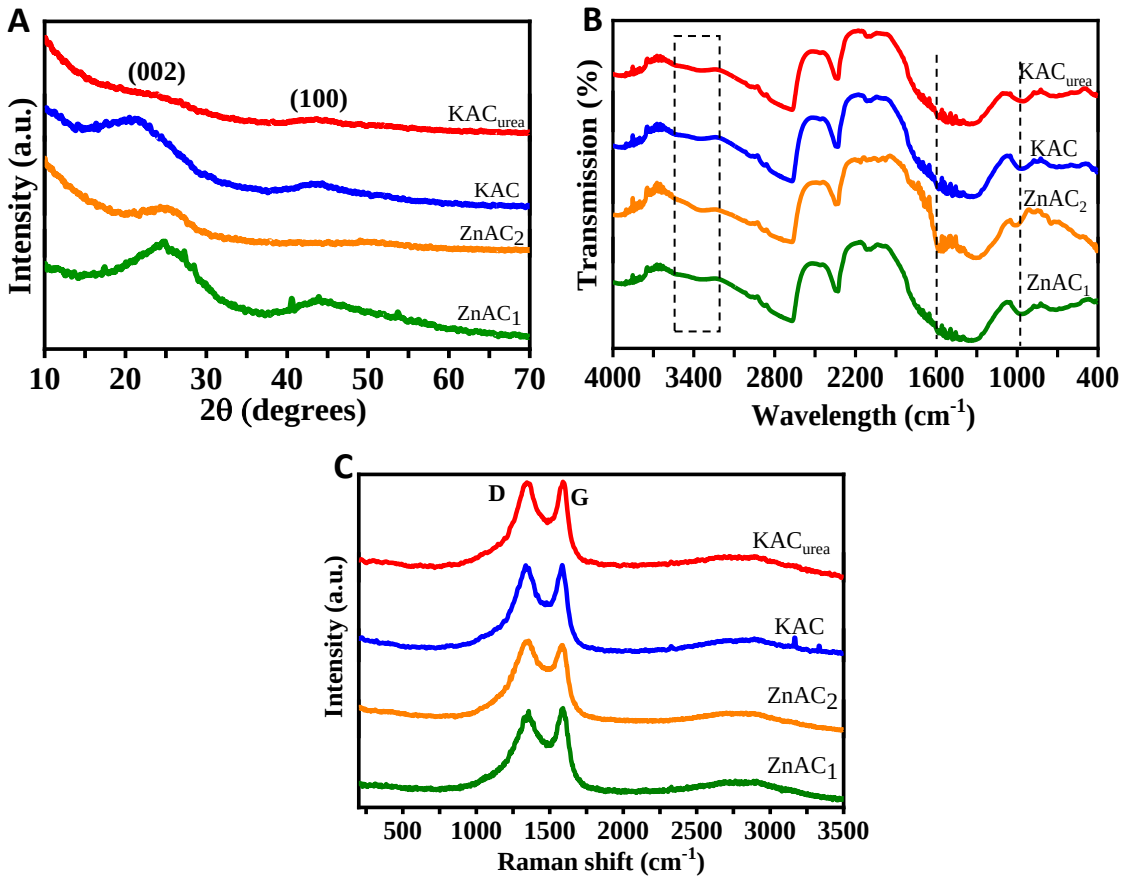

Figure 7.6 (A) XRD pattern, (B) FTIR spectra, and (C) Raman spectra of GM-derived AC, i.e., KAC_{urea}, KAC, $ZnAC_1$, $ZnAC_2$.

Surface area and pore structure. The specific surface area and pore volume of the GM-derived AC, as obtained from N_2 adsorption-desorption measurements, are given in Table 7.2. With the activation of KOH, the KAC sample exhibited a specific area value of 1128 $m^2\ g^{-1}$. For N-doped carbon, the quantity of N_2 adsorption by KAC_{urea} demonstrated a maximum surface area of 1356 $m^2\ g^{-1}$. The key role of the activation process using the KOH activator is to generate pores to increase the surface area available for adsorption/desorption processes at the electrode-electrolyte interface. This is evidenced by the isotherms of KAC and KAC_{urea} shown in Figure 7.7, which do not manifest well-positioned hysteresis loops. KAC recorded a sharp increase in

volume at low relative pressures, followed by reaching a plateau at high relative pressures, giving the behavior of typical type I isotherms of microporous materials according to the IUPAC classification [46]. A slight difference is seen in the KAC_{urea} isotherm; this could be due to an increased mesopore proportion under the influence of urea as a dopant. It could also be related to a combination of type I and IV isotherms, as reported in the literature [37]. Furthermore, from KAC to KAC_{urea}, the pore structure changes from micropores to hierarchical pores, which are more favorable for better electrochemical performance.

The surface area values obtained for the ZnAC samples were lower than those of the KAC and KAC_{urea} samples. $ZnAC_1$, activated at 800 °C using a pre-carbonized sample, gave the lowest surface area of 29.14 $m^2\ g^{-1}$. There was no hysteresis loop between the adsorption-desorption isotherms of $ZnAC_1$ (Figure 7.7), possibly due to the large micropore fraction [47]. This was further verified by the micropore area percentage, which was > 89 %, as calculated from the data in Table 7.2. A larger proportion of micropore-specific surface area lowers the mesopore and macropore surface areas. Due to this outcome, the GM was directly activated at a lower temperature of 450 °C [48]. Although this increased the surface area compared to that of $ZnAC_1$, the micropore area and volume remained noticeably lower, making $ZnAC_2$ less suitable for capacitor fabrication. $ZnAC_2$ showed an obvious hysteresis loop characteristic of a type IV isotherm for mesoporous materials [46]. It can be concluded that choosing an effective synthesis route and a suitable activating agent determines the effective pore structure through the chemical activation process.

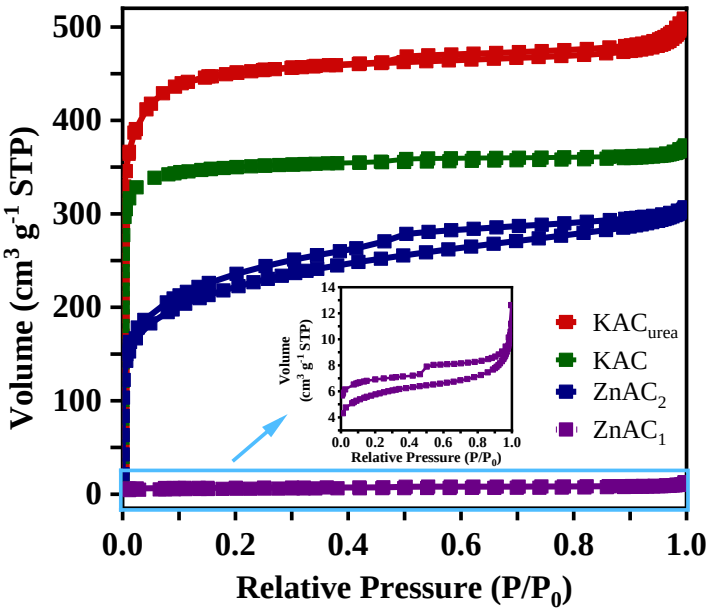

Figure 7.7 Comparison of N_2 adsorption-desorption isotherms of KAC_{urea}, KAC, $ZnAC_1$, $ZnAC_2$. The inset shows the hysteresis loop for $ZnAC_1$.

Table 7.2 Surface area and pore analysis parameters for the GM-derived AC materials.

Sample	BET Surface area ($m^2 g^{-1}$)	t-plot Micropore area ($m^2 g^{-1}$)	Micropore area (%)	Total pore volume ($cm^3 g^{-1}$)	t-plot Micropore volume ($cm^3 g^{-1}$)	Micropore volume (%)
KAC_{urea}	1356	1126	83.0	0.79	0.60	75.9
KAC	1128	998	88.5	0.58	0.53	91.4
$ZnAC_1$	29	26	89.7	0.02	0.01	50.0
$ZnAC_2$	711	275	38.7	0.46	0.15	32.6

In summary, as derived from the physical characterization data, the KAC, KAC_{urea}, and $ZnAC_1$ synthesized under similar thermal conditions had distinct characteristics due to different activation mechanisms. KOH reacts with the GM-derived carbon via KOH etching, metallic K penetration, and CO/CO_2 release to create a porous structure during heat treatment. Reaction, R(6.1 - 6.4) explains the reaction mechanisms in the presence of the KOH activating agent.

$$6KOH + 2C \rightarrow 2K + 3H_2 + 2K_2CO_3 \quad \text{R(6.1)}$$

$$K_2CO_3 + C \rightarrow K_2O + 2CO \quad \text{R(6.2)}$$

$$K_2CO_3 \rightarrow K_2O + CO_2 \quad \text{R(6.3)}$$

$$2K + CO_2 \rightarrow K_2O + CO \quad \text{R(6.4)}$$

The synthesis conditions used here with the KOH activating agent are favorable for high-performance supercapacitor applications. The $ZnCl_2$ evaporates above its boiling point of 732 °C, thereby causing imperfection of the structural and textural properties at the activation temperature of 800 °C [49]. Considering the $ZnAC_1$ and $ZnAC_2$, the $ZnCl_2$ might conduce better activation of GM between 450 °C and 800 °C. Therefore, a suitable activating agent and synthesis route are essential for pore evolution by micropore formation and pore-widening mechanisms [50]. The FESEM images also confirm that the $ZnAC_1$ is highly dense, with no visible open pores on the surface, which would impede the electrolyte ion movements into the electrode structure, plausibly decreasing the electrochemical performance. Additionally, the N-dopant present in GM could enhance the surface chemistry of the KAC_{urea}. The KOH activation is usually accompanied by nitrogen release, leading to a reduced amount of nitrogen. Therefore, it is difficult to obtain higher porosity along with a considerable amount of nitrogen functional groups in KAC [51]. After the carbonization step, the nitrogen functional groups could predominantly present as pyridine-N, pyrrolic N, imine, amine, amide, quaternary-N, and pyridine-N-oxide groups on the surface of the carbon [52]. During activation, the reactions expand the carbon network, forming many more micropores and mesopores in the carbon material while reducing carbon and most nitrogen. In addition, compared to KAC, KAC_{urea} favors the metallic ‘K’ for easy access to the bulk of GM-derived carbon through newly formed channels that enhance the porous nature of carbon [52]. The role of N-functionality on the carbon surface is postulated to be pyridinic-N, and pyrrolic-N can contribute to the pseudocapacitance in alkaline electrolytes. At the same time, quaternary-N and pyridine-N-oxide can improve the charge transfer across the electrode-electrolyte interface and enhance the capacitance. In Section 7.4.3, in the DFT modeling results,

we discuss the N-dopant effect in its most stable form of the pyridine-N-oxide present in the carbon structure.

7.4.2. Supercapacitor applications of GM-derived N-doped AC: electrochemical performance (CV, GCD) of the single electrode and symmetric capacitor device

The CV curves of the KAC and KAC_{urea} samples (Figure 7.8 A and B) encircle much larger areas and give higher current responses. The curves are nearly rectangular due to predominant EDLC charge storage, while the deviations are caused by pseudocapacitance from N-functionalities. Using the GCD measurements (Figure 7.8 C and D) at a 2 mA current rate, the calculated specific capacitances of KAC and KAC_{urea} are 117 F g^{-1} and 139 F g^{-1}, respectively, which are comparable with the reports in the literature [53–55]. The approximately symmetrical triangular shape of the GCD curves can be observed due to EDLC and pseudocapacitor charge-storage mechanisms, which are consistent with the CV measurements.

The shape of the CV curves is retained with an increase in the scan rate from 5 to 50 mV s^{-1}, showing the stability of KAC_{urea}. From the calculated capacitances, KAC_{urea} performs best, ascribed to both the KOH activator along with the N-dopant and the development of a hierarchical pore structure during thermal treatment. With an increase in the current rate from 2 to 10 mA, the specific capacitance of KAC_{urea} decreased gradually from 139 F g^{-1} to 125 F g^{-1} due to limited access available for the electrolyte to flow into the electrode, along with the conductance resistance [56]. The CV and GCD profiles of ZnAC are illustrated in Figure 7.9. The CV curves displayed by the $ZnAC_1$ sample (Figure 7.9A) possess a narrow area under the curve, in elliptical shapes, and give lower current responses. The calculated specific capacitance of $ZnAC_1$ was 29 F g^{-1} at a 2 mA current rate. On the other hand, $ZnAC_2$ exhibited pseudocapacitance characteristics, displaying two redox pairs A/A’ and B/B’, as shown in Figure 7.9B. The functionalization of the carbon surface, heat-treated at an elevated temperature, could enhance the faradaic contributions to the observed capacitance. However, the lower pore volume with no improvement in pore size distribution reduced the interconnection between carbon particles, resulting in a lower

specific capacitance of 41 F g^{-1} at 2 mA. The GCD curves of $ZnAC_1$ and $ZnAC_2$ are given in Figure 7.9 C and D. Similar to the observed CV behavior, the curves are not triangular and do not show many reversible characteristics. A comparison of CV, GCD, and rate performance is given in Figure 7.10 A and B. The CV is measured at a 20 mV s^{-1} scan rate, while GCD is measured at a 3 mA current rate. The elliptical-shaped CV of the $ZnAC_1$ sample gives the lowest charge storage, whereas KACurea shows the optimal charge storage, which matches well with the GCD measurements in Figure 7.10B. Finally, I compared the energy storage capability of all of the samples based on their specific capacitances at different current rates. The retained percentages of the SCs for $ZnAC_1$, $ZnAC_2$, KAC, and KAC_{urea} were 30 %, 66 %, 80 %, and 90 %, respectively, as with the rate performances plotted in Figure 7.10C. The capacitance retention was also increased for the KOH-activated carbon sample. This corresponds to the hierarchical pore formation accompanied by the defects and porous surface morphology induced by doping, along with increased electrode/electrolyte wettability of KAC_{urea}. The specific capacitance of the best-performing KAC_{urea} is compared with the reported values for the biomass-derived carbon in the literature in Figure 7.10D. Further comparison between different parameters was conducted for the carbon obtained from various precursors, as tabulated in Table 7.3.

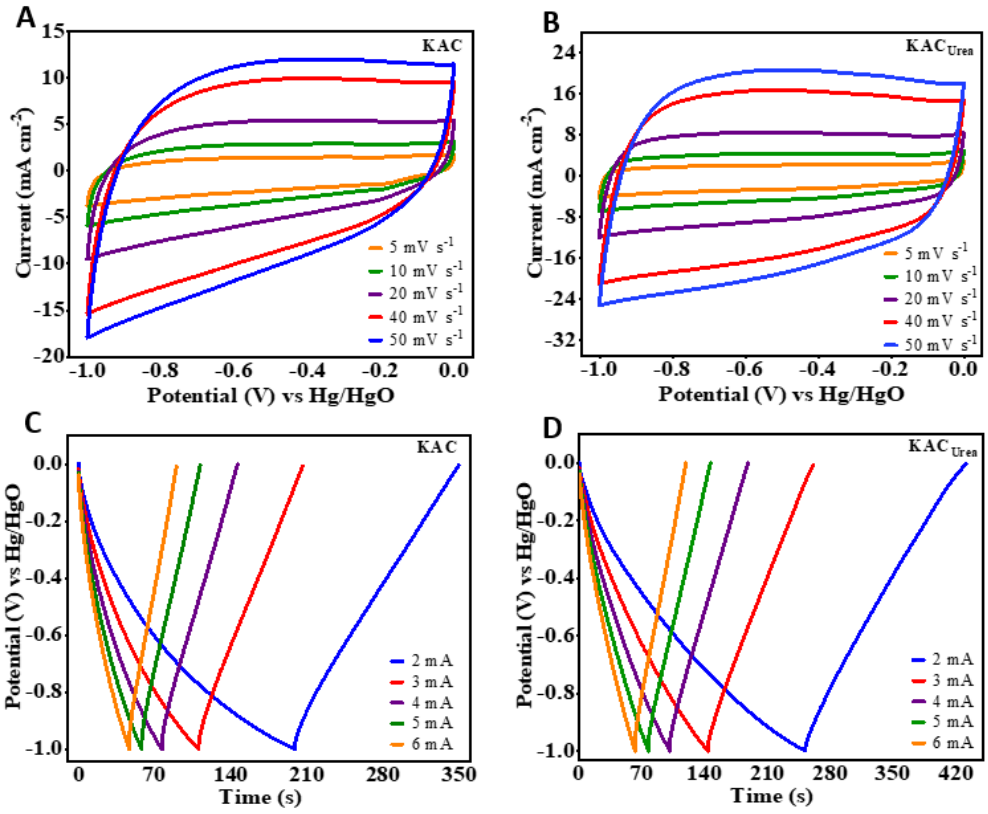

Figure 7.8 (A, B) Cyclic Voltammetry (CV) and (C, D) Galvanostatic Charge-Discharge (GCD) profiles of KAC and KAC_{urea}.

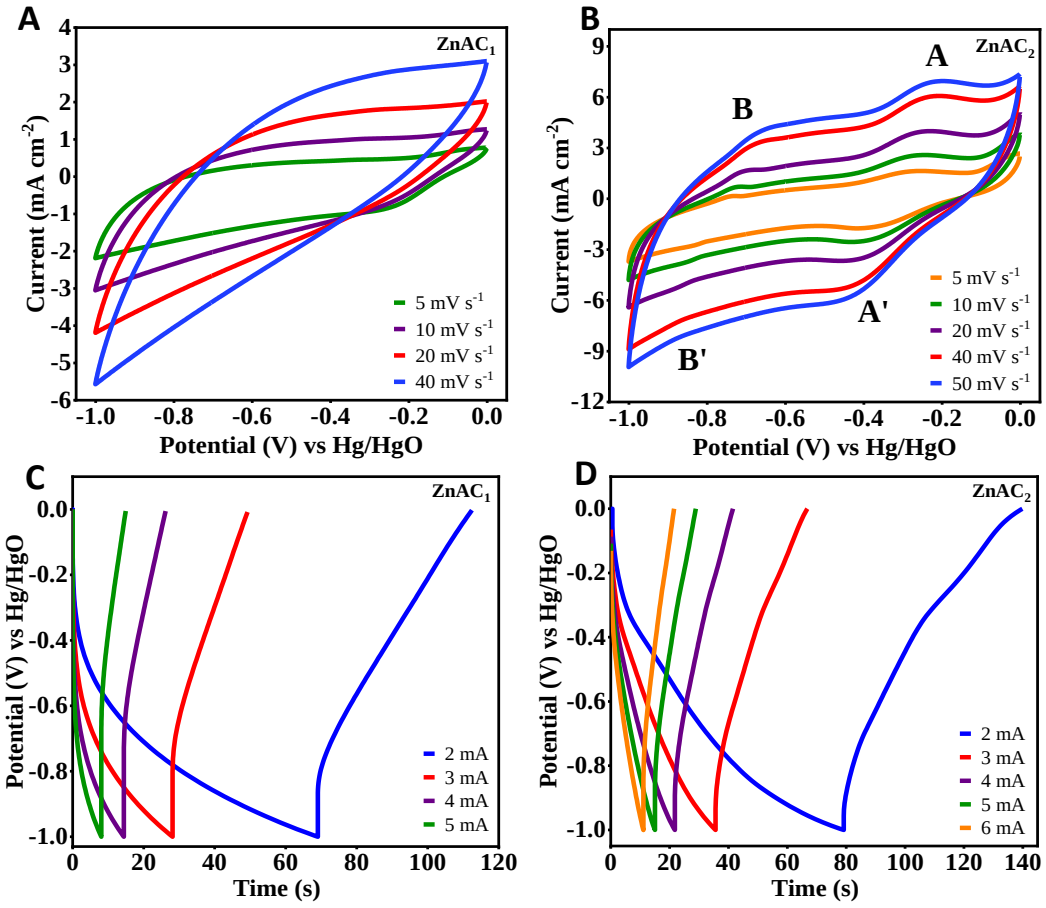

Figure 7.9 (A, B) Cyclic Voltammetry (CV), and (C, D) Galvanostatic charge-discharge curves of Grape marc (GM)-derived AC: $ZnAC_1$ and $ZnAC_2$.

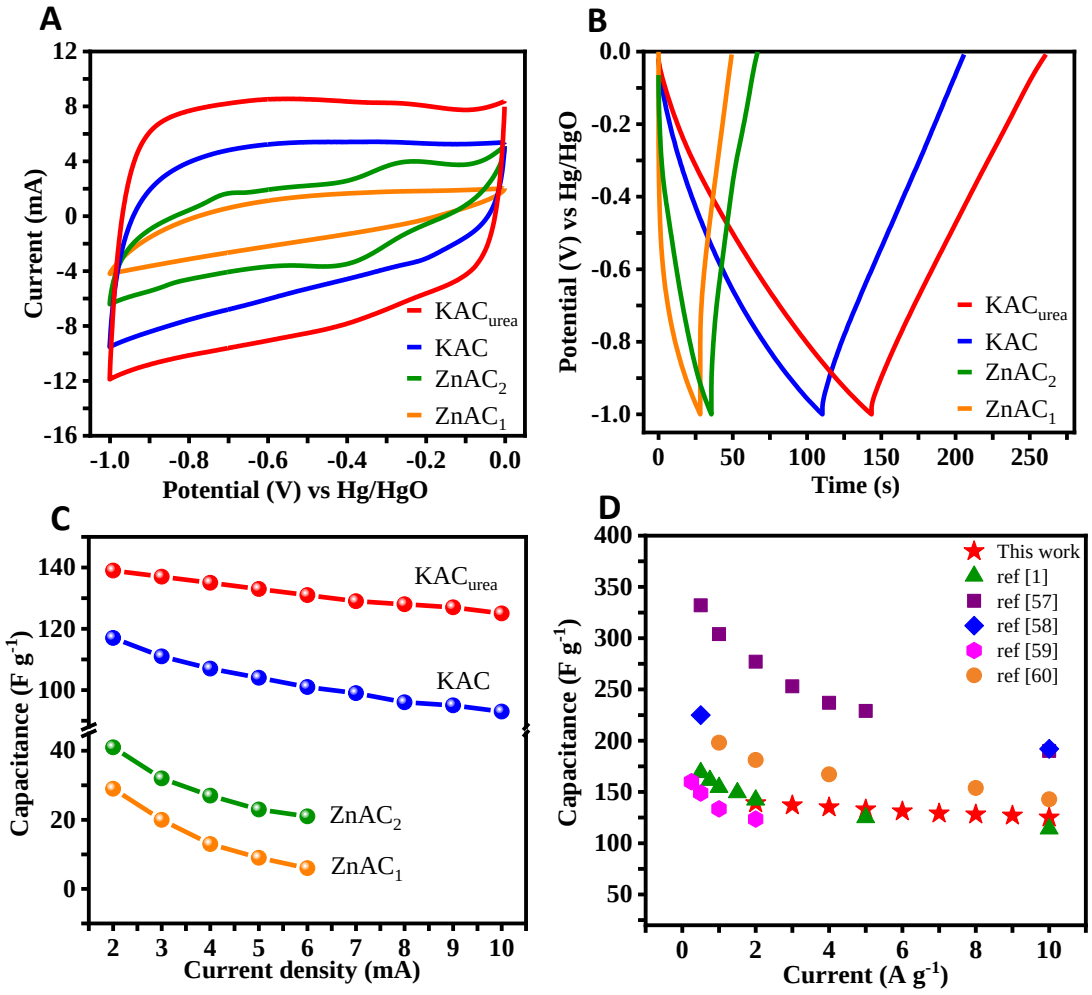

Figure 7.10 (A) CV at 20 mV s^{-1}, (B) GCD at 3 mA of GM-derived N-doped AC, tested in 2M NaOH electrolyte, (C) Specific capacitances at varying applied currents of all the materials: $ZnAC_1$, $ZnAC_2$, KAC, and KAC_{urea} and, (D) Capacitance comparison of the best performed KAC_{urea} with reported values in the literature [1,57–60].

Table 7.3 Comparison of biomass-based carbon derived from various precursors with their reported specific capacitances and other relevant parameters.

Ref.	Biomass precursor	Activating agent	Surface area ($m^2 g^{-1}$)	Electrolyte	Current density	Specific capacitance ($F g^{-1}$)
Wang *et al.*[1]	Apricot shell lignin	H_3PO_4	1474.82	6M KOH	0.5 A g^{-1}	169.05
Subramanian *et al.*[60]	Banana fibres	$ZnCl_2$ KOH	1097 686	1M Na_2SO_4	0.5 A g^{-1}	74 66
Nabais *et al.*[61]	Coffee endocarp	CO_2 KOH	709 361	1M H_2SO_4	10 mA (~ 0.2 A g^{-1})	176 69
Gou *et al.*[62]	Wheat straw	KOH	772	6M KOH	0.5 A g^{-1}	226.2
Yan *et al.*[63]	Macadamia nutshell	KOH	2202	1M Na_2SO_4	1 A g^{-1}	155
Mondal *et al.*[54]	Shrimp shell	KOH	1271	6M KOH	0.5 A g^{-1}	239
Liu *et al.*[64]	Rice straw	KOH	1127	6M KOH	1 A g^{-1}	337
Huang *et al.*[58]	Wood sawdust	KOH	2294	6M KOH	0.5 A g^{-1}	225
Ramirez *et al.*[65]	Coffee husk	Steam K_2CO_3 KOH	1447 1156 2275	6M KOH	0.5 A g^{-1}	138 129 106
Xu *et al.*[66]	Rice straw	$KHCO_3$	2786.5	6M KOH	1 A g^{-1}	317
Dubey *et al.*[67]	Human hair	KOH	1992.4	1M H_2SO_4	1 A g^{-1}	274.5
our work	GM	KOH	1356	2M NaOH	2 A g^{-1}	139

KAC_{urea}, which possesses the largest SC, was studied in different aqueous electrolytes: two alkaline electrolytes with different cations, i.e., NaOH and LiOH, and a salt electrolyte with a different anion, $NaClO_4$, all with a 2 M concentration (Figure 7.11). CV measurements were taken at 20 mV s^{-1} (Figure 7.11A), and the GCD was determined at a 3 mA current rate (Figure 7.11B) in a 0 V to -1 V potential window. The current response observed in the three electrolytes followed the order of NaOH > $NaClO_4$ > LiOH. When the electrolyte (cation/anion) is varied, the differences in the capacitances are observed due to ion mobility, hydrated ion radius, conductivity, and their effect on charge/ion exchange and diffusion [68]. The highest current response is seen in the NaOH compared to the LiOH electrolyte. The Li^+ ions have a larger hydration sphere radius as it strongly interacts with $H_2O^{\delta-}$. Considering the effect of the anions, the presence of OH^- seems comparatively better than ClO_4^- on the electrochemical performance of KAC_{urea}. The higher ionic conductivity, ionic mobility, and the smaller hydration sphere of OH^- ion led to the efficient charge propagation, as evidenced by CV and GCD measurements. Figure 7.11C shows the highest capacitance retention given by NaOH over increasing current rates. The Nyquist plots for the three-electrode system are studied to analyze the ionic diffusion and transport kinetics further. It can be seen in Figure 7.11D that all the plots demonstrate the contributions to the ideal capacitance observed for the three electrolytes with a -90° slope at the low-frequency region. In the middle frequency region, the Warburg impedance with a ~45° gradient inclined line is more understandable for LiOH, implying its slow ion transport kinetics. In summary, both the CV and GCD measurements concluded that the electrochemical performance of GM-derived activated carbon was significantly enhanced by adding N-dopant tested in Na-ion electrolyte as a promising and low-cost alternative to existing electrolytes.

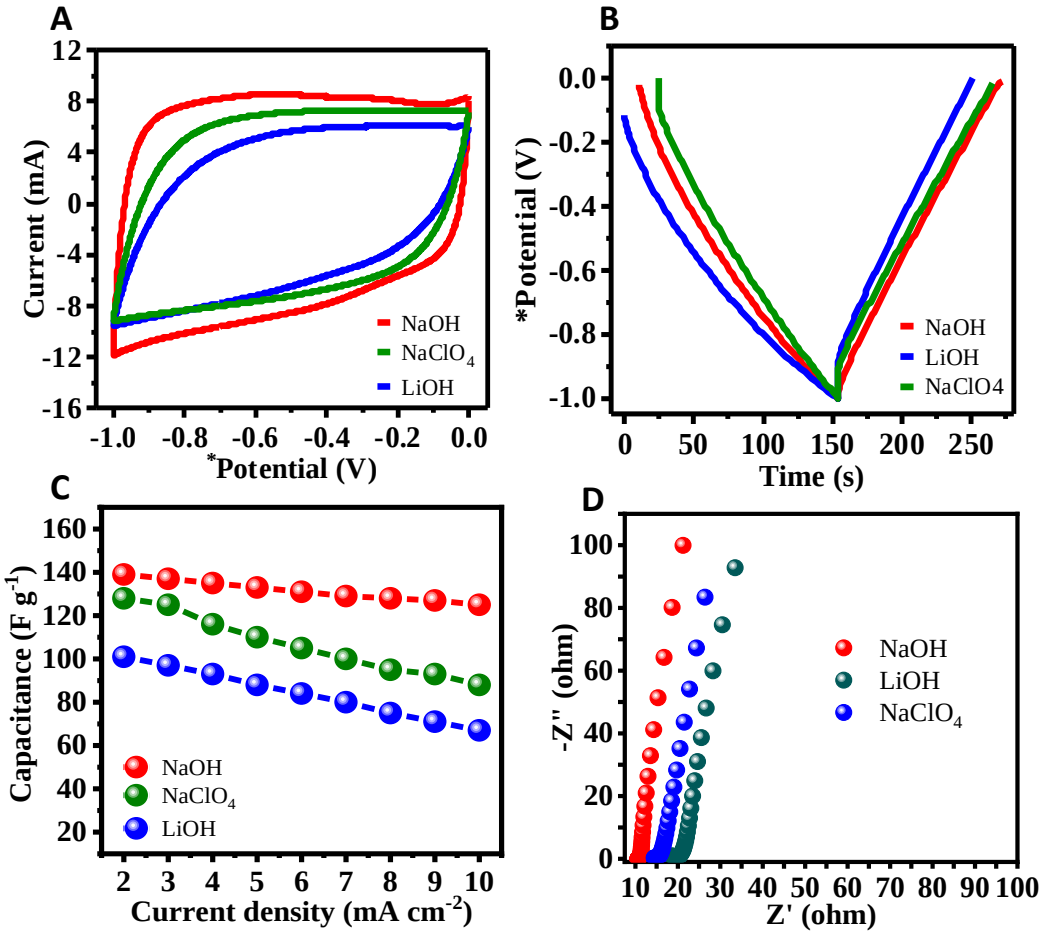

Figure 7.11 (A) Cyclic Voltammetry (CV) and (B) Galvanostatic charge-discharge curves of commercial AC to benchmark the values obtained for GM-derived AC.

The symmetric capacitor device was tested by coupling two electrodes of the best-performing KAC_{urea} material. The CV and GCD profiles of the symmetric capacitor recorded at a 1 V potential window are given in Figure 7.12 A and B, respectively. The shapes of the curves are nearly symmetrical, and the reversible behavior of the cell can be observed in all tested conditions of varied scan rates and current rates. The discharge cell capacitances calculated at current rates of 2, 3, 4, 5, and 6 mA were 47, 44, 41, 38, and 37 F g^{-1}. Furthermore, the capacitance retention of ~84 % and the cell efficiency of ~96 % for 10,000 cycles at 5 mA are displayed in Figure 7.12C.

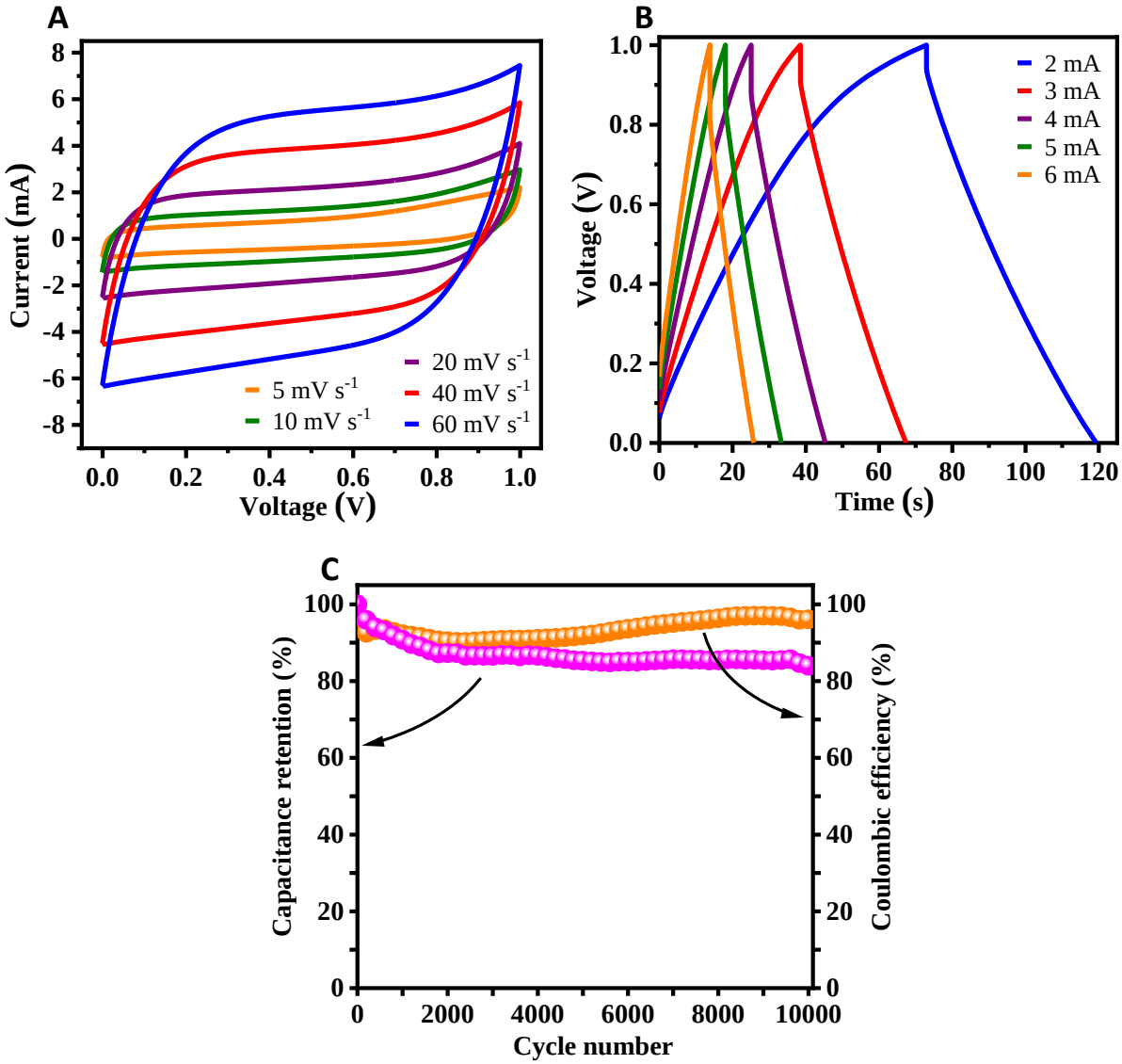

Figure 7.12 (A) CV at varying scan rates (5, 10, 20, 40, and 60 mV s^{-1}) and (B) GCD profiles at varying current rates (2, 3, 4, 5, 6 mA) of symmetric capacitor device (KAC_{urea} *vs.* KAC_{urea}) in an aqueous 2 M NaOH electrolyte at 1 V window, (C) capacitance retention and coulombic efficiency over 10000 cycles.

7.4.3. Theoretical insights: Density Functional Theory (DFT) study

To validate and bring further insights into the experimental findings, first-principles density functional theory (DFT) simulations were performed. Nitrogen-doping in GM can effectively tune the electrical properties of carbon. The optimized lattice parameters of the graphite bilayer supercell were a = b = 2.464 Å, and c = 21.711 Å. Furthermore, the following geometries were simulated: an N atom was substituted for the C atom on the surface, O adsorbate on the pristine graphite, and O adsorbed on the N-atom-substituted graphite. The optimized geometries are shown in Figure 7.13.

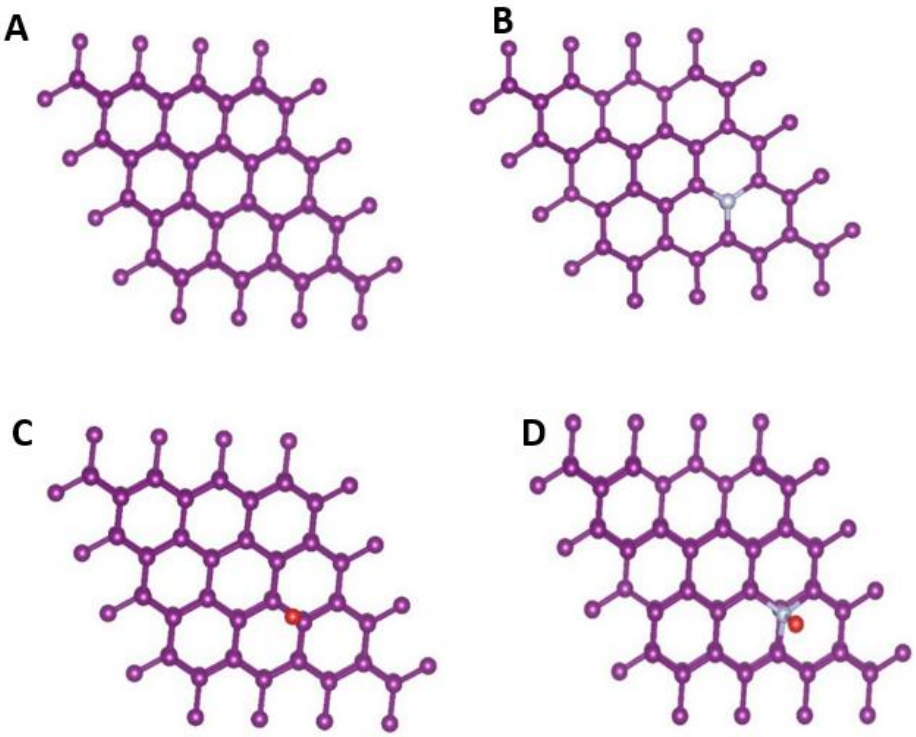

Figure 7.13 The optimized structures of graphite bilayers: (A) pristine graphite, (B) graphite substituted with an N atom on the surface, (C) pristine graphite with O adsorbate, and (D) graphite substituted with an N atom and O adsorbate. The figures were plotted using the VESTA software. The color code of the atoms is as follows- purple: C, white: N, red: O.

The bond distance between the O atom and graphite surfaces was calculated and is presented in Table 7.4. It can be noted that the bond distance for pristine graphite and the O atom is 2.27 Å, and this bond length decreases to 1.40 Å for N-doped graphite. This reduced bond distance indicates that the chemisorption of the O atom onto the graphite surface is enhanced by the presence of the N-functionality on the atomic surface. The C-N bond length also elongates in the presence of O adsorption. Bader charge analysis was carried out to understand the charge-transfer properties on the surfaces, and the results are presented in Table 7.4. On the graphite surface, the O adsorption occurs as a result of charge gain by the O atom and is enhanced by the presence of the N atom (−0.35 to −0.49), indicating stronger chemisorption. The N atom gains electrons from surrounding C atoms, and the charge gain decreases when the O atom is adsorbed on the surface. On the other hand, the C atoms directly bonded or in the nearest-neighbor position of the N atom lose charge to compensate for charge redistribution. Electronic structure analysis was carried out to understand the hybridization of orbitals at the surface. The density of states (DOS) of the pristine and the N-doped graphite surfaces is presented in Figure 7.14.

Table 7.4 Bond distances and Bader charges calculated for the pristine and N-doped graphite surfaces. Bader charges calculated for the atoms nearest to the adsorbed O atom.

Configuration	**Bond length (Å)**			**Bader charges**		
	C–O	**C–N**	**N–O**	**O**	**N**	**C**
Pristine graphite + O	2.27			-0.35		
N doped graphite		1.41			-2.66	0.98 0.84 0.84
N doped graphite + O		1.49	1.40	-0.49	-1.21	0.69 0.39 0.39

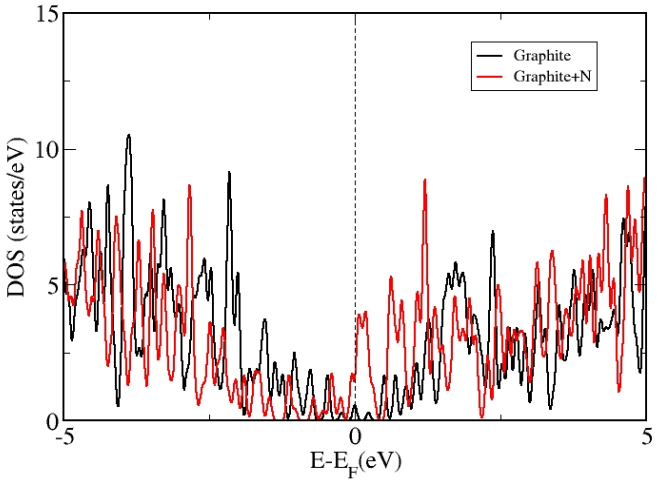

Figure 7.14 The total density of states of the pristine and N-doped graphite surfaces.

In the presence of the N atom, the total DOS at the Fermi level increased, indicating that chances of hybridization with an adsorbate increased. The projected density of states (PDOS) calculated for O adsorbed on pristine and N-doped graphite surfaces is shown in Figure 7.15 A and B, respectively. The PDOS shows metallic behavior and is dominated by the *p* states of C and O. The presence of the N-dopant introduces additional states near the Fermi level, and the probability of hybridization of O *p* states and the graphite surface evidently increases.

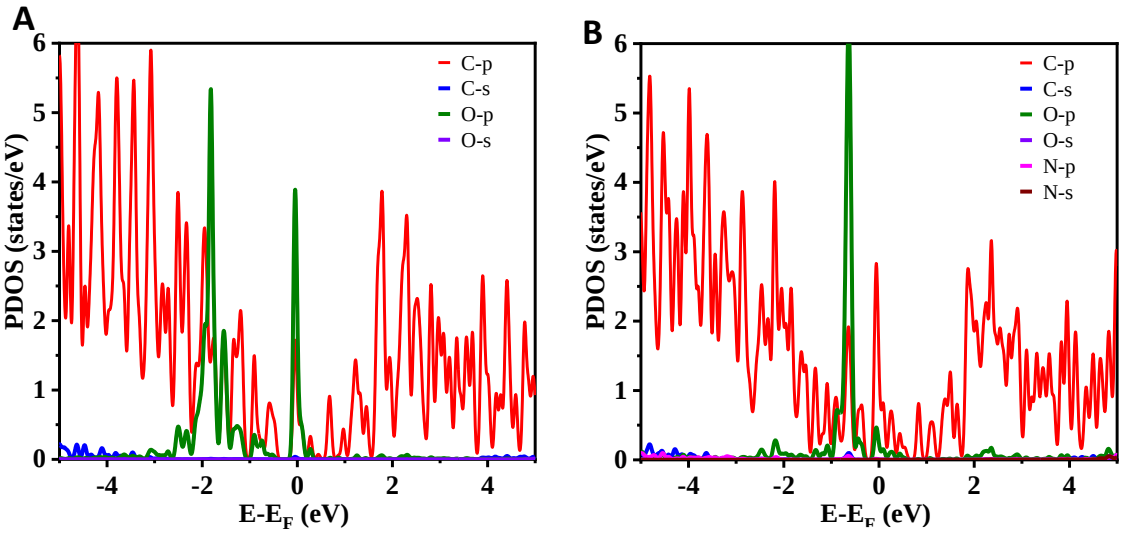

Figure 7.15 The PDOS calculated for (A) O adsorbed on pristine and (B) N-doped graphite surfaces.

The difference in charge density caused by the adsorption of O at the N-doped graphitic surface was calculated. Figure 7.16 shows the charge density difference plot. The yellow and blue isosurfaces indicate charge gain and depletion, respectively. It can be seen that charge gain at the site of N-doping was larger, while the doped O atom also gained charge partially. The C atoms on the surface, which are directly bonded with the N atom, lose charge, and a charge reconstruction occurs at the surface, which helps with the enhanced adsorption of the O atom. The charge density difference analysis and calculated Bader charges are consistent with the shortened bond distances in the presence of N-doping, as presented in Table 7.4. The DFT investigations thus support the concept of N-doping, which very likely occurred during the heat treatment of the GM precursors for carbon.

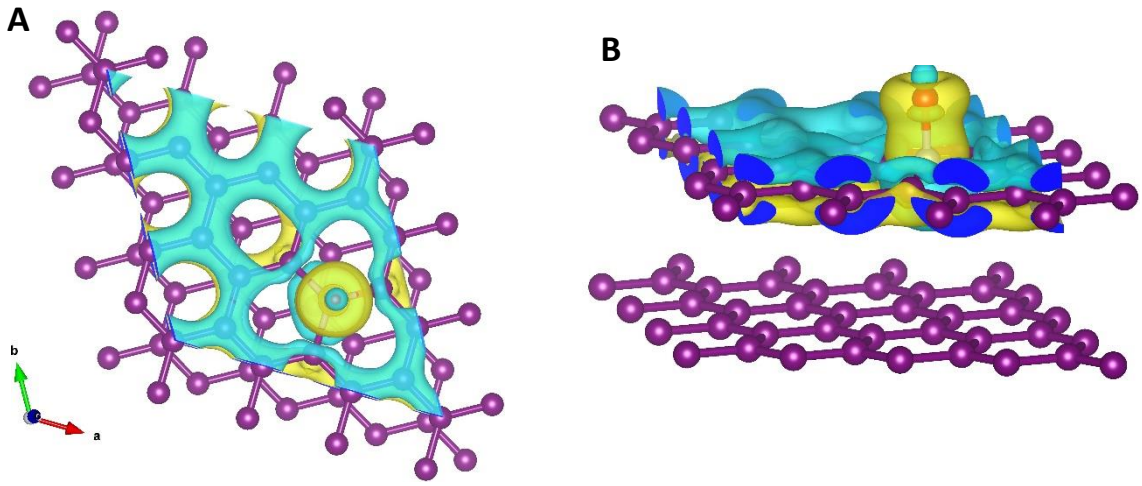

Figure 7.16 The charge density difference calculated for the N-doped graphitic surface with O adsorption. The pristine and N-doped graphite surfaces are also shown. The yellow and blue isosurfaces indicate charge gain and charge depletion, respectively. The isosurface level is 0.062368 e/Å3". The color code of the atoms is as follows - purple: C, red: O, white: N.

7.4.4. Machine Learning insights: MLP Model

Machine learning can dramatically accelerate calculations, improve energy storage prediction accuracy, and make optimized decisions based on comprehensive status information to develop novel materials. Machine learning prediction has also been widely adopted in the field of materials science [69,70]. Depending on its end applications, ML has been classified into material property prediction, the discovery of novel materials, and various other purposes, such as battery management, etc. When constructing the ML models for material property predictions, researchers have extended their insights on various aspects, such as predicting the electronic properties of inorganic crystals [71], geometric features of gas storage and separation using metal-organic frameworks [72], transport properties in granular materials [73], and the effect of the pore size on capacitance [25]. Moreover, ML models are also used for efficient optimization by designing their parameters [74], applying them to DFT problems [75], monitoring the state of the battery during operation [76], etc. However, surface morphology has not been considered in previous ML studies. The particle morphologies can be quite diverse, based on biomass precursor or synthesis conditions affecting energy storage performance [35,77,78]. As a step towards extracting useful information from electrode material texture, two input features, porosity and surface pore size, were extracted from microscope images using MATLAB [79,80]. A statistical overview was obtained through Pearson correlation, as presented in Figure 7.17. The positive and negative correlations are represented by dark blue and red colors, and the colors in the middle region show no or weak correlations.

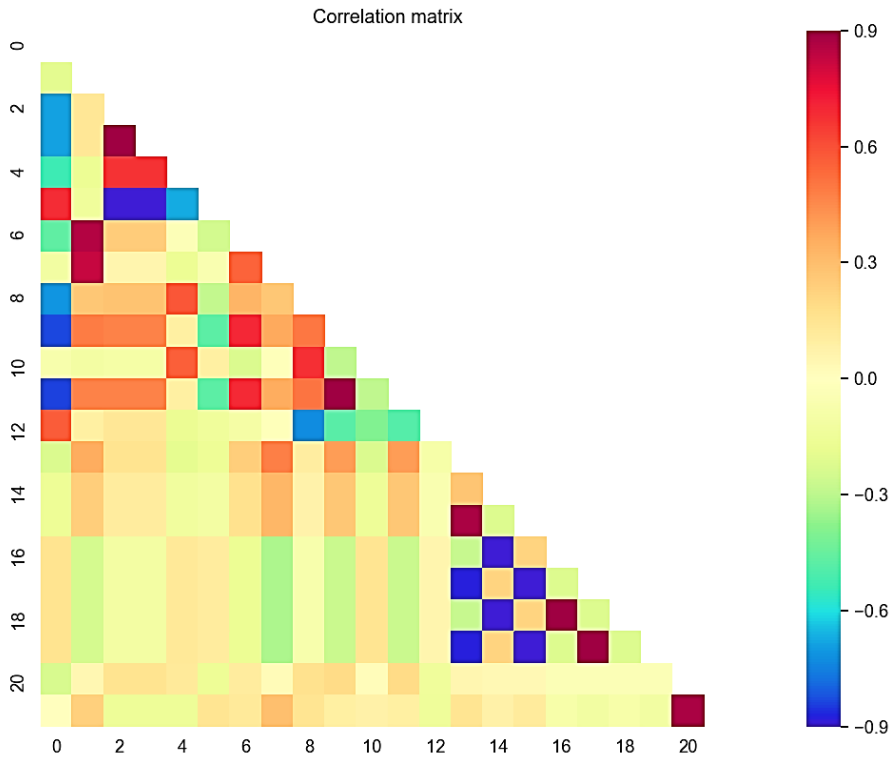

Figure 7.17 Pearson Correlation Coefficient.

A comparison of the MLP model using similar inputs to chapter 6 and the improved number of inputs in this chapter is given in Figure 7.18 A and B. It is shown that the correlation between the actual and predicted capacitances was largely improved from 0.78 (Figure 7.18A) to 0.98 (Figure 7.18B) for R^2 when including more parameters to represent the different samples. In addition, the RMSE value decreased from 14.45 to 4.29, indicating the importance of the additional parameters included in modeling the system. The improved model was used to predict the power density, as shown in Figure 7.18C, which gives 0.97 for R^2 and a value of 0.28 for RMSE. The diagonal line in the figures represents the perfect correlation between experimental values and the predictions. The results indicate that having more material informatics in the model is essential to exploring and designing high-performing materials. This model could accurately retrieve the nonlinear patterns to correlate the inputs and outputs compared

to the traditional theoretical models and speed up these processes in the materials science field.

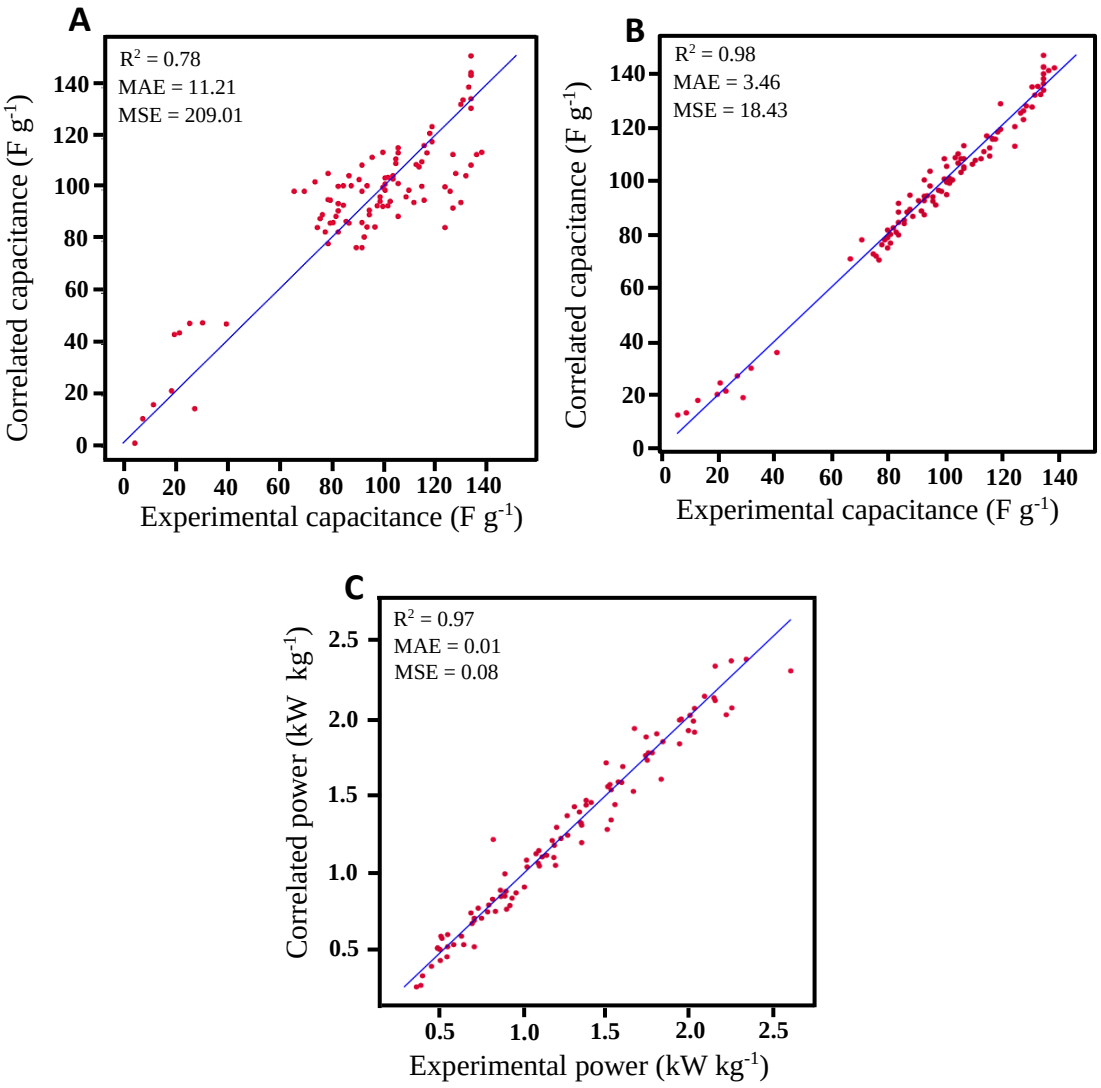

Figure 7.18 Comparison of correlation for the predicted specific capacitance (F g^{-1}) and the actual experimental specific capacitance (F g^{-1}) between (A) MLP model with '6' inputs and (B) MLP model with more inputs, (C) correlated power (kW kg^{-1}), and the actual power density (kW kg^{-1}) of the samples.

7.5. Conclusion

The sustainable GM was effectively tailored into AC, making it a promising material for supercapacitor applications. The physicochemical and electrochemical results showed that KOH activation is preferable to $ZnCl_2$ activation under the tested sequence of the synthesis process. The GM-derived AC (KAC_{urea}) from the precursor of mixed GM and urea for N-doping further improved the physicochemical properties and, hence, the electric double-layer capacitor (EDLC) behavior. KAC_{urea} presented hierarchical pores and the highest specific surface area among the studied samples. Consequently, KAC_{urea} delivered the highest specific capacitance of 139 F g^{-1} at the 2 mA current rate in the alkaline NaOH electrolyte. Therefore, the symmetric capacitor behavior was studied using the best-performing KACurea electrodes in 2 M NaOH with a 1 V potential window. DFT calculations indicated that N-doping enhanced the adsorption of O atoms on the graphitic surface, owing to the charge-transfer mechanism. The electronic structure analysis revealed increased hybridization of orbitals of the adsorbate and graphite surface in the presence of the N-dopant. Therefore, improved ion adsorption occurs during the charge-discharge process. Increasing the number of inputs in the MLP model delivered the best correlations between actual and predicted capacitances. The work in this chapter could support future efforts in interdisciplinary areas such as electrochemistry, materials science, and energy combined with ML applications for energy storage devices.

7.6. References

(1) Wang, L.; Wu, J.; Ma, H.; Han, G.; Yang, D.; Chen, Y.; Zhou, J. H_3PO_4-Assisted Synthesis of Apricot Shell Lignin-Based Activated Carbon for Capacitors: Understanding the Pore Structure/Electrochemical Performance Relationship. *Energy & Fuels* **2021**, *35* (9), 8303–8312.

(2) Strauss, V.; Marsh, K.; Kowal, M. D.; El-Kady, M.; Kaner, R. B. A Simple Route to Porous Graphene from Carbon Nanodots for Supercapacitor Applications. *Adv. Mater.* **2018**, *30* (8), 1–10.

(3) Mofokeng, T. P.; Tetana, Z. N.; Ozoemena, K. I. Defective 3D Nitrogen-Doped Carbon Nanotube-Carbon Fibre Networks for High-Performance Supercapacitor: Transformative Role of Nitrogen-Doping from Surface-Confined to Diffusive Kinetics. *Carbon N. Y.* **2020**, *169*, 312–326.

(4) Simon, P.; Gogotsi, Y. Materials for Electrochemical Capacitors. *Nat. Mater.* **2008**, *7*, 845–854.

(5) Heimböckel, R.; Hoffmann, F.; Fröba, M. Insights into the Influence of the Pore Size and Surface Area of Activated Carbons on the Energy Storage of Electric Double Layer Capacitors with a New Potentially Universally Applicable Capacitor Model. *Phys. Chem. Chem. Phys.* **2019**, *21* (6), 3122–3133.

(6) Bora, M.; Bhattacharjya, D.; Saikia, B. K. Coal-Derived Activated Carbon for Electrochemical Energy Storage: Status on Supercapacitor, Li-Ion Battery, and Li-S Battery Applications. *Energy & Fuels* **2021**, *35* (22), 18285–18307.

(7) Zhang, Y.; Li, X.; Huang, J.; Xing, W.; Yan, Z. Functionalization of Petroleum Coke-Derived Carbon for Synergistically Enhanced Capacitive Performance. *Nanoscale Res. Lett.* **2016**, *11*, 163.

(8) Wei, F.; Zhang, H.; He, X.; Ma, H.; Dong, S.; Xie, X. Synthesis of Porous Carbons from Coal Tar Pitch for High-Performance Supercapacitors. *New Carbon Mater.* **2019**, *34* (2), 132–139.

(9) Khiari, B.; Jeguirim, M.; Limousy, L.; Bennici, S. Biomass Derived Chars for Energy Applications. *Renew. Sustain. Energy Rev.* **2019**, *108*, 253–273.

(10) Niu, Q.; Gao, K.; Tang, Q.; Wang, L.; Han, L.; Fang, H.; Zhang, Y.; Wang, S.; Wang, L. Large-Size Graphene-like Porous Carbon Nanosheets with Controllable N-Doped Surface Derived from Sugarcane Bagasse Pith/Chitosan for High Performance Supercapacitors. *Carbon N. Y.* **2017**, *123*, 290–298.

(11) Yakaboylu, G. A.; Yumak, T.; Jiang, C.; Zondlo, J. W.; Wang, J.; Sabolsky, E. M. Preparation of Highly Porous Carbon through Slow Oxidative Torrefaction, Pyrolysis, and Chemical Activation of Lignocellulosic Biomass

for High-Performance Supercapacitors. *Energy & Fuels* **2019**, *33* (9), 9309–9329.

(12) Wang, J.; Zhang, X.; Li, Z.; Ma, Y.; Ma, L. Recent Progress of Biomass-Derived Carbon Materials for Supercapacitors. *J. Power Sources* **2020**, *451*, 227794.

(13) Xu, Z.; Zhang, X.; Yang, X.; Yu, Y.; Lin, H.; Sheng, K. Synthesis of Fe/N Co-Doped Porous Carbon Spheres Derived from Corncob for Supercapacitors with High Performances. *Energy & Fuels* **2021**, *35* (17), 14157–14168.

(14) Fu, Y.; Shen, Y.; Zhang, Z.; Ge, X.; Chen, M. Activated Bio-Chars Derived from Rice Husk via One- and Two-Step KOH-Catalyzed Pyrolysis for Phenol Adsorption. *Sci. Total Environ.* **2019**, *646*, 1567–1577.

(15) Mu, J.; Wong, S. I.; Li, Q.; Zhou, P.; Zhou, J.; Zhao, Y.; Sunarso, J.; Zhuo, S. Fishbone-Derived N-Doped Hierarchical Porous Carbon as an Electrode Material for Supercapacitor. *J. Alloys Compd.* **2020**, *832*, 1–11.

(16) Zhang, Q.; Han, K.; Li, S.; Li, M.; Li, J.; Ren, K. Synthesis of Garlic Skin-Derived 3D Hierarchical Porous Carbon for High-Performance Supercapacitors. *Nanoscale* **2018**, *10* (5), 2427–2437.

(17) Ma, Y. Comparison of Activated Carbons Prepared from Wheat Straw via $ZnCl_2$ and KOH Activation. *Waste and Biomass Valorization* **2017**, *8* (3), 549–559.

(18) Ranaweera, C. K.; Kahol, P. K.; Ghimire, M.; Mishra, S. R.; Gupta, R. K. Orange-Peel-Derived Carbon: Designing Sustainable and High-Performance Supercapacitor Electrodes. *C* **2017**, *3* (4), 25.

(19) Goldfarb, J. L.; Dou, G.; Salari, M.; Grinstaff, M. W. Biomass-Based Fuels and Activated Carbon Electrode Materials: An Integrated Approach to Green Energy Systems. *ACS Sustain. Chem. Eng.* **2017**, *5* (4), 3046–3054.

(20) McNair, R.; Szekely, G.; Dryfe, R. A. W. Sustainable Processing of Electrodes for Membrane Capacitive Deionization (MCDI). *J. Clean. Prod.* **2022**, *342*, 130922.

(21) Australia, W. *Australian Wine: Production, Sales and Inventory 2019–20*; 2021.

(22) Bacic, T. *Recovery of Valuable Products from Lees and Integrated Approach to Minimise Waste and Add Value to Wine Production*; 2003.

(23) Guardia, L.; Suárez, L.; Querejeta, N.; Pevida, C.; Centeno, T. A. Winery Wastes as Precursors of Sustainable Porous Carbons for Environmental Applications. *J. Clean. Prod.* **2018**, *193*, 614–624.

(24) Muhlack, R. A.; Potumarthi, R.; Jeffery, D. W. Sustainable Wineries through Waste Valorisation: A Review of Grape Marc Utilisation for Value-Added Products. *Waste Manag.* **2018**, *72*, 99–118.

(25) Fang, Y.; Zhang, Q.; Cui, L. Recent Progress of Mesoporous Materials for High Performance Supercapacitors. *Microporous Mesoporous Mater.* **2021**, *314* (December 2020), 110870.

(26) Poonam; Sharma, K.; Arora, A.; Tripathi, S. K. Review of Supercapacitors: Materials and Devices. *J. Energy Storage* **2019**, *21* (October 2018), 801–825.

(27) Kado, Y.; Soneda, Y.; Hatori, H.; Kodama, M. Advanced Carbon Electrode for Electrochemical Capacitors. *J. Solid State Electrochem.* **2019**, *23* (4), 1061–1081.

(28) Bora, M.; Bhattacharjya, D.; Saikia, B. K. Coal-Derived Activated Carbon for Electrochemical Energy Storage: Status on Supercapacitor, Li-Ion Battery, and Li–S Battery Applications. *Energy & Fuels* **2021**, (22), 18285–18307.

(29) Wickramaarachchi, W. A. M. K. P.; Minakshi, M.; Gao, X.; Dabare, R.; Wong, K. W. Hierarchical Porous Carbon from Mango Seed Husk for Electro-Chemical Energy Storage. *Chem. Eng. J. Adv.* **2021**, *8*, 100158.

(30) Kresse, G.; Hafner, J. Ab Initio Molecular-Dynamics Simulation of the Liquid-Metalamorphous-Semiconductor Transition in Germanium. *Phys. Rev. B* **1994**, *49* (20), 14251–14269.

(31) Joubert, D. From Ultrasoft Pseudopotentials to the Projector Augmented-

Wave Method. *Phys. Rev. B - Condens. Matter Mater. Phys.* **1999**, *59* (3), 1758–1775.

(32) Perdew, J. P.; Burke, K.; Ernzerhof, M. Generalized Gradient Approximation Made Simple. *Phys. Rev. Lett.* **1996**, *77* (18), 3865–3868.

(33) Monkhorst, H. J.; Pack, J. D. Special Points for Brillouin-Zone Integration*. *J. Mater. Chem. A* **2019**, *7* (5), 2156–2164.

(34) Su, H.; Lin, S.; Deng, S.; Lian, C.; Shang, Y.; Liu, H. Predicting the Capacitance of Carbon-Based Electric Double Layer Capacitors by Machine Learning. *Nanoscale Adv.* **2019**, *1* (6), 2162–2166.

(35) Krishnamurthy, D.; Weiland, H.; Barati Farimani, A.; Antono, E.; Green, J.; Viswanathan, V. Machine Learning Based Approaches to Accelerate Energy Materials Discovery and Optimization. *ACS Energy Lett.* **2019**, *4* (1), 187–191.

(36) Rogers, S.; Girolami, M. *A First Course of Machine Learning*, 2nd ed.; Taylor & Francis: United Kingdom, 2016.

(37) Ran, F.; Yang, X.; Xu, X.; Li, S.; Liu, Y.; Shao, L. Green Activation of Sustainable Resources to Synthesize Nitrogen-Doped Oxygen-Riched Porous Carbon Nanosheets towards High-Performance Supercapacitor. *Chem. Eng. J.* **2021**, *412*, 128673.

(38) Hong, K. L.; Qie, L.; Zeng, R.; Yi, Z. Q.; Zhang, W.; Wang, D.; Yin, W.; Wu, C.; Fan, Q. J.; Zhang, W. X.; Huang, Y. H. Biomass Derived Hard Carbon Used as a High Performance Anode Material for Sodium Ion Batteries. *J. Mater. Chem. A* **2014**, *2* (32), 12733–12738.

(39) Ghosh, S.; Santhosh, R.; Jeniffer, S.; Raghavan, V.; Jacob, G.; Nanaji, K.; Kollu, P.; Jeong, S. K.; Grace, A. N. Natural Biomass Derived Hard Carbon and Activated Carbons as Electrochemical Supercapacitor Electrodes. *Sci. Rep.* **2019**, *9* (1), 1–15.

(40) Hao, E.; Liu, W.; Liu, S.; Zhang, Y.; Wang, H.; Chen, S.; Cheng, F.; Zhao, S.; Yang, H. Rich Sulfur Doped Porous Carbon Materials Derived from Ginkgo

Leaves for Multiple Electrochemical Energy Storage Devices. *J. Mater. Chem. A* **2017**, *5* (5), 2204–2214.

(41) Mopoung, S.; Moonsri, P.; Palas, W.; Khumpai, S. Characterization and Properties of Activated Carbon Prepared from Tamarind Seeds by KOH Activation for Fe(III) Adsorption from Aqueous Solution. *Sci. World J.* **2015**, *2015*, 415961.

(42) Ji, Y.; Li, T.; Zhu, L.; Wang, X.; Lin, Q. Preparation of Activated Carbons by Microwave Heating KOH Activation. *Appl. Surf. Sci.* **2007**, *254* (2), 506–512.

(43) Cherifi, H.; Fatiha, B.; Salah, H. Kinetic Studies on the Adsorption of Methylene Blue onto Vegetal Fiber Activated Carbons. *Appl. Surf. Sci.* **2013**, *282*, 52–59.

(44) Ding, Z.; Trouillet, V.; Dsoke, S. Are Functional Groups Beneficial or Harmful on the Electrochemical Performance of Activated Carbon Electrodes? *J. Electrochem. Soc.* **2019**, *166* (6), A1004–A1014.

(45) Pimenta, M. A.; Dresselhaus, G.; Dresselhaus, M. S.; Cançado, L. G.; Jorio, A.; Saito, R. Studying Disorder in Graphite-Based Systems by Raman Spectroscopy. *Phys. Chem. Chem. Phys.* **2007**, *9* (11), 1276–1291.

(46) Brunauer, S.; Deming, L. S.; Deming, W. E.; Teller, E. On a Theory of the van Der Waals Adsorption of Gases. *J. Am. Chem. Soc.* **1940**, *62* (7), 1723–1732.

(47) Jiang, H.; Cheng, Y.; Yuan, L. A Langmuir-like Desorption Model for Reflecting the Inhomogeneous Pore Structure of Coal and Its Experimental Verification. *RSC Adv.* **2015**, *5* (4), 2434–2440.

(48) Yagmur, E.; Gokce, Y.; Tekin, S.; Semerci, N. I.; Aktas, Z. Characteristics and Comparison of Activated Carbons Prepared from Oleaster (Elaeagnus Angustifolia L.) Fruit Using KOH and $ZnCl_2$. *Fuel* **2020**, *267* (January), 117232.

(49) Bouchemal, N.; Belhachemi, M.; Merzougui, Z.; Addoun, F. The Effect of Temperature and Impregnation Ratio on the Active Carbon Porosity. *Desalin. Water Treat.* **2009**, *10* (1–3), 115–120.

(50) Ahmadpour, A.; Do, D. D. The Preparation of Activated Carbon from Macadamia Nutshell by Chemical Activation. *Carbon N. Y.* **1997**, *35* (12), 1723–1732.

(51) Wabo, S. G.; Klepel, O. Nitrogen Release and Pore Formation through KOH Activation of Nitrogen-Doped Carbon Materials: An Evaluation of the Literature. *Carbon Lett.* **2021**, *31*, 581–592.

(52) Li, Z.; Guo, K.; Chen, X. Controllable Synthesis of Nitrogen-Doped Mesoporous Carbons for Supercapacitor Applications. *RSC Adv.* **2017**, *7* (49), 30521–30532.

(53) Dubey, P.; Shrivastav, V.; Maheshwari, P. H.; Sundriyal, S. Recent Advances in Biomass Derived Activated Carbon Electrodes for Hybrid Electrochemical Capacitor Applications: Challenges and Opportunities. *Carbon N. Y.* **2020**, *170*, 1–29.

(54) Mondal, A. K.; Kretschmer, K.; Zhao, Y.; Liu, H.; Fan, H.; Wang, G. Naturally Nitrogen Doped Porous Carbon Derived from Waste Shrimp Shells for High-Performance Lithium Ion Batteries and Supercapacitors. *Microporous Mesoporous Mater.* **2017**, *246*, 72–80.

(55) Misnon, I. I.; Zain, N. K. M.; Aziz, R. A.; Vidyadharan, B.; Jose, R. Electrochemical Properties of Carbon from Oil Palm Kernel Shell for High Performance Supercapacitors. *Electrochim. Acta* **2015**, *174* (1), 78–86.

(56) Guo, N.; Li, M.; Wang, Y.; Sun, X.; Wang, F.; Yang, R. Soybean Root-Derived Hierarchical Porous Carbon as Electrode Material for High-Performance Supercapacitors in Ionic Liquids. *ACS Appl. Mater. Interfaces* **2016**, *8* (49), 33626–33634.

(57) Sudhan, N.; Subramani, K.; Karnan, M.; Ilayaraja, N.; Sathish, M. Biomass-Derived Activated Porous Carbon from Rice Straw for a High-Energy Symmetric Supercapacitor in Aqueous and Nonaqueous Electrolytes. *Energy & Fuels* **2017**, *31* (1), 977–985.

(58) Huang, Y.; Peng, L.; Liu, Y.; Zhao, G.; Chen, J. Y.; Yu, G. Biobased Nano

Porous Active Carbon Fibers for High-Performance Supercapacitors. *ACS Appl. Mater. Interfaces* **2016**, *8* (24), 15205–15215.

(59) Yin, H.; Lu, B.; Xu, Y.; Tang, D.; Mao, X.; Xiao, W.; Wang, D.; Alshawabkeh, A. N. Harvesting Capacitive Carbon by Carbonization of Waste Biomass in Molten Salts. *Environ. Sci. Technol.* **2014**, *48* (14), 8101–8108.

(60) Hong, X.; Hui, K. S.; Zeng, Z.; Hui, K. N.; Zhang, L.; Mo, M.; Li, M. Hierarchical Nitrogen-Doped Porous Carbon with High Surface Area Derived from Endothelium Corneum Gigeriae Galli for High-Performance Supercapacitor. *Electrochim. Acta* **2014**, *130*, 464–469.

(61) Subramanian, V.; Luo, C.; Stephan, A. M.; Nahm, K. S.; Thomas, S.; Wei, B. Supercapacitors from Activated Carbon Derived from Banana Fibers. *J. Phys. Chem. C* **2007**, *111* (20), 7527–7531.

(62) Nabais, J. M. V.; Teixeira, J. G.; Almeida, I. Development of Easy Made Low Cost Bindless Monolithic Electrodes from Biomass with Controlled Properties to Be Used as Electrochemical Capacitors. *Bioresour. Technol.* **2011**, *102* (3), 2781–2787.

(63) Gou, G.; Huang, F.; Jiang, M.; Li, J.; Zhou, Z. Hierarchical Porous Carbon Electrode Materials for Supercapacitor Developed from Wheat Straw Cellulosic Foam. *Renew. Energy* **2020**, *149*, 208–216.

(64) Yan, X.; Jia, Y.; Zhuang, L.; Zhang, L.; Wang, K.; Yao, X. Defective Carbons Derived from Macadamia Nut Shell Biomass for Efficient Oxygen Reduction and Supercapacitors. *ChemElectroChem* **2018**, *5* (14), 1874–1879.

(65) Mondal, A. K.; Kretschmer, K.; Zhao, Y.; Liu, H.; Fan, H.; Wang, G. Naturally Nitrogen Doped Porous Carbon Derived from Waste Shrimp Shells for High-Performance Lithium Ion Batteries and Supercapacitors. *Microporous Mesoporous Mater.* **2017**, *246*, 72–80.

(66) Liu, S.; Zhao, Y.; Zhang, B.; Xia, H.; Zhou, J.; Xie, W.; Li, H. Nano-Micro Carbon Spheres Anchored on Porous Carbon Derived from Dual-Biomass as High Rate Performance Supercapacitor Electrodes. *J. Power Sources* **2018**,

381, 116–126.

(67) Ramirez, N.; Sardella, F.; Deiana, C.; Schlosser, A.; Müller, D.; Kißling, P. A.; Klepzig, L. F.; Bigall, N. C. Capacitive Behavior of Activated Carbons Obtained from Coffee Husk. *RSC Adv.* **2020**, *10* (62), 38097–38106.

(68) Xu, Z.; Zhang, X.; Liang, Y.; Lin, H.; Zhang, S.; Liu, J.; Jin, C.; Choe, U.; Sheng, K. Green Synthesis of Nitrogen-Doped Porous Carbon Derived from Rice Straw for High-Performance Supercapacitor Application. *Energy and Fuels* **2020**, *34* (7), 8966–8976.

(69) Dubey, P.; Shrivastav, V.; Kaur, A.; Maheshwari, P. H.; Sundriyal, S. Surface and Diffusion Charge Contribution Studies of Human Hair- Derived Heteroatom-Doped Porous Carbon Electrodes for Supercapacitors. *Energy & Fuels* **2022**, *36* (1), 626–637.

(70) Pal, B.; Yang, S.; Ramesh, S.; Thangadurai, V.; Jose, R. Electrolyte Selection for Supercapacitive Devices: A Critical Review. *Nanoscale Adv.* **2019**, *1* (10), 3807–3835.

(71) Liu, Y.; Zhao, T.; Ju, W.; Shi, S.; Shi, S.; Shi, S. Materials Discovery and Design Using Machine Learning. *J. Mater.* **2017**, *3* (3), 159–177.

(72) Schmidt, J.; Marques, M. R. G.; Botti, S.; Marques, M. A. L. Recent Advances and Applications of Machine Learning in Solid-State Materials Science. *npj Comput. Mater.* **2019**, *5*, 83 (2019).

(73) Isayev, O.; Oses, C.; Toher, C.; Gossett, E.; Curtarolo, S.; Tropsha, A. Universal Fragment Descriptors for Predicting Properties of Inorganic Crystals. *Nat. Commun.* **2017**, *8*, 15679 (2017).

(74) Fernandez, M.; Woo, T. K.; Wilmer, C. E.; Snurr, R. Q. Large-Scale Quantitative Structure-Property Relationship (QSPR) Analysis of Methane Storage in Metal-Organic Frameworks. *J. Phys. Chem. C* **2013**, *117* (15), 7681–7689.

(75) Van Der Linden, J. H.; Narsilio, G. A.; Tordesillas, A. Machine Learning Framework for Analysis of Transport through Complex Networks in Porous,

Granular Media: A Focus on Permeability. *Phys. Rev. E* **2016**, *94* (2), 022904.

(76) Diao, Y.; Yan, L.; Gao, K. A Strategy Assisted Machine Learning to Process Multi-Objective Optimization for Improving Mechanical Properties of Carbon Steels. *J. Mater. Sci. Technol.* **2022**, *109*, 86–93.

(77) Snyder, J. C.; Rupp, M.; Hansen, K.; Müller, K. R.; Burke, K. Finding Density Functionals with Machine Learning. *Phys. Rev. Lett.* **2012**, *108*, 253002.

(78) Shi, S.; Gao, J.; Liu, Y.; Zhao, Y.; Wu, Q.; Ju, W.; Ouyang, C.; Xiao, R. Multi-Scale Computation Methods: Their Applications in Lithium-Ion Battery Research and Development. *Chinese Phys. B* **2015**, *25*, 018212.

(79) Chong, S.; Lee, S.; Kim, B.; Kim, J. Applications of Machine Learning in Metal-Organic Frameworks. *Coord. Chem. Rev.* **2020**, *423*, 213487.

(80) Ge, M.; Su, F.; Zhao, Z.; Su, D. Deep Learning Analysis on Microscopic Imaging in Materials Science. *Mater. Today Nano* **2020**, *11*, 100087.

(81) Rabbani, A.; Salehi, S. Dynamic Modeling of the Formation Damage and Mud Cake Deposition Using Filtration Theories Coupled with SEM Image Processing. *J. Nat. Gas Sci. Eng.* **2017**, *42*, 157–168.

(82) Ezeakacha, C. P.; Rabbani, A.; Salehi, S.; Ghalambor, A. Integrated Image Processing and Computational Techniques to Characterize Formation Damage. In *Proceedings - SPE International Symposium on Formation Damage Control*; Lafayette, Louisiana, USA; February 2018.

Chapter 8 Conclusions and future recommendations

This thesis discussed the electrolytic manganese dioxide (EMD) and biomass waste-derived activated carbon (AC); Mango seed husk (MS-AC) and Grape marc (GM-AC) synthesis, and their physicochemical results, electrochemical performances in supercapacitor (SC) applications. The modified EMD (positive electrode) and biomass-derived AC (negative electrode) materials were coupled to fabricate hybrid capacitors to obtain higher specific capacitances and energy densities. The performance results of the hybrid capacitors showed the potential of the synthesized materials to be utilized in energy storage applications. The concluding remarks of this thesis are further elaborated in the following section, 8.1. Important recommendations for future researchers are given in section 8.2.

8.1. Conclusions

To this end, anodic electrodeposition of manganese dioxide (MnO_2) is conducted at optimized parameters of the electrodeposition current, deposition time period, electrolytic bath temperature with appropriate acid, and Mn salt concentrations. This method results in the bulk synthesis (shown in Figure 1.8 in chapter 1) of the electrochemically active gamma-manganese dioxide (γ-MnO_2, otherwise termed 'EMD'). Lead (Pb) anode and stainless steel (SS) cathode are used as the two electrodes. When using the manganese sulfate ($MnSO_4$) precursor (Mn 50 g l^{-1}), the electrolyte solution was prepared in an acidic medium using sulfuric acid (H_2SO_4 25 g l^{-1}) to electrodeposit the pristine EMD material. It was demonstrated that the applied current density is a significant parameter, which influences the morphology, hence the storage performance. The optimized synthesis conditions to ensure efficient energy consumption during the process with improved specific capacitances of the electrodes are; a current density of 200 A m^{-2} and deposition time duration of 5 hours at 95 °C temperature of the electrolytic bath. Therefore, the EMD material can be synthesized under these conditions via the anodic electrodeposition method. Once the synthesis

conditions are optimized, high-quality EMD can be obtained through a careful selection of additives. In this thesis, we utilized a biopolymer Alginic acid (Alg) and various cationic surfactants as additives in the electrolytic bath, along with optimizing their concentrations, which improved the electrochemical performance of EMD.

By varying the Alginic acid concentrations in the electrolytic bath, the morphology of the EMD deposit was strongly affected. Adding the Alg to the electrolytic bath caused the polymer chains to interact with the Mn^{2+} ions in the solution influencing the EMD morphology, which was examined by the molecular modeling of the specie interactions in the electrolyte solution. The concentration of the Alg determined the level of its effect on the deposit.

On the other hand, when the surfactants were added to the electrolyte solution, their effect was highly correlated to the surfactant molecular structure. Three different molecular structures of quaternary ammonium salts were studied; single chain, double chain, and single-chain structure with an aryl group. When used at different concentrations, all the surfactants tend to show unique morphologies in the deposition. In this case, the Benzyldodecyldimethylammonium bromide (B-AB) surfactant was discovered to be the most influencing structure for uniform nucleation and growth of EMD on the Pb anode, as evidenced by the molecular simulation and the electrochemical performance results. It might have stabilized the Mn^{3+} ions in the solution until it undergoes the disproportionation reaction. Thus, it avoids the formation of MnOOH film across the surface, leading to a smooth, uniform MnO_2 deposit. The pristine and modified EMD-specific capacitances determined by testing at the same conditions are summarized in Table 8.1, and the cyclic voltammetry (CV) galvanostatic charge-discharge (GCD) results are summarized in Figure 8.1. The surfactant-modified EMD sample was the best performed in terms of the specific capacitance, hence most suitable for fabricating the hybrid capacitor (explained by the equation (1.8) in chapter 1).

Table 8.1 Specific capacitances of the Pristine EMD and modified EMD, tested in the three-electrode aqueous cell at a 1 mA cm^{-2} current density using a 2 M NaOH aqueous electrolyte.

EMD material	Specific capacitance ($F\ g^{-1}$)
Pristine EMD	98
EMD/0.5 Alg	487
EMD/ B-AB_{30}	602

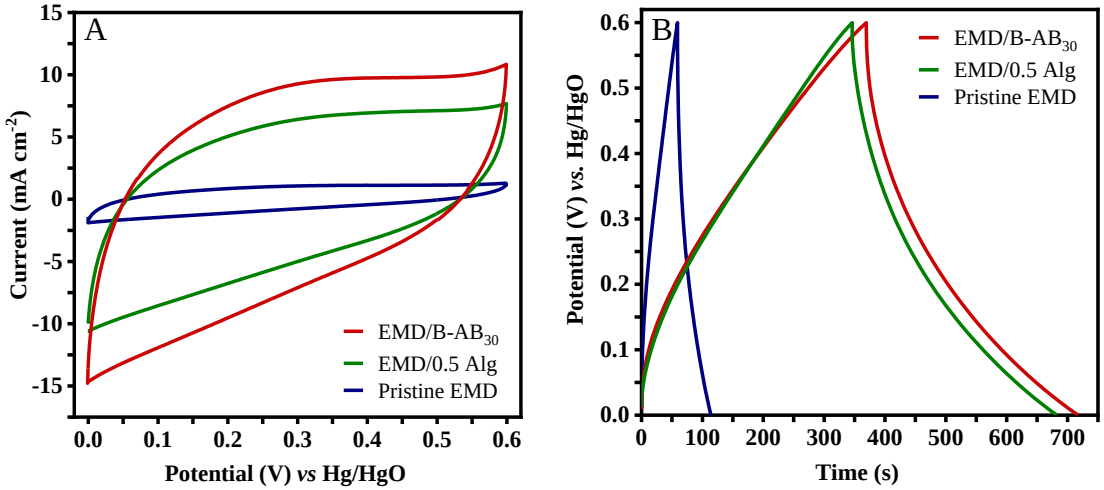

Figure 8.1 (A) CV, (B) GCD results obtained for pristine EMD and modified EMD materials (with biopolymer 0.5 g l^{-1} Alg and B-AB_{30}).

The commercially available AC is widely used to fabricate the capacitors. In this thesis, the commercial AC was compared with biomass-derived AC synthesized with waste biomass materials (Mango seed husk - MS, Grape marc - GM) (Figure 1.9 in chapter 1) which are abundant, low-cost, and sustainable waste materials available in Australia and worldwide. The activation temperatures were varied for synthesizing MS-AC materials, and their performances were analyzed using experimental and machine learning (ML) modeling. Based on their synthesis conditions, activating agents, and dopants, GM-AC performances were analyzed via experimental and theoretical approaches.

It was observed that with increasing activation temperatures (> 800 °C), the AC tends to develop better hierarchical pore structures but reduces material yield. Hierarchical pore structures and surface area of the materials affect the creation of the uninterrupted pathways for electrolyte ion transportation. When the activating agent is a base (KOH), carbonization and activation could be carried out at higher temperatures (≥ 800 °C). For neutral activating agents ($ZnCl_2$), the temperature ranges for carbonization and activation can be relatively lower (≤ 700 °C). For GM carbon, urea was used as a Nitrogen (N) dopant. The N-doped carbon increased its surface functionality, allowing more charge storage capability and increased specific capacitance, which was confirmed by the density functional theory (DFT) studies. Compared to the commercial AC (81 F g^{-1}), the biomass waste-derived MS-AC (135 F g^{-1}) and GM-AC (139 F g^{-1}) showed better electrochemical performance (Table 8.2), indicating that the waste can be a promising alternative to producing porous carbon. Among the MS-AC and GM-AC, the MS-AC showed a better rate capability with increasing current rates in GCD measurements. Figure 8.2 summarizes the CV and GCD results of commercial AC, MS-AC, and GM-AC.

By comparing the different machine learning (ML) models (Decision tree - DT, Liner regression - LR, SVR - Support vector regression, Multi-layer perceptron - MLP), the MLP model can better correlate the physicochemical and electrochemical parameters for specific capacitance prediction. Unlike the other models, MLP is a class of artificial neural network (ANN) and precisely identifies the non-linear relationships between the input and output parameters. Therefore, the MLP model can be improved with more input parameters to develop a generic ML model for predicting the synthesis conditions to obtain desired capacitance values from carbon electrodes. Repurposing the biomass waste into AC, coupled with model predictions, paves the way to produce higher-performing carbon electrodes.

Table 8.2 Specific capacitances of commercial AC and biomass waste-derived AC, tested in the three-electrode aqueous cell at a 2 mA cm^{-2} current density using a 2 M NaOH electrolyte.

AC	Specific capacitance ($F\ g^{-1}$)
Commercial AC	81
MS-AC	135
GM-AC	139

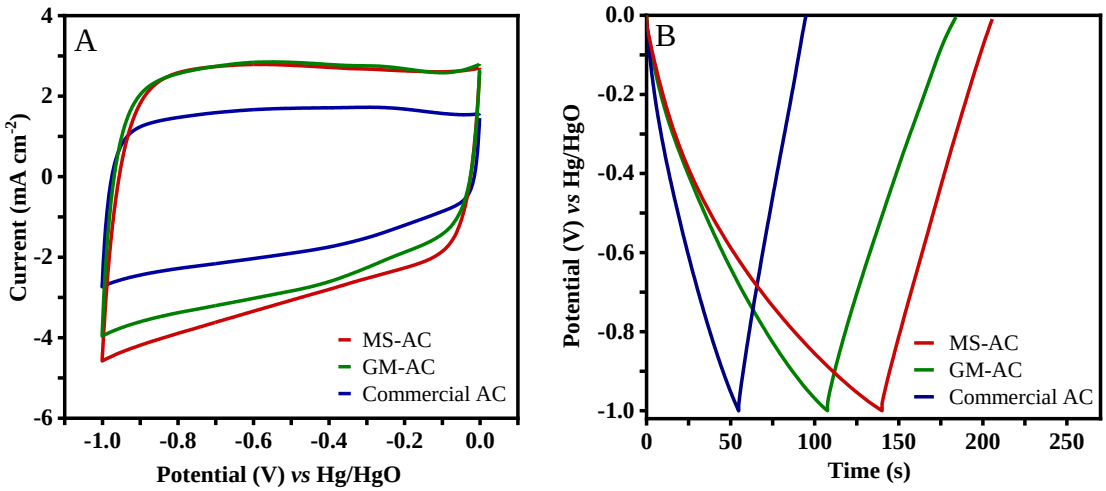

Figure 8.2 (A) CV and (B) GCD results obtained for commercial AC and biomass waste-derived AC materials (MS-AC and GM-AC). (The coated active mass of the electrodes can be varied for each electrode tested).

Finally, the modified EMD and the biomass-derived carbon electrodes were used to fabricate the aqueous hybrid capacitor, which exhibited excellent storage properties. The hybrid capacitor comprises the high-quality EMD/B-AB_{30}, and MS-AC delivered 91 F g^{-1} specific capacitance, an outstanding energy density of 32.4 Wh kg^{-1} for a corresponding power density of 971 W kg^{-1} in 2 M NaOH aqueous electrolyte. On the other hand, the hybrid capacitor comprising pristine EMD delivered a meager value of 36 F g^{-1} specific capacitance, 10 Wh kg^{-1} specific energy, and 2352 W kg^{-1} specific power. The difference is attributed to the unique surfactant molecular structure, which

tailored the deposition of MnO_2 particles, thus the physicochemical properties of EMD.

Overall, this thesis illustrated that the high-quality EMD could be produced in bulk and highlights the opportunities to use biomass waste as an alternative for commercial AC to fabricate the hybrid capacitors for energy storage applications. In summary, Figure 8.3 represents the operating potential windows and the delivered current of the AC electrodes in the (+) and (-) regions and the modified EMD in the (+) region. Clearly, the EMD can be used as a positive electrode in the capacitor; hence the conventional positive AC electrodes from symmetric capacitors can be replaced. Moreover, the cell voltage can be increased from 1 V of the symmetric AC capacitor to 1.6 V of the hybrid capacitor while improving its energy density. Figure 8.4 A and B illustrate an overall comparison of the CV and GCD performances of two hybrid capacitors of EMD/B-AB_{30} *vs.* MS-AC and pristine EMD *vs.* commercial AC.

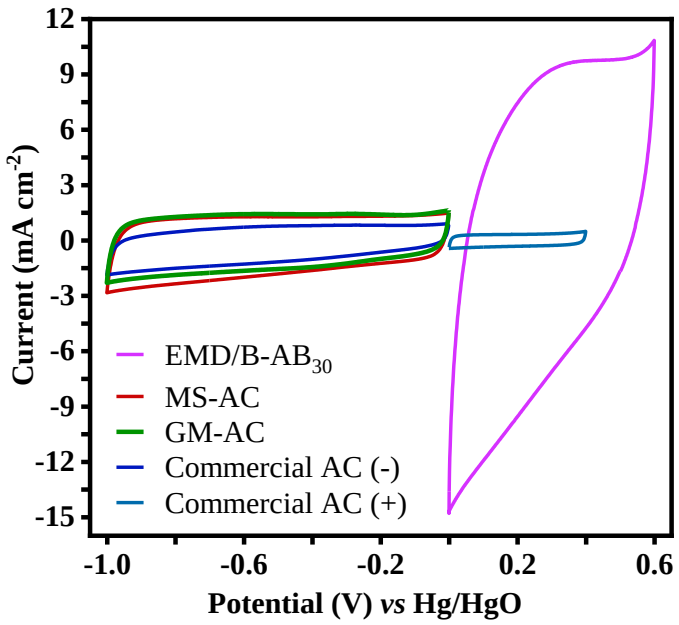

Figure 8.3 Working potential window of a range of single electrodes of commercial AC, GM-AC, MS-AC, and modified EMD (EMD/B-AB_{30}) showing their suitability in the (-) potential window and in the (+) potential window, respectively.

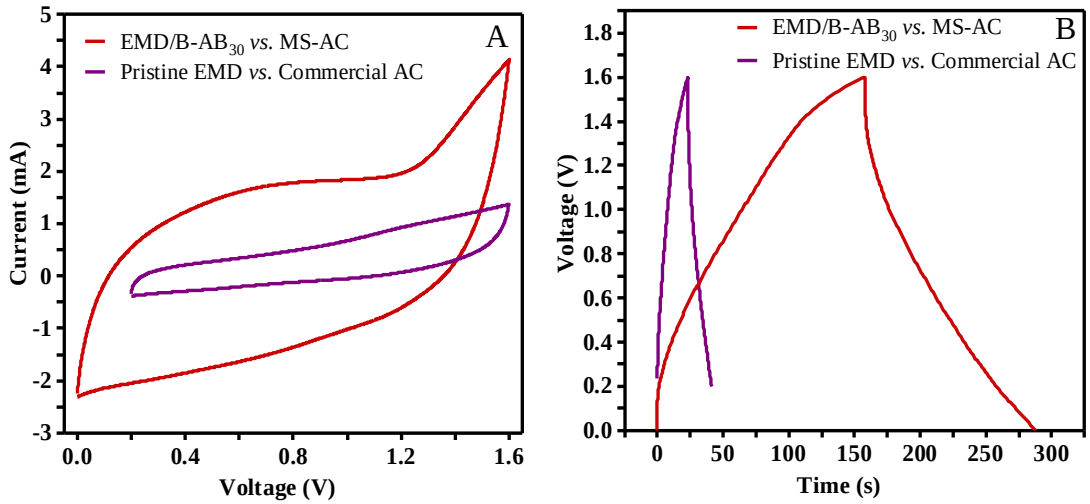

Figure 8.4 (A) CV and (B) GCD results obtained for the hybrid capacitors of pristine EMD *vs.* AC and surfactant modified EMD *vs.* MS-AC illustrating the improvements in electrochemical performance.

8.2. Future recommendations

1. This thesis mainly discussed the experimental aspect of conducting the electrodeposition experiment. However, the experiment can be guided via a computational model for electrochemical synthesis of the material in the future. It would optimize and fine-tune the electrodeposition conditions for pristine EMD synthesis. It can help find the optimum conditions when producing composites using additives in the electrolytic bath. From this thesis, it is evident that the variations of the electrodeposition conditions affect the morphology; therefore, a model can provide an understanding of how to manipulate the material morphology desired for a particular energy storage application.
2. Potential utilization of secondary sources such as battery scrapes and other electronic waste material components (Mn and other metal ion elements, polymer materials, etc.) as additives in the electrolytic bath can be researched. The unknown elemental compositions of these sources can be determined via suitable methods to match the desired material concentrations in the electrolytic bath. The development of this method addresses the waste

problems and creates more opportunities to address the current energy storage demand.

3. Varying biomass waste alternatives can be examined to produce porous carbon materials. Using and improving greener approaches for the synthesis can be followed by utilizing the by-products of bio-oil and biogas for other heat and energy applications to make the process more sustainable when scaling up. In addition, the synthesis can be made more efficient if the synthesis conditions are predicted prior to carrying out the experiments, where machine learning algorithms can be developed and employed in predicting the synthesis conditions of carbon.

4. Na-ion capacitors (SIC) have been developing in recent years and showing a comparable performance with Li-ion and K-ion devices. SICs are composed of the battery type (+) electrode and capacitor type (-) electrode, therefore, it improves the performance and fills the gaps that exist with traditional supercapacitors and Na-ion batteries. Using the aqueous electrolytes in SIC is greener and more sustainable for the field. The narrow voltage window exhibited by the electrodes when using aqueous Na-ion electrolytes has become a significant challenge to expanding its usage in energy storage applications. Therefore, future research directions can be in finding the solutions for mapping high-voltage electrodes to increase the energy density of the aqueous SICs, which would be a significant breakthrough in the energy field.